SOLID OXIDE FUEL CELL SYSTEMS FOR HEAVY GOODS VEHICLE PROPULSION

by

MARCUS ALEXANDER TAYLOR

A thesis submitted to the University of Birmingham for the degree of
DOCTOR OF PHILOSOPHY

Centre for Fuel Cell and Hydrogen Research
School of Chemical Engineering
College of Engineering and Physical Sciences
University of Birmingham
December 15, 2024

Abstract

The performance of solid oxide fuel cell (SOFC) systems is investigated in this thesis for the propulsion of heavy goods vehicles (HGVs) from the perspective of reducing fuel consumption and greenhouse gas emissions in this transport sector. Advantages of SOFC systems over equivalent low-temperature fuel cell systems include their higher electrical efficiencies and their high-temperature off-heat for thermal integration opportunities. Vehicles with SOFC systems can utilise existing liquefied natural gas (LNG) refuelling infrastructure, and are compatible with the phase-in of synthetic natural gas produced from renewable resources. LNG has the advantages over hydrogen of higher volumetric energy density and lower energy requirement for liquefaction.

This thesis presents a dynamic model of an SOFC system. The current density-voltage characteristics of the SOFC stack are validated against experimental results, and steady-state system modelling results including anode off-gas recirculation are compared to modelling results in literature. The chemical reaction and thermal dynamics are studied in the transient response, and control strategies are developed to maintain the SOFC stack temperature, fuel utilisation, and steam-to-carbon ratio.

A novel aspect of this thesis is the investigation of the dynamic response of SOFC systems when subjected to standardised drive cycles for the propulsion of a 40 t HGV, and as part of a hybrid system coupled with a battery. During load changes the time derivative of the stack temperature can be maintained within acceptable limits, helping to maximise the lifetime of the SOFC system, but hybridisation of the SOFC system with a battery is required to handle more violent accelerations of the vehicle. The battery enables

downsizing of the SOFC system power to 54 kW, and for energy recuperation through regenerative braking. The ageing of SOFC stacks reduces their power and efficiency over their lifetimes, and is highlighted as a challenge for their operation in HGV applications.

A heat loss model predicts the cool down of the SOFC systems when the vehicle is not in operation, and a detailed start-up strategy investigates thermal transients set up by the SOFC stack reactions. One challenge for the application of SOFC systems in HGVs is the 30 minutes required to start-up. This means early start-up of the SOFC system before vehicle operation is required, or a larger battery to compensate for the reduced electrical power output of SOFC system during that period. With the predictable usage cycles of commercial vehicles such as HGVs, the slow start-up times of SOFC systems may be more acceptable than for passenger cars.

Start-up also creates larger thermal transients in the SOFC stack than other operating modes. The stack is cooled initially by the endothermal methane steam reforming reaction, before heating from the electrochemical oxidation of hydrogen reaction as the current ramps up. Sufficient insulation of the hotbox components means that they cool by less than 100°C overnight, and therefore the system can be directly started the following morning. After weekend cool-down additional heating is required to bring the SOFC stack back up to its operating temperature, which is provided by electrical heating elements integrated into the hotbox components.

The dynamic modelling framework and transient results provide an insight into the potential and challenges of SOFC systems for HGV propulsion, which advances the progress towards the application of SOFCs systems in commercial vehicles. The framework can be used as a basis for more detailed component design or enhanced for greater insight into the thermal gradients during operation. With a generalised modelling approach, the framework can be adapted to capture future improvements in the performance of SOFC technology and their systems.

Acknowledgements

This work was supported by the Engineering and Physical Sciences Research Council (EPSRC) grant for the Centre for Doctoral Training (CDT) in Fuel Cells and their Fuels. Additional support was provided by Horiba Mira Ltd.

I would like to thank my supervisors Professor Robert Steinberger-Wilckens, Dr Yousif Al-Sagheer, and Dr Ahmad El-Kharouf for their help and advice with this PhD. Thank you to Adam Zucconi, Michele Braglia, Richard Stocker, and the late Martin Watkinson at Horiba Mira for their insight and feedback. Thank you to Rory Adams at Mathworks for his support with Matlab. Thank you to all of the researchers at the Centre for Fuel Cell and Hydrogen Research, in particular to Bhargav Pandya, for support through this PhD journey.

Contents

List of Figures

List of Tables

List of Abbreviations

Anode heat exchanger (AHEX)

Activation, ohmic and concentration (AOC)

Anode off-gas recirculation (AOGR)

Auxiliary power unit (APU)

Balance of plant (BoP)

Catalytic partial oxidation (CPOX)

California Air Resources Board (CARB)

Cathode heat exchanger (CHEX)

Centre for Fuel Cell and Hydrogen Research (CFCHR)

Combined heat and power (CHP)

Compressed natural gas (CNG)

Continuous stirred-tank reactor (CSTR)

Depth of discharge (DoD)

Engineering Equation Solver (EES)

Environmental Protection Agency (EPA)

European Union (EU)

Forschungzentrum Jülich (FZJ)

Greenhouse gas (GHG)

Electrochemical oxidation of hydrogen (H2X)

Heat exchanger (HEX)

Hydrogen fuel cell electric vehicle (HFCEV)

Heavy goods vehicle (HGV)

Heavy Heavy-Duty Diesel Truck (HHDDT)

Internal combustion engine (ICE)

Lower heating value (LHV)

Lithium-ion (Li-ion)

Liquefied natural gas (LNG)

Large-scale (LS)

Methane steam reforming (MSR)

Not applicable (N/A)

New European Driving Cycle (NEDC)

Number of transfer units (NTU)

Open circuit voltage (OCV)

Polymer electrolyte fuel cell (PEFC)

Plug flow reactor (PFR)

Revolutions per minute (RPM)

Steam-to-carbon ratio (S/C ratio)

Synthetic natural gas (SNG)

State-of-charge (SoC)

Solid oxide fuel cell (SOFC)

Single repeating unit (SRU)

Small-scale (SS)

Urban Dynamometer Driving Schedule for Heavy-Duty vehicles (UDDS HD)

United Kingdom (UK)

United Nations Economic Commission for Europe (UNECE)

Water gas shift (WGS)

World Harmonized Vehicle Cycle (WHVC)

Worldwide Harmonised Light Vehicles Test Procedure (WLTP)

Nomenclature

A	area	m^2
a	chemical activity	
ASR	area specific resistance	$\Omega\,\mathrm{m}^2$
C_p	heat capacity	$\mathrm{J\,kg^{-1}\,K^{-1}}$
c_p	molar heat capacity	$\mathrm{J\,mol^{-1}\,K^{-1}}$
D	thickness	m
E	activation energy	$\mathrm{kJ\,mol^{-1}}$
E_0	reversible cell voltage	V
F	Faraday's constant	$\mathrm{C\,mol^{-1}}$
G	transfer function	
g	molar Gibbs free energy	$\mathrm{J\,mol^{-1}}$
h	molar enthalpy	$\mathrm{J\,mol^{-1}}$
I	current	A
i	current density	$\mathrm{A\,cm^{-2}}$
K	reaction equilibrium constant	
k	reaction rate constant	$\mathrm{mol\,m^{-2}\,bar^{-1}\,s^{-1}}$
k_ins	thermal conductivity	$\mathrm{W\,m^{-1}\,K^{-1}}$
LHV	lower heating value	$\mathrm{J\,kg^{-1}}$
M	molecular mass	$\mathrm{kg\,mol^{-1}}$
m	mass	kg
$\dot{m}$	mass flow rate	$\mathrm{kg\,s^{-1}}$

n	number of electrons	
$\dot{n}$	molar flow rate	$\mathrm{mol\,s^{-1}}$
N_{cell}	number of cells	
P	power	kW
p	pressure	bar
p_{stack}	stack power density	$\mathrm{W\,cm^{-2}}$
$\dot{Q}$	heat transfer or production rate	W
R	molar gas constant	$\mathrm{J\,mol^{-1}\,K^{-1}}$
r	rate of reaction	$\mathrm{kg\,s^{-1}}$
RR	recirculation ratio	
s	molar entropy	$\mathrm{J\,mol^{-1}\,K^{-1}}$
T	temperature	K
t	time	s
U	heat transfer coefficient	$\mathrm{W\,m^{-2}\,K^{-1}}$
U_f	fuel utilisation	
V	voltage	V
V_0	open circuit voltage	V
v_0	gas compartment volume	$\mathrm{m^3}$
w_x	Nernst weighting factor	
X	reaction conversion	
x	mass fraction	
y	mole fraction	
ΔP	pressure drop	kPa
ε	heat exchanger effectiveness	
η	efficiency	
γ	specific gas ratio of air	
λ	air stoichiometry	
ν	stoichiometric coefficient	

ρ	density	$\mathrm{kg\,m^{-3}}$

Subscripts

A	on the anode-side of the SOFC stack
C	on the cathode-side of the SOFC stack
cold	on the heat exchanger cold-side
hot	on the heat exchanger hot-side
i	of species i
in	at the gas compartment inlet
j	at port j of the gas compartment
k	of reaction k
max	maximum
min	minimum
out	at the gas compartment outlet
S	of the stack
V	in gas compartment V

Chapter 1

Introduction

1.1 Emissions from heavy goods vehicles

The transport sector contributes significantly to greenhouse gas (GHG) emissions, with the IPCC [1] reporting in 2022 that the transport sector accounted for 15 % of GHG emissions globally. In the European Union (EU) [2] and the United Kingdom (UK) [3], the percentage contribution of the transport sector is even larger, accounting for around 25 % of their GHG emissions in 2022. Furthermore, GHG emissions from the transport sector are rising faster globally than any other sector [1], by an average of 2 % per year from 2010 to 2019.

Figure 1.1 [4] shows the trend in GHG transport emissions in the EU, and specifically from heavy goods vehicles (HGVs). HGVs are all road vehicles over 4 t used for freight transport, primarily trucks. Between 1990 and 2019, annual GHG emissions from HGVs in the EU grew by 29 %, before dropping in 2020 during the Covid-19 pandemic. The UK has fared better [3], with GHG emissions from domestic transport decreasing by 13 % between 1990 and 2021. However, GHG emissions from HGVs in the UK fell by only 1 %. These trends in transport emissions are in sharp contrast to trends in the total emissions in those regions. Between 1990 and 2021, average annual GHG emissions from all sectors fell by 30 % in the EU [2], and by 48 % in the UK [3].

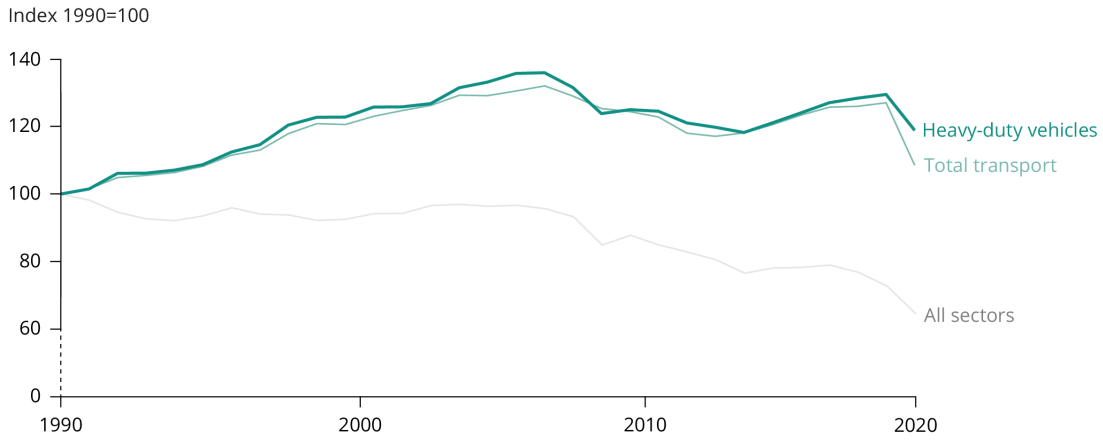

Figure 1.1: Trend of CO_2 emissions from HGVs in the EU, 1990–2020 [4].

HGVs are responsible for about a quarter of GHG emissions from road transport, both in the EU [4] and the UK [3]. This is despite HGVs accounting for only about 4 % of the total number of road vehicles in those regions [5]. The reason for this disparity can be seen when comparing HGVs to passenger cars. HGVs in the EU have an average annual mileage around six times higher than passenger cars [6]. HGVs are much heavier than passenger cars, and hence have relatively low fuel economy. The fuel economy of new HGVs over 25 t in the UK in 2010 was on average 6.5 miles per gallon [7], about seven times less than 45 miles per gallon for new passenger cars produced the same year [8].

Reducing GHG emissions from HGVs is a challenge. As shown in [1, 3, 4], GHG emissions from HGVs remain high. The primary driver for this has been an increased demand for inland freight transport [4], which between 2000 and 2019 increased by nearly 25 % in the EU . This has been somewhat offset by improvements in energy efficiency. Between 2000 and 2019, the energy consumption per tonne-kilometre transported decreased by almost 15 % in the EU [4]. Freight transport by rail or ship is more energy efficient than by road, and hence shifting away from road freight is one way to reduce GHG emissions. However, HGVs will still be required for mid-distance freight transport and local distribution. Therefore, technologies for zero-emission propulsion of HGVs are required.

1.2 Powertrains for heavy goods vehicles

The European Automobile Manufacturers' Association (ACEA) reported the EU to have 6.4 million HGVs in use in 2023 [5], out of which 96 % ran on diesel-fuelled internal combustion engines (ICEs). To eliminate GHG emissions from HGVs, the EU is focused on the adoption of alternative powertrains, in particular of battery electric vehicles (BEVs) and hydrogen fuel cell electric vehicles (HFCEVs) [4]. However, uptake of those technologies for HGVs is currently limited [5], with 0.1 % of HGVs reported to be BEVs in the EU, and only a handful to be HFCEVs.

There are a number of challenges facing the adoption of zero-emission propulsion technologies for HGVs. The powertrains of BEVs are around 20 % heavier than diesel-fuelled ICEs [9]. With the same payload, the range of the HGV is reduced, which impacts the profitability of the operator [6]. An additional problem for BEVs is the slow battery recharging [9]. On the other hand, hydrogen has a high gravimetric density, but its low volumetric density means the fuel tanks take up more space than those for diesel. There is currently limited hydrogen refuelling infrastructure, and 98 % of hydrogen is produced from fossil fuels, mostly from steam reforming of natural gas, known as 'grey hydrogen'. When combined with carbon capture and storage as 'blue hydrogen´, this creates a CO_2 storage issue.

Around 0.8 % of HGVs in the EU ran on natural gas in 2023 [5]. The number of compressed natural gas (CNG) and liquefied natural gas (LNG) vehicles in Europe is growing [10]. The volumetric energy density of LNG is less than diesel, but considerably more than liquefied hydrogen. Uptake of natural gas vehicles is eased by the prevalence of natural gas infrastructure with nearly five thousand refuelling stations in 2023 in Europe. The primary driver for switching from diesel to LNG or CNG is the fuel cost savings, estimated to be 35 % in 2019 [10]. GHG emissions are about 6 % lower than for diesel vehicles [10].

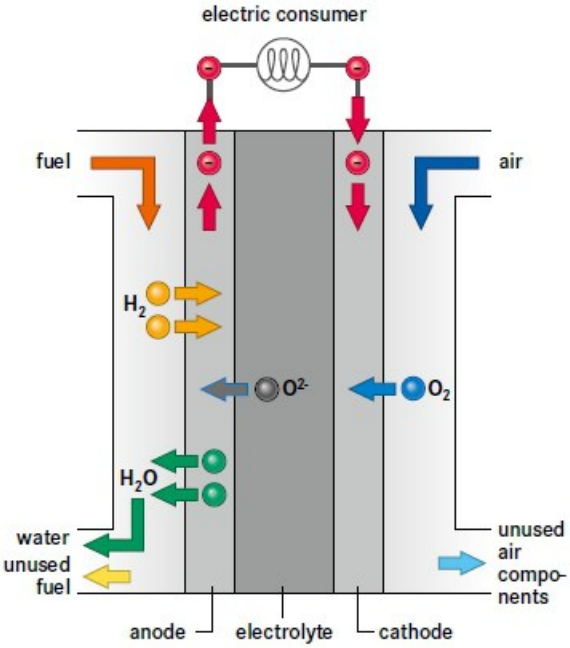

Figure 1.2: Schematic of an SOFC [11].

1.3 Introducing solid oxide fuel cells (SOFCs)

Natural gas-fuelled vehicles use an ICE to do mechanical work to turn the wheels of the vehicle. This thesis proposes replacing the ICE with an electric motor for propulsion and solid oxide fuel cells (SOFCs) for electricity production. Currently, SOFC technology is not widely considered within the transport sector, but further investigation is worthwhile. The reasons why SOFCs are potentially an attractive technology for transportation will be discussed in Section 1.4, but first this section will introduce the fundamentals of SOFC technology.

1.3.1 SOFC concept

The SOFC is an electrochemical device. It converts chemical energy stored in fuel to electricity, through an electrochemical oxidation reaction. A schematic of an SOFC is shown in Figure 1.2. Fuel, for example hydrogen, is supplied to the anode. An oxidant, usually air, is provided to the cathode. Oxygen in the air is reduced to oxygen ions at

the cathode, and the chemical equation is:

$$\frac{1}{2}\,O_2 + 2\,e^- \longrightarrow O^{2-} \tag{1.1}$$

The negatively charged oxygen ions cross the electrolyte to the anode. Hydrogen is oxidised by the oxygen ions to produce water at the anode, and the chemical equation is:

$$H_2 + O^{2-} \longrightarrow H_2O + 2\,e^- \tag{1.2}$$

The electrons flow around the external circuit and generate an electrical current. Combining the two half cell reactions gives the electrochemical oxidation of hydrogen reaction, and the chemical equation is:

$$H_2 + \frac{1}{2}\,O_2 \xrightarrow{r_{H2X}} H_2O \tag{1.3}$$

The majority of SOFC electrolytes are oxygen ion-conducting rather than proton-conducting, so the electrochemical oxidation reaction occurs at the anode. The exhaust streams are water and unused fuel from the anode, and oxygen-depleted air from the cathode.

1.3.2 SOFC materials

SOFCs are characterised by their solid oxide or ceramic electrolyte. High temperatures are required to achieve sufficient oxygen ion conductivity in the electrolyte. Most SOFCs today operate between 600°C and 800°C. The electrolyte must also have low electronic conductivity, high redox stability and good mechanical properties [12]. The metal oxide zirconia (ZrO_2) is commonly doped with yttria (Y_2O_3) to stabilise it in a cubic fluorite structure, known as yttria-stabilised zirconia (YSZ). Ceria (CeO_2) is attractive for low-temperature SOFCs, but an electron blocking layer is required to prevent the reduction

of Ce^{4+}.

The electrodes must have good ionic and electronic conductivity, and high porosity, and hence are made from complex composite microstructures [12]. The electrochemical reactions occur at the triple phase boundary where the gas, electrocatalyst and electrolyte meet. Many anodes use nickel (Ni) as the electrocatalyst, which is sintered with YSZ to produce a Ni/YSZ cermet. At the cathode, lanthanum perovskites are commonly used with lanthanum strontium manganite (LSM) composites working well for high-temperature SOFCs at around 800°C. Lanthanum strontium cobalt ferrite (LSCF) functions well in low-temperature SOFCs, but requires a diffusion barrier layer—commonly cerium-gadolinium oxide (CGO)—to prevent strontium from the LSCF reacting with zirconia in the electrolyte.

Because the SOFC must occasionally be cycled between room temperature and the operating temperature, an additional requirement of the SOFC materials is that their thermal expansion coefficients must match well, in order to give stable interfaces [12].

1.3.3 SOFC repeating units

Originally, many cell configurations were tubular, but nowadays, the majority of commercially available SOFCs are planar, due to their higher power density and lower manufacturing costs. SOFCs may be electrolyte-supported, anode-supported or metal-supported. Anode-supported cells can be operated at lower temperatures than electrolyte-supported cells, because the electrolyte can be made thinner, and hence its contribution to ohmic resistance reduced. Metal-supported cells are generally only feasible in lower temperature designs.

Figure 1.3 shows a schematic of a repeating unit of the anode-supported planar SOFC from Forschungzentrum Jülich [13]. Flow channels on both the anode and cathode sides are required to distribute the reactants over the cell and remove the reaction products. The metallic interconnects conduct the electricity produced in the cell between adjacent cells, whilst also matching the thermal expansion coefficients. These elements form a

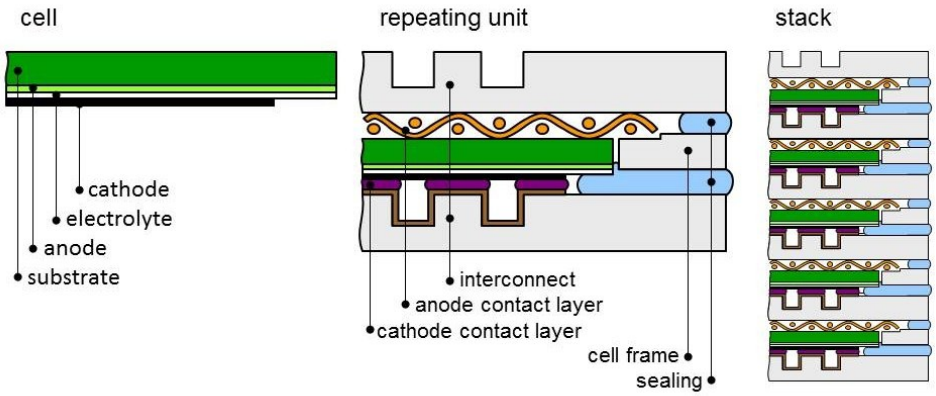

Figure 1.3: Cross-section of a Jülich repeating unit and assembly into a stack [13].

single repeating unit.

SOFCs are modular, meaning that cells can be stacked up to form an SOFC stack. At the stack-level, the air and fuel supply are important design decisions. Manifolding is used to distribute the fuel and air to all cells in the stack. Different flow fields are used to distribute the gases over the cell area; for example, parallel, serpentine, and radial. The flow configuration of the fuel and air can be co-flow, counter-flow or cross-flow. The choice of the stack design will have a great impact on the current and temperature distribution over the stack, and hence the heat management requirements.

1.3.4 SOFC system configurations

The SOFC stack produces electrical power that can be used to meet the power requirements of an application; for example, the electric motor on a vehicle. A number of balance of plant (BoP) components are required to operate the SOFC stack.

1.3.4.1 The BoP components

For automotive applications, fuels such as hydrogen and natural gas are stored under high pressure or as a cryogenic liquid to maximise their volumetric energy density. A throttling valve is used to control the flow rate and pressure of fuel delivered to the SOFC system, and thus no fuel compression is required on-board the vehicle. A fuel pre-heater heats the

fuel before entering the anode. This helps to reduce the thermal gradients in the SOFC stack.

Air is supplied to the cathode from the ambient environment with an air blower. The air blower provides sufficient head pressure to overcome the pressure drop in the pipes and components of the SOFC system, and deliver the required flow rate of air. Like the fuel side, the cathode heat exchanger heats the air before entering the cathode, to reduce the thermal gradients within the SOFC stack. The air provides not only the oxygen for the electrochemical oxidation of hydrogen reaction, but also cools the stack. As a result, the air flow is usually much larger than the fuel flow. Many SOFC systems use an afterburner to oxidise any unreacted fuel and reformate. The heat produced in the afterburner is used to pre-heat the cold air and fuel streams in the heat exchangers.

1.3.4.2 Reforming in SOFC systems

Hydrogen can be oxidised directly within the SOFC stack but natural gas and other hydrocarbon fuels are usually reformed. Peters et al. [14] showed that the majority of SOFC systems reform natural gas with either methane steam reforming (MSR) in the presence of steam, or catalytic partial oxidation (CPOX) in the presence of air. The MSR and CPOX reactions for methane are shown in Equations (1.4) and (1.6), respectively. In the presence of steam in the steam reformer, the water gas shift reaction occurs as a second step, shown in Equation (1.5).

$$\mathrm{CH_4 + H_2O} \xrightarrow{r_{\mathrm{MSR}}} \mathrm{CO + 3\,H_2} \tag{1.4}$$

$$\mathrm{CO + H_2O} \xrightleftharpoons{r_{\mathrm{WGS}}} \mathrm{CO_2 + H_2} \tag{1.5}$$

$$\mathrm{CH_4 + \frac{1}{2}\,O_2} \longrightarrow \mathrm{CO + 2\,H_2} \tag{1.6}$$

While SOFC stacks can internally reform methane through the MSR reaction, most SOFC systems include a CPOX or MSR pre-reformer [14]. This is due to concerns about carbon deposition and high temperature gradients in stacks with internal reforming only

[15].

MSR can be integrated within the fuel pre-heater but requires a supply of water. With anode off-gas recirculation (AOGR), water can be recycled within the SOFC system to avoid the need for an external water supply during normal operation. Peters et al. [16] presented six different concepts for water recirculation. One layout used a condensate trap in the flue gas stream. Three layouts used a blower to recirculate the anode off-gas, with each blower operating at a different temperature. Two layouts used an ejector to recirculate the anode off-gas. Ejectors are easy to operate at high temperatures but are more difficult to control under part-load operation than recirculation blowers.

One particular advantage of SOFC technology is its ability to internally reform methane on the anode through the endothermic MSR reaction within the SOFC stack. This helps to cool the SOFC stack and can help to reduce the air flow required.

CPOX reformers are simpler because they require only a supply of air. Therefore, CPOX reforming can also be useful for systems without an external water supply. However, systems with CPOX reformers have lower electrical efficiencies than systems with steam reformers, since two moles of hydrogen are produced for every mole of methane in Equation (1.6), rather than three for MSR in Equation (1.4).

1.3.4.3 Other components

Thermal insulation of the SOFC stack and the hot BoP components is required [17]. This helps to maintain the stack temperature when operating at part load. It also reduces thermal cycling between operational periods, which helps to extend the lifetime of the stack, and decreases start-up times.

In order to start-up an SOFC system [18] with steam reforming of methane, a supply of steam is required before water is available on the anode, and can be recirculated through AOGR. A water tank and steam generator can be used, or a CPOX reformer.

When the SOFC is connected to a variable load, such as the electric motor on a vehicle, power conditioning is required [19]. A DC-to-DC converter is used to control the

voltage on the DC bus, where the SOFC voltage varies depending on its power settings. In transport applications, a hybrid design with a battery is often used [20]. The battery acts as an energy buffer to reduce the dynamic operation of the fuel cell, and enable regenerative braking. It also allows downsizing of the fuel cell by reducing its peak power rating.

1.4 SOFC technology for vehicle propulsion

The use of SOFCs for vehicle propulsion offers a number of advantages over other propulsion technologies such as ICEs, polymer electrolyte fuel cells (PEFCs), and electric batteries. The main attractions of SOFCs are their high efficiency, fuel flexibility, off-heat availability, and the ease with which they can be integrated into an electric powertrain.

The electrical efficiency of an SOFC running on methane is significantly higher than that of an ICE or PEFC. Elcogen achieved a stack efficiency of 74 % [21] and FuelCell Energy demonstrated SOFC systems with a DC electrical efficiency of 64 % with methane fuel [22]. The higher efficiency results in reduced fuel consumption and lower emissions. In contrast, the range of BEVs are limited by the weight and volume of the batteries.

Like batteries and PEFCs, SOFCs generate electrical work which can be used to power an electric motor. Electric motors have a number of advantages over ICEs [23]: They have higher efficiency, are quieter, and vibrate less than ICEs. Unlike ICEs, electric motors can deliver high torques from zero revolutions per minute [24], and have limited need for a gearbox. A hybrid battery can be easily integrated into an electric drivetrain to meet transient load requirements. These factors provide significant advantages of electric drivetrains over ICEs.

The high operating temperature of SOFCs does present some drawbacks. It means that start-up times tend to be lengthy, and the lifetime of the stack can be sensitive to thermal cycling. These are issues which will be investigated further within the thesis. On the other hand, the high temperature off-heat can be utilised, a feature which none of

the other electric propulsion technologies possess. In stationary applications, SOFCs are commonly used for combined heat and power applications. On a vehicle, SOFCs could be used to meet the thermal requirements, such as powering a vapour absorption refrigeration system [25] for a refrigerated truck. Another potentially attractive application is for the large air conditioning requirements of off-road construction vehicles. SOFCs are also increasingly being considered for maritime applications, where, for example, cruise ships have high hotel heat and power requirements.

1.5 SOFC fuel choices for mobility

SOFC systems are fuel flexible and with appropriate reforming have been demonstrated to run on a range of fuels, including diesel, LPG, methanol, bio-ethanol, natural gas, biogas, ammonia, and hydrogen. The deployment of SOFC systems in different transport applications, and with different fuels will be investigated in Section 2.7.

This thesis focuses on running SOFCs on zero-fossil carbon hydrocarbon fuels, due to their high volumetric energy densities. SOFCs already run today on the existing widespread natural gas infrastructure, such as for micro-CHP applications in Japan. SOFCs can internally reform hydrocarbon fuels, which helps to simplify their system layout when compared to PEFCs running on natural gas. SOFCs can also electrochemically oxidise carbon monoxide, which is a poison in PEFCs. The fuel flexibility and higher efficiency of SOFC systems offers clear advantages when compared to PEFCs.

With SOFC technology, synthetic natural gas (SNG) based on biomass or 'non-fossil' CO_2 can be phased in to replace natural gas, without needing any changes to the refuelling infrastructure or the vehicle drivetrains. SNG can be produced from co-electrolysis of water and biomass-derived carbon dioxide using electricity generated from renewable sources such as wind and solar. This offers a zero emission transport solution, which can better meet the energy density requirements of HGVs than BEVs or HFCEVs.

1.6 Modelling SOFC systems

Computational modelling is increasingly important for the development of SOFC systems. Modelling can provide insight into a range of aspects relating to SOFCs over a wide range of scales, from investigating the interactions that define the reaction mechanisms on the electrodes through to system-level simulations [26]. The computational tools best suited depend on the scale at which the question is being addressed. Detailed cell and stack modelling, in particular CFD, can help to understand the internal physics and electrochemistry of fuel cells which are hard to characterise experimentally [27]. Modelling of fuel cell and stack components can play a role in fuel cell development, by guiding experimental work and helping to reduce the number of experiments that must be conducted [28]. At a system-level, process simulation of SOFCs and the BoP components supports system design and optimisation [27]. Dynamic simulation provides insight into the system performance under variable load, and issues arising during start-up and thermal cycling. In addition, control algorithms [29] can be developed based upon the results of dynamic SOFC system simulation results.

Without experimental validation of the model, there are limitations in the utility of models for detailed design and optimisation of an SOFC system. A generalised SOFC system model, like the model which will be presented in this thesis, can be validated with key system measures, and a variety of different BoP configurations can be studied. In summary, process simulation of SOFC systems is a powerful tool for studying the feasibility of the technology for a range of applications.

1.7 Overview of the thesis

This research conducts dynamic process simulations of SOFC systems to assess their feasibility for propulsion of HGVs. Each chapter of this thesis illustrates a different aspect of the research.

- Chapter 2 reviews the existing literature for the dynamic modelling of SOFC sys-

tems, especially for transport applications. The current state-of-the-art for SOFC system development, especially when deployed in transport applications is investigated, and the research gaps identified are used to form the objectives of this thesis.

- Chapter 3 presents the methodology used within this thesis to construct the dynamic model of the SOFC system.

- Chapter 4 presents the steady-state performance of the SOFC stack and BoP components in the SOFC system model. Results from the literature are used to validate the model.

- Chapter 5 presents the open loop and controlled response of the SOFC system to changes in electrical load and flow rates. The air, fuel, and anode off-gas recirculation flowrates are varied to maintain the desired operating conditions in the controlled response.

- Chapter 6 presents the response of the SOFC system when subjected to a number of standardised drive cycles for HGV propulsion. The performance of a hybrid system with a battery, and the effect of stack ageing are investigated.

- Chapter 7 builds upon Chapter 6 to investigate the behaviour of the SOFC during a week-long load profile for a commercial HGV, including overnight and weekend cool-down.

- Chapter 8 offers a summary of the work presented and an outlook to further research leads.

Chapter 2

Literature review

This chapter reviews the literature to understand how solid oxide fuel cell (SOFC) systems have been modelled, and the results that have been presented. Particular focus is given to authors who conducted dynamic modelling of SOFC systems to investigate their performance under load profiles which include shut-down and start-up. The literature review is divided into a number of sections:

- Section 2.1 reviews the methodology used to model SOFC systems and their components,
- Section 2.2 reviews the steady-state performance and the operating constraints of the SOFC systems modelled,
- Section 2.3 reviews the dynamic response of the SOFC systems modelled,
- Section 2.4 reviews energy management strategies for SOFC-battery hybrid systems,
- Section 2.6 reviews the performance of SOFC systems during shut-down, cool-down, start-up, heat-up, and hot standby, and
- Section 2.7 reviews the deployment of SOFC systems in transport applications.

2.1 Modelling methodology for SOFC systems

In this section, SOFC system models will be categorised according to their dimensions and either their steady state or dynamic state [30]. Then, the generalised approach to modelling components of the SOFC system will be reviewed. Following that, the approaches used to model specific aspects of each component—the SOFC stack, blowers, heat exchangers, burner, and reformer—will be reviewed.

2.1.1 Categorising models according to their dimensions

Each component of an SOFC system can be modelled with a continuum approach from 0D up to 3D. To illustrate the different modelling dimensions, Figure 2.1 shows a simplified diagram of an SOFC stack consisting of 5 cells in the y direction. Each cell has a number of flow channels in the x direction. The gases in the anode and cathode channels flow through each flow channel in the z direction. The spatial variation in current density, temperature, and reaction rate, and gas composition may be considered in each direction. The model dimensions are the number of dimensions in which the spatial variation in each variable is considered, and are defined as:

- A 3D model simulates the spatial variation of variables in the z direction along the length of each flow channel, in the x direction between flow channels in a cell, and in the y direction between cells,
- A 2D model simulates the spatial variation of variables in the z direction along the length of each flow channel, in the x direction between flow channels in a cell, but assumes uniform distribution in the y direction between cells,
- A 1D model simulates the spatial variation of variables in the z direction along the length of each flow channel, but assumes uniform distribution in the x direction between flow channels in a cell, and in the y direction between cells, and
- A 0D model assumes uniform distribution of variables in the z direction along the

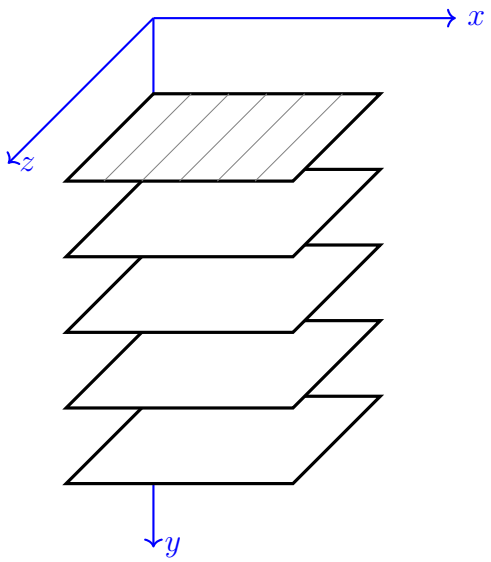

Figure 2.1: Simplified illustration of a 5-cell SOFC stack, showing the x, y and z directions, as used to highlight the differences between the 3D, 2D, 1D and 0D modelling approaches.

length of each flow channel, in the x direction between flow channels in a cell, and in the y direction between cells.

Many detailed 2D and 3D component models exist in the literature, especially for the SOFC stack [31]. 3D models, in particular, benefit from CFD simulation software to resolve the spatial variation of the variables within a component. Such models are an important simulation tool for investigating the detailed relationship between the thermal, chemical and electrical interactions with an SOFC. However, for full SOFC system models which investigate the transient response to drive cycles for vehicles, 3D models of individual components with CFD become too computationally expensive. This is supported by this literature review, in which the SOFC system models found modelled each component in either 0D or 1D. The 0D and 1D modelling approaches provide a suitable compromise between model accuracy and computational burden, for example, when developing the energy management strategy of a hybrid SOFC system with a battery for heavy goods vehicle (HGV) propulsion. For that reason, some additional details of 0D and 1D modelling for SOFC system models will be discussed in the following, and also, 2D and 3D component models are not reviewed in detail within this thesis, nor CFD. For further details of more detailed component models, refer to [31].

2.1.1.1 0D modelling

In 0D modelling, the fluids within each compartment are assumed well-mixed, meaning they have uniform composition and temperature. This is referred to as a continuous stirred-tank reactor in chemical engineering fundamentals. 0D modelling of the SOFC stack also assumes uniform current density across each cell, and uniform distribution of gases across all cells and flow channels. In the same sense, the solid mass of a component can be modelled in 0D, where the temperature distribution within the solid is assumed uniform. In 0D modelling, the temperature of the solid sub-components—e.g., the cell and the interconnects in the SOFC stack—are commonly lumped into a single bulk temperature.

2.1.1.2 1D modelling

1D or distributed modelling of gas compartments captures the temperature and concentration distributions in the streamwise direction. This is referred to as a plug flow reactor in chemical engineering fundamentals. 1D energy balances can also be conducted for the solid mass of the system components to find their temperature distributions. In 1D SOFC stack models, the current density varies along the length of the cell, while the cell voltage is assumed constant, due to the high electrical conductivity of the interconnects.

The 1D approach is particularly relevant for modelling SOFC stacks with internal reforming [32]. The endothermic methane steam reforming (MSR) reaction proceeds quickly and influences the temperature distribution in the stack considerably. Many authors have conducted 1D, 2D or 3D stack modelling to investigate the cooling effect that occurs near the anode inlet and the resultant thermal gradients.

To ease the computational burden, 1D component models are commonly discretised using the finite difference method. The number of nodes for the discretisation are selected as a compromise between good spatial resolution and high computational speed.

2.1.2 Categorising models according to their state

SOFC systems can be modelled at a fixed operating point with the conservation equations for each component conducted under steady-state or constant conditions, meaning they have no dependence on time.

Other models have included dynamic energy balances, and sometimes also dynamic species balances, to simulate the transient response of the SOFC system. Dynamic energy balances take into account the thermal inertia of the gases in each compartment and/or the solid mass of the component. Dynamic species balances consider the inertia of the gas volume within each compartment. Dynamic momentum balances are rarely conducted in the literature when simulating SOFC systems, although they would be required for pressure drop calculations. Through dynamic modelling of SOFC systems, their transient response to load changes, and during start-up and shut-down, can be investigated. SOFC system models can be applied to the load requirements of a HGV, but limited literature was found to be available.

2.1.3 Introducing the modelling approaches

Table 2.1 tabulates the generalised approach used to model the SOFC system components in the literature, according to their dimensions, state, and the approach to simulating heat losses. The table divides the models between those that modelled all of the components in 0D, and those that modelled some or all of the components in 1D. The state of the species and energy balances are listed, as well as the approaches used to estimate the heat losses. Each of these aspects will be discussed in turn in the following, before the specific approach to modelling each component of the SOFC system is discussed thereafter.

2.1.3.1 0D models

Peters et al. [16], Chitsaz et al. [33], Yilmaz et al. [34], Akroot et al. [35], Lisbona et al. [36], and Kupecki [37] all modelled SOFC systems in 0D under steady-state conditions. Sorrentino et al. [38] used a hierarchical approach to reduce a 1D model to 0D to reduce

Table 2.1: Overview of generalised component modelling approaches in the literature.

		Species	Energy	Heat losses
0D				
Peters et al. [16]		Steady	Steady	Adiabatic
Chitsaz et al. [33]		Steady	Steady	Adiabatic
Yilmaz et al. [34]		Steady	Steady	Adiabatic
Akroot et al. [35]		Steady	Steady	Adiabatic
Lisbona et al. [36]		Steady	Steady	Stack only
Kupecki [37]		Steady	Steady	5 % LHV
Sorrentino et al. [38]		Steady	Dynamic	Adiabatic
Gallo et al. [39]		Steady	Dynamic	Coupled
Saarinen et al. [40]		Steady	Dynamic	Furnace
1D	(In 0D)			
Saebea et al. [41]	(BoP)	Steady	Steady	Adiabatic
Huang et al. [42]	(BoP)	Steady	Steady	Adiabatic
Braun et al. [43]	(BoP)	Steady	Steady	$\sim$ 9 % LHV
Mantelli et al. [44]	(Burner)	Steady	Steady	Stack only
Nousch et al. [45]	(Stack)	Steady	Dynamic	Hot box
Albrecht et al. [46]	(BoP)	Mix	Dynamic	1.9 % LHV
Mueller et al. [47]	(Burner)	Dynamic	Dynamic	Adiabatic
Lin Zhang et al. [48]	(Burner)	Dynamic	Dynamic	Adiabatic
Roberts et al. [49]	(Stack)	Dynamic	Dynamic	Burner only
Engelbracht et al. [50]		Dynamic	Dynamic	Adiabatic
D. Andersson et al. [51]		?	Dynamic	?
Mazumder et al. [52]		Dynamic	Dynamic	Blower only

the computational burden without sacrificing accuracy. Sorrentino et al. [38] and Gallo et al. [39] both conducted dynamic energy balances on each component to find the thermal transients of the SOFC system under dynamic conditions. The species balances on each component were conducted at quasi-steady-state, since the chemical reaction transients are much faster than the thermal transients in an SOFC system. Modelling the thermal transients of the SOFC stack is important because those transients induce thermal gradients and hence thermal stresses, which can accelerate degradation of the SOFC stack [53].

2.1.3.2 1D models

Although 1D models can be more accurate than 0D models, discretising each component model increases the computational burden. As a compromise, most of the 1D models depicted at least some of the components in 0D, as shown in brackets in Table 2.1. Saebea et al. [41] and Braun et al. [43] modelled the SOFC stack in 1D and the balance of plant (BoP) components in 0D, to study the steady-state performance of SOFC systems. Albrecht et al. [46] conducted similar modelling, but included a transient analysis. They demonstrated the impact of the thermal inertia of the BoP components on the transient response of the SOFC system. Their model consisted of dynamic energy balances for all components, dynamic species balances for the stack, and quasi-steady state species balances for the BoP components. Within the 1D SOFC stack model, separate energy and species balances were calculated at each node and each layer of the single repeating unit, with heat transfer accounted for between adjacent nodes and layers. Engelbracht et al. [50] and Mazumder et al. [52] modelled all SOFC system components in 1D to study the transient response with dynamic energy and species balances. Mueller et al. [47] and Lin Zhang et al. [48] took the same approach but modelled the burner in 0D for simplicity. Roberts et al. [49] and Nousch et al. [45] modelled the BoP components in 1D, but the stack only in 0D.

To discretise 1D component models, the number of nodes were selected as a compromise between model accuracy and computational time. Engelbracht et al. discretised each flow channel in each component into six nodes [50]. Mueller et al. [47] used ten nodes for each flow channel in the SOFC stack and five nodes for each flow channel in the reformer. Braun et al.'s model [43] was based upon the author's PhD thesis, where they used twenty nodes to model the SOFC stack consisting of cells 10 cm in length [54]. Mantelli et al. used ten nodes in their SOFC stack model [44]. D. Andersson et al. [51] varied the number of nodes in their 1D model between four and fifty, and found that four nodes gave sufficient accuracy. Albrecht et al. [46], Lin Zhang et al. [48] and Mazumder et al. [52] all used discretised 1D models but did not specify the number of nodes in each

component. Saebea et al. [41] and Roberts et al. [49] did not specify how their 1D energy and species balances were established.

2.1.3.3 Heat losses

In order to study the performance of the SOFC system, consideration of heat losses is important, particularly when assessing transient operation including cool-down and start-up. However, many of the authors [16, 33, 34, 38, 41, 47, 48, 50] reviewed in Table 2.1 assumed that each of the system components operated adiabatically. This would require the components to be perfectly insulated, which is an unrealistic assumption. The approaches used by models which have included heat losses are discussed in the following. SOFC system hotboxes are not perfectly insulated, and heat losses must be accounted for to model thermal cycling and other transient conditions.

A number of authors assumed that the heat losses $\dot{Q}_{\text{loss}}$ in W from each component, illustrated in Figure 2.2, were a fixed percentage heat losses (PHL) of the product of the fuel flow rate $\dot{m}_{\text{fuel}}$ in $\text{kg}\,\text{s}^{-1}$, and a lower heating value in $\text{J}\,\text{kg}^{-1}$, and are calculated from:

$$\dot{Q}_{\text{loss}} = \frac{PHL}{100} \cdot LHV \cdot \dot{m}_{\text{fuel}} \tag{2.1}$$

Braun et al. [43] conducted experiments to estimate heat losses from a hot box large enough to contain an SOFC system producing net 1.5 kW of AC power. The hot box was insulated with 5 cm of silica aerogel with a thermal conductivity of $0.03\,\text{W}\,\text{m}^{-1}\,\text{K}^{-1}$. The resulting rate of heat loss was estimated to be 446 W or 9 % of the fuel energy input. The hot box temperature was assumed to be the average of the burner and the SOFC stack temperatures. The results showed that heat losses can indeed be significant, but depend on the geometry, insulation and temperature of the SOFC system.

Some of the authors that implemented heat losses in their SOFC system model, assumed the heat losses all originated from a single component, while the other components

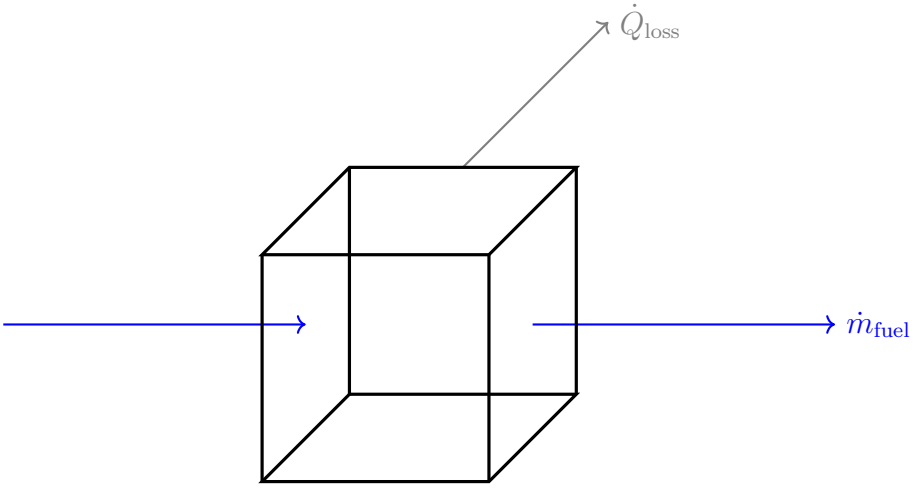

Figure 2.2: Heat losses from the hot box of an SOFC system.

operated adiabatically. This simplified the analysis. Braun et al. [43] and Lisbona et al. [36] assumed all heat losses originated from the SOFC stack, estimated to be 3 % [43], and 7 % [36] of the fuel input, respectively. The decision to assume all other components operated adiabatically was not justified, but one valid reason could be that the stack typically has the largest mass of all SOFC system components [55], and thus dominates the thermal dynamics. Albrecht et al. [46] assumed all heat losses were from the burner and equal to 1.9 % of the fuel energy input. Roberts et al. [49] made the same assumption, arguing that the burner had the highest heat losses of all system components, but the magnitude of those heat losses was not defined. The problem with considering heat losses from a single component, however, is that it is not useful for simulating thermal cycling; for example, with cool-down of an SOFC system. The other components would remain at their operating temperature, which is unrealistic.

Kupecki [37] assumed heat losses equivalent to 5 % of the fuel energy input, but it is not clear how they applied this to their SOFC system component models. Mazumder et al. [52] accounted for heat losses only from the air blower to the ambient environment with a conduction model with a constant heat transfer coefficient; the hotbox components were assumed to be perfectly insulated.

Gallo et al. [39] took into account the heat transfer between the system components but assumed that the hot-box was perfectly insulated. They found reduced thermal

gradients within the components as a result but a quantitative analysis of the findings was not presented. Nousch et al. [45] went further than this by not only including thermal coupling between the SOFC system components within the hot-box, but also the heat losses through the hot box insulation. By modelling both thermal coupling and the ambient heat losses, their paper is the only reviewed that can realistically model the variation in temperature of the SOFC system components during thermal cycling.

Now that the generalised modelling approach has been reviewed, the following sections will review the approaches to modelling specific components: the stack, heat exchangers, burner, pre-reformer, and blowers.

2.1.4 Approach to modelling the SOFC stack

There are a number of differences in methodology between each model of the SOFC stack. Table 2.2 tabulates the approach for each of the models reviewed. Models differ in their approach used to find the rate of the reforming reactions, and in their method for finding the current density-voltage (iV) characteristics. The iV characteristics depend upon the open circuit voltage (OCV) and the voltage losses. The value of the OCV is a function of the gas mole fractions at the anode and cathode, and different authors made different assumptions about their values. Authors used one of two main approaches to find the voltage losses. The modelling approaches are discussed in more detail in the following.

Even so, there were models that did not fit neat categorisation. Whilst most SOFC system models reviewed used used a thermo-physical modelling framework, both Kupecki [37] and Rossi et al. [56] relied heavily on experimental data to formulate their models, and are thus considered separately.

2.1.4.1 Fuels and the chemical reactions within the stack

This literature review focuses on models of SOFC systems that are methane-fuelled, due to its advantages as a transportation fuel, as outlined in Section 1.4. With external pre-reforming, the gas composition at the anode inlet is a mixture of reformate, unreacted fuel,

Table 2.2: Overview of SOFC stack modelling approaches in the literature, where MSR is the methane steam reforming reaction, WGS is the water gas shift reaction, OCV is the open circuit voltage, ASR is the area specific resistance, and AOC are the activation, ohmic and concentration voltage losses.

	MSR rate	**WGS rate**	y_i **for OCV**	**Losses**
0D				
Peters et al. [16]	Equilibrium	Equilibrium	Undefined	ASR
Akroot et al. [35]	Equilibrium	Equilibrium	Undefined	AOC
Chitsaz et al. [33]	Completion	Equilibrium	Outlet	AOC
Lisbona et al. [36]	Completion	Equilibrium	Undefined	AOC
Kupecki [37]	N/A	N/A	Outlet	Other
Sorrentino et al. [38]	Completion	Equilibrium	Hierarchical	AOC
Gallo et al. [39]	Completion	Equilibrium	Average	ASR
Saarinen et al. [40]	Completion	Equilibrium	Average	ASR
Yilmaz et al. [34]	Completion	Completion	Undefined	AOC
Lee et al. [57]	Kinetics	Equilibrium	Undefined	AOC
1D				
Saebea et al. [41]	Kinetics	Kinetics	Nodal	AOC
Braun et al. [43]	Kinetics	Equilibrium	Nodal	AOC
Albrecht et al. [46]	Kinetics	Equilibrium	Nodal	AOC
Mueller et al. [47]	Kinetics	Equilibrium	Nodal	AOC
Huang et al. [42]	Kinetics	Equilibrium	Nodal	AOC
Roberts et al. [49]	Kinetics	Kinetics	Nodal	AOC
Engelbracht et al. [58]	Kinetics	Equilibrium	Nodal	ASR
D. Andersson et al. [51]	Kinetics	Kinetics	Nodal	AOC/ASR
Mazumder et al. [52]	Undefined	Equilibrium	Nodal	ASR

and water. The remaining methane is reformed internally through the methane steam reforming (MSR) reaction, and carbon monoxide and water are shifted to hydrogen and carbon dioxide in the water gas shift (WGS) reaction, as introduced in Section 1.3.1.

When internally reforming hydrocarbon fuels within the SOFC stack, carbon deposition is a risk. The majority of the models neglected the carbon deposition reactions by assuming that by keeping the steam-to-carbon ratio (S/C ratio) at the anode inlet high, usually above two [43], none of the carbon deposition reactions would proceed. Peters et al. [16] did, however, assess the potential for carbon deposition in the stack through the Boudouard reaction, which they assumed to be at equilibrium. The advantage of

this approach is that it takes into account the effect of temperature on the risk of carbon deposition. Any operating points that risked carbon deposition were considered infeasible.

In the SOFC system models listed in Table 2.2, all authors assumed the electrochemical oxidation of hydrogen to be the driving force of electrical power production in the fuel cell. The electrochemical oxidation of carbon monoxide was neglected, since it proceeds much slower than the hydrogen oxidation, and is instead assumed to contribute to hydrogen production through the WGS reaction [59].

2.1.4.2 Calculating the rate of the MSR reaction

The rate of the reforming reactions were found in the literature, either using chemical reaction kinetics, or by assuming the reactions were at chemical equilibrium. The assumption of chemical equilibrium is the simpler to calculate but is likely to overestimate the reaction rate, since it neglects all mass transport and reaction kinetics limitations. Chemical reaction kinetics expressions are usually found empirically, and require knowledge of reaction geometries.

All 1D models listed in Table 2.2 calculated the rate of MSR reaction from chemical reaction kinetics. In a 1D SOFC stack model, the reaction rate varies along the streamwise direction of the anode channel as a function of the composition and temperature of the gases. A common kinetics model is the Arrhenius expression presented by Achenbach [60]:

$$r_{\mathrm{CH_4}} = k_{\mathrm{CH_4}} p_{\mathrm{CH_4}} \exp\left(\frac{-E_{\mathrm{CH_4}}}{RT}\right) A \tag{2.2}$$

where the rate of consumption of methane on the anode ($r_{\mathrm{CH_4}}$ in $\mathrm{mol\,s^{-1}}$) has a first order dependency on the methane partial pressure ($p_{\mathrm{CH_4}}$ in bar). The activation energy ($E_{\mathrm{CH_4}}$) has a value of $82\,\mathrm{kJ\,mol^{-1}}$, and the pre-exponential factor ($k_{\mathrm{CH_4}}$) is equal to $4274\,\mathrm{mol\,m^{-2}\,bar^{-1}\,s^{-1}}$. A is the reaction area in $\mathrm{m^2}$.

For 0D models the composition and temperature throughout the SOFC stack are

assumed uniform. The average values can vary significantly from the local values predicted by the 1D models. Lee et al. used the rate expression from Achenbach to calculate the rate of the MSR reaction [57], whilst Peters et al. and Akroot et al. [16, 35] assumed the MSR reaction to be at chemical equilibrium. At the high temperatures found in SOFC stacks, the Gibbs free energy of the MSR reaction is highly negative, and, therefore the reaction tends to completion. As a result, the other 0D stack models listed in Table 2.2 assumed complete conversion of the MSR reaction in the SOFC stack.

R. T. Leah et al. [61] reported achieving 90 % conversion of methane in an SOFC system with only internal reforming. With a pre-reformer, the overall methane conversion increased up to 97 %, depending on the operating temperature of the reformer.

2.1.4.3 Calculating the rate of the WGS reaction

Most of the 0D models listed in Table 2.2 assumed the WGS reaction to be at chemical equilibrium. This assumption is considered reasonable because the kinetics of the WGS reaction are much faster than those of the MSR reaction [60]. Yilmaz et al. assumed the WGS reaction to go to completion, but without justification [34].

The authors of five of the 1D stack models listed in Table 2.2 [43, 46, 47, 50, 52] assumed the WGS reaction to be at equilibrium at each node of the anode channel of the SOFC stack. Saebea et al. [41] used an equilibrium-limited WGS rate expression first presented by Aguiar et al. [63]. Roberts et al. [49] used the rate expressions first presented by Xu et al. [64] for both the MSR and WGS reactions. The various approaches for estimating the chemical reaction kinetics of the MSR and WGS reactions have already been extensively reviewed in the literature [31, 65].

2.1.4.4 Calculating the OCV

All the authors listed in Table 2.2 calculated the OCV using the Nernst equation, where the OCV depends upon the composition and temperature of the gases in the SOFC stack. In the discretised 1D stack models, the composition and temperature are calculated at

each node. In this case, the voltage at each node is assumed equal to the cell voltage, and the current density varies with composition and temperature in each node.

In the 0D SOFC stack models, the composition and temperature are uniform, and therefore, the OCV is uniform, too. Chitsaz et al. [33] and Milewski [66] both took the outlet composition for calculating the OCV, but that underestimates it, since the average mole fraction of hydrogen will be larger within the SOFC stack than at the outlet.

Gallo et al. [39] and Saarinen et al. [40] both took the average of the inlet and outlet concentrations to calculate the OCV. However, for SOFC stacks with internal reforming of methane, this average mole fraction is still likely to underestimate the OCV. This is due to hydrogen production within the stack from the internal reforming reactions, meaning that the hydrogen mole fraction is larger within the stack than at the inlet and outlet.

Sorrentino et al. [38] used a hierarchical approach first presented in their previous journal article [67], which reduced 1D profiles to 0D averages, to better estimate the average composition, temperature and current density within the stack. X. Zhang et al. [68] used a similar hierarchical approach to construct a 0D model of an SOFC stack.

Peters et al. [16] and Lisbona et al. [36] did not declare the approach for finding the composition in the OCV calculation of their 0D stack models.

2.1.4.5 Calculating the voltage losses

Many of the models listed in Table 2.2 calculated voltage loss contributions as separate activation, ohmic and concentration losses. Activation losses are typically calculated from the Butler-Volmer equation, or at high current density, using the simplified Tafel equation, and reflect the reaction kinetics and associated activation energy of the electrochemical oxidation of hydrogen (H2X) reaction [69]. Ohmic losses or charge transport losses are calculated from ionic and electrical conductivity data for the cell components. They are associated with the resistance of the fuel cell components to charge transport, and therefore obey Ohm's law [70]. Concentration losses or mass transport losses are commonly calculated based on a limiting current density. They represent the losses associated with

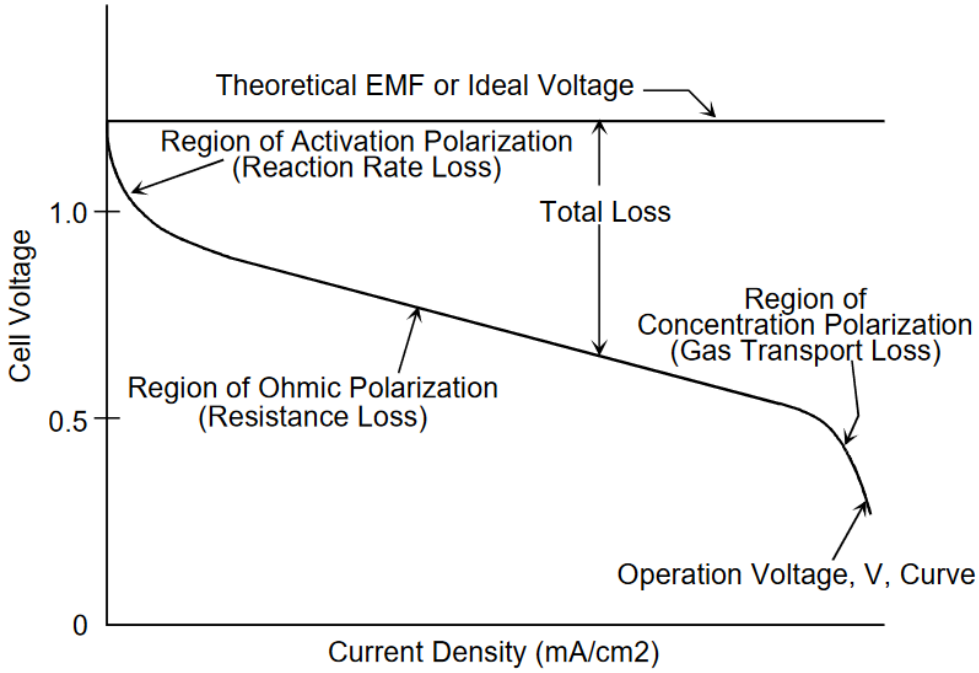

Figure 2.3: An example of an iIV characteristic illustrating activation, ohmic and concentration losses [27].

the transfer of reactants and products to and from the reaction site [70]. The three different categories of voltage losses are illustrated in Figure 2.3 [27].

The separate voltage losses in a fuel cell depend on current density, temperature, composition, and the electrochemical properties of the fuel cell materials. To calculate the separate voltage losses, many parameters must be estimated that are difficult to determine accurately and are specific to the stack design and materials. For example, many SOFC stack models calculated ionic and electronic conductivities using experimental data from IEA benchmark testing for planar SOFCs [71] or from Siemens Westinghouse for tubular SOFCs [72] in calculating the ohmic losses. However, since then SOFC stack designs and materials have changed, and the empirical correlations used may no longer be accurate.

In an SOFC, the activation losses are relatively small due to the high operating temperatures. Additionally, the ohmic losses are linear, as they correspond to a charge resistance. Therefore, at moderate current densities, the iv characteristic of an SOFC may be approximated as linear. As a result, some of the models listed in Table 2.2 employed

an area specific resistance (ASR) approach that lumps the voltage losses into a single temperature-dependent resistance derived from experimental data, such as the experiments reported by Gubner [73]. The ASR approach is useful for 0D modelling because it is generalised, and many manufacturers have reported the ASR for their SOFC cells or stacks. Alternatively, the ASR can be inferred from the iV characteristics. Whilst simple, the ASR approach may not be valid for a fuel utilisation (U_f) above 0.85 or at high current density due to the significant mass transport losses under those conditions, which are not well reflected in the ASR approach [74].

2.1.5 Approach to modelling the heat exchangers

The heat exchangers (HEXs) are important components of SOFC systems. The authors listed in Table 2.3 used HEXs to pre-heat the fuel and air streams to the SOFC stack. The core part of the HEX modelling approach is the energy balance to find the rate of heat transfer between the hot side and cold side. The HEXs are sized for their required performance at nominal load, whilst dynamic models must be capable of finding their performance at part load.

2.1.5.1 Sizing the heat exchangers at nominal load

The 0D HEX models listed in Table 2.3 used a simple approach to HEX modelling, without needing to define the geometry of the component. SOFC stack manufacturers [21] typically define a maximum stack temperature and a maximum temperature difference across the stack. The anode and cathode pre-heaters can be sized such that at nominal load their outlet temperatures meet those requirements. The steady-state SOFC system models listed in Table 2.3 sized their cathode pre-heaters to give a temperature difference of 100 K across the stack. The dynamic models of Sorrentino et al. [38] and Albrecht et al. [46] sized the HEXs based upon a larger stack temperature difference of 125 K and 150 K respectively. Gallo et al. [39], Akroot et al. [35], Huang et al. [42] and Schmidt [75] did not define the stack temperature difference but instead the effectiveness of the HEXs, and

Table 2.3: Overview of heat exchanger modelling approaches in the literature.

Steady-state, 0D HEX	Sizing method		
Peters et al. [16]	$\Delta T_{\text{cathode}} = 100\,\text{K}$		
Chitsaz et al. [33]	$\Delta T_{\text{cathode}} = 100\,\text{K}$		
Lisbona et al. [36]	$\Delta T_{\text{cathode}} = 100\,\text{K}$		
Saebea et al. [41]	$\Delta T_{\text{cathode}} = 100\,\text{K}$		
Braun et al. [43]	$\Delta T_{\text{cathode}} = 100\,\text{K}$		
Akroot et al. [35]	$\varepsilon = 0.80$		
Huang et al. [42]	$\varepsilon = 0.93$		
Kupecki [37]	NTU method		
Dynamic, 0D HEX	**Sizing method**	**Part-load**	T_{HEX}
Sorrentino et al. [38]	$\Delta T_{\text{cathode}} = 125\,\text{K}$	$U = 200\,\text{W}\,\text{m}^{-2}\,\text{K}^{-1}$	Hot out
Albrecht et al. [46]	$\Delta T_{\text{cathode}} = 150\,\text{K}$	$U = 163\,\text{W}\,\text{m}^{-2}\,\text{K}^{-1}$	
Gallo et al. [39]	$\varepsilon = 0.85$	$\varepsilon = 0.85$	Hot out
Schmidt [75]	$\varepsilon = 0.80$	$\varepsilon = 0.80$	
Saarinen et al. [40]	Experimental	Experimental	
Dynamic, 1D HEX	**Modelling approach**		
Lin Zhang et al. [48]	Detailed		
Engelbracht et al. [50]	Correlation		
Lee et al. [57]	$\Delta T_{\text{cathode}} = 100\,\text{K}$	NTU method	

from that calculated their performance.

Peters et al. [16] and Braun et al. [43] both considered a number of different system configurations for steady-state operation. Peters et al. [16] stipulated that the terminal temperature difference of the HEXs should be at least 50 K to limit their size and cost, otherwise the configuration was considered infeasible. Braun et al. [43] calculated the performance characteristic UA of the cathode pre-heater in each configuration.

Sorrentino et al. [38] and Kupecki [37] both used the number of transfer units (NTU) method presented by Kays et al. [76] to find UA and hence the HEX area A in m^2. Kupecki [37] defined the geometry of the HEXs to calculate their pressure drop. The pressure drop in the air pre-heater is typically largest of all the SOFC system components [77], and therefore is an important parameter in determining the parasitic losses of the air blower, which will be discussed in Section 2.1.8.

2.1.5.2 Calculating performance under part load

The dynamic HEX models listed in Table 2.3 calculated the rate of heat transfer and hence performance under part load. Sorrentino et al. [38] and Albrecht et al. [46] assumed the overall heat transfer coefficient U remained constant, while Gallo et al. [39] and Schmidt [75] assumed the HEX effectiveness remained constant. In reality, both the heat transfer coefficient and effectiveness will vary with the mass flow rate of gas through the HEX, and therefore at part load. Bosal [78] published an online tool to find the variation in HEX effectiveness and pressure drop at up to six different operating points. Using this tool, the extent to which the constant effectiveness assumption overestimates the hot-side outlet temperature of the HEXs at part load was studied. The variation in effectiveness at part load was found to be less than 5 pp using the tool.

Lee et al. used the effectiveness-NTU method to calculate the performance of the heat exchangers in part load, and use the Bell-Delaware method to derive the heat transfer coefficients for a shell-and-tube heat exchanger [57]. They were able to verify their modelling results with the experimental set-up in their laboratory.

When establishing the dynamic energy balance in the HEX models, the lumped HEX temperature must be estimated. Since the solid heat capacity of the HEXs dominates the thermal inertia, the estimation is likely to affect the calculated performance of the HEXs, especially for 0D dynamic models. Based on their energy balances, Sorrentino et al. [38] and Gallo et al. [39] assumed the HEX temperature was equal to the temperature at outlet of the hot side of the HEX; however this assumption was not further justified.

Some authors defined the HEX size and geometry to match a physical HEX in the laboratory [40, 48, 79]. Engelbracht et al. [50] and Hong et al. [79] both used the effectiveness-NTU method to find the dynamic performance of the HEXs under part load using convection correlations from the literature. A number of other SOFC system models gave little or no information about their HEX modelling approach [49, 47, 51, 52].

2.1.6 Approach to modelling the burner

Table 2.4: Overview of burner modelling approaches in the literature.

Steady-state	Reaction conversion	Temperature
Chitsaz et al. [33]	To completion	Design 843°C
Sorrentino et al. [38]	To completion	Design 1057°C
Peters et al. [16]	Equilibrium	Maximum 1000°C
Kupecki [37]	Equilibrium	
Yilmaz et al. [34]	99 %	Undefined
Akroot et al. [35]	99 %	Undefined
Saebea et al. [41]	98 %	Up to 950°C
Lisbona et al. [36]	95 %	Design 1378°C
Braun et al. [43]	?	851–1008°C
Dynamic	**Reaction conversion**	**Temperature**
Lin Zhang et al. [48]	To completion	Maximum 1000°C
Gallo et al. [39]	To completion	?
Mueller et al. [47]	To completion	?
Albrecht et al. [46]	Kinetics	Maximum 850°C
Roberts et al. [49]	?	?

SOFC system models usually also include a burner. During normal operation, the burner combusts hydrogen, carbon monoxide and any unreacted methane from the anode off-gas with oxygen from the cathode off-gas, shown by the following chemical equations:

$$\mathrm{H_2} + \frac{1}{2}\,\mathrm{O_2} \longrightarrow \mathrm{H_2O} \tag{2.3}$$

$$\mathrm{CO} + \frac{1}{2}\,\mathrm{O_2} \longrightarrow \mathrm{CO_2} \tag{2.4}$$

$$\mathrm{CH_4} + 2\,\mathrm{O_2} \longrightarrow \mathrm{CO_2} + 2\,\mathrm{H_2O} \tag{2.5}$$

Fuel can be also fed directly to the burner to heat-up an SOFC system. Heat-up of the SOFC system will be reviewed in Section 2.6.

All burner models listed in Table 2.4 conducted a material balance to find the composition of the off-gas, and an energy balance to find the temperature of the off-gas. In addition to the model dimensions, state, and heat losses presented in Section 2.1, the burner models made different assumptions about the conversion of the combustion reac-

tions, and designed their burners to operate at different temperatures.

2.1.6.1 Conversion of the burner combustion reactions

Peters et al. [16] and Kupecki et al. [37] assumed that the combustion reactions were at chemical equilibrium. Due to the fuel-lean conditions and high operating temperature, the combustion reactions go to completion under the equilibrium assumption. Therefore, five of the authors in Table 2.4 assumed the combustion reactions go to completion. However, Saebea et al. [41] and Lisbona et al. [36] assumed only near-complete combustion with a constant conversion of combustible gases of 98 % [41] and 95 % [36], respectively . S. Yu et al. [81] presented experimental work showing that methane is the most difficult component to completely combust, and hence Albrecht et al. [46] used chemical reaction kinetics to describe the rate of combustion of methane, whilst assuming the combustion of hydrogen and carbon monoxide were at equilibrium.

2.1.6.2 Burner off-gas temperature

The reaction conversion determines the burner off-gas composition. Due to the complete combustion assumption and air-rich conditions, the off-gas composition varies very little. The combustion reactions are highly exothermic. Therefore, slight variations in the composition of the SOFC anode off-gas can have a significant impact on the burner off-gas temperature. The models listed in Table 2.4 show that there is a significant range in the temperature values reported in the literature.

Metallic HEXs are often preferred over ceramic HEXs, especially for transport applications, since they are smaller, lighter and cheaper to manufacture [82]. However, metallic HEXs are limited by their maximum operating temperature. The HEXs of Bosal ECI operate up to 1100°C [83], and therefore Peters et al. [16] and Lin Zhang et al. [48] limited the burner off-gas temperature to a maximum of 1000°C.

Albrecht et al. [46] limited the maximum burner temperature to 850°C—due to the thermal limits of the catalysts used in their catalytic combustor—by supplying additional

air to the burner. However, the relatively low temperature of the burner limited the performance of the air and fuel pre-heaters, and hence the temperature change along the cathode was high at 150°C, which might increase degradation rates within the SOFC stack.

Saebea et al. [41] simulated an SOFC-gas turbine hybrid power system and manipulated the air-to-fuel ratio of the burner to control the downstream temperature of the turbine inlet to between 600°C and 950°C . Roberts et al. did not impose a limit of the maximum burner temperature, but the temperature was around 800°C at the design point [49]. Braun et al. [43] explored various different system configurations with burner temperatures varying between 851°C and 1008°C. In some system layouts, they considered providing additional air to the burner to reduce its temperature and hence avoid the use of expensive metallic alloys in the downstream HEXs.

Sorrentino et al. [38] modelled an SOFC system with a ceramic air pre-heater, and therefore the relatively high burner temperature of 1057°C under design conditions would likely be acceptable. The 1378°C design burner off-gas temperature reported by Lisbona et al. [36] is somewhat higher, and could therefore require careful design of the HEX components if used to pre-heat the inlet streams [16].

2.1.7 Approach to modelling the pre-reformer

Operating an SOFC system with complete internal reforming of methane increases the system efficiency by reducing the large air flow requirement to the stack for cooling. However, it can lead to carbon formation and large temperature gradients at the anode [32]. Therefore, most methane-fuelled SOFC system models found in the literature included a degree of pre-reforming, the majority of which used an external steam-reformer. None of the authors considered that anode off-gas recirculation (AOGR) reduces the need for a pre-reformer during steady-state operation, because it increases the hydrogen mole fraction at the anode inlet. Saarinen et al. [40] and D. Andersson et al. [51] both modelled auto-thermal reforming, and Nousch et al. [45] modelled catalytic partial oxidation

Table 2.5: Overview of external steam reformer modelling approaches in the literature.

	X_{MSR}	X_{WGS}	S/C ratio (RR)	T_{reformer}
Peters et al. [16]	Equilibrium	Equilibrium	(0.5–0.7)	500°C
Saebea et al. [41]	Equilibrium	Equilibrium	1.5	700°C
Mantelli et al. [44]	Equilibrium	Equilibrium	1.8	640°C
Huang et al. [42]	Equilibrium	Equilibrium	2	727°C
Wang et al. [84]	Equilibrium	Equilibrium	1.2-2.4	700°C
Gallo et al. [39]	Eqm (0.5)	Equilibrium	?	?
Sorrentino et al. [38]	0.3	Equilibrium	2.5	700°C
Braun et al. [43]	0, 0.5, 1	Equilibrium	2	700°C
Lisbona et al. [36]	0.2 (0.1–0.7)	?	3.25 (0.7)	700°C
Engelbracht et al. [50]	Kinetics	Equilibrium	(0.5–0.9)	?
Albrecht et al. [46]	Kinetics (0.2)	Kinetics	2	650°C
Mueller et al. [47]	Kinetics	Kinetics	?	?
Roberts et al. [49]	Kinetics	Kinetics	?	?
Lee et al. [57]	Kinetics	Kinetics	2.5	544°C
Kupecki [37]	?	?	2.2	?
Mazumder et al. [52]	?	?	?	?

(CPOX) reforming, neither of which will be considered further in this review. Lin Zhang et al. [48] modelled a hydrogen-fuelled system, so no reforming was required.

Table 2.5 lists the approaches used to model the external steam reformer. The models differ in their approach to model the MSR and WGS reactions. In addition, authors operated their steam reformer under different conditions. In particular, the S/C ratio at the pre-reformer inlet, and at the reformer temperature varied.

2.1.7.1 Calculating the conversion of reforming reactions

The majority of reformer models in Table 2.5 assumed the WGS reaction to be at equilibrium, for the same reasons as within the SOFC stack in Section 2.1.4. However, three differing approaches were taken to finding the rate of the MSR reaction in the reformer.

The first approach taken by Peters et al. [16], Saebea et al. [41], Mantelli et al. [44], Huang et al. [42], Wang et al. [84] and Gallo et al. [85] assumed the MSR reaction to be at equilibrium. Under this assumption, the equilibrium constant of the MSR reaction, and hence the methane conversion, was determined by the reformer temperature.

Other authors sized the pre-reformer to give a desired conversion of methane. A certain conversion can be obtained by selecting the required mass of catalyst in the reformer. Sorrentino et al. [38] designed for 30 % conversion and Albrecht et al. [46] sized for 20 % conversion. Braun et al. [43] modelled a number of different system concepts, each with a methane conversion of either 100 % or 50 % in the pre-reformer. They also modelled complete internal reforming with no pre-reformer at all, as did Chitsaz et al. [33] to reduce system complexity, an approach which has been demonstrated in practice by R. T. Leah et al. [61]. Lisbona et al. [36] studied the variation in performance of an SOFC system with methane conversion in the pre-reformer varying from 10 % to 70 %. They identified that the desired conversion of methane was a compromise between avoiding carbon deposition and the amount of cooling required to the stack. The authors set the conversion at 20 % for their design case, but how they arrived at this value is unclear, since they did not model carbon deposition or temperature gradients within the stack. Additionally, fixed conversion of the reforming reaction is feasible under steady-state operation, but unlikely to occur under dynamic operation.

The third approach found was to calculate the rate of the MSR reaction using chemical reaction kinetics expressions, similar to those presented for the SOFC stack in Table 2.2 [50, 46, 47, 49, 57]. Some of those authors also found the rate of the WGS reaction through chemical reaction kinetics [46, 47, 49, 57].

2.1.7.2 Setting the S/C ratio

Steam is required for the steam reforming reactions to prevent carbon deposition. In the extreme case that both the MSR and WGS reactions were both to go to completion before the H2X reaction commenced, for example, in a pre-reformer, then an S/C ratio of at least two at the anode inlet would be required. With AOGR, the steam produced in the H2X reaction in the SOFC stack can be used. This removes the need for an external steam supply [86], an approach taken by the majority of models listed in Table 2.5. Saebea et al. [41] and Lisbona et al. [36] both utilised AOGR to achieve the desired S/C ratio at their

steady-state operating point. Saebea et al. [41] operated their pre-reformer at a low S/C ratio of 1.5 but were using ethanol as a fuel, which requires less steam than methane.

The recirculation ratio (RR) is the proportion of the anode off-gas recirculated, and is calculated from:

$$RR = \frac{\dot{n}_{\text{anode recycle}}}{\dot{n}_{\text{anode out}}} \tag{2.6}$$

The AOGR flowrate can be manipulated to achieve the desired S/C ratio at the pre-reformer inlet. A recirculation blower is typically used to control the AOGR flowrate and hence S/C ratio at part-load. Albrecht et al. [46] assumed, however, that an ejector for AOGR could operate to ensure a constant S/C ratio of two at the reformer inlet, which would be difficult to achieve in a real SOFC system. This is observed in the dynamic modelling of Mantelli et al. [44], in which sufficient S/C ratio could not be maintained for all operating points in their sensitivity analysis with a single ejector, because the RR could not be independently controlled.

Some authors specified the RR of the AOGR rather than the S/C ratio. Peters et al. [16] and Engelbracht et al. [50] modelled the SOFC system with AOGR and an external steam reformer. Both authors studied the effect of the RR and U_f on the potential for carbon deposition in the stack. Engelbracht et al. [50] found that for a U_f of 0.75, an RR of nearly 0.7 was required.

A number of the models listed in Table 2.5 used an external steam supply for the steam reformer [42, 38, 39, 43]. This is feasible for micro-combined heat and power (CHP) applications, but requires an onboard water tank for the automotive auxiliary power unit (APU) envisaged by Sorrentino et al. [38]. For the case of complete internal reforming, Braun et al. [43] used AOGR, and in both cases maintained a S/C ratio of 2 at the anode inlet at the design point.

2.1.7.3 Calculating the reformer temperature

The MSR reaction is strongly endothermic and additional heat is required to maintain the reformer temperature. Therefore, many models [43, 39, 38, 16, 52] integrated the pre-reformer within the fuel pre-heater, with heat from the burner off-gas supporting the steam reforming reactions. Mueller et al. [47] took the same approach, and mixed the AOGR and fresh fuel within the same component. Lisbona et al. [36] placed the fuel pre-heater HEX upstream of the pre-reformer. Saebea et al. [41] and Kupecki [37] have not shown how the heat was delivered to the steam reformer, and therefore more information is required to evaluate the feasibility of their system. Without additional heat, a very high RR or low MSR conversion in the pre-reformer would be required [87].

Sorrentino et al. [38] modelled the same integrated reformer and fuel pre-heater, but added a bypass valve to maintain the reformer temperature at part load. Gallo et al. [39] maintained a 50 % conversion of the MSR reaction, by manipulating the valve position of the same bypass concept, and hence control the reformer temperature. Roberts et al. [49] integrated their reformer into the assembly of the SOFC stack, usually referred to as indirect internal reforming.

Braun et al. [43] and Lisbona et al. [36] sized their integrated reformer and pre-heater such that the reformer was able to maintain a temperature of 700°C under their design conditions. Peters et al. [16] sized their system to give a lower operating temperature of 500°C for the reformer, which led to a lower conversion of methane in the MSR reaction.

2.1.8 Approach to modelling the air and recirculation blowers

SOFC systems consist of one or more blowers, which do mechanical work on the gases flowing through them, to raise their pressure, overcome the back pressure of the system, and enable gas flow. The mechanical work of each blower is delivered by an electric motor. The electrical power required depends on the mass flow rate and temperature of the gases, the pressure rise required, and the efficiency of the blower.

The blowers are the primary parasitic losses of the SOFC system. The air blower

Table 2.6: Performance of air and recirculation blowers modelled in the literature, where P_{system} is the rated electrical power of the system, ΔP (kPa) is the pressure drop of the system, $\eta_{\text{isentropic}}$ is isentropic efficiency of the blower, and $\eta_{\text{mechanical}}$ is the mechanical efficiency of the blower. Values are shown for the air side/fuel side, where applicable.

Author	P_{system} (kW)	ΔP (kPa)	$\eta_{\text{isentropic}}$	$\eta_{\text{mechanical}}$
Fixed pressure drop and fixed efficiency				
Chitsaz et al. [33]	390	20/20	0.85/0.85	
Lisbona et al. [36]	1	30/30	0.90/0.90	0.90/0.90
Saebea et al. [41]	$\sim$ 400	10/10	0.78/0.70	0.94/?
Braun et al. [43]	$\sim$ 1.5	32/34	0.63/0.70	
Schmidt [75]	46	32/32	0.80/0.80	0.92/0.92
Akroot et al. [35]	700	20	0.85/0.85	
Variable pressure drop and fixed efficiency				
Peters et al. (a) [16]	250	10/2.5	0.60/0.60	0.50/0.50
Peters et al. (b) [16]	3	2/1.5	0.60/0.60	0.50/0.50
Mueller et al. [29]	5	15/—	0.85/—	
Fixed pressure drop and variable efficiency				
Sorrentino et al. [38]	5	30/—	0.21–0.61/—	
Albrecht et al. [46]	25	26/40	?	?
Variable pressure drop and efficiency				
Roberts et al. [49]	180	?	?	
Kupecki [37]	1.6	min 2.0/1.5	min 0.15/0.27	
		max 16/3.0	max 0.40/0.78	

has the largest parasitic load because the cathode flow rate is usually much higher than the anode flow rate. SOFC systems commonly recycle anode off-gas with a recirculation blower, so these are also considered. Some authors modelled upstream fuel compression, but this is neglected in this review, since natural gas is stored under high pressure or as a cryogenic liquid for transport applications.

The approaches to modelling the blowers in SOFC system models in the literature are summarised in Table 2.6. The key differences between each of the models are the pressure rise values and the efficiency values. This section discusses those different values and any differences in modelling approach.

2.1.8.1 Calculating the system pressure drop

The pressure drop in SOFC systems depends not only on the gas flow rates, but also on the system layout, and the size and geometry of the components. New component designs can reduce pressure drop and improve system performance. The pressure drop can be calculated through detailed modelling of the fluid dynamics in each component, or found through experimental studies. Many authors in Table 2.6 estimated their pressure losses based on values reported in the literature.

A number of steady-state models [33, 36, 41, 43, 35] assumed constant pressure drop on both the air and fuel side of the SOFC system. Braun et al. [43] modelled both hydrogen-fuelled and methane-fuelled systems. The pressure drop on the fuel side for the hydrogen-fuelled system was 30 % lower than reported in Table 2.6 for a methane-fuelled system due to the fewer BoP components required. They assumed a 5 % pressure drop in each system component, relative to atmospheric pressure. Akroot et al. also assumed fixed percentage pressure drops across each component [35].

Some authors [75, 38, 46] who conducted dynamic modelling of SOFC systems, assumed the pressure drop to be constant even at part load. However, as the air and fuel flow rates reduce at part load, the pressure drops will reduce. One option is to operate at constant blower power, with a throttling valve to control the pressure drop and flow rate. This results in high parasitic losses at part load, but means that the blower speed can remain constant.

A few authors found pressure drop as a function of flow rate using the conservation of momentum equations through each component and the interconnecting pipes. Mueller et al. [29] and Roberts et al. [49] both assumed all flow regimes to be laminar, and therefore for incompressible flow, the pressure drop was directly proportional to the flow rate. The nominal values are reported in Table 2.6. Peters et al. [16] took the same approach for the fuel side of the SOFC system, but for the air side assumed that 20 % of the pressure drop could be attributed to turbulent flow within the components, with a quadratic dependency of pressure drop on flow rate.

Table 2.6 shows that the nominal pressure drop values reported in the literature vary from 2 kPa to 32 kPa for the air side and from 1.5 kPa to 40 kPa for the fuel side. There appears to be no relationship between the net system power and the pressure drop reported; the pressure drop depends more on the geometry and system design. The SOFC system models usually did not present experimental data to verify their pressure drop values.

The pressure drop depends on the design and geometry of all the system components and is often dominated by the air pre-heater, reported [77] to be as high as 10 kPa for a single pass. Improvements in air pre-heater design have reduced pressure drop, for example, Bosal ECI [83] reported a pressure drop of less than 2 kPa for air flow rates less than $30\,\mathrm{g\,s^{-1}}$ in their welded plate HEXs, which leads to lower parasitic losses and increases the system efficiency.

2.1.8.2 Calculating the blower efficiency and power demand

Energy must be transferred from the blower to the air to achieve the desired pressure rise. The theoretical minimum energy input is the change in enthalpy of the air if the process were to occur isentropically. Almost all authors in Table 2.6 defined an isentropic efficiency to account for the irreversible losses in the blower. There are losses involved within the electrical motor and the mechanical components of the blower itself, and many authors in Table 2.6 reported values for the mechanical efficiency.

The first ten authors in Table 2.6 assumed fixed efficiencies of the air and recirculation blowers but they did not assess the validity of this assumption, nor justify the values they used. The final four authors in Table 2.6 used efficiency maps to find the efficiency of the blowers. Kupecki [37] presented efficiency maps for the air blower and recirculation blower, and Roberts et al. [49] presented a solution strategy. An iterative process was required to find the mass flow rate to give the desired pressure rise, because changing the flow rate changed the pressure drop downstream [49]. Once the mass flow rate and blower speed to achieve the desired pressure ratio were found, the second map was used

to find the isentropic efficiency of the blower. The isentropic efficiency was used to find the outlet temperature, and hence the blower work.

Kupecki [37] presented efficiency maps with a range of isentropic efficiencies between 0.15 and 0.78. Some of the steady-state models [33, 36] in Table 2.6 defined fixed efficiencies even higher than this range, without justifying how they can be achieved. The constant efficiency values reported by Braun et al. [43] and Peters et al. [16] seem to be more realistic. Relatively low mechanical efficiencies of 0.5 were assumed by Peters et al. [16], while three authors [36, 41, 75] assumed high mechanical efficiencies of 0.9 or greater, and the other authors did not consider mechanical inefficiencies at all.

2.1.8.3 Accounting for the rotational inertia of the blowers

The majority of authors who conducted dynamic modelling in Table 2.6 assumed the speed of the blowers could be adjusted instantaneously at variable load. However, some models did consider the rotational inertia of the blower blades [46, 49, 29]. Mueller et al. [29] estimated the response time of the blower was about two orders of magnitude faster than the thermal response of the stack, so was unlikely to impact the thermal dynamics of the SOFC system when subjected to a dynamic load profile.

2.2 Steady-state performance of SOFC systems

Many of the models introduced in Section 2.1 studied the steady-state performance of SOFC systems. Understanding steady-state performance is an important first step in evaluating the potential of SOFC technology for transport applications.

2.2.1 Electrical efficiency as a performance indicator

The vast majority of models used the electrical efficiency of the SOFC system as its main steady-state performance parameter. Each reference listed in Table 2.7 conducted a sensitivity analysis to understand the steady-state performance of SOFC systems under a

range of operating conditions and configurations. A majority of the models listed fixed the current density and stack temperature, and studied the variation in electrical efficiency with varying U_f and RR.

The electrical efficiency of the SOFC stack decreases with increasing current density, due to the increased voltage losses. With increasing current density, the cooling requirement to maintain the stack temperature increases, and therefore the parasitic power of the air blower increases. This further reduces the electrical system efficiency. On the other hand, at low air flow rates, the efficiency of the blower decreases, too. Kupecki [37] showed that at low current density, increasing current density increased the system efficiency. This is likely because of the low blower efficiency under those operating points, and shows the importance of an accurate air blower model when estimating system efficiency under part load conditions. Lisbona et al. [36] did not fix the current density. They solved for the current density to meet the 1.1 kW stack power requirement under various operating conditions. Braun et al. [43] also investigated constant power mode for their SOFC system configuration.

2.2.1.1 Sensitivity of efficiency to U_f

Some of the models [50, 48, 41] listed in Table 2.7 showed that the electrical efficiency of SOFC systems increases with U_f. This is because less fuel is required to produce the same electrical power.

The reduction in the fuel flow rate reduced the mass flow on the anode, and the amount of heat absorbed through the endothermic MSR reaction, and therefore, more cooling was required to maintain constant stack temperature [16, 36, 50]. Under this operating strategy, the variation in electrical efficiency of the SOFC system with increasing U_f becomes a balance between the increasing stack efficiency and the increasing parasitic losses of the air blower. Peters et al. [16] studied two different SOFC systems with different performance characteristics. In the small system operating at lower current density, the system efficiency increased with U_f. In the large system operating at higher current

Table 2.7: A review of sensitivity analyses of SOFC system models, where i is the current density in $\mathrm{A\,cm^{-2}}$, P is the system power in kW, U_f is the fuel utilisation in %, RR is the recirculation ratio in %, SC is the S/C ratio, X_R is the MSR conversion in the reformer in %, λ is the air stoichiometry, T_S is the stack temperature in °C, and η is the AC system efficiency in % of the LHV.

	i (P)	U_f	RR (SC)	X_R	λ (T_S)	η
Peters et al. [16]	0.40	60–80	50–70		(750)	52–60
Peters et al. [16]	0.25	60–80	50–70		(850)	56–63
Engelbracht et al. [50]	0.50	50–85	55–90		(780)	48–63
Lisbona et al. [36]	(1.1)	45–95	30–90	10–70	(800)	39–52
Chitsaz et al. [33]	0.55	80	10–60			
Braun et al. [43]	0.57	85	(2.0)	0,50,100	(800)	30–41
Kupecki [37]	0.17–0.25	65–85	(2.2)		3–7	36–44
Saebea et al. [41]	0.40	55–80	(1.5)		(800–900)	46–62
Lin Zhang et al. [48]	0.60	60–90	N/A		6–12	41–56
Yilmaz et al. [34]		85		(700-950)	58-62	
Inac et al. [88]	0.55-0.95	85			(600-900)	30-50
Akroot et al. [35]	0.55-0.95	85	(2-4)		(600-1100)	55-65
Huang et al.	0.55	45-90	(2)	(635-835)	50-75	

density, the parasitic losses increased more sharply with high U_f, and hence the system efficiency decreased with U_f, especially at high RR . Lisbona et al. [36] and Huang et al. [42] also showed that operating at both high U_f and RR could decrease the electrical efficiency of the system. Lisbona et al. also showed that operating with a low conversion of methane in the pre-reformer could reduce the system efficiency at U_f of 0.8 or higher, but it was not clear why.

Kupecki [37] did not fix the stack temperature, but instead varied U_f, air stoichiometry (λ) and current density. They found U_f had a much stronger effect on efficiency at low λ, due to the lower parasitic losses from the air blower under those conditions. They showed that above 80 % U_f, the electrical efficiency of the SOFC system decreased.

2.2.1.2 Sensitivity of efficiency to RR

A number of authors [16, 50, 36, 33] studied the effect of RR ratio on the electrical efficiency for systems with anode off-gas recirculation.

Engelbracht et al. [50] showed that the electrical efficiency increased with RR, for U_f below 80 %. Under these conditions the mole fraction of unreacted fuel in the anode off-gas was significant. Therefore, the system-level U_f, and hence efficiency, increased with RR. Above 80 % U_f, the efficiency decreased with RR. Under these conditions, there was very little fuel remaining at the anode outlet, so the reaction products diluted the fuel and cause the stack voltage to drop. At high RR above 85 %, the electrical efficiency decreased, due to the high power demand of the recirculation blower and the low cell voltage . Lisbona et al. [36] showed very similar trends for the variation in efficiency with RR and U_f in their sensitivity analysis.

2.2.1.3 Sensitivity to methane conversion in the pre-reformer

Lisbona et al. [36] studied the variation in electrical efficiency depending on between 10 % and 70 % of methane conversion in the pre-reformer. They found that increasing methane pre-conversion, increased the OCV of the SOFC stack. However, increasing the conversion of methane in the pre-reformer also increased the amount of cooling required to maintain the stack temperature. Therefore, the power demand of the air blower increased, but not by much, since they assumed a high blower efficiency of 90 %.

Braun et al. [43] found that the parasitic load of the air blower had a major effect on the system efficiency when comparing external and internal reforming. They found that switching from external to internal reforming reduced the power demand of the air blower by 54 % and the size of the cathode pre-heater by 86 %. This led to an increase in the electrical efficiency of the system from 34 % to 41 %, and also reduced the capital cost of the system components.

2.2.1.4 Sensitivity of efficiency to λ

Kupecki [37] and Lin Zhang et al. [48] varied λ, without defining the stack temperature. Increasing λ increased the power demand of the air blower, and hence led to a reduction in the electrical efficiency of the system. Chitsaz et al. [33] varied the cathode off-gas RR,

but did not present the ensuing results for electrical efficiency of the SOFC system; they combined their efficiency metric with that of the refrigeration unit they had coupled to the SOFC.

Inac et al. [88], Mantelli et al. [44] and Akroot et al. [35] all showed that electrical efficiencies were increased with operating temperature, but the system limitations of high operating temperatures were not considered.

2.2.1.5 Summary of sensitivity analyses

Table 2.7 shows a significant variation in the electrical efficiency of SOFC systems between different models. The efficiency depended on the operating strategies, operating conditions, and also the models of the system components themselves, as reviewed in Section 2.1. System efficiencies as low as 30 % and as high as 63 % were found in the models reviewed. This shows good agreement with real SOFC system, with a review finding manufacturers reporting net AC system efficiencies between 47 % and 65 % [89]. The highest efficiencies are achieved through a trade-off between the electrical efficiency of the stack, and parasitic power demand, in particular, that of the air blower. High electrical efficiency can be achieved when operating with a U_f of around 80 %, an AOGR ratio of around 70 %, with internal reforming to reduce the blower power, and at moderate current densities, of around $0.4\,\mathrm{A\,cm^{-2}}$.

2.2.2 Other performance indicators

Electrical efficiency was not the only performance indicator. A number of authors [33, 36, 43, 37] modelled SOFC systems for micro-CHP, absorption refrigeration or gas turbine applications. For those applications, the thermal and combined efficiency were also calculated. For example, Braun et al. [43] compared the 2^{nd} law efficiency for an exergetic analysis of different SOFC system configurations, and Chitsaz et al. [33] estimated the system cost.

Further papers have studied the exergetic efficiency of an SOFC system. Yilmaz et al.

studied the variation in energetic and exergetic efficiencies of an SOFC plant with both ambient temperatures and SOFC operating temperatures [34]. Inac et al. investigated the exergetic efficiency of a system consisting not only of an SOFC stack, but also a polymer electrolyte electrolyser, a photovoltaic system, and an anaerobic digester for biogas production [88]. Both papers used similar modelling assumptions to the other steady-state SOFC system models investigated in Section 2.1.

Mantelli et al. conducted a sensitivity analysis of electrical efficiency to methane content in biogas [44]. They showed that higher concentrations of methane in the fuel led to higher system efficiencies. Wang et al. conducted a similar analysis, where they studied also the effect of varying S/C ratio on the electrical efficiency of an SOFC system.

For HGV applications, an important performance indicator is the system footprint, since this directly affects the payload that can be carried. This is not something which has been analysed in any of the system models presented in Table 2.7. The models reviewed did not provide data about the mass or volume of their system or components. This, therefore, is identified as a gap in the literature on SOFC system modelling. As a first estimate, the power density of the stack can be calculated.

2.2.3 Operating constraints of SOFC systems

In addition to operating at high efficiency or power density, an important consideration is the lifetime of the SOFC system. None of the system models in Table 2.7 accounted for ageing in the SOFC systems, and characterised their performance as constant throughout their lifetime from first-use to end-of-life. Including an ageing sub-model in an SOFC system model, would provide additional benefit and insight into the potential for SOFC systems for a range of applications. However, a few of the authors did constrain the operating points of the SOFC system to ensure safe operation and maximise lifetime. Those constraints are discussed in the following.

2.2.3.1 Thermal constraints

There are a number of thermal constraints to ensure long lifetime of the SOFC system, and in particular of the SOFC stack.

In 1D models of SOFC stacks, the internal temperature gradients are calculated in the flow direction. Zeng et al. reviewed the literature on thermal gradients in planar SOFC stacks, and found simulations show that internal steam reforming can lead to larger thermal gradients, due to the strongly endothermic MSR reaction at the fuel inlet [90]. They found various simulations reporting temperature gradients from $5\,\mathrm{K\,cm^{-1}}$ to $70\,\mathrm{K\,cm^{-1}}$ for planar co-flow SOFC stacks with internal reforming. Aguiar et al. defined a maximum temperature gradient of $10\,\mathrm{K\,cm^{-1}}$, corresponding to a maximum safe stress-induced strain of 0.1 % [91].

In contrast, 0D models do not resolve the spatial variation of temperature within the SOFC stack, but only the temperature at the inlets and outlets. Elcogen [21] reported that the maximum allowable temperature for their stack is 720°C, the minimum cathode inlet temperature is 580°C, and the maximum temperature difference between the stack and the cathode air is 100°C. A large stack temperature difference is likely to lead to large temperature gradients in the stack, which can lead to accelerated ageing of the stack. Aguiar et al. defined a maximum temperature difference of 100 K along a 10 cm SOFC stack [91]. However, the temperature difference between the terminals does not give insight into whether the $10\,\mathrm{K\,cm^{-1}}$ is exceeded internally within the SOFC stack, which was shown to be possible for internal reforming in the review by Zeng et al. [90].

During steady-state operation, the models listed in Table 2.7 typically maintained constant stack temperature. This was achieved by manipulating the air flow rate to the SOFC stack depending on the heat load. As shown in Section 2.1.6.2, some authors [16] restricted the burner temperature to a maximum of 1000°C. This was achieved by avoiding any operating points which raised the burner temperature, for example, at low U_f and low RR [16], or by providing additional air to the burner. Peters et al. [16] also stipulated that the terminal temperature difference for gas-to-gas HEXs should be at least

50°C and 100°C for the heated reformer, in order to keep size and costs of components feasible, as discussed in Section 2.1.5.1.

Some authors reported maximum spatial thermal gradients within the SOFC stack for 1D models, however for 0D models spatial thermal gradients were not resolved.

While those thermal constraints can be satisfied with correct sizing and design of the BoP components, the time derivative of the stack temperature ($\mathrm{d}T_S/\mathrm{d}t$) depends on the transient performance of the system. None of the authors reviewed stipulated a maximum $\mathrm{d}T_S/\mathrm{d}t$ during dynamic operation.

2.2.3.2 Fuel-side chemical reaction constraints

To promote the steam reforming reactions in the pre-reformer and SOFC stack, sufficient steam must be provided. With too little steam, there is a risk of carbon deposition on the nickel catalyst of the pre-reformer or the anode, thus degrading those components. Peters et al. [16] and Engelbracht et al. [50] both estimated the potential for carbon formation in the pre-reformer or stack through the Boudouard reaction, depending on the operating conditions. Engelbracht et al. produced an operating map to avoid carbon deposition, showing that a relatively high RR and U_f were required.

The stoichiometry of the MSR and WGS reactions dictates that up to two moles of water are required for each mole of methane reformed. Therefore, Braun et al. [43], Kupecki [37] and Saebea et al. [41] assumed that by supplying sufficient steam to the pre-reformer or anode inlet, they could avoid carbon deposition. They adjusted the RR to achieve the S/C ratio values reported in Table 2.7.

The authors in Table 2.7 provided a range of U_f values. Fang et al. [74] tested two SOFC stacks up to 90 % U_f and reported concentration polarisation becoming apparent from 80 % U_f. Concentration polarisation is caused by mass transport losses and indicates fuel starvation.

2.2.3.3 Air-side chemical reaction constraints

The air flow rate can be adjusted to control the stack temperature. At part load, the required air flow rate reduces, which increases the risk of oxygen starvation on the cathode, and hence poor cell performance. Therefore, Peters et al. [16] provided the constraint that the λ must be kept above 2 with the stack temperature maintained constant. Nousch et al. [45] reported this to be at around 50 % part load for their SOFC system. Operating points at lower part load were therefore excluded.

2.3 Dynamic performance of SOFC systems

The power requirements for transport applications are typically dynamic. Therefore, the transient performance of SOFC systems in response to load dynamics should be investigated.

This section reviews models which report the dynamic performance of the SOFC system. Firstly, the open loop response of SOFC system models are investigated, followed by control strategies to maintain the SOFC system operating safely and within the constraints outlined in Section 2.2.3.

2.3.1 Open loop response

The open loop response of an SOFC system is its transient response to a step change in a single input variable, with all other variables kept constant. The open loop response most commonly studied for SOFCs is a step change in the fuel cell current, with the fuel and air flow rates held constant. The results of interest are the magnitude of the response of the main system parameters such as temperature, voltage and composition, and the response time. Achenbach [92] defined the relaxation time as "the period necessary to recover 90 % of the dynamic voltage drop" in the voltage dynamics.

The open loop response has been studied for SOFC stack models, but such models do not account for the inertia of the the BoP components. This review discusses the limited

Table 2.8: Open loop response to a step change in load, where τ is the response time, i is the current density in $\mathrm{mA\,cm^{-2}}$, V is the cell voltage in V, U_f is the fuel utilisation in %, T_s is the stack temperature in °C and $y_{\mathrm{H_2}}$ is the hydrogen mole fraction in the anode channel.

	τ	i	V	U_f	T_s	$y_{\mathrm{H_2}}$
Saarinen et al. [40]	0	220	0.87	70	760	
	10 s	410	0.78		760	
	4 h	410	0.82		780	
Mueller et al. [47]	0	244	0.671	0.84	1046	0.10
	0.1 s	254	0.664	0.84	1046	0.10
	20 s	252	0.663	0.86	1047	0.08
	30 min	250	0.661	0.87	1059	0.08

literature studying the open loop response of SOFC systems in the following.

2.3.1.1 Step change in load

Saarinen et al. [40] and Mueller et al. [47] both presented the open loop response of their SOFC system models to a change in load, with their results summarised in Table 2.8.

Saarinen et al. [40] investigated the open loop response to a step increase in the cell current density from $220\,\mathrm{mA\,cm^{-2}}$ to $410\,\mathrm{mA\,cm^{-2}}$ with the stack temperature at 760°C and 70 % U_f initially. During the first 10 seconds the cell voltage dropped from 0.87 V to 0.78 V. During the following 4 hours, the stack temperature increased from 760°C to 780°C, which caused the cell voltage to recover partially to 0.82 V. This showed the thermal transients are orders of magnitude slower than the chemical reaction transients in response to the change in load, in agreement with the response reported for SOFC stack models. The authors simulated the system without thermal insulation, but in a furnace at 760°C. Therefore, the magnitude of the thermal response is not considered representative of an SOFC cell system on a vehicle, since the heat loss characteristics would be different.

Saarinen et al. [40] also presented the open loop thermal response of the HEXs and afterburner. The afterburner temperature initially increased due to the raised temperature of the anode off-gas before decreasing due to the increased U_f of the SOFC stack. The

Table 2.9: Open loop response to step changes in flowrate from Cao et al. [93].

	$\dot{n}_{\text{air}}$ ($\text{mol}\,\text{h}^{-1}$)	$\dot{n}_{\text{fuel}}$ ($\text{mol}\,\text{h}^{-1}$)	i ($\text{mA}\,\text{cm}^{-2}$)	U_f	T_{stack} (°C)	$T_{\text{stack,in}}$ (°C)
Initial	1240	95	356	0.90	789	706
Step air	1368		348	0.88	765	681
Step fuel		104	380	0.88	869	797

temperature of the anode and cathode pre-heaters increased, due to the increase in stack temperature. The decrease in the burner temperature had no effect on the heat exchanger temperatures due to being decoupled in the system layout. Air was provided to the burner in a separate stream to the stack, so opportunities for heat integration of the burner off-gas were lost. The thermal response of the burner and anode pre-heater were faster than the stack and cathode pre-heater due to their lower masses.

Mueller et al. [47] published the open loop response for a 5 % drop in the load. This is rather small, so the magnitude of the transients were very small. They simulated a Siemens-Westinghouse tubular stack within their SOFC system, which operated at a far higher temperature than planar SOFC stacks today, at around 1000°C.

However, what is particularly informative about the open loop response presented by Mueller et al. [47], is that it provides a clear division between the instantaneous electrical transients, the fast chemical reaction transients with a relaxation time of 20 s, and the subsequent slow thermal transients with a relaxation time of 30 min. A similar distinction will be investigated in Chapter 5 of this thesis.

Mazumder et al. [52] also presented results of the open loop response to a step change in load. However, their model included the DC bus and power electronics; so their results accounted for the effect of these components and are not directly comparable to stand alone SOFC systems.

2.3.1.2 Step changes in gas flow

Table 2.9 tabulates the open loop response to 10 % increases in air and fuel flow rate, from simulations conducted by Cao et al. [93] for a hydrogen-fuelled SOFC system. The stack was operated at constant power, so the current density varied during the dynamic response. The increase in air flow rate provided additional cooling to the stack, and therefore caused the stack temperature to drop from 789°C to 765°C. On the other hand, the increase in fuel flow rate caused the stack temperature to increase from 789°C to 869°C. With internal reforming of methane, a decrease in stack temperature would be expected, due to the increased cooling rate of the endothermic MSR reaction.

Xing et al. performed a number of analyses on a 0D SOFC system model contained within a furnace [94]. A local stability and time response analysis provided information about the settling times of the dynamic responses for variations in current and furnace temperature. In addition, a frequency analysis was conducted which was useful to identify coupling of parameters when designing controllers for an SOFC system.

2.3.2 Control strategies

Many papers have discussed the control of SOFC systems in detail, and presented various control strategies. The review of the open loop response showed that changes in load and flowrate can cause significant changes in the operating conditions of the SOFC stack including U_f, temperature and voltage, as well as of the BoP components. The aim here is to investigate control pairings and strategies to operate the SOFC system safely while it is subjected to a dynamic load profile. The design and implementation of the controllers is not considered; the purpose of this work is as a feasibility study.

Albrecht et al. [46] studied the response of an SOFC system in a worst case scenario where the AC power demand was increased from 9.6 kW to 24 kW. They used their steady-state model to calculate the step in the flowrates of air and fuel required to maintain constant operating conditions. The key operating conditions were U_f, stack temperature, S/C ratio and cathode off-gas recirculation ratio.

In response, the cell voltage decreased immediately from 0.88 V to 0.77 V [46]. The authors showed that a larger decrease in cell voltage occured when the inertia of the fuel compressor and BoP components were accounted for, and the fuel on the anode became temporarily depleted for about 2 seconds. Over the remaining 500 s, the thermal response caused the cell voltage to decrease from 0.77 V by about 0.01 V. The thermal response of the system was not presented, which makes it difficult to evaluate how realistic the results presented were.

Sorrentino et al. [38] and Mueller et al. [29] both used lookup tables as feed-forward controllers to find the current required to meet the requested stack power. Two further lookup tables were used by Sorrentino et al. [38] to find the valve positions of the two bypasses for the anode and cathode pre-heater, in order to maintain the anode and cathode inlet temperatures at 700°C. Mueller et al. [29] used a feedback controller to maintain the cathode inlet temperature at 723°C. A feedback controller was used by both authors to manipulate the air flow rate to maintain a stack outlet temperature of 825 K and 877 K, respectively [38, 29]. This approach worked well because the thermal transients are slow. Mueller et al. [29] used a feed-forward controller to maintain U_f, but Sorrentino et al. [38] did not present any control strategies to maintain U_f or S/C ratio. Mueller et al. presented additional advanced control strategies to prevent fuel depletion on the anode and to reduce thermal gradients in the burner [29].

Sorrentino et al. [38] presented the response of an SOFC system to an increase in current from 40 A to 70 A during the first 15 seconds. The overshoot of the cell voltage was relatively small, but plotting for only 15 seconds is not enough time to observe the thermal transients, so it is hard to interpret their results. Mueller et al. [29] studied the system response when increasing the load demand from 2 kW to 5 kW.

Mueller et al. [29] gave particular insight into strategies for controlling SOFC systems when operating at variable load. A feedback controller was used to control the stack temperature by manipulating the air flow rate.

In real SOFC systems, control tasks can be more complicated. Xue et al. observed that

variations in steam supply for a stationary SOFC system had a significant impact on the burner temperature [95]. Therefore, they developed a fuzzy control method to respond to changes in steam flow. Such control strategies are considered beyond the scope of this thesis, since a reliable supply of reactants is consumed, but should also be considered in the detailed design of an SOFC powertrain.

Rafikiran et al. simulated the electrical powertrain of a vehicle including an SOFC system [96]. Particular attention was given to modelling the DC/DC converter which is controlled with an MMP-fuzzy controller. However, exceedingly faster dynamics were shown, far shorter than 1 second, and it is unclear how such fast dynamics could be occur on a real SOFC system. X.-l. Wu et al. designed a predictive controller for an SOFC system as a range extender for a passenger vehicle, to handle thermoelectric surge resulting in high SOFC operating temperatures [97].

2.4 Energy management strategies for SOFC hybrid systems

A number of models studied the performance of SOFC systems in response to dynamic load profiles across a range of applications and are listed in Table 2.10. Each of the models used a battery as an energy buffer between the electrical power demand of the load profile and the electrical power delivered by the SOFC system. This section outlines the methods used to size the SOFC system and the battery, and how the power was split between the two devices during operation. The various applications, drive cycles and performance metrics presented by each author are also investigated. The models are discussed below in order of increasingly dynamic operation for the SOFC system.

Sandrini et al. utilised a previously developed SOFC-battery model to simulate propulsion of a small waste collection vehicle with a weight when empty of 2 t with an existing SOFC model [98]. A number of duty cycles with varying payload were investigated, with data collected from an equivalent diesel vehicle. SOFC technology provided the advan-

tage of being able to use existing natural gas or bio-methane refuelling infrastructure. However, the SOFC stack was run at a constant power of 3 kW, with the assumption that the vehicle could be connected to mains power connection when not operational. This appear to be highly impractical for a vehicle operation, and would lead to a significant increase in fuel consumption.

Yang et al. simulated a 10 kW SOFC-CHP system consisting of two SOFC stacks, with particular consideration for fuel and air maldistribution to the stacks [99]. They simulated the SOFC-CHP system for a building with a full load requirement 8 hours each day. The remaining 16 hours, the SOFC system was operated in 30 % part load, but at reduced temperature. They showed that maldistribution of fuel between stacks had a stronger effect on electrical power than the stack temperature.

Z. Wu et al. simulated a vehicle with SOFC and internal combustion engine (ICE) for vehicle propulsion [100]. During vehicle operation, the SOFC system operated at a constant power of 150 kW, and the ICE met the transient power requirements. However, no consideration was made for turndown of the SOFC system power when the vehicle required less than 150 kW, for example during braking.

Ismael et al. introduced an cooperation search algorithm to solve the system of algebraic equations to model and SOFC system on an electric vehicle [101]. However, no comparison in the performance of their algorithm is made to the highly efficient equation-based solvers included in process simulation software like Engineering Equation Solver. They simulated the SOFC system and vehicle model dynamically using the built-in solvers in Matlab/Simulink, however a very short drive cycle lasting only 40 seconds. They also presented an SOFC power output of 5 kW, despite the SOFC system being sized for 100 kW, without justification.

Elakya et al. presented a small SOFC module as form of range extender for battery electric HGVs [102]. The SOFC system was run at a constant power of 50 kW in order to reduce the charging requirements of the HGV whilst stationary.

In the ABSOLUTE project, Brandon et al. [19] simulated an SOFC system hybridised

Table 2.10: Energy management strategies for SOFC-battery hybrid systems.

	For	Cycle	Sizing	States (Constraint)
Brandon et al. [19]	Van	24 h 6 h NEDC	Always-on	1
Sandrini et al. [98]	Refuse	10 x 6 h	?	1, off (SoC)
Dimitrova et al. [103]	Car	NEDC repeat	max(range) min(cost)	1, off (SoC)
Bessekon et al. [20]	Car	WLTP , US06 NEDC	FC charge 50 % B in 0.5 h–3 h	2, off (SoC)
Yang et al. [99]	Building	4 x 24 h	10 kW	2, off
Nousch et al. [104]	Building	1 year VDI 4655	min(energy)	3 + idle (SoC)
Kistner et al. [105]	Ship APU	72 h 2 peaks	min(cost)	8 (SoC, η_{FC})
Sorrentino et al. [38]	Truck APU	120 min $\bar{P} = 2$ kW	B for FC start	Map (SoC, P)

with a sodium-nickel chloride (ZEBRA) battery for the propulsion of a delivery van. The 24 h duty cycle consisted of repeated New European Driving Cycle (NEDC) drive cycles for 6 h, with the vehicle stationary the rest of the day. The SOFC system operated at constant power, even when the vehicle was stationary. The battery was sized to meet the energy requirements and peak power requirements of the vehicle whilst driving. The SOFC system was sized to fully recharge the battery during the 18 h that the vehicle was stationary. The drive cycle was adapted to include stops between deliveries and a break over lunch. A battery with a capacity of 22.6 kW h and an SOFC system with 1.58 kW power were required. A sensitivity analysis was conducted to investigate the impact of the traction power requirements and number of hours driving per day on the SOFC power and battery energy requirements. The fuel consumption was another key performance parameter.

Dimitrova et al. studied the performance of an SOFC-gas turbine system hybridised with a lithium-ion (Li-ion) battery in a passenger car based on repeated NEDC duty cycles [103]. They studied the effect of varying SOFC-GT power, battery capacity, and fuel tank capacity on vehicle cost and range. The SOFC-GT system operated at constant

power, only switching off if the battery became fully charged, and then switching back on immediately if the battery started to deplete in charge, with no rate limiter.

Bessekon et al. [20] studied the performance of an SOFC system hybridised with a battery also on a passenger car. They studied the performance of the vehicle following the Worldwide Harmonised Light Vehicles Test Procedure , US06, and NEDC drive cycles. They sized the SOFC system to charge the battery 50 % within 3 h. The battery size of 30 kW h was the same as used in the existing Nissan Leaf battery electric vehicle. The authors used a state machine to switch the SOFC system between its nominal power mode and a reduced power mode depending on the battery state-of-charge. A state machine has a number of modes: Depending on a number of inputs and outputs, the machine, in this case a vehicle powertrain, can move between different states. Bessekon et al. had not only the nominal and reduced power modes, but also a heat-up mode, where the SOFC system starts from cold and only heats-up once the vehicle starts moving and the battery discharges below 20 % depth of discharge. They conducted a sensitivity analysis of vehicle range and energy consumption on a number of variables including battery charging time, SOFC heating time, battery capacity, tank volume, and choice of fuel.

Nousch et al. [104] simulated a 1 kW SOFC system for delivering electrical power to a residential home in Germany with a battery for energy storage using the Modelica software. The model was validated experimentally. The VDI 4655 load profile represented household electricity usage over a one year cycle. A state machine varied the stack power based upon the battery state-of-charge (SoC) between the nominal power and 50 % power. Below that, the SOFC system struggled to maintain sufficiently high stack temperature. A comparison of system performance was made between hot standby and shut-down modes when no electricity was required overnight.

Kistner et al. [105] simulated an SOFC-battery hybrid system on a ship 330 m in length and 156 kt in weight. The system was designed to meet the auxiliary electrical power requirements (hotel load) for a 72 h duty cycle, with a base load varying from 10 MW to 14 MW and a peak load around 30 MW during harbour manoeuvres. A total

SOFC power of 14.1 MW and battery capacity of 3.65 MW h were found to give the lowest costs of around EUR 7 million per year. Potential equipment failure of the battery or fuel cell modules were accounted for.

Kistner et al. [105] operated each SOFC module above 50 % part load to maintain a suitable stack temperature. They used a state machine firstly to maintain battery SoC within critical limits, which were adjusted during the optimisation. Within those SoC limits, the state machine secondly maintained the stack operation within 60 % to 80 % part load in which the efficiency of the SOFC system was highest. Each 300 kW SOFC module was limited to a maximum ramp rate of $30\,\mathrm{kW\,min^{-1}}$, and limitations were also placed on the charge and discharge rates of the battery.

Sorrentino et al. [38] simulated an SOFC system and battery to meet the auxiliary power requirements of a truck. A randomly generated 120 min duty cycle was used with an average power demand of 2 kW and maximum power demand of 7 kW. The performance was compared when the SOFC system started the duty cycle cold or warmed-up. A battery capacity of 4.5 kW h was required to follow the duty cycle while the 5 kW SOFC system was heated from cold using burner off-gas to heat the cathode air.

Sorrentino et al. [38] used a supervisory controller with an operating map which defined the ratio between the battery power and power demand as a function of the battery state of charge and power demand. A rate limiter for the stack power gradient was set at $30\,\mathrm{W\,s^{-1}}$. However, the rules for the generation of the operating map with fuzzy logic were not explained.

This section has shown that a variety of energy management strategies have been published in the literature. However, relatively few of the authors conducted dynamic SOFC system modelling as part of their SOFC-battery energy management strategy [45, 38]. Only the strategies of Sorrentino et al. [38] and Kistner et al. [105] allow for dynamic operation of the SOFC system, by limiting the power ramp rate. None of the authors go further to relate this to the thermal or material limitations of the SOFC system, for example the thermal gradients within the SOFC stack.

2.5 Lifetime of SOFC stacks

Like other electrical devices, SOFCs degrade through ageing of their materials during their operating lifetimes. This ageing may be described as a reduction in cell voltage, which thereby reduces the electrical efficiency of the SOFC stack. Therefore, as SOFC stacks age, increased current densities would be required to deliver the same electrical power to the powertrain of an HGV. Increased current densities would also increase fuel consumption, and thereby increase operating costs. At the end of its life, the SOFC stack is too degraded to fulfil its function and should be replaced. This reduction in performance should be factored into the design of an SOFC system for an HGV powertrain.

There are a wide range of phenomena which can result in degradation of SOFC stacks. Many stem from changes to microstructure of the SOFC materials under different operating conditions, and through ageing. McPhail et al. reviewed some of the more common degradation mechanisms [106]. One mechanism is the re-oxidation of the SOFC anode may occur as a result of local leakages or fuel starvation. Another is the poisoning of the SOFC cathode through contaminants such as chromium or sulphur. Many of the degradation mechanisms result in the delamination of layers of the SOFC repeating unit, which can for example be caused caused by differences in thermal expansion coefficients between different layers.

2.5.1 Defining the degradation rate

In the literature, degradation rates are most commonly reported as a change in voltage at constant current. The disadvantage of this approach is that it does not allow comparison of SOFC stacks tested under differing conditions. Therefore, McPhail et al. and Skafte et al. both encouraged the use of changes in ASR as a means to quantify degradation [107, 106]. The degradation rate, in $\Omega\,\mathrm{cm}^2\,\mathrm{kh}^{-1}$, can therefore be written as:

$$\text{Degradation rate} = (ASR(t = t_1) - ASR(t = 0)) \times \frac{1000}{t_1} \tag{2.7}$$

where $ASR(t = t_1)$ is the ASR in $\Omega\,\mathrm{cm}^2$ at time t_1 in seconds, $ASR(t = 0)$ is the ASR in $\Omega\,\mathrm{cm}^2$ at beginning of stack life.

A degradation rate of this form could be incorporated into the SOFC stack models reviewed in Section 2.1.4. However, selecting experimental data of degradation rates in the literature can be a complicated task, as highlighted by Skafte et al. [107] and McPhail et al. [106]. One of the important considerations is that degradation rates depend not only on operating time, but also on operating conditions, and even on the laboratory setups used to measure SOFC stack performance, which may differ significantly from commercial cells [106]. Skafte et al. conducted a review of previous studies, and found a wide range in degradation rates between different authors [107]. SOFC stack manufacturers [108] have reported a more rapid degradation at the beginning of life of stack, followed by a slower degradation over the remainder of its lifetime. Furthermore, degradation analysis of SOFCs is by its nature a time consuming process, and therefore there has been increased focus on introducing accelerated stress tests [106]. Such tests are designed to simulate real operation under more extreme conditions by ensuring the degradation pathways match those of long term operation.

2.5.2 Experimental degradation rates

At Forschungzentrum Jülich (FZJ), a short SOFC stack was subjected to 10,000 hours of operation [109]. Over that period, the stack was operated under a range of current densities and U_f. Degradation rates between $0.35\,\%\,\mathrm{kh}^{-1}$ and $0.88\,\%\,\mathrm{kh}^{-1}$, or between $6.1\,\mathrm{m}\Omega\,\mathrm{cm}^2\,\mathrm{kh}^{-1}$ and $12.4\,\mathrm{m}\Omega\,\mathrm{cm}^2\,\mathrm{kh}^{-1}$ were observed over each period of operation. In the post mortem analysis of the stack, delamination of the cathode and the interconnect was identified as the primary degradation mechanism. It is believed the degradation was caused by local air starvation, and an inhomogeneous contact between the two layers. For similar reasons, degradation due to localised fuel starvation was observed on the anode.

Long term SOFC operations have been undertaken as part of the NEDO project in Japan with a number of SOFC stack manufacturers showing degradation rates between

$0.3\,\%\,\mathrm{kh}^{-1}$ and $0.5\,\%\,\mathrm{kh}^{-1}$ with cumulative operating times of 130 kh [110]. R. Leah et al. reported a break-in period in long-term testing of Ceres Power 5 kW stacks, after which a near constant degradation rate of $15\,\mathrm{m\Omega\,cm^2\,kh^{-1}}$ was observed [108]. 2000-hour testing of the 119-layer E3000 SOFC stack at Elcogen exhibited degradation rates of $0.56\,\%\,\mathrm{kh}^{-1}$ or $20\,\mathrm{m\Omega\,cm^2\,kh^{-1}}$, a slight increase on their shorter E350 stacks [111]. Mai et al. reported stack degradation rates of $0.3\,\%\,\mathrm{kh}^{-1}$ or $13\,\mathrm{m\Omega\,cm^2\,kh^{-1}}$ at Hexis [112], and Walter et al. reported degradation rates of $11\,\mathrm{m\Omega\,cm^2\,kh^{-1}}$ in long term testing at Sunfire [113].

2.6 Thermal cycling of SOFC systems

When no electrical power is required, the SOFC system can be shut down. The SOFC system then moves through a number of operational modes until electrical power is again required. A flowchart illustrating these operational modes is shown in Figure 2.4.

- Shut-down: First of all, the SOFC system is shut down. During shut-down the power, fuel and air supplies are ramped down until the SOFC system is idle.
- Cool-down: When the SOFC system is left idle, there is no heat generation and the hot components will cool down through heat losses to the ambient environment.
- Start-up: When electrical power is required, the SOFC system starts up. Start-up is the process of supplying fuel and air to the system and gradually drawing load until the nominal power is reached.
- Heat-up: After extended periods of idling, the SOFC system can cool significantly, and therefore heat-up of the SOFC system is required before start-up. Heat-up can be achieved either by burning fuel or by electrical heating.
- Hot standby: In hot standby mode, fuel is provided to the SOFC stack or the burner to generate heat and maintain the temperature of the SOFC system components. Hot standby modes replaces cool-down mode and avoids the need for heat-up after extended periods of idling.

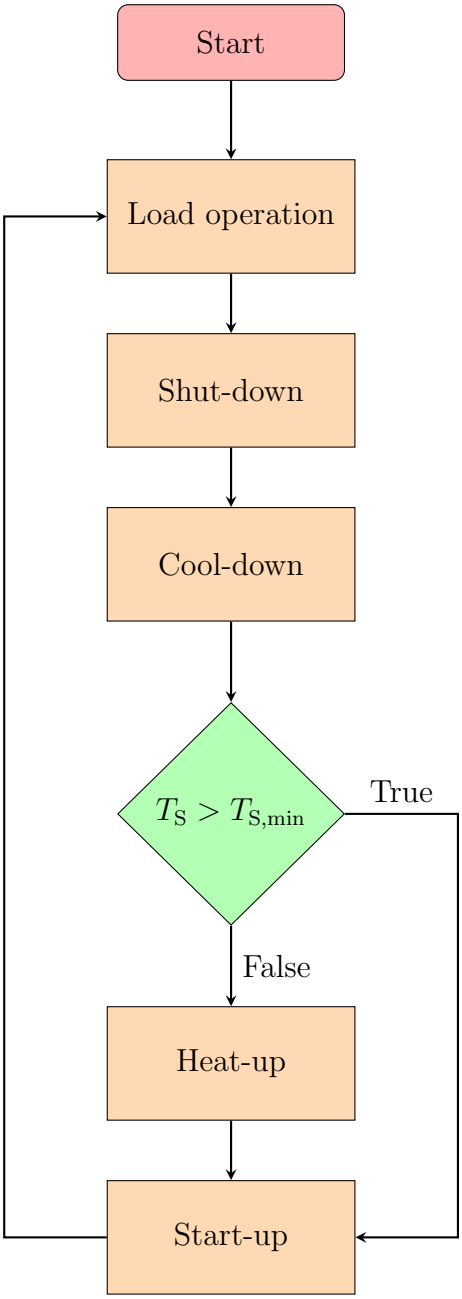

(a) Cool-down.

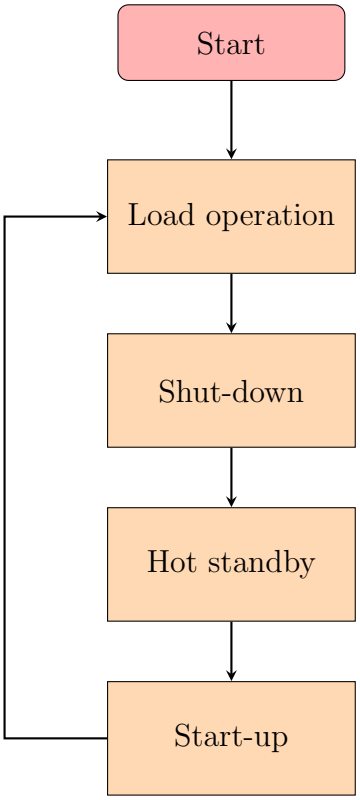

(b) Hot standby.

Figure 2.4: Operational modes of the SOFC system.

Each operational mode is investigated further in the following.

2.6.1 Shut-down

Shut-down of the SOFC system is relatively simple. The electrical power output of the SOFC stack can be reduced to zero, the air blower switched off, and the valve from the fuel supply closed. This can be achieved within a few seconds.

2.6.2 Cool-down

When the SOFC system is idle, the temperature of the SOFC system components decrease through heat losses to the ambient environment. To maintain their high temperature for as long as possible, the hot SOFC components are typically surrounded by insulation, and are thus housed within a hotbox [114]. The rate of cool-down depends on the performance of the insulation of the system components, and is related to heat losses presented in Section 2.1.3.3. For HGV applications, the insulation should be designed to ensure the temperature loss is not significant, so that start-up can proceed rapidly.

Of the SOFC system models studied in Section 2.1, the majority either neglected heat losses altogether or assumed that only specific components in the SOFC system experienced heat losses. Those models were not sufficient to model cool-down of the SOFC system, and therefore additional literature is reviewed in this section to investigate cool-down dynamics.

Holtappels et al. [114] studied the cool-down characteristics of a 5 kW and a 50 kW SOFC system with 5 cm, 10 cm and 15 cm of microporous insulation with a thermal conductivity of $0.024\,\mathrm{W\,m^{-1}\,K^{-1}}$ at 800°C. They assumed that immediate start-up without prior heat-up could be achieved if the hotbox temperature remained above 600°C. They showed that the 50 kW system retained its heat far longer than the 5 kW system, and that immediate start-up would be possible after 33 hours with only 5 cm of insulation. Therefore, such a SOFC system on a vehicle could start-up in the morning after being stationary overnight. For immediate start-up following weekend shut-down, nearly 15 cm

of thermal insulation would be required. For comparison, the 5 kW SOFC module at FZJ, was insulated with a micro-porous material of 10 cm thickness [14].

Apfel et al. [17] compared the thermal conductivity of different insulation materials as a function of temperature. The material with the lowest thermal conductivity was manufactured by Microtherm. They also presented the cool-down characteristic of a 50 kW SOFC stack with different insulation thicknesses. Petruzzi et al. [115] presented the cool-down characteristics depending on the ratio between the thermal conductivity and insulation thickness. Their results showed that increasing the insulation thickness, or using a material with lower thermal conductivity, reduced the rate of cool-down of the stack.

2.6.2.1 Forced cool-down

Some authors provided active cooling of the SOFC system using the air blower during cool down. Selimovic et al. [116] cooled the cells over 4 h by maintaining the temperature difference of the stack at 100°C. It is not explained how this was achieved, or what the purpose of the relatively fast cool-down was. Hanasaki et al. [117] investigated the impact of different shut-down approaches on stack ageing caused by thermal cycling. In one approach, the stack was cooled at a rate of 100 $^{\circ}\mathrm{C}\,\mathrm{h}^{-1}$ down to 200°C, and in another case, an emergency shut-down was performed where the stack cooled at a rate of up to 400 $^{\circ}\mathrm{C}\,\mathrm{h}^{-1}$ down to 400°C. They showed forced thermal cycling in cool-down of the SOFC system led to accelerated degradation, with the mechanisms discussed in the report.

2.6.3 Start-up

Provided the SOFC system is still hot, start-up can proceed immediately when electrical power is required, for example, when a vehicle is first switched on in the morning. The basis of start-up procedure is the shut-down procedure in reverse: Fuel supply to the anode and air supply to the cathode are ramped up, and an increasing current is drawn from the SOFC stack, until the nominal operating point of the SOFC system is reached. However,

when compared to shut-down, start-up must also consider the start-up temperature and water supply, which are discussed in the following.

2.6.3.1 Stack temperature requirement

The first question is the temperature at which start-up can proceed without requiring prior heat-up. When reforming methane, the pre-reformer and SOFC stack need to be hot enough to ensure there is no carbon deposition, and that the H2X reaction can proceed.

Both Petruzzi et al. [115] and Holtappels et al. [114] proceeded with start-up, provided the SOFC stack temperature was at least 600°C, while its nominal operating temperature was 800°C. Petruzzi et al. identified that start-up can commence above 600°C because the heat produced from the H2X reaction was more than can be deposited in the stack through the cathode air. To achieve that, the SOFC stack had to be controlled to operate at lower cell voltage and hence high thermal power, to maximise the heat production in the stack.

Halinen et al. [18] presented an experimental study where they started drawing load at an SOFC stack temperature of 700°C, where its nominal operating temperature was about 780°C. However, fuel supply to the reformer was started when the SOFC stack temperature was only 300°C. Yang et al. also commenced fuel cell operation from 700°C [99]. Z. Wu et al. presented a dynamic SOFC system model hybridised with an ICE for vehicle propulsion [100]. They presented a 50 s start-up of the SOFC system, but without any consideration of the temperature gradients with such a rapid start-up.

At the beginning of start-up, the endothermic MSR reaction commences before the current increases and the H2X reaction rate increases. Therefore, Lee et al. provided additional fuel to a burner to counteract the reformer cooling before the fuel cell current had increased [57]. They also commenced start-up with a stack temperature of 700°C.

2.6.3.2 Water supply

Before a methane-fuelled SOFC system can start producing electrical power, the reforming reactions must be started. Many of the SOFC system models presented in Section 2.1.7 included steam reforming of natural gas, and used AOGR to recycle steam produced from the H2X reaction. However, during start-up, no water is available from the H2X reaction and water must be provided otherwise.

Both Kim et al. [118] and M.-H. Chen et al. [119] presented SOFC stack models with internal steam reforming of methane, including a start-up strategy. However, they did not include any consideration of how steam would be supplied during start-up, which shows the limitations of such an analysis without modelling the BoP components.

Halinen et al. [18], Lawlor [120] and Lee et al. [57] all used an external steam supply for start-up of the steam reformer. However, on a vehicle this would require an additional water tank and steam generator.

Therefore, Carré et al. [121] proposed using a CPOX reformer for start-up to reform the methane and produce steam. Once the load had increased and AOGR has started, steam from the H2X reaction was recycled to the reformer, and the CPOX reformer could be switched off. With steam reforming of methane, higher electrical system efficiency was achieved.

2.6.4 Heat-up

Heat-up is required whenever the temperature of the stack and BoP components within the hotbox are too cold to immediately start-up the SOFC system. The most common approach for heat-up reported in the literature is by burning fuel, but some authors also used electrical heating plates, or a combination of the two. In both methods, the rate of heat-up is limited by the maximum allowable thermal gradients within the SOFC stack. According to Zeng et al. [90], thermal gradients in the stack should not exceed $10\,\mathrm{K\,cm^{-1}}$ during heat-up. Once the required SOFC stack temperature is reached, start-up of the SOFC system can commence.

2.6.4.1 Cathode air heating

In cathode air heating, fuel is combusted directly in the burner and the hot off-gas is exchanged with cold air in the air pre-heater. The heated air is fed through the cathode-side of the SOFC stack to heat it. The rate of SOFC stack heating that can be achieved is relatively low because the heat capacity of the air within the system is much smaller than that of the solid mass, even at high flowrates. In addition, gas-to-solid heat transfer is relatively slow.

The rate of heating is commonly specified based on the burner power, which is the lower heating value of the fuel multiplied by the mass flow rate of fuel fed to the burner [122]. One approach for heat-up is to operate the burner at constant power by fixing the fuel flow rate. This can lead to high burner temperatures and therefore, Carré et al. [121] manipulated the cathode air flow rate to control the burner temperature. Kim et al. [118] showed that internal temperature gradients within the SOFC stack during heat-up can be significant. Therefore, some authors manipulated the cathode air flow rate to limit the temperature difference between the SOFC stack temperature and the air temperature at the cathode inlet during heat-up. Selimovic et al. [116] and Sorrentino et al. [38] maintained a constant stack temperature difference of 100°C, and Apfel et al. of 150°C [17].

Hagen et al. fabricated and tested two short SOFC stacks [123]. They demonstrated heat-up times as fast as 1 hour using external cathode air heating with good robustness towards thermal stress. Despite thermal gradients as large as $30\,^{\circ}\mathrm{C\,cm^{-1}}$, no signs of leakage, loss of contact or mechanical failure were observed after repeated thermal cycles of the SOFC stacks, which was identified as promising for their potential application in vehicle applications.

2.6.4.2 Electric heating

Rather than combusting fuel, heat-up of the SOFC system can also be achieved with electric heating. This could be an attractive solution for transport applications, where a

battery is likely present to provide electrical energy.

U. Bossel [124] presented a 200 W SOFC stack with electric heating plates sandwiched between the two halves of the bipolar plates of each cell. It was capable of heating the stack up to 700°C in less than 5 minutes, and thus for the stack to undergo rapid thermal cycling.

Peters et al. [14] presented a 5 kW SOFC system as an integrated module at FZJ with three electric heating plates. The heating plates were placed between the air pre-heater and the burner, between the burner and the stack, and on top of the stack. Each heating plate had a maximum power of 2 kW, and the power was manipulated to maintain a constant stack temperature ramp-rate. Peksen [125] presented a heat-up strategy for the module. The electric heaters were heated to 850°C over a 2 hour period, and subsequently the heaters were maintained at constant temperature until the system components reached 750°C, which took around 16 hours.

The experimental SOFC system presented by Halinen et al. [18] consisted of an electric heater within the stack module to heat the solid and the air. An additional smaller electric heater was placed in the AOGR loop. Although Carré et al. [121] used a burner and cathode air heating to heat the SOFC stack, they integrated an electric heater into the CPOX reformer to ease start-up by heating it to 300°C first. An electric heater was also placed within the steam pre-reformer.

Lee et al. presented a strategy for heat-up of a 5 kW SOFC-engine hybrid system [57]. In their simulations, the SOFC system was heated electrically using electrical heaters in the stack, which were heated at a rate of $40\,^{\circ}\mathrm{C\,h^{-1}}$. The other components in the system, such as the burner, reformers and heat exchangers, were heated by blowing air and nitrogen through the system, and heated more slowly due to their thermal inertia. Similar heat-up characteristics were observed in their experimental SOFC system in the laboratory.

2.6.5 Hot standby

Ideally, start-up of the SOFC system should proceed immediately when electrical power is required. Section 2.6.2 showed this is feasible with suitable insulation. However, extended cool-down leads to deeper thermal cycling, meaning that the subsequent heat-up of the system takes longer and requires more fuel. In addition, repeated deep thermal cycles can significantly increase degradation of the SOFC stack, because of the introduces thermal stresses it introduces. These thermal stresses originate from the large spatial temperature gradients created within the stack during thermal cycling, especially during heat-up [117]. Additionally, any mismatch in the thermal expansion coefficients of the SOFC materials creates additional thermal stresses as the temperature of the SOFC stack decreases [12]. For HGV applications, even if cool-down can be limited during weekends, full thermal cycles will occasionally occur during maintenance, for example. In general, full thermal cycles should be avoided as far as possible.

Alternatively, the SOFC system can be left in hot standby, by continuing to heat the system. A possible flowchart for operation modes including hot standby is shown in Figure 2.4b. The heat to maintain the temperature of the system could be provided by electrical heating or burner fuel. This means that start-up can proceed immediately when electrical power is required, and eliminates thermal gradients associated with thermal cycling. Hanasaki et al. [117] showed that hot standby significantly reduced thermal degradation when compared to thermal cycling with successive cool-down and heat-up cycles.

Nousch et al. [104] proposed leaving a micro-CHP system in hot standby to maintain the temperature of hot box components overnight. They simulated operating the SOFC stack at low part load, producing enough electrical power to support only the auxiliary power requirements, and enough thermal power to maintain the stack temperature. Furthermore, the hot standby operation did not necessarily increase fuel consumption over that required for heat-up of the SOFC system in the morning when the system was left to cool-down overnight.

2.7 Deployment of SOFC systems in transport

In order to put this thesis within a broader context, this section investigates the deployment of SOFC transport in the literature. The majority of SOFC units sold are for stationary heat and power applications, in particular micro-CHP units which provide heat and electricity to buildings at high efficiency utilising pre-existing natural gas infrastructure. Around 27 000 SOFC units with a total capacity of around 249 MW were shipped in 2022, predominantly through the Enefarm initiative in Japan, and sales of Bloom Energy in the USA and South Korea [126]. Deployment of SOFCs in the transport sector is very limited. The relatively long start-up time of SOFCs has been a barrier to deployment in transport applications, and the increased thermal cycling in mobility can lead to reduced stack lifetime. Developing SOFC systems with high energy and power density will also be crucial for transport applications. In light of this, this section outlines the deployment of SOFCs in the automotive, maritime and aviation sectors.

2.7.1 In the automotive sectors

Much of the initial research on SOFCs in transport focused on automotive applications. Both APUs and range extenders have been demonstrated at the prototype or proof-of-concept stage.

2.7.1.1 SOFC systems as auxiliary power units

APUs provide electrical power for ancillary services on vehicles. APUs reduce idling losses, since the ICE can switch off while the vehicle is stationary. SOFCs have high efficiencies and can theoretically run on petrol or diesel, so can directly replace existing electrical generators while reducing fuel consumption. NO_x and particulate matter emissions are eliminated when switching to an SOFC APU and noise pollution is reduced. The first SOFC APU was developed by Delphi Automotive Systems and BMW to meet the electrical power demand of the air conditioning unit on a petrol-fuelled passenger car [127].

The fuel was reformed in a CPOX reformer, and the SOFC was hybridised with a Li-ion battery.

A number of projects have demonstrated SOFC as APUs in the sleeper cab of long haul trucks. With onboard electrical appliances such as a television, microwave, kettle and refrigerator, trucks in the USA have a considerable auxiliary electrical power requirement. Delphi, Volvo and PACCAR developed a 2.5 kW SOFC APU running on diesel, with demonstration on a Peterbilt drayage truck [128, 129]. Cummins and Protonex built a tubular SOFC APU for a diesel truck, though it was only demonstrated in a laboratory environment [130]. Eberspächer and Volvo demonstrated a 3 kW diesel SOFC APU onboard a truck in the DESTA project [131]. The SAFARI project aimed to install a 100 W micro-tubular SOFC APU on a truck running on liquefied natural gas (LNG) [132]. LNG is a more attractive fuel for SOFC systems than diesel, as it can be reformed easier with less risk of degrading the SOFC stack, and a higher electrical efficiency can be achieved.

In the Centre for Fuel Cell and Hydrogen Research (CFCHR) in the University of Birmingham, the potential of using the off-heat from SOFC systems in a HGV APU has also been researched. Venkataraman and Pandya both investigated coupling the heat produced from an SOFC system with a vapour absorption refrigeration system intended for an HGV [133, 134]. Their experimental set-up used an air heater as an analogue for the thermal power of the SOFC offgas.

2.7.1.2 SOFC systems as range extenders

SOFCs systems have been installed as range extenders in the drivetrains of battery electric vehicles. The tractive force at the wheels of the vehicle is still provided with power from the battery. The SOFC system runs at constant load, delivering power to the battery, recharging it, and thereby increasing the range of the vehicle.

Delphi Automotive Systems modelled a 5 kW to 10 kW SOFC module used to charge a lithium-ion battery pack on an electric passenger car (the GM EV1) fuelled with petrol or diesel [135]. Nissan built a prototype vehicle, the e-Bio Fuel Cell (e-NV200), with a

5 kW SOFC module to charge a Li-ion battery with 24 kW h capacity [136]. The SOFC system was fuelled by a 30 L tank of bio-ethanol-water mixture and the vehicle had over 600 km range. The vehicle was designed for Brazil where there is already a bio-ethanol refuelling infrastructure.

AVL aimed to develop a 5 kW SOFC range extender for passenger cars in the MeStREx (Austria) and COMPASS (European Union) projects [137]. The key performance indicator targets of the SOFC module in the COMPASS project were 15 min start-up, 8000 h durability and 55 % net electrical efficiency. 70 min start-up, 1000 h durability and 30 % efficiency were identified as the state-of-the-art for SOFC APU systems [138].

Ceres Power and Weichai Power [139] were developing a 30 kW SOFC module comprised of six 5 kW stacks with compressed natural gas (CNG) fuel as a range extender for an electric bus in China. However, Ceres Power have since reported [140] that the project is unlikely to be successfully completed. Ascend Energy [141] retrofitted a Polaris utility vehicle designed for mobility on farms in California with a 1 kW SOFC range extender to give a range of over 100 miles. The range extender features tubular SOFC technology from Atrex Energy with CNG fuel reformed internally. The vehicle was found to offer 30 % fuel savings relative to an equivalent petrol vehicle, and there were also plans to test the vehicle on propane.

Qin et al. reviewed the use of SOFC systems for automotive applications, in particular in APUs for trucks, and as range extenders for battery electric vehicles (BEVs) [142]. They identified lengthy start-up times and thermal management as the main challenges for utilising SOFC technology in automotive applications. The reforming performance has been also identified as an important aspect for operation of SOFC systems on vehicles. Miura et al. investigated an improved method of low temperature internal reforming of SOFC cells to support their application for vehicle propulsion [143].

Similarly, research in the CFCHR at the University of Birmingham has investigated fuel reforming for SOFC technology. Tsai et al. modelled an SOFC with internal steam and dry reforming with a focus on methane conversion, hydrogen production, and carbon

deposition [144]. Majewski et al. tested configurations of number of CPOX reformer technologies intended for use in an SOFC system fuelled with natural gas, as part of an APU on an HGV [145].

Whilst most of the other work on SOFC technology in the CFCHR has focused on materials and cells research, Hodjati-Pugh developed a short micro-tubular SOFC stack [146]. The utility of their research is limited for this analysis, however, since all commercial SOFC manufacturers produce planar cells, which are hence the SOFC design considered in this work for HGV propulsion.

In the CFCHR, previous studies for vehicle propulsion considered only polymer electrolyte fuel cells (PEFCs) technology. Al-Sagheer et al. developed a controller for power split between a PEFC and a battery onboard a hydrogen fuel cell electric vehicle (HFCEV) [147]. Khan et al. performed experiments on a 5 kW PEFC system to investigated operating strategies for an HFCEV [148].

2.7.1.3 Comparison with PEFCs

In comparison to SOFCs, deployment of PEFCs for automotive transport is more advanced. Focusing on the HGV sector, in China 3,744 new PEFC HGVs were registered in 2022 [126]. Hyundai has delivered 47 of its XCIENT PEFC HGV model in Switzerland, and plans to expand deployment globally. The European manufacturers such as Daimler and Volvo are mostly still in the prototype stage for their first PEFC HGV models [126].

2.7.2 Alternative fuels for SOFC vehicles

SOFC technology as a propulsion technology has not only the advantage of high drivetrain efficiency, but also of fuel flexibility. This gives the potential for utilising existing infrastructure to refuel SOFC-powered vehicles but with lower fuel consumption and lower emissions than vehicles with ICEs [149].

2.7.2.1 Bio-ethanol in Brazil

Bio-ethanol is a widely used transport fuel in Brazil for ICE vehicles. The bio-ethanol could alternatively be used to fuel SOFC vehicles, with an external reformer within the SOFC system to produce syngas for the SOFC stack. Ma et al. considered the use of bio-ethanol as a fuel for SOFC vehicles also, and simulated their potential as an APU [150]. The authors compared different reforming pathways for bio-ethanol: steam, dry, CPOX, and autothermal.

The potential of SOFC vehicles fuelled with bio-ethanol in Brazil has also been assessed through life cycle assessments conducted by Velandia Vargas et al. [151] and De Oliveira Gonçalves et al. [149]. Velandia Vargas et al. highlighted the ability of SOFC systems to reform bio-ethanol onboard the vehicle, in comparison to PEFCs systems which require pure hydrogen as a fuel [151]. De Oliveira Gonçalves et al. highlighted the existing bio-ethanol refuelling infrastructure as an advantage for SOFC-powered vehicles, when compared to plug-in BEVs, since in Brazil there is a shortage of recharging infrastructure [149].

2.7.2.2 Natural gas in Iran

Iran has extensive natural gas resources, and distribution and refuelling infrastructures for CNG vehicles. As a result, 15 % of energy consumption from transport in 2019 was from CNG [152]. Due to the ability of SOFC systems to directly reform natural gas, Heidary et al. conducted a techno-economic analysis of SOFC passenger cars fuelled with natural gas in Iran [152]. They found that due to the existing CNG infrastructure, and high efficiency of SOFCs, SOFC vehicles fuelled with CNG showed potential to have lower well-to-wheel energy consumption than PEFC, battery or gasoline vehicles.

2.7.2.3 Ammonia

Liao et al. conducted a life cycle assessment of an SOFC vehicle power with liquid ammonia fuel [153]. They found that the majority of the greenhouse gas (GHG) emissions

were produced during the manufacturing process, and the life cycle GHG emissions were attractive compared to competing zero emission propulsion technologies. These assumptions would only hold true if the ammonia could be produced from renewable energy.

2.7.3 In the waterborne sectors

The shipping and wider waterborne sectors are some of the more challenging sectors for decarbonisation. Most ships are bespoke with a huge range of sizes, types and power requirements. Ships have long lifetimes of over 20 years, meaning there is greater urgency for new ships to be zero-emission. In the last few years, shipping is the transport sector that has received the most attention for SOFC technology. Fuel flexibility is a particular attraction of SOFCs for shipping because it allows for the use of more energy dense fuels compared to other zero-emission electrification technologies.

SOFC maritime projects cover a wide range of fuels, different power requirements and vessel types. Early projects involved small scale APUs, such as the METHAPU project [154] where Wärtsilä developed and operated a 20 kW SOFC unit fuelled with methanol, on a car carrier in Bremerhaven, Germany. Since then, projects have begun to scale up. The SchiBZ projects [155] led by TyssenKrupp Marine Systems initially developed a diesel 50 kW SOFC system with Sunfire. The unit is being scaled up to 300 kW with external reforming of LNG fuel, to be installed on a special purpose vessel, the MS Forester. Challenges in scale-up have been the operation of the auxiliary systems and thermal management [156]. At larger scale, SOFCs can be the prime mover, usually when hybridised with a battery for peak power requirements. In 2024 the ShipFC project [157] is due to demonstrate a 2 MW SOFC fuelled with green ammonia for the propulsion of an offshore vessel, Viking Energy. Wärtsilä are developing the ammonia fuelling system, and Prototech the SOFC system.

A number of different fuels are considered for SOFC propulsion. Prototech [158] will test a 1.2 MW SOFC unit with a number of fuels including ammonia, LNG and hydrogen on a chemical tanker in Norway. SOFC4Maritime [159] is another project developing an

SOFC system running on ammonia for shipping vessels.

Cruise ships have not only high power requirements for propulsion, but also heat and power for the hotel load. Total power requirements can be over 100 MW. The NAUTILUS [160] and PACBOAT [161] projects will demonstrate small 60 kW and 50 kW SOFC units on cruise ships. In both projects, the SOFCs will run on LNG, reducing GHG emissions relative to heavy marine oil, and eliminating pollution at ports. This is important since cruise ships spend 50 % of the operating time docked in ports. The SOFC is hybridised with a Li-ion battery to meet the dynamic load requirements. Future projects could scale up the SOFC system to replace one or more engines on the ship [160].

SOFCs are also being considered for fuel tankers, particularly if alternative fuels become more widespread. In the future, fuel tankers may carry liquefied hydrogen or ammonia, rather than oil. Bloom Energy have signed an agreement with Samsung Heavy Industries [162] to develop SOFC-powered ships running on LNG, with the aim to present a prototype at the LNG pilot facility at the Geoje Shipyard in South Korea. Doosan Fuel Cell and Navig8 [163] are developing an SOFC system for a 50 kt chemical tanker using the SteelCell stack technology from Ceres Power.

2.7.4 In the aviation sectors

A number of studies have looked at the potential of SOFCs in the aviation sectors, but demonstration has been limited. SOFCs are usually hybridised with a battery to meet peak power requirements during take-off. Like in the maritime sector, SOFCs allow for more energy-dense fuels.

Initial prototypes have been for unmanned aerial vehicles (UAVs). Pro Drone developed an 800 W SOFC Atsumitech module featuring Elcogen SOC technology [164, 165]. The SOFC cassette cylinders reformed LPG fuel internally and were hybridised with 0.2 kW h capacity battery. The drone was capable of carrying 30 kg for up to 2 hours. The SUAV project built a 300 W SOFC system hybridised with a Li-ion battery and CPOX reforming of propane fuel [166]. Li et al. modelled an SOFC-GT system for

propulsion of a supersonic aircraft [167]. The SOFC system components were modelled in 0D, and the steady-state performance of the system was studied with varying U_f and current density.

There are nine projects under REEACH (Range Extenders for Electric Aviation with Low Carbon and High Efficiency) in the USA with energy-dense carbon neutral liquid fuels, with a developmental prototype the ultimate aim [168]. Many of the projects use an SOFC system for propulsion. The FLyCLEEN project uses a pressurised metal-supported SOFC running on synthetic fuel. The University of California, San Diego project will develop a 4 kW SOFC stack in the laboratory running on bio-LNG. A project in Louisiana uses an SOFC with synthetic fuel.

2.8 Research gaps and objectives

In this chapter, the state-of-the-art for the simulation of HGV propulsion with SOFC systems has been reviewed. The literature review identified several research gaps, which in this section will be discussed and highlighted to set the objectives of this thesis. The research gaps are grouped into the following three categories:

- Dynamic modelling of SOFC systems in Section 2.8.1,
- Fulfilling the power requirements of HGV propulsion in Section 2.8.2, and
- SOFC operation when the vehicle is stationary in Section 2.8.3.

In light of the identified research gaps, the objectives of this thesis will be identified in Section 2.8.4.

2.8.1 Dynamic modelling of SOFC systems

Like other road vehicles, HGVs are subject to frequent accelerations and braking, and therefore, their power requirements for propulsion are highly dynamic. If SOFC systems are to meet those requirements, it is important to investigate their performance under

such operating conditions. For this purpose, dynamic modelling is a powerful tool to analyse the system response not only to dynamic changes in load, but also to fuel flow and air flow rates.

Important to dynamic performance of SOFC systems are both the chemical reaction transients captured through the species balances, and the thermal transients captured through the energy balances within each component. Furthermore, control strategies are required to maintain the SOFC system parameters during the changes in load associated with dynamic operation. Therefore, there is a research gap identified in simulations studying the dynamic performance of SOFC systems, and control strategies to maintain those variables. These aspects should be addressed within this thesis.

2.8.2 Fulfilling the power requirements of HGV propulsion

Of the papers which have studied the use of SOFC systems for road transport applications, the majority have focused on range extenders for passenger cars. In contrast, the propulsion of HGVs for long-haul road freight with SOFC systems has not been investigated in the prior literature. For the intense operation of HGVs, fuel efficiency is of greater importance, and their greater mass means their power requirements can be significantly higher than for passenger cars. Therefore, there exists a research gap for studies that model the performance of SOFC systems for HGV vehicles. The existing studies for HGVs modelled only APUs, which have a smaller and less dynamic power requirements of around 5 kW.

Additionally, the studies which investigated the use of SOFC systems as range extenders mostly modelled the SOFC system at constant power, with a battery or ICE meeting the transient requirements [98, 97, 102, 19, 103]. However, this may not be an optimum solution. Vehicle drive cycles are highly dynamic, and an energy management strategy which varies the SOFC power as a function of the state of charge of the battery is required. This can allow downsizing of the battery, and a reduced footprint and weight of the overall propulsion system. Bessekon et al. did include a reduced power mode for

an SOFC system as a range extender on a BEV [20]. However, their model did not include a dynamic process model, so they were not able to study thermal and chemical reaction transients during SOFC system operation. There exists a research gap for the development of energy management strategies for SOFC-battery systems which factor in the chemical reaction and thermal transients of the SOFC system.

An additional research gap in the simulation of SOFC systems for vehicle applications is the consideration of SOFC stack ageing over its operating lifetime. The literature review has shown that the degradation plays an important role in SOFC system performance but has not been simulated in any of the SOFC system modelling studies which focused on vehicle applications. This should be addressed in this thesis.

2.8.3 SOFC operation when the vehicle is stationary

Of the studies which investigated SOFC systems for vehicles, the majority made no consideration of SOFC operation when the vehicle is stationary for longer periods, for example, when parked overnight. Brandon et al. and Elakya et al. both used always-on strategies in which the SOFC systems continued to run even whilst the vehicle was not in use, either recharging the battery or delivering the power to the mains grid [19, 102]. These options are inefficient, and impractical for real vehicle applications, especially if several days of idling are possible. There exists a need for studying the performance of the SOFC system over a weekly period, where the system is left to cool and restart before further usage.

To evaluate how an SOFC system cools down when out of operation, a model of the heat losses from the hotbox components is required. However, very few of the papers reviewed considered heat losses in the model satisfactorily, and especially not in simulations for transport applications. Therefore, the development of a heat network for modelling the cool-down of the SOFC system is required. The performance of hotbox insulation has been reported in the literature, and can be embedded into such a model.

The cool-down of SOFC systems also plays an important role in their long start-up times, which has been highlighted by Qin et al. as a challenge for the application of SOFC

systems in transport [142]. However, there is a lack of modelling work or experimental studies investigating this further. Bessekon et al. allowed extra time for start-up of the SOFC system before vehicle operation [20], but did not model the start-up process or investigate ways to optimise it for transport applications. A research gap exists in the investigation of the thermal and chemical reaction transients during start-up, and should be investigated further in this thesis.

2.8.4 Research objectives

In light of the research gaps identified in this section, the following objectives are set for this thesis:

- To construct a transient model of an SOFC system including dynamic mass and energy balances of the SOFC stack and BoP components. This enables investigation of both the chemical reaction and thermal transients of the SOFC system during dynamic operation, which has often been inadequately performed in the existing literature. The model should be validated against existing experimental and modelling studies in the literature.

- To develop a control strategy to maintain the important SOFC parameters within their operating constraints, necessary for the dynamic operation of an SOFC system. A particular focus should be made on stack temperature transients, U_f and S/C ratio. Other constraints such as λ, stack temperature difference and burner temperature can be maintained with suitable sizing of the BoP components.

- To simulate the dynamic performance of an SOFC system when subjected to drive cycles for HGV propulsion. To the authors knowledge, a similar study has not been conducted previously in the literature. By studying the transient response of the SOFC system, its performance for HGV propulsion can be assessed.

- To develop a SOFC-battery hybrid system to meet the dynamic power requirements of an HGV, and investigate the system's performance with various drive cycles for

HGV propulsion. Most previous studies for similar systems on passenger vehicles kept the SOFC power constant. Power modulation of the SOFC system to reduce the powertrain footprint will be implemented, and addresses a research gap identified in the literature review.

- The literature review showed that the impact of SOFC stack degradation on SOFC system performance on a vehicle has not yet been studied. This thesis will investigate its impact on performance and operation throughout the lifetime of the SOFC system.

- The SOFC system model should include a heat network for calculation of the heat losses of the hotbox components, in particular to simulate how the SOFC system cools down when the vehicle is out of operation for example overnight or during weekend. This is an aspect which has been neglected in existing papers on SOFC systems for vehicle propulsion, even though vehicles may spend significant periods stationary.

- To investigate start-up of the SOFC system, including the thermal and chemical reaction transients. Particular attention will be paid to the duration of start-up, and its impact on the operational requirements of HGVs as commercial vehicles.

Chapter 3

Methodology

This chapter presents the methodology of the solid oxide fuel cell (SOFC) system model used to obtain the results that will be presented in Chapters 4 to 7.

This chapter is divided into the following sections:

- Firstly, the modelling approach and the main assumptions are introduced in Section 3.1,
- The system layout used within this thesis is presented in Section 3.2,
- Next, the assumptions and equations used to construct the SOFC system model are presented. The building blocks for modelling each of SOFC system components are presented:
  - The gas compartments in Section 3.3,
  - The reaction sites in Section 3.4, and
  - The component-level energy balances in Section 3.5.
- The approach used to model specific components of the SOFC system is then presented:
  - Modelling the SOFC stack in Section 3.6,
  - Modelling the heat exchangers in Section 3.7,

  - Modelling the burner in Section 3.8,
  - Modelling the blowers in Section 3.9, and
  - Modelling the pre-reformer in Section 3.10.

- The approach used to assess the system performance is presented in Section 3.11,
- The operating constraints of the SOFC system are presented in Section 3.12,
- The parameters of the SOFC system are presented in Section 3.13,
- The control strategy used during dynamic simulations is presented in Section 3.14,
- The software used to conduct the simulations is presented in Section 3.15, and
- The simulation workflow is presented in Section 3.16.

3.1 Modelling approach and main assumptions

The model includes dynamic mass and energy balances so that the transient response of the SOFC system can be investigated, for example, when subject to various drive cycles in Chapter 6, and when starting up after cool-down in Chapter 7. In the dynamic analysis, each of the material and energy balance equations are formulated with an accumulation term to capture their transients.

Momentum balances are neglected as part of this modelling approach, since their inclusion would increase the complexity of the model, and the accurate estimation of pressure losses is not required to achieve the objectives of this laid out in Chapter 2. Instead, pressure losses are estimated based on the experimental values reported in the literature, and reviewed in Section 2.1.8. This aligns with the SOFC system models reviewed in Section 2.1.3. Pressure drop calculations would be required for detailed component sizing and design but that is beyond the scope of this generalised model.

The electrical transients are assumed to be instantaneous, and modelled in quasi-steady-state, since they were shown in the literature review in Chapter 2 to proceed faster

than the chemical reaction and thermal transients, from which the dynamic performance of the SOFC system is limited. For example, the response times of power electronics for fuel cell systems have been shown to be in the range of 10 ms to 100 ms [169], and therefore can be neglected in these process simulations.

It is assumed that there are no chemical kinetics or mass transport limitations and the reactions in each of the components proceed instantaneously. Like the electrical transients, this is a reasonable assumption provided these processes are much faster than the chemical volume transients, which are shown to last around 20 seconds [47]. This assumption will also be validated by the experimental current density-voltage (iV) characteristics in Chapter 4 which will show that mass transport limitations and concentration polarisation are not prevalent in SOFC stacks provided the current density is not increased too much. This can be achieved by avoiding operating the SOFC stack at high current densities where the voltage losses becomes significant.

Each component in the SOFC system is modelled in 0D to ensure the simulations remain computationally efficient throughout the transient analyses, in a similar approach to Gallo et al. [39]. The variations investigated in the following chapters are computationally intensive, and a 0D approach allows an insight into the SOFC system to be gained more readily; whether in the design of controllers for dynamic SOFC operation in Chapter 5, responding to the transient requirements of heavy goods vehicle (HGV) propulsion in Chapter 6, or when the SOFC system starts up following cool-down in Chapter 7. The SOFC system model from Sorrentino et al. showed that the SOFC stack could be reduced to 0D without a sacrifice in accuracy of the electrical model [38].

The main limitation of the 0D modelling approach is for the SOFC stack, since spatial distribution, composition and current density are not resolved. The literature review in Chapter 2 showed that in particular, thermal gradients within the SOFC stack are an important parameter since they relate to thermal stresses within the stack materials. How thermal gradients are assessed in the model will be described in Section 3.11.

The 0D, dynamic SOFC system model was implemented in Matlab Simscape, and is

generalised in order to investigate the feasibility of SOFC technology for HGV propulsion, without needing to conduct detailed design work.

Further discussion of these assumptions and this modelling approach will be made in this chapter.

3.2 System layout

An SOFC system consists of an SOFC stack and a number of balance of plant (BoP) components. These components were introduced in Section 1.3.4. The approach in the literature to model those components was reviewed in Section 2.1. Based upon the findings of the literature review, a fixed system layout of the SOFC components has been chosen for this thesis. This layout is depicted in Figure 3.1. Methane fuel is supplied from the tank to the fuel pre-heater which heats the fuel. The fuel then enters the anode inlet of the SOFC stack. Air is supplied from the ambient environment through an air blower and pre-heated before being fed to the cathode inlet of the SOFC stack. The stack reforms the methane internally and produces electrical power through the electrochemical oxidation of hydrogen (H2X) reaction. A proportion of the anode off-gas is recycled with a recirculation blower to the anode inlet, and the rest is combusted in the burner with the oxygen in the cathode off-gas. The heat from the burner off-gas is used to pre-heat the cathode and anode inlet streams.

3.3 Modelling the gas compartments

In the 0D approach chosen for modelling the SOFC system, each component consists of one or more gas compartments. In this section the methodology used to model the gas compartments will be introduced. The specific details of each component model will be discussed later in this chapter but a short overview of the function of each gas compartment of the components shown in Figure 3.1 is a follows:

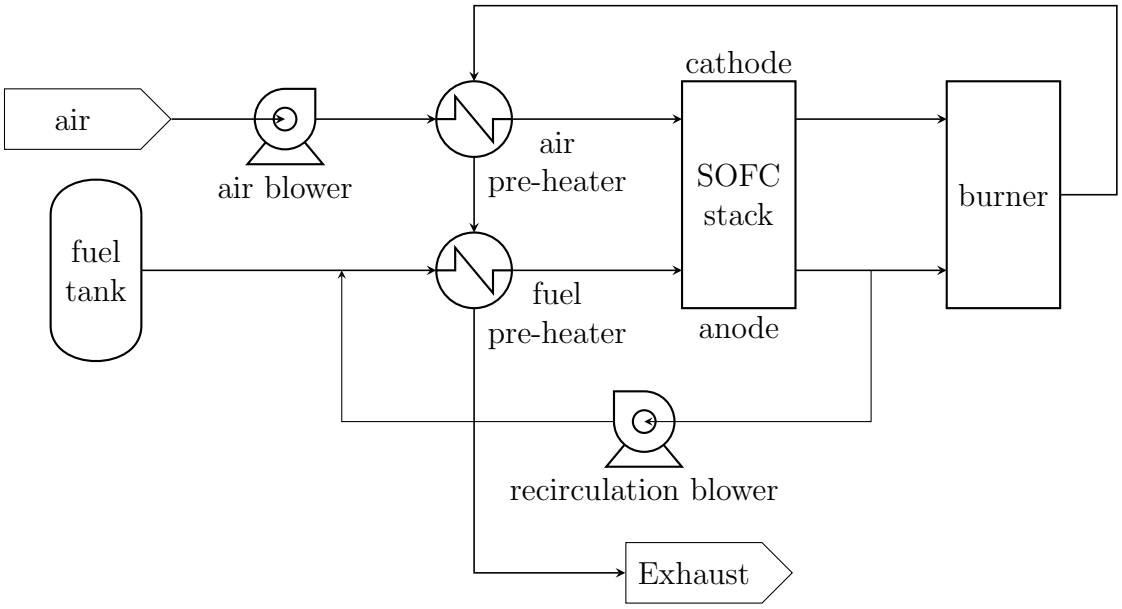

Figure 3.1: The SOFC system layout used within this thesis.

- The reformer consists of one gas compartment in which the reforming reactions take place,
- The burner consists of one gas compartment in which the stack off-gases are mixed, and the combustion reactions take place,
- The blowers consist of one gas compartment each, in which the gases are compressed,
- The heat exchangers (HEXs) consist of two gas compartments each, one for the hot side and one for the cold side, with heat transferred from the hot side to the cold side of each HEX, and
- The SOFC stack consists of two gas compartments, one for the anode side and one for the cathode side.

3.3.1 Modelling principles

Each gas compartment contains a fixed volume of gas. A number of assumptions about the thermodynamic properties of the gases are made.

3.3.1.1 Ideal gases

The ideal gas equation of state is assumed to be a good approximation for the behaviour of the gases within the SOFC system. Ideal gases differ from real gases in that the gases have negligible molecular size relative to the volume of the container, and the molecules are far enough apart that there are no intermolecular interactions. Whilst this is strictly only true for gases in the limit of infinite volume and zero pressure, ideal gas properties are reported to be accurate for gases at pressures under 2 atmospheres [170]. SOFC operating pressures close to 1 atmosphere, and the relatively high temperature within the SOFC system components modelled in this thesis, mean that the ideal gas law is an appropriate assumption for their process simulation. The ideal gas law assumption would not be appropriate for simulating pressurised SOFC operation, for example at 10 bar, or for modelling a steam generator for SOFC start-up, however, neither of those aspects are considered within this thesis.

3.3.1.2 Atmospheric pressure

All gases in the SOFC system are assumed to be at atmospheric pressure. In reality, SOFC systems are typically operated slightly above atmospheric pressure to overcome the pressure losses of the system and thereby ensure sufficient overpressure at the exhaust to vent the carbon dioxide, water and depleted air. The 20 kW system demonstrated at Forschungzentrum Jülich (FZJ) had a pressure drop of 200 mbar on the air-side [14]. When comparing to an SOFC stack operating at 200 mbarg, the atmospheric pressure assumption leads to an approximately 1 % or 0.01 V reduction in the open circuit voltage (OCV). This difference in the OCV comes from a combination of the slightly less negative Gibbs free energy of the H2X reaction at atmospheric pressure, and the lower hydrogen and oxidation partial pressures on the anodes, as shown in the Nernst Equation (3.24). This difference is much smaller than the uncertainty in the 0D model, and therefore, the differences in SOFC system performance over the range of operating pressures may be neglected.

3.3.1.3 Gas phase only

All steam-serviced components of the SOFC system model are maintained above 300°C during normal operation, and hence all water is in the vapour phase. During normal operation the steam is produced through the H2X reaction in the SOFC stack, and recirculated to the anode heat exchanger with the recirculation blower. During start-up of the SOFC system, steam can be generated by an evaporator or a catalytic partial oxidation reformer, but neither of which are modelled in this thesis.

3.3.1.4 Heat capacities

Due to the wide temperature range of SOFC system components, from the air blower at ambient temperature to the burner at up to around 1000°C, the variation in heat capacity with temperature is considered. For ideal gas mixtures, this is known as the semi-perfect gas model [170]. The variation in gas heat capacity over this temperature range is about 25 % [171], and thus has a significant impact on the energy balances conducted for each of the SOFC system components.

3.3.2 Thermodynamic properties

Thermodynamic properties of these gases describe their behaviour as a function of temperature. The thermodynamic properties of each gas species are taken from the NIST-JANAF Thermochemical Tables [171] which are built into the Engineering Equation Solver software, and are implemented in the Simscape environment in Matlab/Simulink using a look-up table.

The NIST-JANAF thermodynamic tables [171] list the specific heat capacity $c_{\mathrm{p},i}$ of each species i as a function of temperature T, in the form of a polynomial equation:

$$c_{\mathrm{p},i} = A_i + B_i T + C_i T^2 + D_i T^3 + E_i T^{-}2 \tag{3.1}$$

where A_i, B_i, C_i, D_i, and E_i are the the polynomial coefficients for species i listed in the

tables.

From heat capacity, the enthalpy and entropy of each species are found, followed by the enthalpy, entropy and Gibbs free energy, and equilibrium constant of each chemical reaction. Due to the ideal gas law assumption, the thermodynamic properties of the gas mixtures are the average of the thermodynamic properties of each species, weighted by their mole fraction [170].

The specific molar enthalpy h_i° of a species i at temperature T_V relative to 298 K and standard pressure is calculated from:

$$h_i^\circ(T_\mathrm{V}) = \int_{298\,\mathrm{K}}^{T_\mathrm{V}} c_{\mathrm{p},i}(T)\mathrm{d}T \tag{3.2}$$

where T is the temperature variable. The specific molar entropy s_i° of a species i at temperature T_V and standard pressure is calculated from:

$$s_i^\circ(T_\mathrm{V}) = \int_{298\,\mathrm{K}}^{T_\mathrm{V}} \frac{c_{\mathrm{p},i}(T)}{T}\mathrm{d}T \tag{3.3}$$

The specific molar enthalpy change Δh_k° of reaction k at temperature T_V and standard pressure is calculated from:

$$\Delta h_k^\circ(T_\mathrm{V}) = \sum_i \nu_{i,k}\left(h_{\mathrm{f},i} + h_i^\circ\right) \tag{3.4}$$

where $h_{\mathrm{f},i}$ is the specific molar enthalpy of formation of each species, and $\nu_{i,k}$ are the stoichiometric coefficients of reaction k. Similarly, the specific molar entropy change Δs_k° of reaction k at temperature T_V and standard pressure is calculated from:

$$\Delta s_k^\circ(T_\mathrm{V}) = \sum_i \nu_{i,k} s_i^\circ \tag{3.5}$$

The specific molar Gibbs free energy Δg_k° of reaction k at temperature T_V and standard

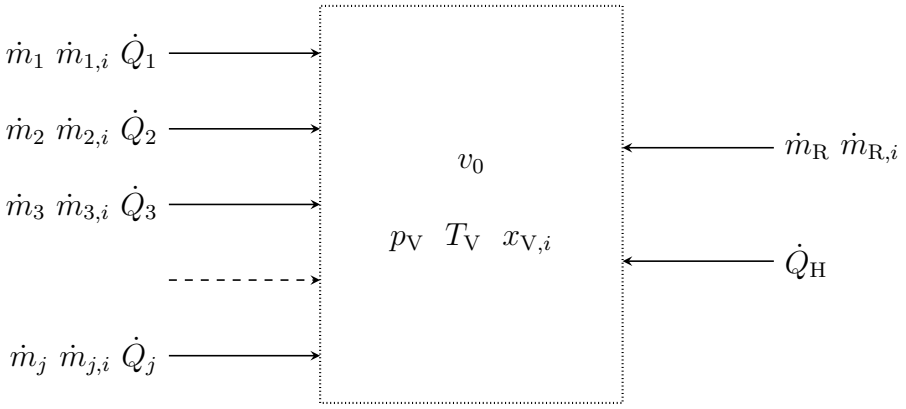

Figure 3.2: Gas compartment control volume definition.

pressure is calculated from:

$$\Delta g_k^\circ(T_\mathrm{V}) = \Delta h_k^\circ - T_\mathrm{V} \Delta s_k^\circ \tag{3.6}$$

The equilibrium constant K_k of reaction k at temperature T_V and standard pressure is calculated from:

$$K_k = \exp\left(-\frac{\Delta g_k^\circ}{R T_\mathrm{V}}\right) \tag{3.7}$$

3.3.3 Defining the control volume

Following on from the thermodynamic properties of the gases, the gas compartment as a control volume is defined. To reduce the computational burden, all compartments are all modelled in 0D, meaning that any spatial variation in pressure, temperature and composition is neglected. This is likely to be a reasonable assumption for the BoP components, but 1D models reviewed in Section 2.1.4 showed that temperature, composition, and current density varied significantly in an SOFC stack with internal reforming of methane, and therefore is a limitation of 0D modelling. Whilst a simplifying assumption, the literature review in Chapter 2 showed that this could be done with sufficient accuracy for control-orientated system modelling.

A generalised gas compartment control volume is shown in Figure 3.2. The compart-

ment has a fixed volume v_0 and the gases within the compartment have a pressure p_{V}, temperature T_{V}, composition $x_{\mathrm{V},i}$, mass m_{V} and specific enthalpy h_{V}. Each arrow on the left-hand side of Figure 3.2 represents a physical connection—or port—that brings material and heat into or out of the compartment, such as the inlet and outlet of the anode compartment in the SOFC stack. In general, the j^{th} port has a total mass flow rate $\dot{m}_j$, species mass flow rate $\dot{m}_{i,j}$ and heat flow rate $\dot{Q}_j$ in to the gas compartment. $\dot{m}_{\mathrm{R}}$ and $\dot{m}_{\mathrm{R},i}$ are the rate of production of material and species in the chemical reactions of the component. These are defined in the reaction site material balance in Section 3.4, and include, for example, the reactions on the electrodes of the SOFC stack. $\dot{Q}_{\mathrm{H}}$ is the heat flow rate to the gas compartment, as defined in the component-level energy balance in Section 3.5.

The gas thermodynamic properties outlined in Section 3.3.2 are assumed to apply within each gas compartment, with each gas volume at constant and atmospheric pressure. All SOFC system components were found to operate close to atmospheric pressure [14]. Therefore, as discussed in the assumptions above, the ideal gas equation of state (3.8) applies,

$$p_{\mathrm{V}} V_0 = m_{\mathrm{V}} R_{\mathrm{V}} T_{\mathrm{V}} \tag{3.8}$$

where $R_{\mathrm{V}} = \sum_i x_{\mathrm{V},i} R_i$.

For the purposes of the gas compartment modelling, the pressure drop across each gas compartment is neglected[1], because their operating pressures are all close to atmospheric. The modelling approach conducts mass and energy balances, but not momentum balances so no consideration of pressure drop is necessary. Detailed sizing of component and piping geometries would require momentum balances to be conducted, but that is considered beyond the scope of this generalised system model.

The activity of each species in each gas compartment $a_{\mathrm{V},i}$ is related directly to its

[1]Pressure drop is not neglected when calculating the required electrical power of the air and recirculation blowers, see Section 3.9.

partial pressure $p_{\mathrm{V},i}$ or mole fraction $y_{\mathrm{V},i}$, since the fugacity coefficient is equal to one for an ideal gas, and is calculated from:

$$a_{\mathrm{V},i} = \frac{p_{\mathrm{V},i}}{p_{\mathrm{V}}} = y_{\mathrm{V},i} \tag{3.9}$$

3.3.4 Conservation equations

The conservation of mass (3.10), energy (3.11) and species (3.13) equations are established for a gas compartment, based on its definition in Section 3.3.3. The equations are based on those published by Mathworks [172] for a constant volume chamber, but with the addition of the conservation of species for gas mixtures (3.13).

The conservation of mass equation is calculated from:

$$V_0 \left(\frac{\partial \rho}{\partial p} \frac{dp_{\mathrm{V}}}{dt} + \frac{\partial \rho}{\partial T} \frac{dT_{\mathrm{V}}}{dt} + \sum_i \frac{\partial \rho}{\partial x_i} \frac{dx_{\mathrm{V},i}}{dt} \right) = \sum_j \dot{m}_j + \dot{m}_{\mathrm{R}} \tag{3.10}$$

The conservation of energy equation is calculated from:

$$\begin{aligned} &V_0 h_{\mathrm{V}} \left(\frac{\partial \rho}{\partial p} \frac{dp_{\mathrm{V}}}{dt} + \frac{\partial \rho}{\partial T} \frac{dT_{\mathrm{V}}}{dt} + \sum_i \frac{\partial \rho}{\partial x_i} \frac{dx_{\mathrm{V},i}}{dt} \right) + \rho_{\mathrm{V}} V_0 \left(\frac{\partial h}{\partial T} \frac{dT_{\mathrm{V}}}{dt} + \sum_i \frac{\partial h}{\partial x_i} \frac{dx_{\mathrm{V},i}}{dt} \right) \\ &- V_0 \frac{dp_{\mathrm{V}}}{dt} = \sum_j \dot{Q}_j + \dot{Q}_H \end{aligned} \tag{3.11}$$

where:

$$\begin{aligned} \frac{\partial \rho}{\partial p} &= \frac{1}{R_{\mathrm{V}} T_{\mathrm{V}}} \\ \frac{\partial \rho}{\partial T} &= -\frac{p_{\mathrm{V}}}{R_{\mathrm{V}} {T_{\mathrm{V}}}^2} \\ \frac{\partial \rho}{\partial x_i} &= -\frac{p_{\mathrm{V}}}{{R_{\mathrm{V}}}^2 T_{\mathrm{V}}} (R_i - R_{\mathrm{O}_2}) \\ \frac{\partial h}{\partial T} &= c_{\mathrm{p}} \\ \frac{\partial h}{\partial x_i} &= h_{I,i} - h_{I,\mathrm{O}_2} \end{aligned} \tag{3.12}$$

The conservation of species equation is calculated from:

$$\frac{dx_{\mathrm{V},i}}{dt} m_{\mathrm{V}} + x_{\mathrm{V},i} \left(\sum_j \dot{m}_j + \sum_i r_i \right) = \sum_j \dot{m}_{j,i} + \dot{m}_{\mathrm{R},i} \tag{3.13}$$

where r_i is the rate of material production of each species in the chemical reactions in the conservation equations in $\mathrm{kg\,s^{-1}}$. All other parameters were defined in Section 3.3.3.

The volume and thermal inertia of the interconnecting pipes between fuel cell system components are neglected. This is a reasonable assumption for the thermal inertia, since the mass of the piping will be significantly lower than the mass of the components such as the stack and HEXs [55]. For HGV applications, the SOFC system should be tightly packaged to fit within the volumetric constraints of a vehicle, and aligns with the approach taken by Whyatt et al. for an SOFC system on an aircraft [55]. As a result, the process simulation of the SOFC system is considered to consist of a network of gas compartments or continuous stirred-tank reactors. Such an assumption could be limiting for simulating large-scale stationary power generation applications with multiple SOFC stacks and more complicated pipe networks. In such cases, the pipe network would have a greater impact on volume and thermal inertia, as well as the pressure losses and momentum balances of the SOFC system, but that is not the focus of this thesis. Moreover, the overall system transient response times to be presented in Chapter 5 will be aligned with those reported in the literature [47].

3.4 Modelling the reaction sites

The SOFC stack, burner and reformer components are all sites of chemical reactions, and the SOFC stack is also the site of electrical power production in the SOFC system. To model the reaction sites, a number of assumptions are made:

- Since the gas compartments are modelled in 0D, the sites of the chemical reactions and electrical power production are included in 0D, too. This means the rate of reac-

tion is assumed constant throughout the component. This assumption is necessary to remain consistent with the definition of the gas compartments in Section 3.3.

- All reforming and combustion reactions are at thermodynamic equilibrium; an assumption is consistent with many of the SOFC system models reviewed in Chapter 2 [16]. This assumption may somewhat overestimate their reaction rates, estimated to be by approximately 10 % [61]. In terms of the energy balance, this would lead to an overestimation of the methane steam reforming (MSR) cooling, and an overestimation of the combustion heating, which may somewhat balance each other out. The approach also has the advantage that that it can be universally applied without knowledge of the component geometries, or catalyst surface areas. This suits the simulation approach taken in this thesis which is focussed on simplifying the process simulation assumptions to model the SOFC system as part of a larger powertrain for an HGV.

- The material produced in the chemical reactions sites are delivered instantaneously to the gas compartments. There are no chemical kinetics or mass transport limitations and the reactions proceed instantaneously. The system models investigated in Chapter 2 showed that this was a reasonable assumption for the reforming reactions, since they proceeded faster than the H2X reaction. The iV characteristics which will be investigated in Chapter 4 will show that mass transport limitations and concentration polarisation are not prevalent in SOFC stacks provided the current density is not increased too much. This can be achieved with suitable selection of the nominal current density of the SOFC stack.

- Similarly, the production of electrical power in the SOFC stack is assumed to occur instantaneously, or at least much faster than the composition transients which were shown to last around 20 seconds [47]. The literature studied shows this to be a reasonable assumption with response times of power electronics for fuel cell systems to be of the order of 10 ms to 100 ms [169].

- The heat produced at the chemical reaction sites is delivered instantaneously to the solid mass of the fuel cell system component. There are no heat transport limitations between the site of the chemical reaction and the solid mass of the component. This is seen as a reasonable assumptions because of the large thermal mass of the SOFC system components, and hence their slow transient responses.

The 0D models reviewed in Section 2.1.3 made similar assumptions.

3.4.1 Conservation equations

Conservation of mass, energy and species are considered over the reaction site. The rate of production of mass $\dot{m}_{\mathrm{R}}$ in reaction site R in $\mathrm{kg\,s^{-1}}$ is calculated from:

$$\dot{m}_{\mathrm{R}} = 0 \tag{3.14}$$

The rate of heat production $\dot{Q}_{\mathrm{R}}$ in reaction site R in W is calculated from:

$$\dot{Q}_{\mathrm{R}} = -\sum_{k} r_k h_k \tag{3.15}$$

where r_k is the rate of reaction k in $\mathrm{mol\,s^{-1}}$ and h_k is the molar enthalpy of reaction k in $\mathrm{J\,mol^{-1}}$. This term is used in the component-level energy balances in Section 3.5. The rate of production $\dot{m}_{\mathrm{R},i}$ of species i at reaction site R in $\mathrm{kg\,s^{-1}}$ is calculated from:

$$\dot{m}_{\mathrm{R},i} = M_i \left(\nu_{i,k} r_k\right) \tag{3.16}$$

where M_i is the molar mass of species i in $\mathrm{kg\,mol^{-1}}$, $\nu_{i,k}$ are the stoichiometric coefficients of species i and reaction k.

The SOFC stack reaction site is also the site of electrical power production, and the electrical model will be discussed in Section 3.6.1.2.

3.5 Establishing the component-level energy balance

Each fuel cell system component consists not only of the gas compartments and reaction sites, but also the solid mass of the component itself. The solid mass is assumed to be 0D, i.e., a single point with no volume, with a mass m_{S} and specific heat capacity $c_{\mathrm{p},S}$ which is independent of temperature. This is a particular limitation of the 0D modelling approach, because it does not resolve the internal variation in temperature of the SOFC stacks, or thermal gradients. These are important parameters for the SOFC stack, because of their impact on thermal stresses in the stack, especially when operating with internal reforming [173]. Instead, in the 0D modelling approach, the temperature different between the cathode air and the stack temperature and the time derivative of the stack temperature ($\mathrm{d}T_S/\mathrm{d}t$) are used to estimate thermal gradients within the stack. The solid mass temperature T_{S} is assumed to be uniform, as the temperature distribution within the component can't be resolved in a 0D model. A more detailed model would be required to identify hot-spots.

The conservation of energy balance for the solid mass of the component is calculated from:

$$m_{\mathrm{S}} C_{\mathrm{P},S} \frac{dT_{\mathrm{S}}}{dt} = \dot{Q}_{\mathrm{R}} - \dot{Q}_{\mathrm{L}} - \sum \dot{Q}_{\mathrm{H}} \tag{3.17}$$

where $\dot{Q}_{\mathrm{R}}$ is the rate of heat production at the reaction site from Equation (3.15), and $\dot{Q}_{\mathrm{H}}$ is the rate of heat transfer from the solid mass to each gas compartment from Equation (3.11). It is assumed there is no heat transfer resistance between the gas compartments, the reaction site and the solid mass of the components, so they are all at identical temperature [39]. This assumption is applied to the burner, reformer, and blowers which each have a single gas compartment. The application of this assumption to the SOFC stack means that the anode and cathode channels are assumed to have the same temperature.

However, in the HEX model, heat is exchanged between the hot and cold gas compartments, which by definition different temperatures. As discussed in Section 2.1.5,

Sorrentino et al. and Gallo et al. both assumed the solid mass to be at the same temperature as the hot side gas compartment [38, 39]. Therefore, the same approach is used in Section 3.7. This is considered a reasonable assumption since Section 2.1.5 showed that a HEX effectiveness of close to 90 % can be achieved, meaning a small temperature approach of each HEX is attainable. Accurate calculation of the HEX temperature is not crucial for system design; instead the temperatures of the fuel and air fed to the SOFC stack from each HEX are far more important measure of their performance.

$\dot{Q}_L$ is the rate of heat loss from the component to the ambient surroundings, estimated using a conduction model through the hot box insulation, and is calculated from:

$$\dot{Q}_{\mathrm{L}} = \frac{k_{\mathrm{ins}} A_{\mathrm{ins}}}{D_{\mathrm{ins}}} (T_{\mathrm{S}} - T_{\mathrm{ambient}}) \tag{3.18}$$

where k_{ins}, A_{ins} and D_{ins} are the thermal conductivity, outside surface area and thickness of the hot box insulation, respectively.

Heat transfer between components within the hotbox is neglected; the components are assumed to be perfectly insulated from each other. This simplifies the heat network, and avoids definition of geometries of the individual components which Nousch et al. was able to do with an experimental test system for reference [45]. In an experimental SOFC system, the components are usually housed within a single hotbox insulation. Heat transfer between components means that during cool-down the temperature of the hotbox components equilibriate [125]. In the approach taken in this thesis, the larger components are instead assumed to have larger surface areas, and hence higher rates of heat losses.

Furthermore, radiation from the hot box components and convection from the exterior surface of the insulation to the ambient environment are neglected. Neglecting convection from the external surface is considered a reasonable assumption, provided that the performance of the insulation is such that the outer surface of the insulation is cool. This is a requirement of engineering norm ISO 15536-1:2006 which specifies 80°C maximum

[174]. Thus the insulation performance is sufficient, such that:

$$T_{\mathrm{S}} - T_{\mathrm{ambient}} \gg T_{\mathrm{exterior}} - T_{\mathrm{ambient}}. \tag{3.19}$$

where T_{exterior} is the temperature of the exterior surface of the hotbox insulation. This is consistent with the approach taken by Biert et al. [173].

3.6 Modelling the SOFC stack

From the building blocks presented in Section 3.3, Section 3.4 and Section 3.5, the models of each SOFC system component are constructed. Firstly, the SOFC stack model is introduced, a schematic of which is shown in Figure 3.3. This is a simplified version from Matlab Simscape, in which the dynamic SOFC system model was implemented.

The SOFC stack model consists of two gas compartments, one representing the anode chamber and the other the cathode chamber. Each compartment is modelled as per Section 3.3 and has a single inlet and outlet stream, denoted by nodes 1 to 4 in Figure 3.3.

Reactants and reaction products are transferred between the compartments and the reaction site through the physical signal 'mdot_R_i' in Figure 3.3, as described in Section 3.4. In the stack model, the reaction site is also the site of electrical power production. The nodes 5 and 6 represent the positive and negative electrical terminals of SOFC stack.

Heat is exchanged between the gas compartments, the reaction site, the solid mass, and the ambient environment via the hot box insulation, as per the component-level energy balance described in Section 3.5, and illustrated by the thermal connections in orange.

3.6.1 The reaction site

The reaction site block in Figure 3.3 is specific to the SOFC stack. It describes the rate of the chemical reactions, rate of electrical power production, and the rate of heat production in the SOFC stack.

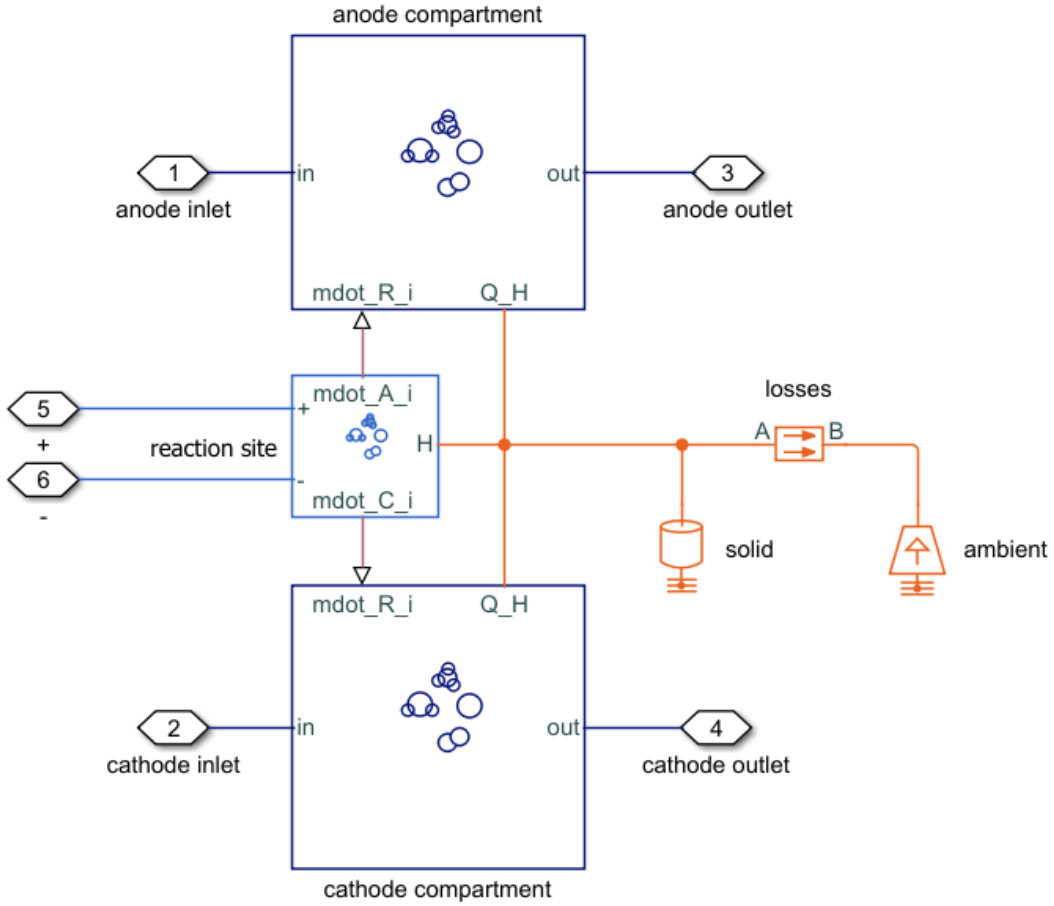

Figure 3.3: Fuel cell stack modelling schematic from Matlab Simscape.

3.6.1.1 Stack reactions

The SOFC stack model considers three reactions. Methane is reformed in the presence of water in the MSR reaction (1.4). Since one mole of methane produces three moles of hydrogen, this is the primary driver of the production of hydrogen within the stack. The water gas shift (WGS) reaction (1.5) converts the carbon monoxide from the MSR reaction to carbon dioxide and produces more hydrogen in the presence of steam. Lastly, the H2X reaction (1.3) produces the electrical power. All reaction products are produced and all reactants are consumed at the anode, except the consumption of oxygen in the H2X reaction stems from the cathode. The oxygen ions produced at the cathode are assumed to pass through the electrolyte to the anode instantaneously.

As discussed in the literature review in Section 2.1.4.1, the electrochemical oxidation

of carbon monoxide is neglected, and carbon deposition is avoided by keeping the steam-to-carbon ratio (S/C ratio) sufficiently high [91]. Whilst in reality carbon monoxide oxidation does contribute to electrical power production, this assumption has minimal impact on the overall electrical performance of the SOFC stack since the consumption of carbon monoxide through the WGS reaction produces hydrogen which can then be consumed in the H2X reaction.

The reaction rates are calculated through the same approach as Peters et al. [16]. The MSR reaction is assumed to be at thermodynamic equilibrium, which at temperatures above 600°C means that the reaction will proceed to completion, as shown in Equation (3.20). The WGS reaction is also assumed at thermodynamic equilibrium, and hence its conversion is determined by its equilibrium constant K_{WGS} in (3.21).The rate of the H2X reaction is determined by the electrical load through Faraday's Law in (3.22).

$$r_{\mathrm{MSR}} = \dot{n}_{\mathrm{CH_4,in}} \tag{3.20}$$

$$K_{\mathrm{WGS}} = \prod_i {a_{\mathrm{o},i}}^{\nu_{i,\mathrm{WGS}}} \tag{3.21}$$

$$r_{\mathrm{H2X}} = \frac{N_{\mathrm{cell}} I}{nF} \tag{3.22}$$

With the ideal gas mixture and equilibrium assumptions, the rate constant of the WGS reaction has no dependency on pressure, because the number of gaseous moles are conserved in the WGS reaction.

3.6.1.2 Electrical model

The electrical model within the reaction site block of the SOFC stack describes the relationship between the current, voltage and electrical power. The electrical performance of the fuel cell depends on the variation in voltage with current, which is represented by the iV characteristics. As described in Section 3.6.1.1, only the H2X reaction is considered to produce an electrical current. From thermodynamic theory, the reversible voltage of the H2X reaction E_0 is a function of the specific molar Gibbs free energy of reaction for the

oxidation of hydrogen, $\Delta g^{\circ}_{\mathrm{H2X}}$, at the respective stack temperature and standard pressure, and is calculated from:

$$E_0 = -\frac{\Delta g^{\circ}_{\mathrm{H2X}}(T_S)}{nF} \tag{3.23}$$

The voltage measured across a single cell when no current is drawn is the OCV (V_0) and is calculated using the Nernst Equation (3.24). It takes into account the impact of a deviation in partial pressure of reactants and reaction products on the reversible voltage (E_0) at the stack temperature based on the mole fraction of each species in the anode and cathode gas compartments, and is calculated from:

$$V_0 = E_0 - \frac{RT_S}{nF} \ln\left(\frac{y_{\mathrm{H_2O,A}}}{y_{\mathrm{H_2,A}} {y_{\mathrm{O_2,C}}}^{\frac{1}{2}}}\right) \tag{3.24}$$

In this electrical model, the SOFC stack is assumed to operate under atmospheric conditions, whilst 200 mbarg is a typical operating pressure of an SOFC stack [14]. Increasing the pressure from atmospheric to 200 mbarg results in a slight increase in the partial pressures of hydrogen, oxygen and water in the Nernst equation. Combined with a slight increase in reversible cell voltage, due to the variation in the Gibbs free energy of the H2X reaction with pressure, operating at 200 mbarg is expected to lead to a 1 % or 0.01 V increase in the OCV, when compared to atmospheric pressure. This variation is much smaller than other uncertainties in the model and may be neglected.

As shown in Section 2.1.4.4, the existing 0D SOFC stack models in the literature took different approaches for estimating the anode and cathode composition with internal reforming of methane. In this thesis, a weighting factor w_x is proposed. The mole fraction of species i is calculated from:

$$y_i = w_x y_{i,\mathrm{ar}} + (1 - w_x) y_{i,\mathrm{out}} \tag{3.25}$$

Where $y_{i,\mathrm{ar}}$ is the mole fraction of species i following reforming, and $y_{i,\mathrm{out}}$ is the mole

fraction of species i at the stack outlet. The internal reforming reactions take place on the anode, and therefore $y_{\mathrm{o_2,ar}}$ is equal to $y_{\mathrm{o_2,in}}$ at the cathode inlet. $y_{i,\mathrm{ar}}$ on the anode-side is the mole fraction of each species calculated by discounting the H2X reaction from the gas compartment material balance in (3.16). w_x has a value between 0 and 1 inclusive. Appropriate values of w_x are investigated in Chapter 4. In the extreme case that $w_x = 0$, the composition at the stack outlet is taken.

The voltage losses are approximated as an area specific resistance (ASR), an approach taken by a number of authors in the literature review in Section 2.1.4.5. The ASR is calculated as a function of temperature from an integrated form of the Arrhenius equation:

$$ASR = ASR_0 \cdot \exp\left[\frac{E_a}{R}\left(\frac{1}{T} - \frac{1}{T_0}\right)\right] \tag{3.26}$$

where ASR_0 is the area specific resistance of the cell at the reference temperature T_0. The activation energy E_a describes how quickly the ASR varies at temperatures above or below T_0.

The iV characteristics describe the variation in cell voltage V with current density i. The cell voltage is calculated from:

$$V = V_0 - ASR \cdot i \tag{3.27}$$

The advantage of calculating the voltage losses based on the ASR is that the parameters E_a, ASR_0 and T_0 of Equation (3.26) can be found by experimental iV characteristics in the literature, and therefore do not require a detailed electrochemical model of the SOFC stack itself.

One of the main limitations of the ASR approach is that all of the voltage losses can be lumped into a parameter with a linear dependency on current. This is a reasonable assumption at moderate current densities, where ohmic losses dominate, but is less accurate at low and high current densities. At low current densities, the relatively small activation

losses of SOFC stacks are still significant, and the ASR approach will overestimate the cell voltage. However, SOFC systems can't be operated at low current densities without becoming too cold [104]. Instead SOFC stacks are operated at moderate current densities, where sufficient heat is produced through the H2X reaction, and the ohmic voltage losses dominate.

At high current densities, concentration losses becomes significant, and the linear ASR approach once again overestimates the current. However, at high current densities and low cell voltages, the SOFC electrical efficiency drops significantly, and therefore these high current densities are avoided in operation of real SOFC systems. High fuel utilisation (U_f) above 0.85 can also lead to higher concentration losses, but in real SOFC systems, this is avoided because it leads to fuel starvation [74]. Therefore, within the operating window of an SOFC stack, the ohmic losses are expected to dominate. The ASR approach will be validated in Section 4.1.

The SOFC stack consists of N_{cell} cells, each with an active area A_{cell}. The stack voltage V_S is the product of the cell voltage and the number of cells.

$$V_S = V N_{\text{cell}} \tag{3.28}$$

The cell current I is calculated as the product of the current density and the cell area:

$$I = i A_{\text{cell}} \tag{3.29}$$

The stack power P_S is calculated as the product of the stack voltage and the cell current:

$$P_S = V_S I; \tag{3.30}$$

3.6.1.3 Heat production

The SOFC stack converts the chemical energy of the hydrogen into electrical energy. The heat produced by the H2X reaction is the difference between the enthalpy of the H2X reaction and the stack power. Heat is consumed through the endothermic MSR reaction; the WGS reaction is mildly exothermic. The rate of heat production at the reaction site of the SOFC stack is calculated as the sum of the heat production of those three reactions:

$$\dot{Q}_{\mathrm{R,stack}} = -\sum_{k} r_k h_k - P_{\mathrm{S}} \tag{3.31}$$

3.6.2 Degradation

The experimental studies reviewed in Section 2.5 show that commercial stack manufacturers have achieved long term degradation rates approaching $0.3\,\%\,\mathrm{kh}^{-1}$ or $10\,\mathrm{m\Omega\,cm^2\,kh^{-1}}$.

Equation (3.26) can be modified to include the impact of ageing. Rearranging Equation (2.7), the reference ASR_0 in $\Omega\,\mathrm{cm}^2$ after t_1 hours of operation is calculated from:

$$ASR_0(t = t_1) = ASR_0(t = 0) + DGR\frac{t_1}{1000} \tag{3.32}$$

where $ASR_0(t = 0)$ is the reference ASR_0 at the beginning of the SOFC stack's life and DGR is the degradation rate in $\Omega\,\mathrm{cm}^2\,\mathrm{kh}^{-1}$ of the SOFC stack.

3.7 Modelling the heat exchangers

The purpose of the HEXs is to transfer heat from the hot burner off-gas to the cold anode and cathode feed-gases. The HEX model is used to predict the outlet temperatures of the anode and cathode pre-heaters under dynamic conditions. The model is generalised as far as possible, and the specific geometries of the HEXs are not defined. Figure 3.4 shows

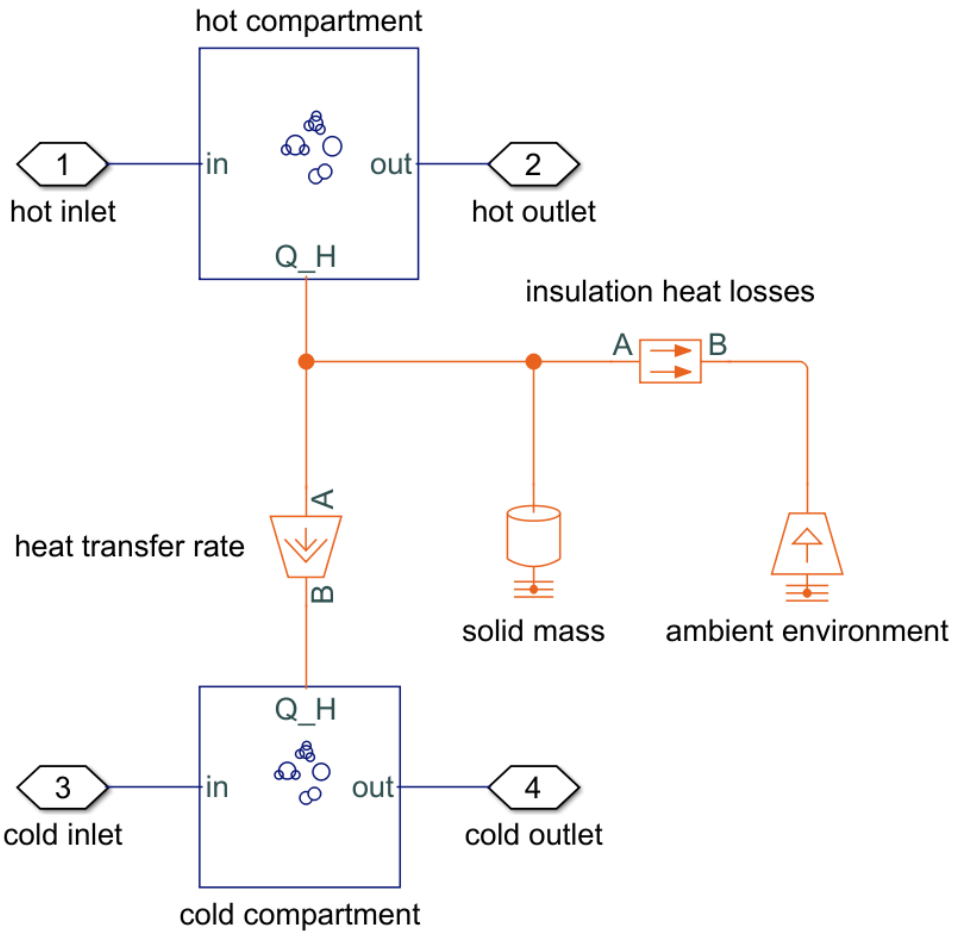

Figure 3.4: Heat exchanger modelling schematic from Matlab Simscape.

the schematic for modelling both HEXs. Heat from the hot compartment is transferred to the cold compartment. The solid mass is assumed to be at the same temperature as the hot side gas compartment [38, 39], as discussed in Section 2.1.5 of the literature review.

3.7.1 Sizing

The pre-heaters are required to increase the temperature of the stack inlet streams to reduce temperature gradients within the stack. For the 0D model of the SOFC stack in Section 3.6, the spatial temperature gradients are approximated based on the temperature difference between inlet streams and the stack itself.

$$\Delta T_{\text{stack}} = T_{\text{stack}} - T_{\text{stack,in}} \tag{3.33}$$

Section 3.7 showed that models in the literature commonly specified the stack temperature difference ΔT_{stack}, with a maximum value of 100°C. The temperature of the cathode air is more critical, since the air flow rate is much larger than the fuel flow rate. In this model, when the SOFC stack operates at its maximum current density, or peak load, the HEX is sized such that the stack temperature difference ΔT_{stack} is equal to maximum allowable temperature difference. This is achieved by increasing the stack inlet temperature $T_{\text{stack,in}}$ sufficiently.

From this the effectiveness ε of the HEX at peak load is found,

$$\varepsilon = \frac{\dot{Q}}{\dot{Q}_{\text{max}}} \tag{3.34}$$

where $\dot{Q}$ is the heat transfer rate and $\dot{Q}_{\text{max}}$ is the maximum possible heat transfer rate.

$$\dot{Q}_{\text{max}} = \min\left(\dot{m}_{\text{hot}} c_{\text{p,hot,in}}, \dot{m}_{\text{cold}} c_{\text{p,cold,in}}\right)\left(T_{\text{hot,in}} - T_{\text{cold,in}}\right) \tag{3.35}$$

3.7.2 Part load performance

At part load, the effectiveness of each heat exchanger is assumed constant [39, 75], an approach seen in Section 2.1.5 of the literature review. The heat exchanger calculation tool provided by Bosal ECI [83], shows that for the range of typical mass flow rates in the cathode heat exchanger, the effectiveness of a real heat exchanger varies by a maximum of 3 percentage points. This assumption therefore appears to give a relatively accurate estimate of the outlet temperatures of the HEXs.

3.8 Modelling the burner

The burner consists of a single gas compartment in which the anode off-gas and cathode off-gas are mixed, as the schematic in Figure 3.5 shows. As outlined earlier in this chapter, the combustion reactions are assumed to be at chemical equilibrium. Under this assumption, the combustion reactions go to completion, due to the highly negative Δg_k°

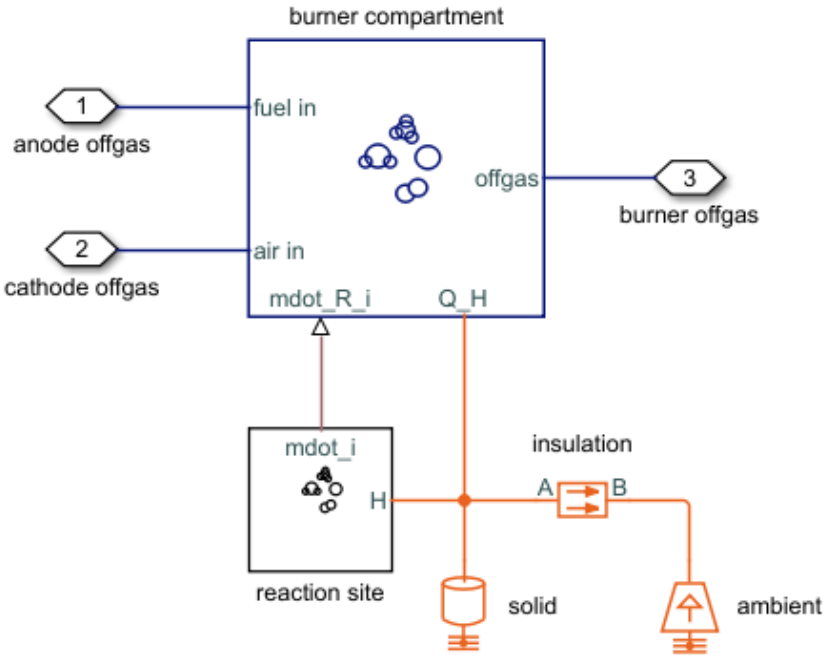

Figure 3.5: Burner modelling schematic from Matlab Simscape.

for each reaction and the air-rich environment. This is in agreement with the approach shown in Section 2.1.6 of the literature review. Conservation of energy for the burner is conducted between the gas compartment, the reaction site, the solid mass and the ambient environment via the hot box insulation.

3.9 Modelling the blowers

The air blower and the recirculation blower are the primary power drains of an SOFC system. Their power requirements can have a significant impact on overall system efficiency. The models of the blowers are simplified. Their pressure ratios are assumed constant, and their speed fixed, so the blowers operate under steady-state conditions. A throttling valve could be used to manipulate the flow rate at part load. The blowers are assumed to have constant isentropic and mechanical efficiency. These assumptions align with the blower models reviewed in Section 2.1.8. These simplifications in the blower models do reduce the accuracy of the net electrical efficiency calculations, since the air blower has been shown to have the largest parasitic power requirement of the SOFC system BoP

components. That said, this thesis focuses on the control and dynamic performance of the SOFC system when exposed drive cycles for HGV propulsion, where accurate estimate of the electrical efficiency is less critical.

In an isentropic process, entropy is conserved:

$$T_{\text{isentropic}} = T_{\text{in}} \left(\frac{p_{\text{out}}}{p_{\text{in}}} \right)^{\frac{\gamma-1}{\gamma}} \tag{3.36}$$

The specific gas ratio of air γ is 1.4. The outlet temperature of the gases T_{out} depends on the isentropic efficiency of the blower $\eta_{\text{isentropic}}$ [16], and is calculated from:

$$T_{\text{out}} = T_{\text{in}} + \frac{T_{\text{isentropic}} - T_{\text{in}}}{\eta_{\text{isentropic}}} \tag{3.37}$$

The electrical power requirement of each blower P_{blower} depends on its mechanical efficiency $\eta_{\text{mechanical}}$, and is calculated as:

$$P_{\text{blower}} = \frac{\dot{m} \left(h_{\text{out}} - h_{\text{in}} \right)}{\eta_{\text{mechanical}}} \tag{3.38}$$

It is assumed that the recirculation blower is capable of handling compressing the anode offgas directly without pre-cooling, which has been demonstrated by CAP Co.,Ltd [175]. This simplifies system design, since no cooling and re-heating of the anode off-gas is required to operate the recirculation blower.

3.10 Modelling the pre-reformer

A steam pre-reformer is optionally included in the SOFC system model. It is assumed to be integrated into the anode pre-heater, a common approach presented in Section 2.1.7 of the literature review. It is used for steady-state validation of the SOFC system model, but discarded in the dynamic simulation, where it is assumed that internal reforming only is adequate for safe operation of the stack without carbon deposition [61]. Internal

reforming only is achieved through anode off-gas recirculation (AOGR) which maintains the S/C ratio ratio at the anode inlet to avoid carbon deposition, and thereby reduces system complexity [33].

The pre-reformer is modelled following the generalised approach in Section 3.3. The reformer model is identical to the anode channel in the SOFC stack model without the hydrogen oxidation and corresponding electrical sub-model. Only the MSR (1.4) and WGS (1.5) reactions are considered. Refer to Section 3.6.1.1 for further details.

Due to the lower operating temperature of the reformer compared to the stack, the MSR reaction may not proceed to completion. In the reformer both the MSR and WGS reactions are assumed to be at chemical equilibrium; a similar approach is used by Peters et al. [16]. Their equilibrium constants are calculated in Equation (3.7) and then used to solve for the outlet composition in Equation 3.21. The mass and energy balances in Equations (3.10) and (3.11) are established to calculate the flow rate, composition and temperature of the reformer off-gas.

3.11 Assessing the steady-state system performance

Section 2.2 showed that most of the literature reviewed focused on the electrical efficiency of the SOFC system as the main parameter for assessing the steady-state performance. Operating the SOFC system with high electrical efficiency is desirable for transport applications because it reduces fuel consumption, which means lower operating costs and improved vehicle range. The electrical efficiency of an SOFC system, η_{system} is calculated by dividing the net electrical power of the system by the energy input of the fuel.

$$\eta_{\text{system}} = \frac{P_{\text{stack}} - P_{\text{parasitic}}}{\dot{m}_{\text{fuel,in}} LHV_{\text{fuel}}} \tag{3.39}$$

The energy input of the fuel is its flow rate multiplied by its lower heating value LHV_{fuel}. LHV_{fuel} is the specific enthalpy of reaction for the combustion of the fuel, with water produced in the vapour phase, due to the high temperature of SOFC operation.

As discussed, in Section 1.2, the footprint, in terms of weight and volume, of the propulsion system on a vehicle is important. Section 1.2 showed that the volumetric energy density of methane is greater than that of hydrogen or batteries. However, estimating the weight and volume of the whole powertrain depends on many factors and is considered beyond the scope of this thesis. Because SOFC technology is a less mature technology for transport applications, it is hard to make a direct comparison to other propulsion technologies. Therefore, in this thesis, the focus is on the power density of the SOFC stack p_{stack} which is the rated stack power divided by the total active area of the SOFC stack.

$$p_{\text{stack}} = \frac{P_{\text{stack}}}{N_{\text{cell}} A_{\text{cell}}} \tag{3.40}$$

The thermal efficiency of the SOFC stack is one minus the electrical efficiency of the stack. One of the advantages of the SOFC system is that the high temperature off-heat can be used for applications such as running a refrigeration cycle on a refrigerated HGV. Venkataraman et al. found that a cooling power of 10 kW was sufficient for a vapour absorption refrigeration system on an HGV [25]. Whether the SOFC system designed in this thesis for vehicle propulsion would also be appropriate for refrigeration will be briefly discussed in Chapter 6. Other steady-state performance parameters such as cost and environmental impact are not studied in this thesis, but the work could easily be extended to include them.

3.12 Defining the operating window

As well as achieving high efficiency and power density, it is important that an SOFC system has sufficient lifetime and reliability to meet the requirements of an HGV drivetrain. In this work, an ageing model is incorporated, and to maximise lifetime, an operating window is defined for safe operation of the system. The operating window parameters are summarised in Table 3.1, based upon the design conditions and constraints presented in

Table 3.1: Material and thermal system constraints, where U_f is the fuel utilisation, S/C ratio is the steam-to-carbon ratio, λ is the air stoichiometry, and $\mathrm{d}T_S/\mathrm{d}t$ is the time derivative of the stack temperature.

Parameter	Minimum	Design	Maximum	
U_f		0.7	0.8	[74]
S/C ratio	2	2.5		[54]
λ	2			[16]
Stack temperature	600°C	700°C	720°C	[21]
Burner temperature		Variable	1000°C	[16]
Stack temperature difference		Variable	100°C	[21]
$\mathrm{d}T_S/\mathrm{d}t$			$2\,^{\circ}\mathrm{C\,min^{-1}}$	

Section 2.2.3 of the literature review.

3.12.1 Fuel utilisation

The U_f is a measure of the proportion of the fuel that is used for electrical power production in the SOFC stack, i.e., through the H2X reaction. The U_f of the stack is calculated from:

$$U_f = \frac{r_{\mathrm{H2X}}}{4\dot{n}_{\mathrm{CH_4,anode,in}} + \dot{n}_{\mathrm{CO,anode,in}} + \dot{n}_{\mathrm{H_2,anode,in}}} \tag{3.41}$$

Each mole of CH_4 can produce up to four moles of H_2 through the MSR and WGS reactions, and each mole of CO can produce up to one mole of H_2 through the WGS reaction.

With AOGR, the system fuel utilisation $U_{f,\mathrm{system}}$ is larger than U_f, because unreacted fuel is recycled to the anode inlet. $U_{f,\mathrm{system}}$ is calculated from:

$$U_{f,\mathrm{system}} = \frac{r_{\mathrm{H2X}}}{4\dot{n}_{\mathrm{CH_4,in,system}}} \tag{3.42}$$

One mole of methane can produce up to four moles of hydrogen, if both the MSR reaction (1.4) and WGS reaction (1.5) were to go to completion.

Due to the risk of fuel starvation at high U_f demonstrated by Fang et al. [74] in the literature review, the SOFC system in this model is designed to operate at 70 % stack U_f with a maximum allowable stack U_f of 80 % during transients.

3.12.2 Steam-to-carbon ratio

Following the approach taken by other authors, as presented in Section 2.2.3 of the literature review, the carbon deposition reactions are neglected, and the SOFC system is designed to operate with a S/C ratio of 2.5 at the anode inlet. During transients, the S/C ratio should not drop below 2. The S/C ratio is calculated from the flow rates at the anode inlet:

$$S/C = \frac{\dot{n}_{\mathrm{H_2O,in}}}{\dot{n}_{\mathrm{CH_4,in}}} \tag{3.43}$$

3.12.3 Air stoichiometry

Sufficient oxygen must be supplied to the cathode to support the H2X reaction. As shown in Section 2.2.3 of the literature review, Peters et al. [16] reported that the air stoichiometry (λ) should be at least two to avoid oxygen depletion on the cathode. Operation of the SOFC stack at low current densities will not be possible without the stack temperature reducing. At higher current densities, the air flow rate is adjusted to maintain constant stack temperature. The λ is defined as the ratio between the flow rate of oxygen supplied to the SOFC stack and the rate of oxygen consumption through the H2X reaction in Equation (3.44).

$$\lambda = \frac{2\dot{n}_{\mathrm{O_2,in,stack}}}{r_{\mathrm{H2X}}} \tag{3.44}$$

In some cases, it is more convenient to present the oxygen utilisation instead, which is the reciprocal of λ.

3.12.4 Thermal constraints

In addition to the gas composition constraints, there are a number of thermal constraints to ensure long lifetime of the SOFC system. The thermal constraints depend on the materials and design of the SOFC stack and BoP components. The SOFC stack modelled in this thesis is designed to operate at 700°C, with a maximum temperature of 720°C during transients [21]. At part load, the SOFC stack temperature can be maintained by manipulating the air flow rate.

The minimum part load is defined by the current at which the SOFC system is unable to maintain the SOFC stack temperature at 700°C with an λ of 2 [16]. The one exception is during heat-up and cool-down, where thermal cycling occurs. As argued by Petruzzi et al., start-up of the SOFC stack can commence already from 600°C, using the heat produced by the H2X reaction to assist with heat-up [115]. However, such wide variation in temperature during steady load operation would be be problematic for stack health, after start-up the SOFC stack should be operated close to a constant temperature of 700°C.

A large stack temperature difference is likely to lead to large temperature gradients in the stack, which can lead to accelerated ageing of the stack [176]. A maximum temperature difference between the SOFC stack and the cathode and anode inlet of 100°C is allowed [16]. At part load, the cathode and anode inlet temperatures vary, and hence the SOFC stack temperature difference will vary too.

In addition, the temperature of the burner should remain below 1000°C due to material constraints of the HEXs [16]. The burner temperature is determined by the temperature and composition of the anode and cathode off-gas, and will vary at part load.

These thermal constraints can be satisfied with correct sizing and design of the BoP components. However, during load changes, the temperature of the SOFC stack and BoP will vary. The SOFC stack is most sensitive to those changes, and its rate of change of temperature is set as a design parameter during dynamic operation of the SOFC system. Initially, the rate of change of the SOFC stack temperature is assigned a maximum allow-

able value of $2\,^{\circ}\mathrm{C\,min^{-1}}$ during dynamic operation. No reference values have been found in the literature.

Many of the 1D models reviewed in Section 2.1.4 reported the calculated internal thermal gradients within the SOFC stack in $\mathrm{K\,cm^{-1}}$, with Aguiar et al. reporting a maximum allowable value of $10\,\mathrm{K\,cm^{-1}}$. The stack thermal gradients relate to their thermal stresses which are an important lifetime issue for SOFC stack operation [53]. One disadvantage of this constraint, however, is that measurement of internal temperature gradients is experimentally challenging. The variations can be non-linear, especially with the cold front reported for internal reforming SOFC stacks [173].

Whilst the lack of ability to calculate internal thermal gradients is a limitation of 0D modelling, this also speaks to the simplicity of the modelling approach. The stack temperature, stack temperature difference, and $\mathrm{d}T_S/\mathrm{d}t$ can all be measured experimentally with thermocouples, and therefore are more relevant practical constraints for experimental SOFC system operation.

3.13 Defining system parameters

In addition to the operating window presented in presented in Section 3.12, this section defines the system parameters. The model is generalised, and thus relatively few parameters need to be defined. Where possible, their values are defined based on experimental data in the literature. Some parameters are independent of the size of the SOFC system, while others will need to be scaled with system size. Some of the parameters are design parameters and can be varied to investigate how they affect performance.

3.13.1 Independent of system size

The values of the parameters which are assumed to be independent of the the system size are listed in Table 3.2. The ASR parameters describe the deviation of the ASR from a reference ASR at a known temperature. The reference ASR is taken from testing of

Table 3.2: SOFC system parameters independent of the system size.

Parameter	Value	
Area specific resistance at T_0, ASR_0	$0.60\,\Omega\,\mathrm{cm}^2$	[177]
ASR reference temperature, T_0	$930\,\mathrm{K}$	[177]
ASR activation energy, E_a	$0.65\,\mathrm{eV}$	[73]
Single cell active area, A_{cell}	$360\,\mathrm{cm}^2$	[16]
Air side pressure drop ΔP_{air}	$10\,\mathrm{kPa}$	[16]
Fuel side pressure drop ΔP_{fuel}	$2.5\,\mathrm{kPa}$	[16]
Blower isentropic efficiency $\eta_{\mathrm{isentropic}}$	0.6	[16]
Blower mechanical efficiency $\eta_{\mathrm{mechanical}}$	0.5	[16]
Component solid heat capacity, $c_{\mathrm{P,c}}$	$500\,\mathrm{J\,kg^{-1}}$	[173]
Insulation thickness, D_{ins}	$0.15\,\mathrm{m}$	[114]
Insulation thermal conductivity, k_{ins}	$0.035\,\mathrm{W\,m^{-1}\,K^{-1}}$	[178]

an SOFC system at VTT with two 3 kW SOFC stacks from Elcogen [177], because the results were extracted from an SOFC system, whereas many other experimental results report ASR results only for an SOFC cell or stack tested in a furnace. The validation in Section 4.1 will show that ASR values from other studies could also chosen; the most important aspect is that a reliable experimental study is used. The ASR activation energy describes the variation in ASR with temperature, by fitting a model to experimental data from anode-supported cell testing at FZJ [73].

Section 4.1 will seek to show that the activation energy of the Arrhenius expression is relatively good fit for the variation in ASR with temperature, regardless of the specific SOFC stack technology, by comparing the model to experimental iV characteristics reported in the literature. The single cell area A_{cell} is quoted from a 250 kW SOFC system [16]. Since the model is 0D, the SOFC stack performance does not depend on cell area, but is instead used to relate current density and current in the sizing of the SOFC stack.

The pressure drop and blower performance parameters are based on a steady-state SOFC system model published by FZJ [16]. For simplicity, the heat capacity of each system component is assumed to be independent of temperature, and equal to the heat capacity of steel. The insulation thickness is a design parameter, initially set to 15 cm based on the literature review, while the insulation thermal conductivity is taken from

Table 3.3: SOFC system parameters that scale with the system size.

Parameter	Value	Scaling
For a 6.29 kW Delphi Gen4 SOFC system [55]:		
Stack mass, m_{stack}	62 kg	$\sim N_{\text{cell}}$
Cathode pre-heater mass, m_{chex}	7.912 kg	$\sim \dot{m}_{\text{air}}$
Anode pre-heater mass, m_{ahex}	3.33 kg	$\sim \dot{m}_{\text{fuel}}$
Reformer mass, m_{reformer}	4.336 kg	$\sim \dot{m}_{\text{fuel}}$
For a 50 kW SOFC system from Holtappels et al. [114]:		
System outer surface area, A_{system}	1.1 m^2	$\sim \frac{1}{4} P_{\text{net}}$

the data sheet of Etex Industry, a supplier of microporous insulation [178].

3.13.2 Scaling with system size

In the modelling conducted in this thesis, the SOFC system is sized based on the power requirement for the propulsion of an HGV. A number of parameters defined in the SOFC system model depend on the system size. As the size of each component increases, their mass increases, the outer surface area of the hot box insulation increases, and the volume of the gas within each component increases. The increase in mass slows the thermal dynamics of each component, as per the component-level energy balances presented in Section 3.5. The increase in outer surface area increases the rate of heat loss, also following Section 3.5. The increase in the compartment volume slows the mass dynamics in Section 3.3.

Whyatt et al. [55] estimated the mass of the SOFC system components relative to a Delphi Gen4 system of 6.29 kW at 0.75 V. The authors scaled the mass of the stack based on the number of cells, and the mass of the BoP components based on the flow rate of air or fuel through them.

Holtappels et al. modelled thermal cycling of a 5 kW and a 50 kW SOFC system [114]. The volume of the SOFC system increased by a factor of four from 20 L to 80 L, for a factor of ten increase in power. As a result, the surface area of the system increased by a factor of 2.5. This thesis assumes that this scaling factor can also be applied at higher stack powers.

Mueller et al. [47] presented the open loop response to a step change in load, as discussed in Section 2.3.1. They showed that the relaxation time of the chemical reaction transients was about 20 s for a 25 kW SOFC system. This thesis assumes that the relaxation time of the chemical reaction transients are independent of the system size, and therefore, the volume of the gas compartments are adjusted with scale to maintain a relaxation time of approximately 20 s.

3.14 Control strategy during dynamic simulations

Under dynamic operation, the power requirement of the SOFC system is variable. The dynamic model of the SOFC system includes a control strategy to meet the transient power requirement, whilst maintaining the material and thermal system constraints within their operating window, as defined in Section 3.12. A control strategy is presented here based upon the two strategies of Sorrentino et al. [38] and Mueller et al. [29] reviewed in Section 2.3.2. The purpose of such a control strategy is to assist in investigating the transient response of the SOFC system model. As part of the control strategy, the current, and the flow rates of fuel, AOGR, and air are varied. The implementation of such controllers on a real system is not considered within the scope of this thesis.

In the SOFC system model, a lookup table is used to find the current required at which the system can produce the requested electrical power. The lookup table is generated by running the steady-state SOFC system model at varying current densities, from the nominal current density down to the minimum current density. Likewise, the fuel flow rate is varied to maintain the U_f, and the AOGR flow rate is varied to maintain the S/C ratio at the anode inlet. The required fuel and AOGR flow rates are found as a function of power using lookup tables, which are generated from the same steady-state simulations. This is a reasonable approach, due to the fast material response of SOFC systems, as shown in Section 2.3 of the literature review. The relationship between power and current, U_f, and S/C ratio may be described by the transfer functions $G_I(s)$, $G_{FU}(s)$,

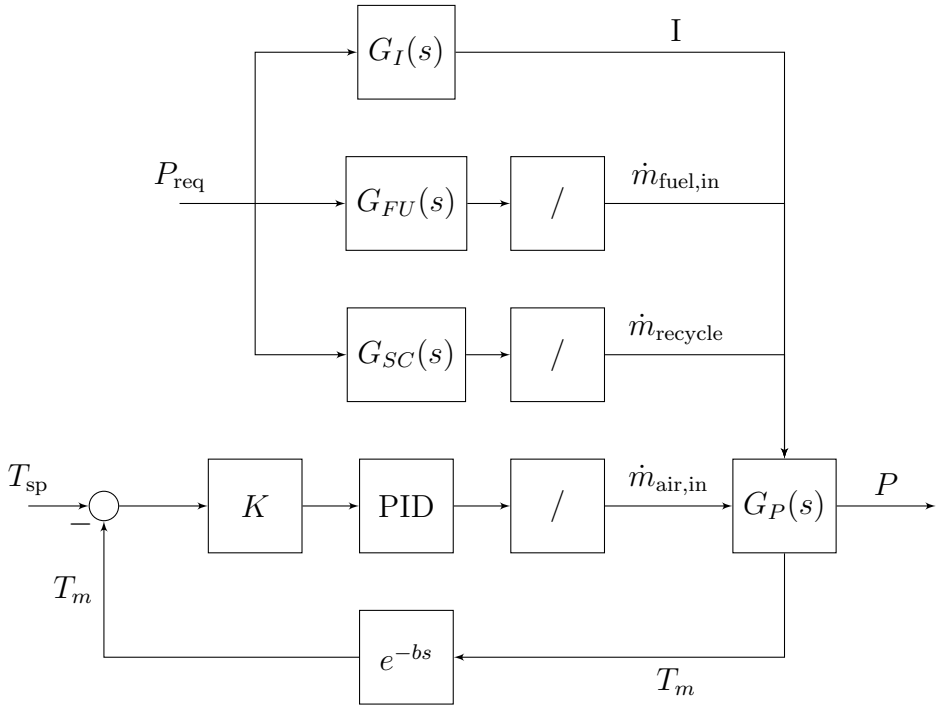

Figure 3.6: SOFC system control diagram, where all parameters are defined in Section 3.14.

and $G_{SC}(s)$, as shown in the control diagram presented in Figure 3.6. The rate limiters (/) in Figure 3.6 are used to represent the delay in opening and closing flow control valves in a real SOFC system.

During dynamic operation, it is required also to maintain the stack temperature, and limit the $\mathrm{d}T_S/\mathrm{d}t$. This can be achieved by varying the air flow rate, but as a result of the slow thermal response of the SOFC system, a lookup table approach is not appropriate. Therefore, a PID feedback controller is used to maintain the stack temperature, as shown in Figure 3.6. The controller varies the air flow rate based upon the temperature difference T_E between the set point of the stack temperature T_{sp}, and the calculated stack temperature T_m. The temperature difference T_E is multiplied by the air flow rate under nominal conditions in block K shown in Figure 3.6. The stack temperature is found from the dynamic SOFC system model $G_P(s)$, which is governed by the equations presented in Sections 3.3 to 3.9. The stack temperature signal is delayed by a single time step b, typically manually set to 1 second in the solvers used for the dynamic simulations conducted. The time step can be adjusted as a compromise between accuracy and computational

speed. The PID parameters used will be reported in Section 5.7.

The controller diagram presented in Figure 3.6 will be utilised in Chapters 5 to 6. However, a limitation of this simple controller is that it only functions whilst the SOFC stack temperature is above its set point. If the stack temperature drops, for example, during cool-down, then a different control approach must be used. Therefore, in Chapter 7, during start-up after cool-down, the control of the air flow rate switches to a lookup table approach based upon the power requirement.

3.15 Software for conducting the simulations

For steady-state analysis of the SOFC system, simulations were conducted using the Engineering Equation Solver (EES) software, whilst the dynamic simulations were conducted in Simscape within the Matlab/Simulink environment. This section introduces both software programmes and describes how the models are implemented.

3.15.1 Steady-state modelling in EES

EES is a useful tool for solving systems of non-linear algebraic and differential equations, which are entered into an '.ees' script file. At the top of the script file, the values of the parameters associated with the operating point from Table 3.1 and the component properties from Table 3.2 and Table 3.3 are defined. Their values may also be imported from a Matlab script. Following that, the system of equations is entered line-by-line. The system of equations defines the thermodynamic properties of the fluids in each gas compartment of the SOFC system, the conservation of mass and energy for each component, and describes the electrical model for the SOFC stack. For the steady-state analysis with each component modelled in 0D, the system of equations consists only of algebraic equations. The simulation is run in EES and the results are exported to Matlab.

One advantage of EES for the steady-state analysis is that the equations can be entered in any order; thus making switching the independent and dependent variables very

straightforward. For the system to solve, the number of equations must match the number of variables, and suitable initial guesses and bounds for each variable are defined. Another advantage of EES is the availability of built-in functions that describe the thermodynamic properties of the fluids. One disadvantage is that EES is not able to perform matrix algebra. This means that species material balances must be performed as separate operations for each species, whereas in Matlab they can be performed as a single operation. However, the use of parametric tables in EES facilitates running the model at different operating points; for example, for a sensitivity analysis or for generating a lookup table.

3.15.2 Dynamic modelling in Simscape

Simscape is part of the Matlab/Simulink environment and is used for the modelling of systems of physical components with physical connections [179]. The solvers within Simscape are well suited to solving the non-linear time-dependent differential and algebraic system of equations for the transient analysis of SOFC systems. In contrast to Simulink, in which signals represent mathematical operations, connection ports in Simscape are non-directional and represent real physical connections. Simscape yields better stability and handling of algebraic loops than Simulink.

3.15.2.1 Domains in Simscape

The Simscape environment consists of a number of different domains. The SOFC system model developed in this thesis consists of an electrical domain, a thermal domain, and a custom gas mixture domain which is based upon the gas domain in the Fluids library. The electrical domain consists of an electrical circuit connecting the reaction site of the cell stack in Section 3.6 to the electrical load. The thermal domain performs the component-level energy balance as described in Section 3.5. The gas mixture domain describes the flow of the gases between and through the gas compartments of the SOFC system, as described in Section 3.3. The physiochemical properties of the gases were considered as outlined in Section 3.3.2, including the assumption of ideal gas mixtures.

The gas domain is one of the fluid system domains packaged with Simscape [180] which is designed for the modelling of a system containing a single gas species. It utilises a Simscape domain file which contains a look-up table that tabulates the variation of gas thermodynamic properties with temperature: namely enthalpy, viscosity, thermal conductivity, and heat capacity. The 'through' variables are the heat flow rate and mass flow rate, and the 'across' variables are the pressure and temperature. With support from Mathworks, the gas domain was extended in this thesis to model semi-perfect gas mixtures. The functionality of the Simscape domain file is extended such that its lookup table tabulated the variation of the thermodynamic properties of each species with temperature. For an SOFC system running on methane, the gas species considered were hydrogen, methane, carbon monoxide, carbon dioxide, water, nitrogen, and oxygen. Air was assumed to consist only of nitrogen and oxygen. The gas mixture custom domain created the mass fraction as an additional 'across' variable to carry information about the composition within the domain.

3.15.2.2 Constructing the dynamic model

The fundamental structure of the component models within Simscape was shown in the schematics of Figures 3.3 to 3.5. Each component consists of the gas mixture and thermal domains, and the stack also includes the electrical domain. A physical signal is used to represent the flow of material between the reaction sites and the gas compartments. A number of other Simscape blocks were constructed for the gas mixture domain, and are utilised in this model. 'Reservoir' blocks are used to represent the fuel supply from the storage tank and the air supply from the ambient environment as well as the exhaust to the ambient environment. 'Mass flow rate source' blocks are used to specify the flow rates of the fuel, air, and off-gas recycle. 'Sensor' blocks are used to save information about the mass flow rate, composition and temperature of each stream in the SOFC system to the Matlab workspace for data processing. For further information about these blocks in the single-species gas domain, refer to the documentation provided by Mathworks [181].

There is no functionality to describe the gain or loss of material by chemical reaction in the gas compartments provided in the Simscape library by Mathworks. Therefore, the reaction sites were constructed using Simscape custom component files; one for the stack reactions, and one for the burner. The composition and gas properties were passed from the gas compartment to the reaction site as physical signals in Simscape. The custom component file calculated the rate of each chemical reaction, and sent this information back to the gas compartment with a physical signal, where the mass balance was established. The custom component files for the reaction sites had a thermal port to connect the heat produced or consumed by the chemical reactions to the overall component-level energy balance.

3.15.3 Summary

In summary, the steady-state modelling was conducted in EES, which allowed the system sizing to be done efficiently. The transient analysis was conducted in Simscape. The simulation workload was split in this way, since the solvers available in each software, were particularly suited to their required tasks, as outlined in Section 3.15. Whilst Simscape can simulate under steady-state conditions, conducting the system sizing in Simscape or MATLAB generally would have been iterative, and therefore, cumbersome, since the software lacks the equation-based solvers that EES possesses.

3.16 Simulation work flow

This section introduces the simulation workflow used throughout the results chapters of this thesis. Each chapter required a specific simulation work flow, which are best represented in flowcharts. In general, there were a number of key processes involved.

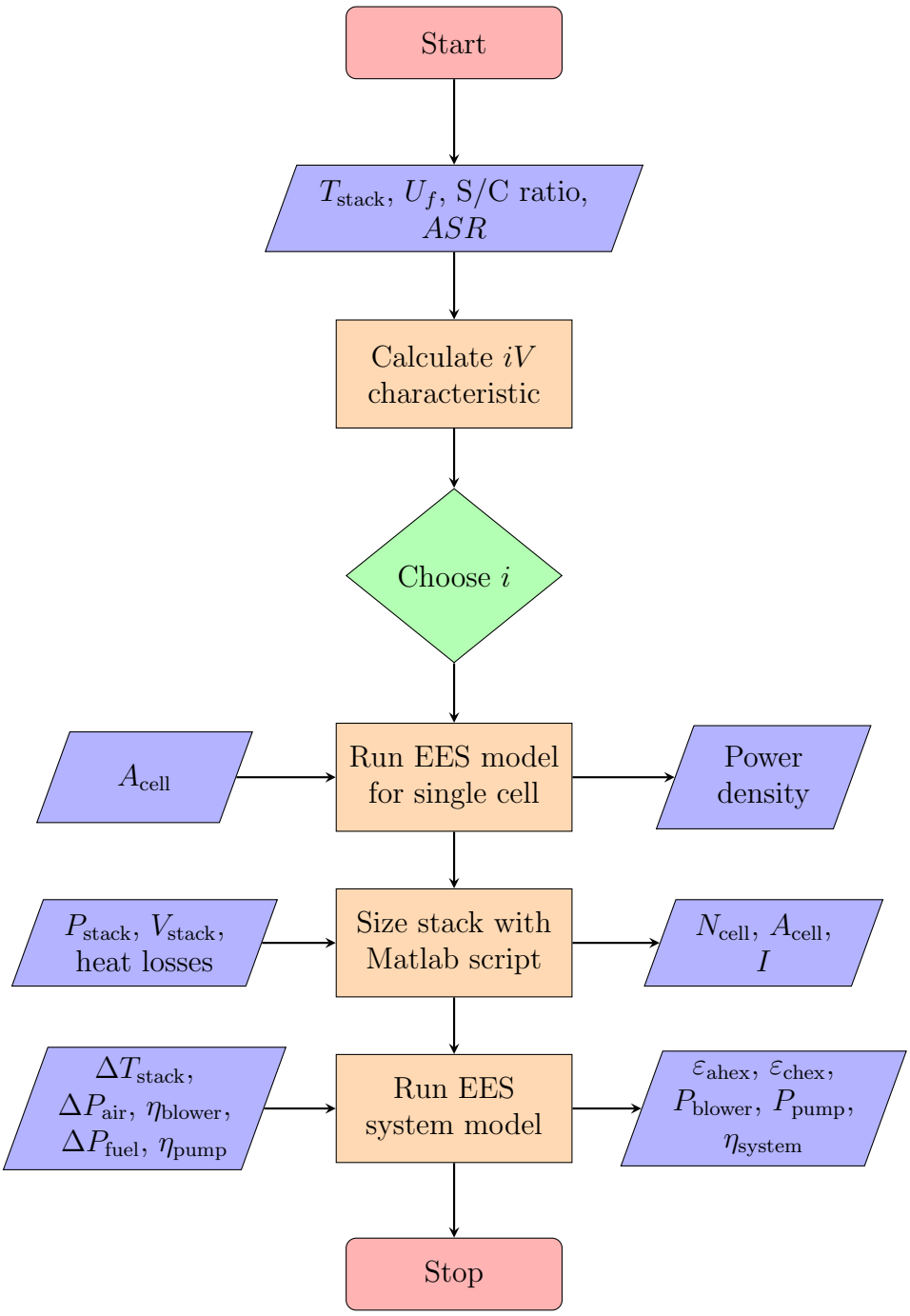

Figure 3.7: System sizing for operation at nominal load.

Table 3.4: Defining the nominal operating point.

Aspect	Parameters
Stack size	Number of cells and active cell area
Voltage losses	Area specific resistance as a function of temperature
Insulation	Thickness, conductivity and surface area
Operating conditions	Current density, U_f and S/C ratio
Operating temperatures	Stack, air and fuel at stack inlet, and system inlet

3.16.1 Sizing the SOFC system

On a vehicle, the power requirements are determined by the drive cycle. The SOFC system is sized to meet those load requirements, with a series of steady-state models simulated in EES. A flowchart outlining the sizing process is shown in Figure 3.7. Table 3.4 lists the parameters which were defined to set the nominal operating points of the SOFC system.

Firstly, the iV characteristics of the SOFC stack were generated using EES. The iV characteristics track the variation in cell voltage, power density, and electrical efficiency as a function of current density. The design values of the stack temperature T_{stack}, U_f, and S/C ratio are specified in the base Matlab script, as listed in Table 3.1. The ASR parameter values listed in Table 3.2 were also defined. Based upon the iV characteristics, the current density i at which each cell in the SOFC stack should operate at under nominal load was chosen.

The cell area A_{cell} was specified and hence the power of a single cell at the nominal current density was found, as per Equation (3.29). The number of cells N_{cell} within the SOFC stack required to meet the load demand was calculated as per Equation (3.28). For large load demands, multiple SOFC stacks can be connected electrically in series or in parallel, to meet the DC voltage and power requirements.

Once the size and number of SOFC stacks were specified, the SOFC system was simulated at the nominal load requirement in EES. The remaining steady-state system parameters from Tables 3.1 to 3.3 were specified: namely, the stack inlet temperature, the hot box insulation properties, the air and fuel side pressure drops, and the blower prop-

erties. From the steady-state system model, the effectiveness of the anode and cathode pre-heaters, the net system power accounting for the parasitic load of the blower, and the net electrical system efficiency were found.

3.16.2 Running the steady-state model in EES

The EES script computed the steady-state material and energy balances for each component of the SOFC system as well as the electrochemical model of the SOFC stack. The EES script contained a header to import the nominal operating point from the Matlab workspace and a footer to export the results back to the Matlab workspace. The steady-state model calculated the mass flow rate of air and fuel at the system inlet and the mass flow rate of the AOGR. The effectiveness of the anode and cathode pre-heaters were calculated to meet the required stack inlet temperature. The gas composition and temperature within each component were calculated. The voltage and power were also calculated.

3.16.3 Setting up the transient model in Simscape

Model inputs The transient model was simulated in the Matlab/Simulink environment. Simulink read all parameters required from the Matlab workspace. The mass flow rate of the air, fuel and AOGR streams and the current were gathered from the steady-state results. The time dependence of any of the variables during the transient simulation were set up using the 'timetable' functionality in Matlab. The temperature of the inlet air and fuel streams were defined too.

Transient parameters In moving from the steady-state to the dynamic model, a number of additional parameters were defined in the Matlab script. For the dynamic species balance, the volume of each gas volume was defined, and for the dynamic energy balance, the mass and specific heat capacity of each lumped component were defined.

Initial conditions For each gas volume, the initial temperature and composition for each gas volume were defined and the initial temperature of each solid mass, based upon the results of the steady-state modelling.

Table 3.5: Setting up the transient model in Simscape.

Parameters	Type	Origin
Mass flow rates of air, fuel and off-gas	Inputs	EES script
ASR parameters of stack	Fixed parameters	Defined
Insulation properties of each component	Fixed parameters	Defined
Gas volume of each component	Fixed parameters	Defined
Thermal capacity of each component	Fixed parameters	Defined
Temperature of each component	Initial condition	Defined/EES script
Gas composition of each component	Initial condition	EES script
Effectiveness of each HEX	Fixed	EES script

3.16.4 Running the transient model in Simscape

The 0D direct internal reforming SOFC model was defined by the current density i that was needed to meet the required fuel cell load. Suitable values for U_f, the S/C ratio and λ ensured that the fuel cell ran at a suitable operating point. In this stand-alone SOFC model, the temperatures of the gas mixtures in the fuel channel and air channel at the inlet were defined and constant. The stack temperature was solved through the thermal block in the model, with an appropriate initial condition chosen. The material block calculated the rate of each reaction, and the inlet and outlet flow rate and composition.

The variable step-size *daessc* solver from Simscape was used where possible, to reduce the computational burden. For simulations which included a state machine, and/or feedback control, a fixed time-step solver was used. A time step of 1 second gave reasonable resolution, and the appropriate fixed time-step solver was auto-selected by Matlab Simulink.

The variables of interest were logged, and exported to the Matlab workspace. It was there that the plots presented in the results Chapters 4 to 7 were generated. The model

in Simscape was also run under steady-state conditions to ensure consistency with the results from the steady-state simulations in EES.

Chapter 4

Steady-state validation

This chapter investigates the performance of solid oxide fuel cell (SOFC) systems under steady-state conditions, as a means to validate the model introduced in Chapter 3. This is done within the following sections:

- The SOFC stack model is validated against current density-voltage (iV) characteristics from experiments in Section 4.1, and
- The SOFC system model is validated against another system model in Section 4.2.

Model validation is important because it offers confidence that the underlying behaviour of the model matches that of its experimental counterpart, and therefore allows the model to provide insight into operating the fuel cell system under a range of different operating conditions and in different applications, such as part of a vehicle powertrain.

4.1 Validating the SOFC stack model

The SOFC stack is the core component of the SOFC system. It produces the electrical power, and its performance has the largest influence on the overall system performance. The SOFC stack also has a number of operating constraints, since various components of the repeating unit are sensitive to their operating conditions. Therefore, accurate

modelling of the SOFC stack is a crucial aspect of the overall system model. To ensure that, this section presents validation of the SOFC stack model.

4.1.1 Introducing iV characteristics

The steady-state performance of the SOFC stack is determined by its cell iV characteristics, which describe the variation in cell voltage with current density. The iV characteristics describe the electrical performance of the SOFC stack. They determine the variation in power density with current density. In combination with fuel utilisation (U_f), the iV characteristics define the variation in stack efficiency with current density. The iV characteristics also influence the thermal behaviour of the stack, since larger voltage losses means more heat production in the stack, as per Equation (3.31).

4.1.2 Procedure for validation

In the electrical model presented in Section 3.6.1.2, the iV characteristics described by Equation (3.27) are a straight line with a negative gradient equal in magnitude to the area specific resistance (ASR), and a y-intercept equal to the open circuit voltage (OCV). In Equation (3.24), the OCV is described as a function of temperature and gas partial pressures in the SOFC stack. In Equation (3.26), the ASR is described as a function of the SOFC stack temperature. In order to verify iV characteristics, the following process is followed:

1. Verify that the OCV is described accurately by the Nernst Equation (3.24) by studying the OCV reported experimentally at varying temperature and fuel composition in the literature,

2. Verify the assumption that the iV characteristics of an SOFC stack are of constant gradient is a reasonable one, by studying iV characteristics produced experimentally in the literature, and

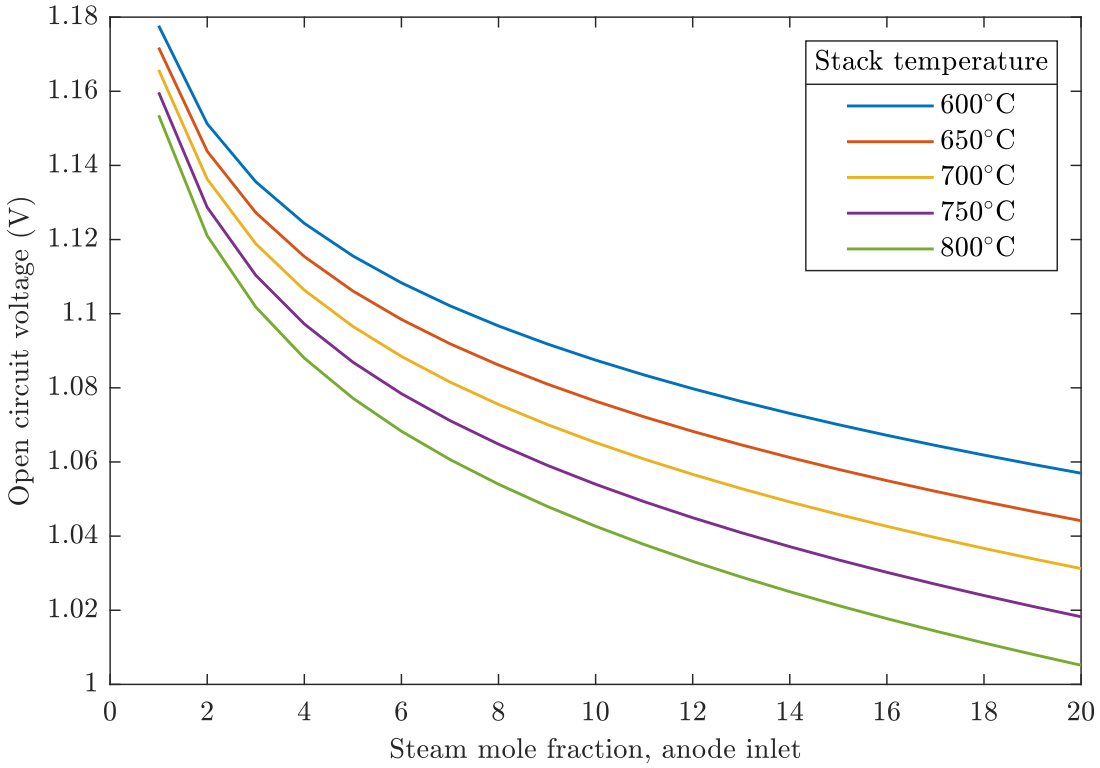

Figure 4.1: Open circuit voltage as a function of stack temperature and water mole fraction at the anode inlet.

3. Verify that the temperature dependence of the ASR is accurately described by the form of the Arrhenius expression in Equation (3.26), by the ASR predicted by the model with experimental data reported in the literature.

4.1.3 Validating the OCV

In the SOFC stack model presented in Section 3.6, the OCV was determined by the Nernst Equation (3.24), as a function of stack temperature, the partial pressures of water and hydrogen on the anode, and the partial pressure of oxygen on the cathode.

In the literature, iV characteristics are typically reported when supplied with wet hydrogen and air. The absolute pressures on both the anode and cathode are typically close to atmospheric. Figure 4.1 shows the expected variation in OCV as a function of temperature and steam mole fraction in hydrogen, as predicted by Equation (3.24) of the SOFC stack model. Figure 4.1 shows that as the SOFC stack temperature increases, the OCV decreases. This is because the Gibbs free energy of the electrochemical oxidation of

Table 4.1: Validating the calculated OCV with experimental data in the literature.

y_{H_2O}	T_{stack} (°C)	$V_{0,model}$ (V)	$V_{0,exp}$ (V)	ΔV_0 (V)	
0.03	860	1.091	1.092	0.001	Riegraf et al. [182]
0.04	650	1.115	1.111	-0.004	Ferchaud et al. [183]
0.04	700	1.106	1.103	-0.003	Ferchaud et al. [183]
0.055	800	1.073	1.071	-0.002	Golani et al. [184]
0.20	700	1.031	1.033	0.002	Blum et al. [185]
0.20	750	1.018	1.019	0.001	Blum et al. [185]
0.20	800	1.005	1.007	0.002	Blum et al. [185]
0.50	700	0.973	0.972	-0.001	Sun et al. [186]
0.50	715	0.968	0.972	0.004	Hauck et al. [187]
0.50	762	0.953	0.955	0.002	Hauck et al. [187]
0.50	809	0.938	0.938	0	Hauck et al. [187]
0.50	800	0.977	0.975	-0.002	M. Yu et al. [188]

hydrogen (H2X) reaction in Equation (3.6) becomes less negative with increasing temperature. Figure 4.1 also shows that the OCV decreases as the water mole fraction increases. This can be seen by the form of Equation (3.24) which displays an asymptote as the water partial pressure tends towards zero.

In order to validate the calculated values of the OCV in this model, they are compared with the OCVs values reported from experimental results in the literature for SOFC stacks operated with wet hydrogen. Table 4.1 lists a number of experimental results over a range of operating conditions: for water mole fraction in hydrogen at the anode inlet from 0.03 to 0.50, and SOFC stack temperature from 650°C to 860°C. The model agrees with all experimental results within 0.004 V. Such a small deviation is well within the measurement uncertainty of the voltage. This suggests that the widely used Nernst equation (3.24) does well define the OCV of an SOFC stack, and is therefore considered validated for this model.

For the purposes of the OCV validation, experimental results with dry hydrogen were not considered due to the asymptote as the water mole fraction approaches zero in the Nernst equation. Methane iV characteristics are not considered here, because such SOFC systems usually include a pre-reformer, so the gas composition at the anode inlet is often not well defined.

4.1.4 Validating iV characteristics as straight lines

In the SOFC stack models reviewed in Section 2.1.4, the voltage losses were simulated either by calculating the activation, ohmic and concentration losses separately, or by using a data fit to estimate the ASR. The ASR simplifies the modelling approach by assuming the voltage losses are a linear function of temperature in the form of an Arrhenius expression, and independent of current density. In this section, the assumption that the ASR is independent of current density is investigated.

Of the iV characteristics found in the literature, the most common fuels fed to the anode inlet were dry hydrogen, wet hydrogen, or pre-reformed natural gas. Whilst iV characteristics in the literature produced with dry hydrogen display curvature at low current densities, iV characteristics for wet hydrogen and natural gas were much straighter. A number of experimental iV characteristics for wet hydrogen are shown in Figure 4.2, for a range of stack temperatures from 600°C to 800°C. All of the iV characteristics show relatively straight iV characteristics which is primarily caused by the reduced OCV, when compared to iV characteristics with dry hydrogen. This shows that provided steam is supplied to the anode, the assumption of straight iV characteristics in the model presented in Chapter 3 is reasonable one. The deviations in the modelled voltage to the experimental voltage are typically around 0.02 V, which shows that the ASR modelling approach is less accurate than the OCV calculation in the Nernst equation (3.24). These deviations are observable especially at lower and higher current densities in Figure 4.2, and are caused by neglecting the non-linear activation and concentration voltage losses in the model.

Authors more seldom present iV characteristics with methane, but those found in the literature from S. Chen et al. [191], Mai et al. [192] and Noponen et al. [111] all show straight iV characteristics like those for wet hydrogen in Figure 4.2. This is because SOFC stacks which internally reform methane also have a significant mole fraction of water at the anode inlet. This shows the assumption of a straight iV characteristic for the SOFC system, simulated in this thesis with internal steam reforming of methane, is a reasonable

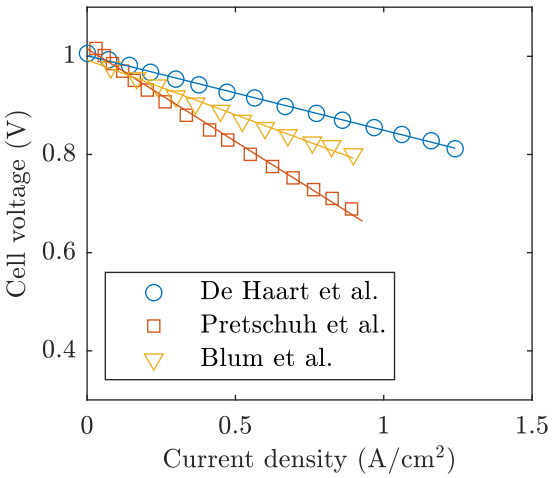

(a) 800°C [189, 190, 185].

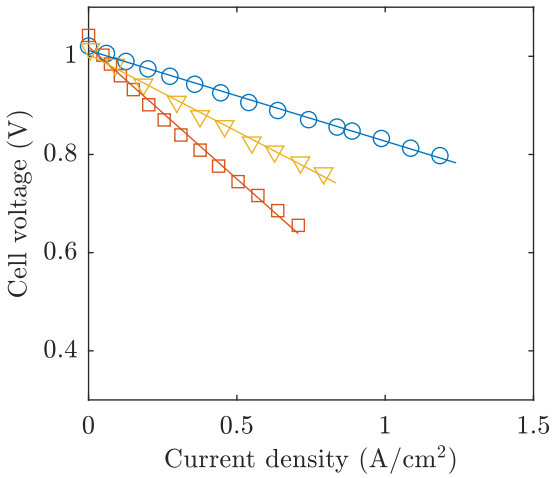

(b) 750°C [189, 190, 185].

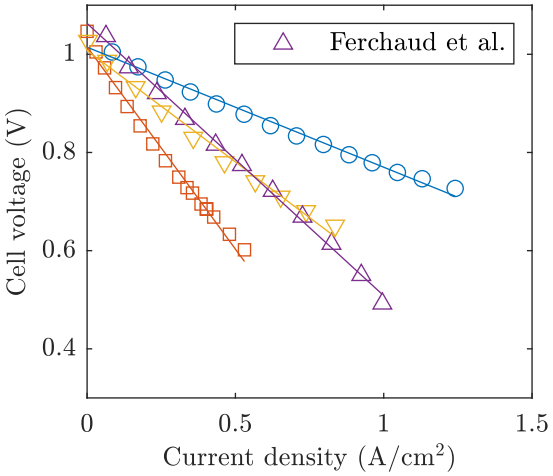

(c) 700°C [189, 190, 185, 183].

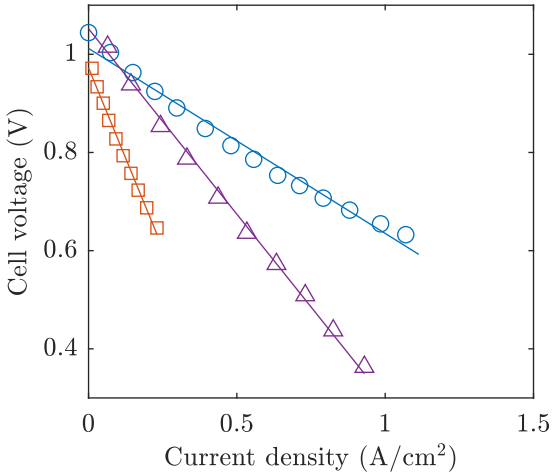

(d) 650°C [189, 190, 183].

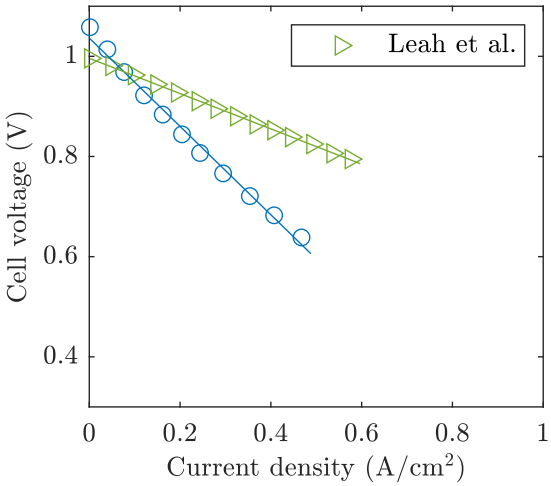

(e) 600°C [189, 108].

Figure 4.2: iV characteristics with wet hydrogen.

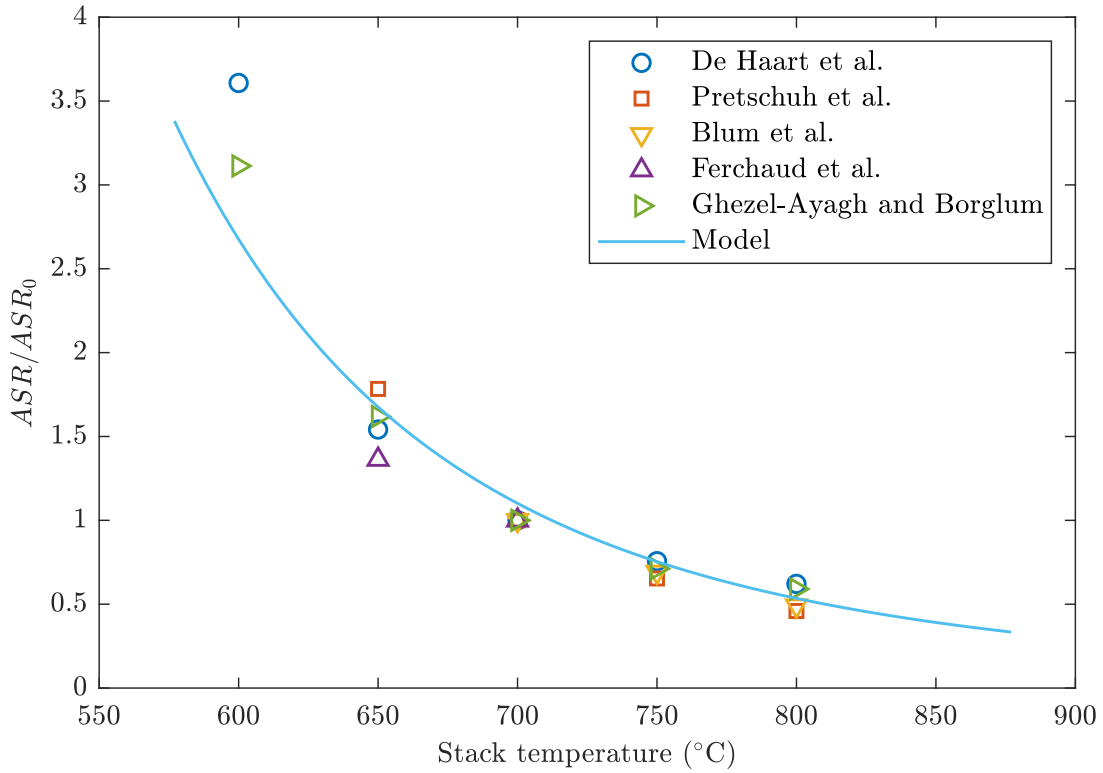

Figure 4.3: Normalised ASR as a function of temperature, from the literature [189, 190, 185, 183, 193].

one.

4.1.5 Validating ASR as a function of temperature

Whilst Figure 4.2 showed that iV characteristics on wet hydrogen were relatively straight, it also showed large variation in ASR at fixed stack temperature between different experimental studies. That is because the ASR itself is dependent on material properties such as the electrolyte conductivity, and geometric properties such as electrolyte thickness, which vary between different experimental set-ups. The consideration of such effects is beyond the scope of this thesis. Instead, the ASR is modelled in Equation (3.26) as an Arrhenius expression as a function of temperature relative to a reference ASR_0 at a reference temperature T_0. The value for the ASR_0 is taken always from an experimental set-up in the literature, and is specific to a particular SOFC stack. The parameter E_a in Equation (3.26) describes the variation in ASR with temperature, which is reported to

be 0.65 eV for experiments conducted by Gubner [73].

In order to validate the variation in ASR described by Equation (3.26), its variation is compared to other experimental results in the literature in Figure 4.3. Since the ASR of different SOFC stacks varies significantly between different studies even at fixed temperature, the ASR values shown in Figure 4.3 are normalised against their ASRs at 700°C. Figure 4.3 shows that as the stack temperature increases, the model predicts that that the ASR decreases. From 600°C to 700°C the ASR decreased steeply, and from 700°C to 800°C the ASR begins to level off. This is in good agreement with the variation in ASR with temperature from a number of experimental studies reported in the literature, at least above 650°C [189, 190, 185, 183, 193]. Therefore, the Arrhenius expression in Equation (3.26), with an activation energy, E_a of 0.65 eV is seen to be a reasonable method for estimating the variation in a known experimental ASR with temperature.

4.1.6 Summary

This section validated the stack model presented in Section 2.1.4 by comparing the iV characteristics predicted by the model with experimental results presented in the literature. The OCV was validated in Section 4.1.3. The calculated values of the OCV as a function of temperature and composition from Equation (3.24) showed good agreement with experimental values from seven different papers. The assumption that the voltage losses can be suitably modelled with a single ASR expression was verified in Section 4.1.4. iV characteristics from eight different papers showed that the voltage losses are indeed relatively linear over a range of temperatures, provided that the fuel, either hydrogen or methane, is provided with steam to the SOFC stack. This shows the assumption of linear voltage losses as reasonable one. Whilst the ASR is a function of stack temperature, it also depends on the electrochemical materials and geometries of the SOFC stack, and therefore, the reference ASR_0 at temperature T_0 are taken from the experimental studies in the literature. Section 4.1.5 validated the Arrhenius expression of the variation in ASR with temperature, and showed that the activation energy E_a of 0.65 eV was a relatively

good fit across 5 different SOFC stacks, particularly between 650°C and 800°C.

4.2 Validating the SOFC system model

Validation of the SOFC system model is required in addition to the stack model to ensure that the interactions between the SOFC stack and balance of plant components are modelled correctly. Two authors [86, 87] presented experimental results from SOFC system testing, however their results were difficult to validate a system model against, because many of the operating details were not provided. Furthermore, there may be considerations specific to their experimental set-up not captured in a generalised model.

SOFC system modelling papers tend to present clearly their operating conditions, which makes it possible to validate the model developed here against their results. Peters et al. [16] modelled an SOFC system using a similar approach to this thesis. Their model is considered most appropriate and will be used in the following to validate the SOFC system model presented in Chapter 3.

4.2.1 Setting up the steady-state system model

Peters et al. [16] modelled a large-scale (LS) and a small-scale (SS) SOFC system with anode off-gas recirculation (AOGR). The values of the parameters associated with each SOFC system model are listed in Table 4.2, which defines the size and properties of the SOFC stack. The U_f and recirculation ratio (RR) are defined. The heat exchangers are sized to give the required stack inlet temperature. The air and recirculation blowers are assumed to have constant efficiency. Peters et al. presented a correlation relating the pressure drop to the flow-rate on both the air side and fuel side. From the model, the electrical power of the SOFC stack and the parasitic power demand of the air blowers were found. Hence, the electrical system efficiency was calculated. Peters et al. presented the electrical efficiency of each SOFC system with varying U_f and RR.

The model presented in this thesis is constructed and the results are compared to the

Table 4.2: System parameters and operating point for system model validation [16].

Parameter	SS system	LS system
Nominal power output (kW)	3	250
Stack temperature (°C)	850	750
Active cell area (cm^2)	100	360
Cells per system	180	2500
Current density ($A\,cm^{-2}$)	0.25	0.4
Area specific resistance ($\Omega\,cm^2$)	0.4	0.25
Stack inlet temperature (°C)	750	650
System inlet temperature (°C)	25	
Pre-reformer temperature (°C)	500	
Blower isentropic efficiency	60 %	
Blower mechanical efficiency	50 %	
DC/AC inverter efficiency	95 %	
Nernst composition weighting factor	0.25	0.17

results of Peters et al. [16]. Component models of the SOFC stack, pre-reformer, and blowers are implemented according to the methodology set out in Chapter 3:

- All reforming reactions are assumed to be at thermodynamic equilibrium, as justified in Chapter 3. This enables calculation of reaction rates without knowledge of component geometries. By neglecting kinetics, the reaction conversion is likely to be overestimated, but not significantly. For example, Ceres Power showed that 90 % methane steam reforming (MSR) reaction conversion can be achieved in the SOFC stack, even at relatively low operating temperatures [61].

- The SOFC stack model is unchanged, consisting of the mass and energy balances, and the electrical sub-model.

- A mass balance is established across the pre-reformer to find the anode inlet composition, but the energy balance is not required because the pre-reformer temperature was pre-defined by Peters et al. [16]. This could be achieved with an electrical heater.

- The blower models utilise the correlations presented by Peters et al. [16] to find the

pressure ratio as a function of mass flow rate.

- The burner and heat exchanger (HEX) models are not required to calculate the efficiency since the stack inlet temperatures were pre-defined by Peters et al. [16].
- The fuel is considered 100 % methane, and steam is recirculated in the anode off-gas.

Peters et al. stated only the assumptions of their analysis, but did not define their governing equations [16]. Whilst they defined the ASR of their stacks, the electrical models were not defined. In the results, they reported only the electrical efficiencies calculated for the SOFC system. Therefore, it is not clear which compositions they used in the Nernst potential calculation (3.24). In trying to validate the model, this thesis initially calculated the OCV based on the composition of the anode and cathode at their outlets, but this significantly underestimated the system efficiency compared to Peters et al. Therefore, a weighted average composition was used, averaged between the composition following reforming and that at the outlet, as presented in Section 3.6.1.2.

The steady-state simulations were conducted in Engineering Equation Solver. The computational workflow is illustrated as a flowchart in Figure 4.4. Based on the temperature of the components in Table 4.2, the thermodynamic properties of the gases in each compartment were calculated. Faraday's law was used to find the rate of the H2X reaction. Conservation of mass on components within the AOGR loop was used to find the required fuel flow rate. Conservation of mass and energy across all components, and the electrical model, were used to find the required air flow rate, and the electrical performance of the SOFC stack. The blower models were used to calculate the parasitic losses of the system, and finally the net system efficiency was calculated.

4.2.2 Introducing the steady-state system results

By modelling the SOFC system, validation took place not only by comparison of the results with those presented by Peters et al., but also by plotting each parameter in turn

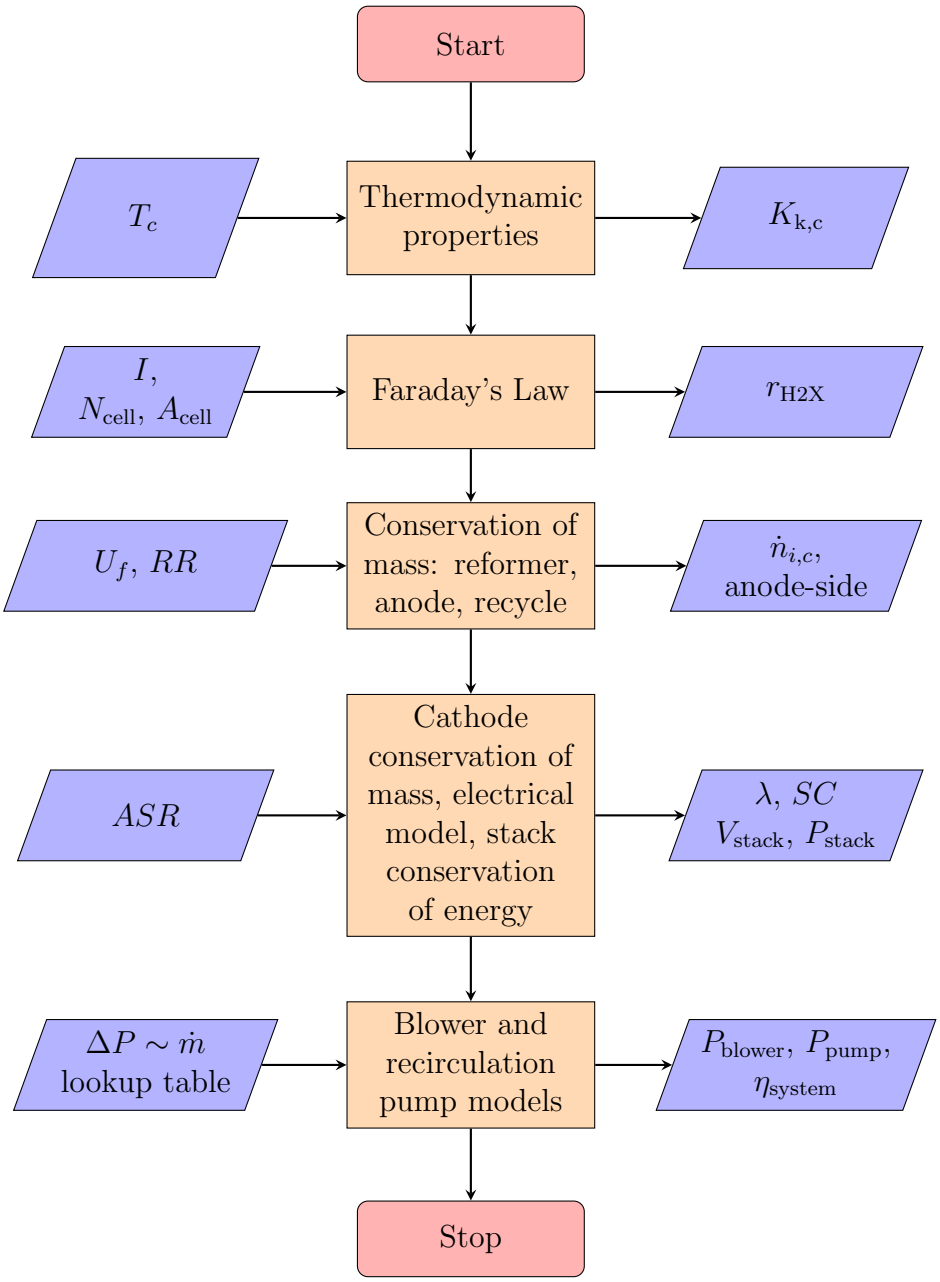

Figure 4.4: EES computational workflow for system validation.

and sense-checking them. In this way, the validity of the model would be ensured. In the following sections, the results of the steady-state modelling are presented:

- The fuel requirements of the SOFC system are presented in Section 4.2.3,
- The anode-side composition of the SOFC system is presented in Section 4.2.4,
- The cathode-side composition of the SOFC system is presented in Section 4.2.5,
- The electrical performance of the SOFC stack is presented in Section 4.2.6,
- The electrical performance of the SOFC system is presented in Section 4.2.7, and
- The efficiency of the SOFC system including comparison to the results from Peters et al. [16] are presented in Section 4.2.8.

In all plots, the parameter values in Table 4.2 are maintained, whilst RR and U_f are varied. Where relevant, the calculated variables are normalised by dividing by the SOFC stack active area to enable comparison between the LS and SS systems.

4.2.3 Rate of fuel consumption

Figure 4.5 plots the variation in the rate of system fuel consumption with RR and stack U_f. The LS system is shown in Figure 4.5a and the SS system in Figure 4.5b. As RR increases, a greater proportion of unreacted fuel is recycled to the anode inlet. Therefore less fuel is required to meet the required power output, and the fuel consumption rate decreases. As the stack U_f increases, a greater proportion of the fuel reacts, and therefore the fuel consumption rate decreases.

4.2.4 Anode composition

Figure 4.6 shows the variation in composition for each species with RR and U_f at the inlet (dashed line) and at the outlet (solid line) of the anode. The compositions of each species are compared in the following.

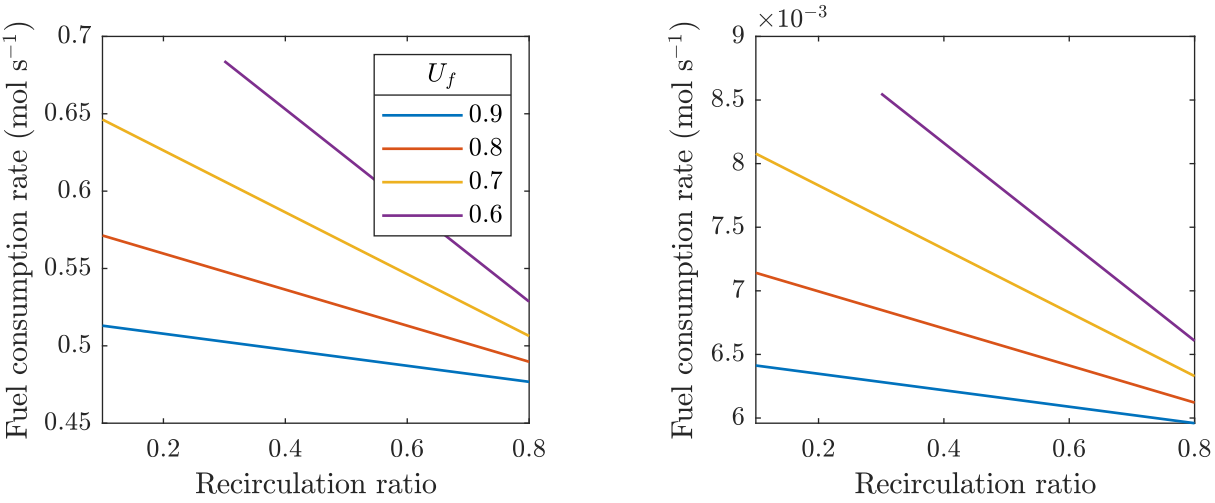

(a) LS system.

(b) SS system.

Figure 4.5: Variation in rate of fuel consumption with RR and U_f.

4.2.4.1 Comparing inlet and outlet compositions

The mole fraction of methane at the anode outlet in Figures 4.6a and 4.6b is always zero, because the MSR reaction on the anode goes to completion when assumed at equilibrium.

Carbon monoxide is both consumed through the water gas shift (WGS) reaction and produced through the MSR reaction on the SOFC anode. The rates of those reactions determine whether the carbon monoxide mole fraction is higher at the anode inlet and outlet. Figures 4.6c and 4.6d show that under most conditions the mole fraction of carbon monoxide is higher at the outlet than at the inlet. The exception to this is at high U_f where the high consumption of hydrogen in the H2X reaction shifts the WGS equilibrium reaction to the right, and hence more carbon monoxide is consumed.

Under most operating conditions the mole fraction of hydrogen at the anode outlet is lower than at the anode inlet, as shown in Figures 4.6e and 4.6f. This is because a significant proportion of the hydrogen is produced within the pre-reformer.

Figures 4.6g to 4.6j show that the mole fractions of water and carbon monoxide tend to be higher at the anode outlet than the anode inlet. All of the water is produced on the anode through the H2X reaction, whilst production of carbon dioxide through the WGS reaction is split between the pre-reformer and the SOFC anode.

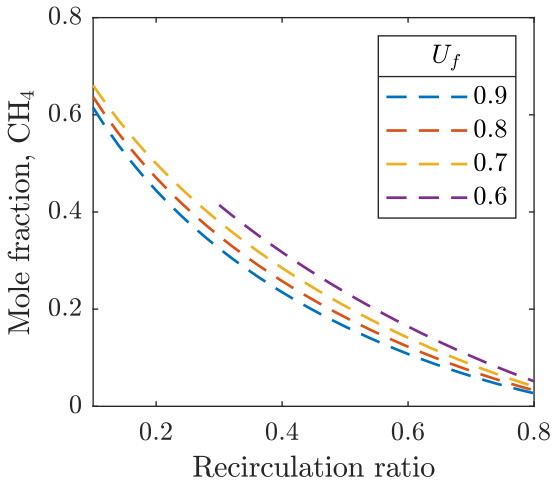

(a) Methane, LS system.

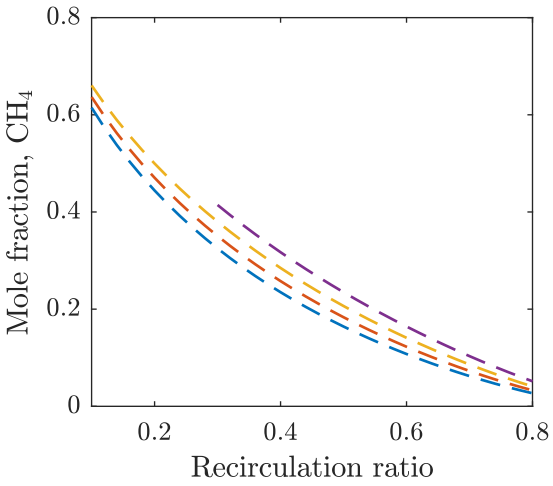

(b) Methane, SS system.

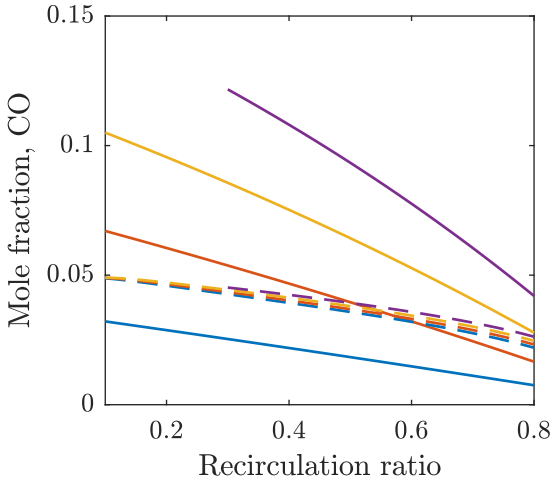

(c) Carbon monoxide, LS system.

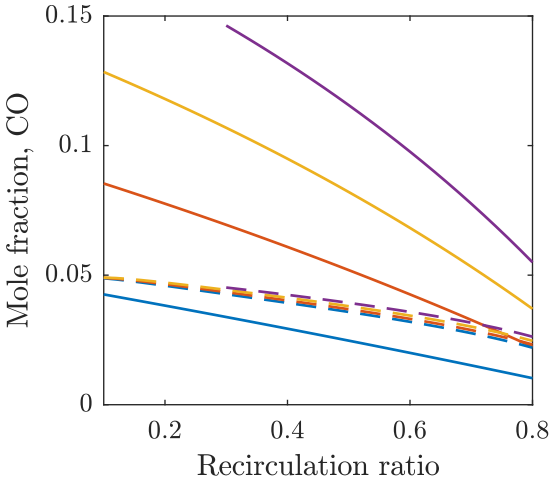

(d) Carbon monoxide, SS system.

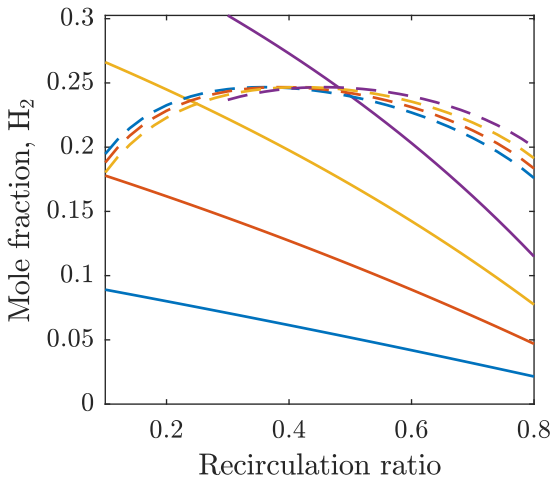

(e) Hydrogen, LS system.

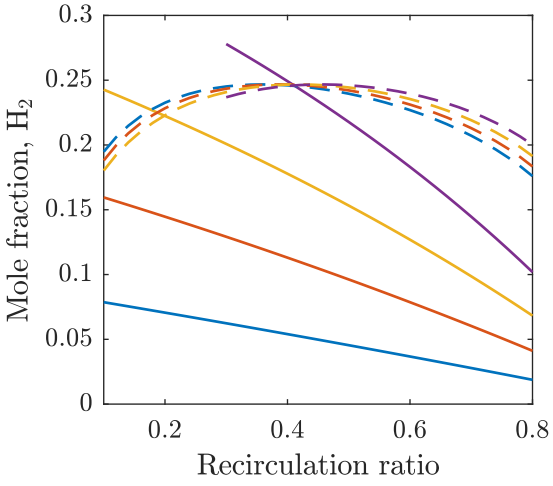

(f) Hydrogen, SS system.

Figure 4.6: Composition at anode inlet (dashed) and outlet (solid).

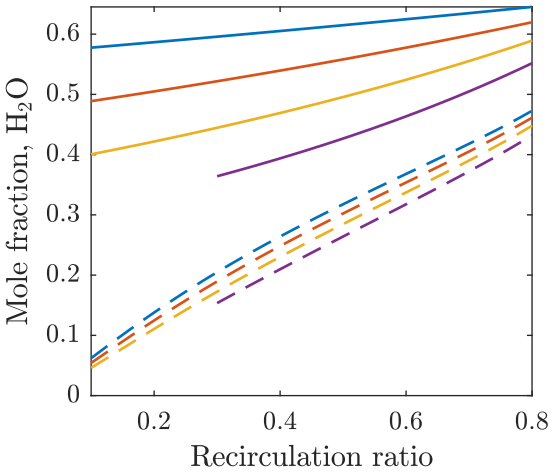

(g) Water, LS system.

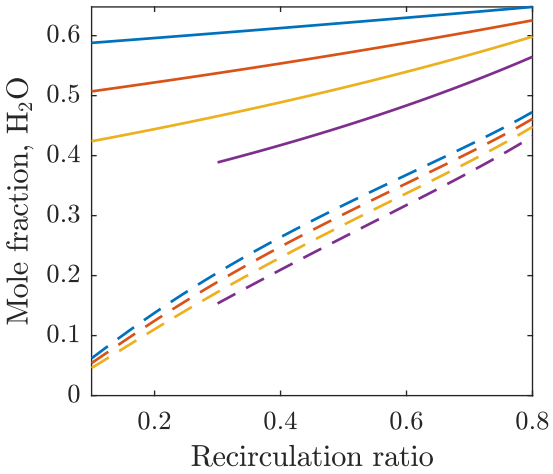

(h) Water, SS system.

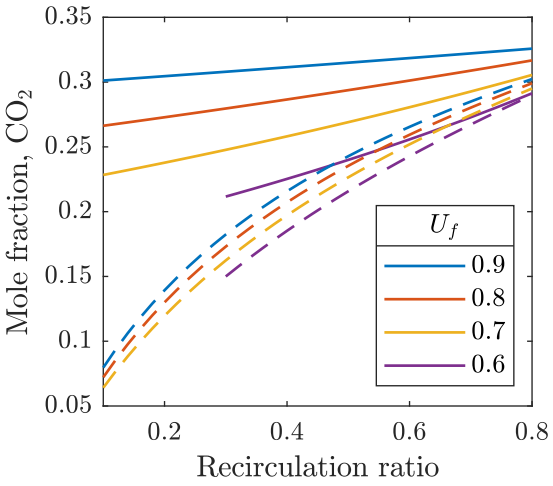

(i) Carbon dioxide, LS system.

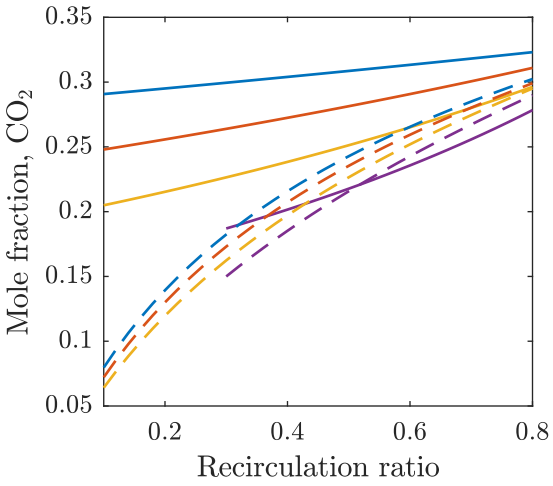

(j) Carbon dioxide, SS system.

Figure 4.6: (ctd.) Composition at anode inlet (dashed) and outlet (solid).

4.2.4.2 Composition with varying RR

As RR increases, an increasing proportion of the anode off-gas is recirculated. This increases the flowrates of carbon dioxide and water through the SOFC stack. Hence, the mole fractions of carbon dioxide and water at the anode inlet and outlet increase with RR, as show in Figures 4.6g to 4.6j. This dilutes the methane, hydrogen and carbon monoxide, and hence their mole fractions decrease with increasing RR, as shown in Figures 4.6a to 4.6f.

Figures 4.6a to 4.6f show that only for RR greater than 0.42 does the mole fraction of hydrogen at the anode inlet decrease with increasing RR. At an RR of 0.42 there is a

maximum hydrogen mole fraction of 0.24. As RR decreases below 0.42, the mole fraction of hydrogen at the anode inlet decreases, because there is not enough steam for the MSR and WGS reactions in the pre-reformer. This is confirmed by Figures 4.7a and 4.7b which shows the steam-to-carbon ratio (S/C ratio) falling below 2.

4.2.4.3 Composition with varying U_f

As U_f increases, the rate of consumption of hydrogen and rate of production of water through the H2X reaction in the SOFC stack increases. This shifts the equilibrium position of the WGS reaction in the SOFC stack to promote the consumption of carbon monoxide and production of carbon dioxide. Therefore, Figures 4.6c to 4.6f show that the mole fractions of the hydrogen and carbon monoxide at the anode outlet decrease with increasing U_f. Likewise, Figures 4.6i to 4.6j show that the mole fractions of water and carbon dioxide at the anode outlet increase with increasing U_f.

The trends in composition at the anode inlet with varying U_f are similar to the anode outlet, but the dependence on U_f is weaker. This is because the composition at the anode inlet is determined primarily by the conversion of the MSR and WGS reactions in the pre-reformer, which are assumed at equilibrium.

4.2.4.4 Comparing the species

Figures 4.6c to 4.6f show the trends in the mole fractions of hydrogen and carbon monoxide are very similar at the anode outlet. The hydrogen mole fraction is two to three times larger than the carbon monoxide mole fraction, since the reforming reactions produce more moles of hydrogen than carbon monoxide. Both species are both produced and consumed in the SOFC stack.

According to the stoichiometry of the MSR, WGS and H2X reactions, one mole of methane produces up to two moles of water and up to one mole of carbon dioxide. Therefore, Figures 4.6g to 4.6j show that the mole fraction of water at the anode outlet is approximately double that of carbon dioxide.

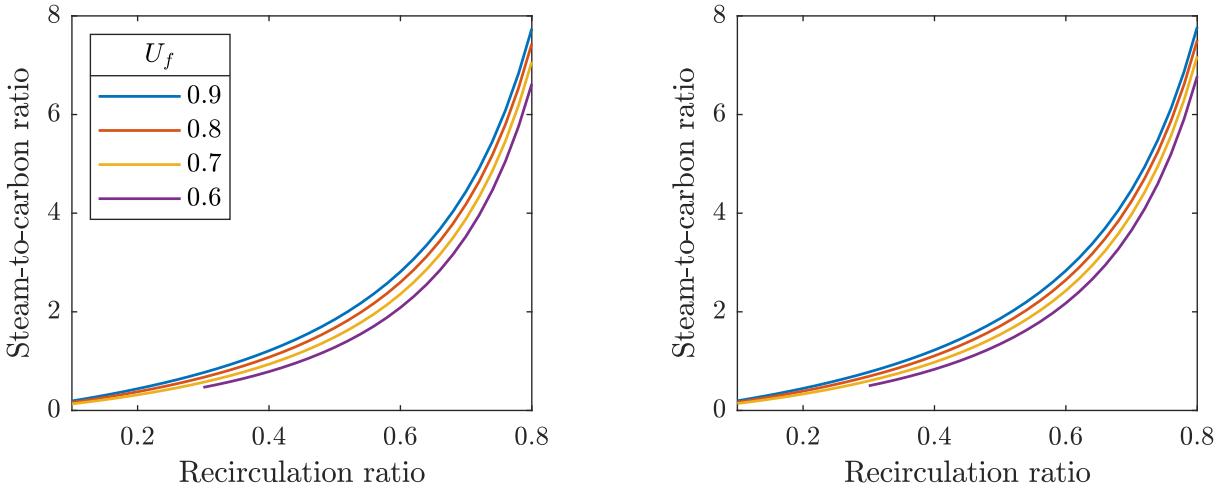

(a) LS system.

(b) SS system.

Figure 4.7: S/C ratio at the reformer inlet.

4.2.4.5 Comparing the LS and SS systems

Figure 4.6 shows that the trends in anode composition for the LS system and SS system are very similar. One noticeable difference is that the mole fractions of water and carbon monoxide for the SS system are two to three hundredths larger than for the LS system, while the mole fractions of hydrogen and carbon dioxide are two to three hundredths lower. This is caused by the higher operating temperature of the SOFC stack in the SS system. This means the equilibrium conversion of the mildly exothermic WGS reaction is lower, so less hydrogen and carbon dioxide are produced.

4.2.4.6 S/C ratio

As discussed in Section 3.6.1.1 of the methodology chapter, it is assumed that by keeping the S/C ratio at the reformer inlet above two, carbon deposition can be neglected. Figure 4.7 shows that to keep the S/C ratio above two, RR must be kept above approximately 0.55 for all values of U_f. Therefore, operation of the SOFC system below an RR of 0.6 should be avoided to prevent carbon deposition. The S/C ratio is also weakly dependent on U_f. At fixed RR, the S/C ratio increases with U_f because more steam is produced through the H2X reaction.

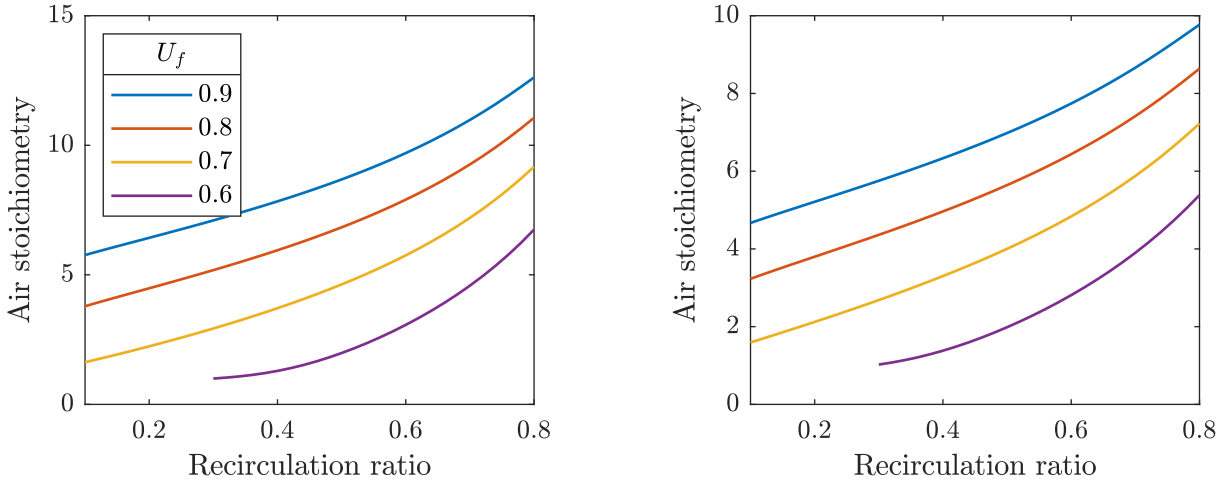

(a) LS system. (b) SS system.

Figure 4.8: Air stoichiometry.

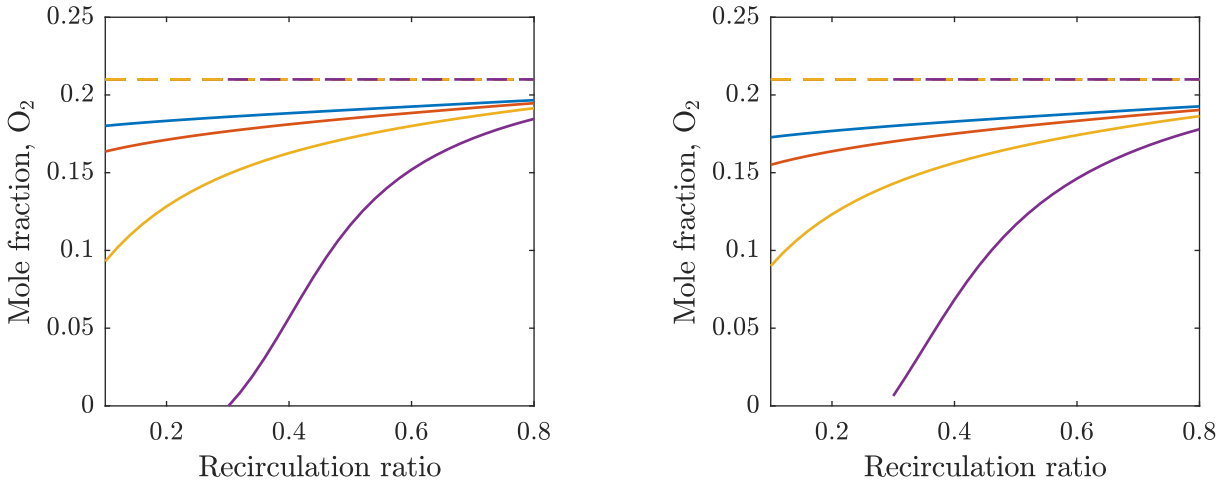

(a) Oxygen, LS system. (b) Oxygen, SS system.

Figure 4.9: Cathode composition.

4.2.5 Cathode composition

In this section the variation in the cathode composition is presented: specifically, the varying air flow requirement for stack cooling, and the resultant effect on the oxygen mole fraction at the cathode.

4.2.5.1 Cooling requirements

Figure 4.8 plots the variation in the air stoichiometry defined in (3.44), with RR and U_f.

As RR increases, the mole fraction of methane at the anode inlet in Figure 4.6a

decreases. This means the rate of the endothermic MSR reaction reduces, which increases the cooling requirements to maintain the stack temperature. Therefore, the air flow rate and hence the air stoichiometry increase with increasing RR.

As U_f increases, the cooling requirements increase, and hence the air stoichiometry increases in Figure 4.8 to maintain the stack temperature. Like with increasing RR, this is caused by the reduced contribution of the endothermic MSR reaction to the SOFC stack cooling.

The air stoichiometry for the SS system in Figure 4.8b is smaller than for the LS system in Figure 4.8a. This is because the SOFC stack in the SS system operates at lower current density, so there is less heat production from the exothermic H2X reaction than in the LS system.

As discussed in Section 2.2.3, Peters et al. [16] provided the constraint that the air stoichiometry should remain above two to avoid oxygen starvation on the cathode. When applying the limitation presented in Section 4.2.4 that RR should remain above 0.6 to ensure the S/C ratio remains above 2, the air stoichiometry also remains above 2, provided U_f is at least 0.6, as shown in Figure 4.8.

4.2.5.2 Oxygen mole fraction

Figure 4.9 shows that the oxygen mole fraction at the cathode inlet is fixed at 0.21 because fresh air is supplied to the cathode. As RR and U_f increase, the mole fraction of oxygen at the cathode outlet increases. This is caused by the increase in air stoichiometry shown in Figure 4.8, so a decreasing proportion of the oxygen in the air is consumed in the SOFC stack through the H2X reaction. When U_f is 0.6, and RR approaches 0.3, all of the oxygen on the cathode is consumed. This is also shown by the air stoichiometry of 1 in Figure 4.8. Therefore, if RR were to be reduced further, it would not be able to maintain the stack temperature and provide enough oxygen for the H2X reaction.

The cathode air is assumed to consist of only oxygen and nitrogen. The mole fraction of nitrogen is not plotted because it is considered an inert gas.

4.2.6 Electrical performance of the SOFC stack

Figure 4.10 shows the electrical performance of the SOFC stack as a function of RR and stack U_f. The OCV, cell voltage and power density for the LS and SS systems are presented in the following.

4.2.6.1 Open circuit voltage

The OCV was calculated from the Nernst equation (3.24). Figures 4.10a and 4.10b show that as RR or U_f increase, the OCV decreases. This is caused by the change in composition at the anode and cathode. As RR or U_f increase:

- The mole fraction of hydrogen on the anode decreases, as shown in Figures 4.6e and 4.6f,
- The mole fraction of water on the anode increases, as shown in Figures 4.6g and 4.6h,
- And the mole fraction of oxygen on the cathode increases, as shown in Figures 4.9a and 4.9b.

The decrease in hydrogen mole fraction and increase in water mole fraction on the anode causes the decrease in the OCV, despite the increase in the oxygen mole fraction on the cathode. This is because of the relatively high air flow rates shown in Figure 4.8, meaning the oxygen mole fraction varies less considerably. The exception for this is an U_f of 0.6, where the cooling requirements are small, and hence oxygen starvation starts to occur on the cathode. Therefore, a tail in OCV is observed for an RR less than 0.44 in Figures 4.10a and 4.10b.

The OCV for the SS system in Figure 4.10b is about 0.03 V lower than for the LS system in Figure 4.10a. This is caused by the higher operating temperature of the SOFC stack in the SS system. This reduces the Gibbs free energy of the exothermic H2X reaction, and hence the reversible cell voltage (3.23) decreases, too. The OCV of the SS system is also reduced because the mole fraction of hydrogen is lower and that of water

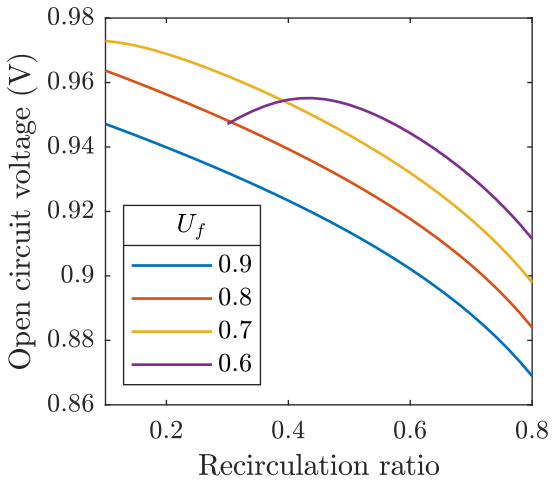

(a) OCV, LS system.

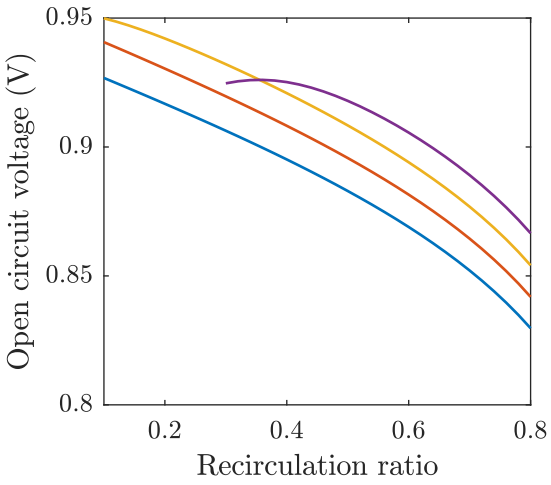

(b) OCV, SS system.

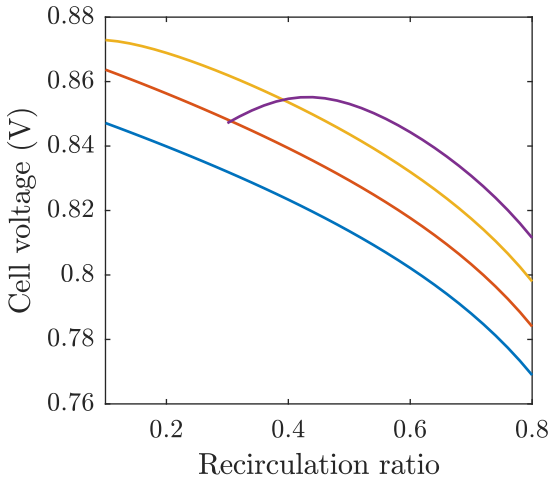

(c) Cell voltage, LS system.

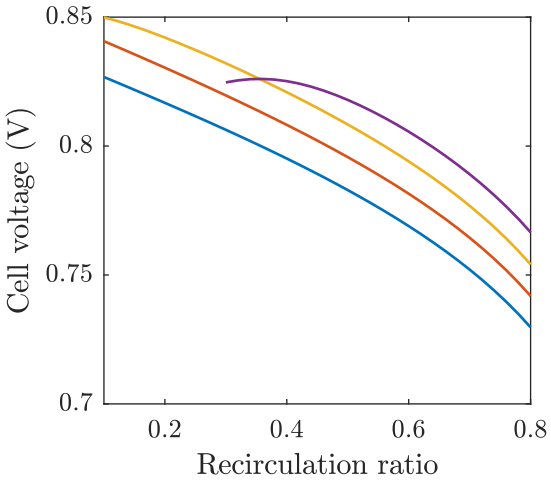

(d) Cell voltage, SS system.

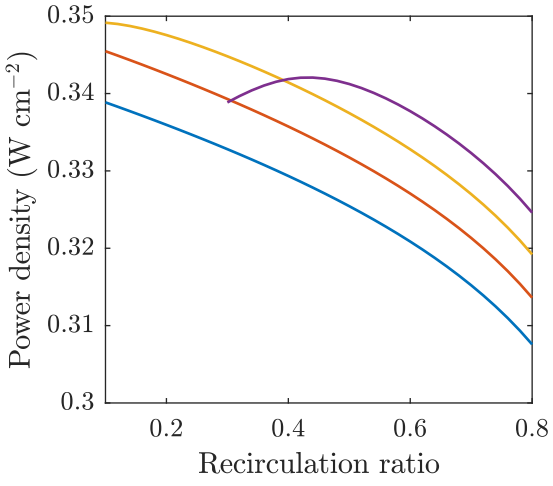

(e) Power density, LS system.

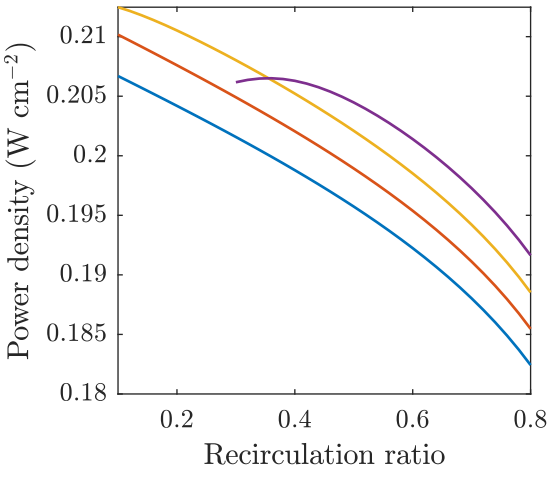

(f) Power density, SS system.

Figure 4.10: Steady-state electrical performance of SOFC stack.

is higher at the anode outlet in the SS system. Additionally, the oxygen mole fraction at the cathode outlet is lower due to the lower air stoichiometry of the SS system.

4.2.6.2 Cell voltage and power density

The cell voltage was calculated by subtracting the voltage losses from the OCV (3.27), and the power density was calculated by multiplying the cell voltage by the current density. The cell voltage in Figures 4.10c and 4.10d, and power density in Figures 4.10e and 4.10f show the same trend with varying RR and U_f as the OCV in Figures 4.10a and 4.10b. The voltage losses of the LS and SS systems are both 0.1 V, and therefore, the cell voltage is 0.1 V lower than the OCV for both systems. The power density of the SOFC stack in the SS system is lower than in the LS system, not only because of the lower cell voltage, but also because the SOFC stack in the SS system operates at lower current density.

4.2.7 System power

The parasitic power requirements of the air blower and the recirculation blower reduce the net power of the SOFC system. The large air flow rates mean that the power requirements of the air blower are usually the largest of the two. Figures 4.11a and 4.11b show that as RR and U_f increase, the total parasitic power increases, steeper than the increase in air stoichiometry in Figure 4.8. This is because the increase in pressure drop with flowrate compounds the power requirement of the blowers.

The parasitic power is subtracted from the stack power to find the net power of the SOFC system. The increasing parasitic power and decreasing power density with increasing U_f and RR, cause the net power to decrease, as shown in Figures 4.11c and 4.11d. At an U_f of 0.6, there is a maximum in the net power in Figures 4.11c and 4.11d which is caused by the low air flow rates and hence low parasitic power requirements under those conditions.

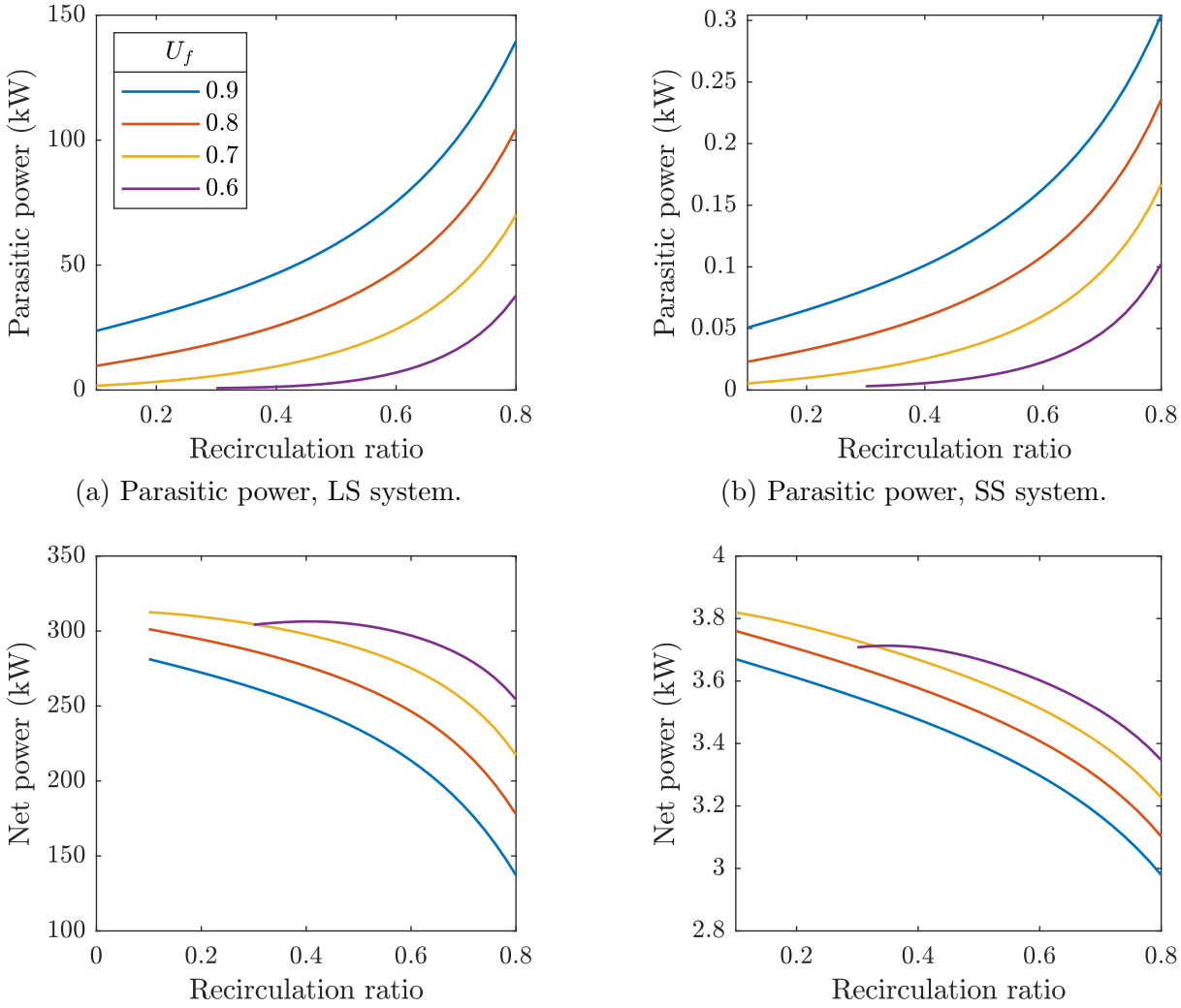

(a) Parasitic power, LS system.

(b) Parasitic power, SS system.

(c) Net power, LS system.

(d) Net power, SS system.

Figure 4.11: Steady-state performance of SOFC system.

4.2.8 System efficiency

The system efficiency is calculated taking into account the losses of the inverter. Figure 4.12 plots the system efficiency at varying RR and U_f, both for the results of this model and the results presented by Peters et al. [16].

Increasing RR and U_f reduced fuel consumption in Figure 4.5, while it reduced the net power in Figures 4.11c and 4.11d. To achieve high efficiency, there is therefore a balance between the power and the fuel consumption.

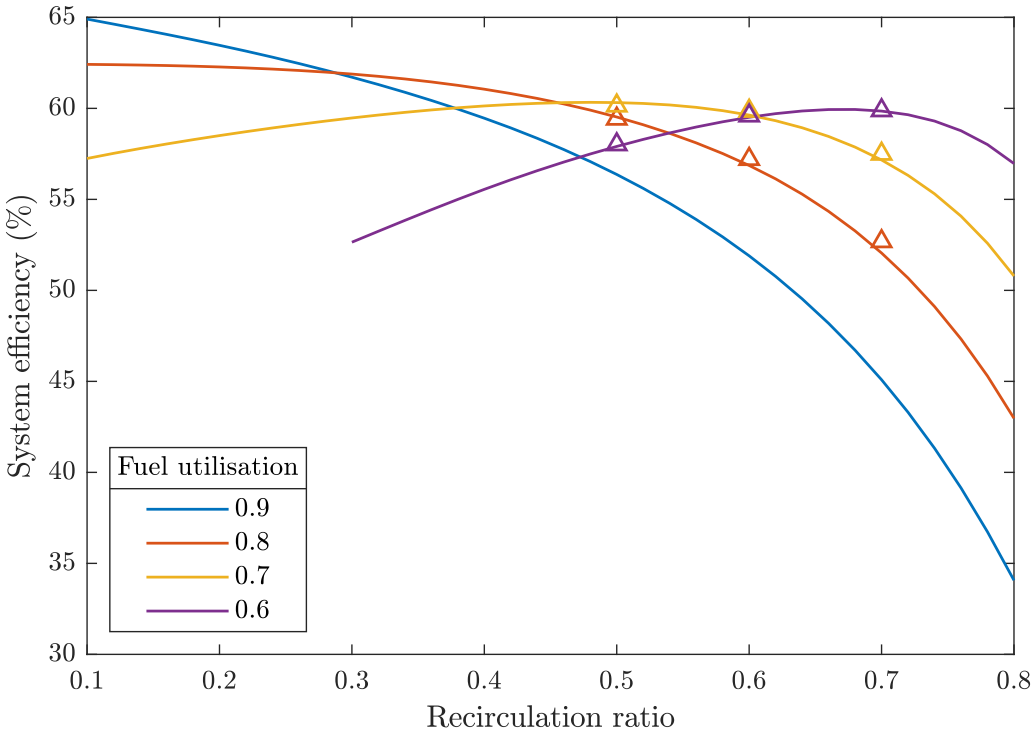

(a) Large-scale system.

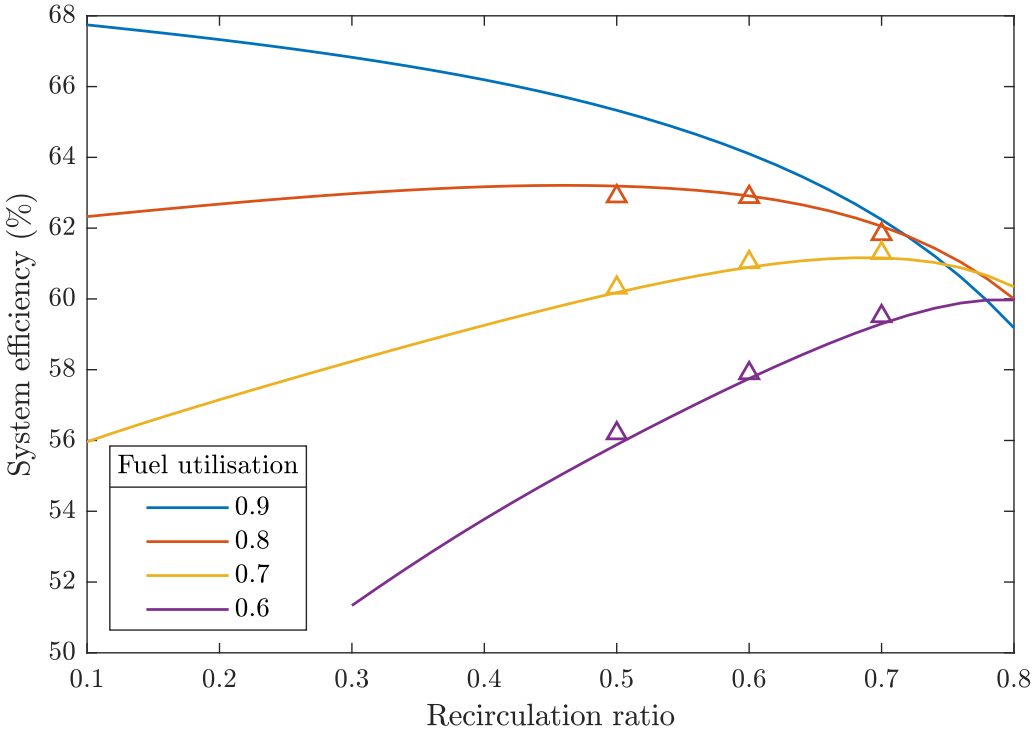

(b) Small-scale system.

Figure 4.12: Verification of system efficiency for SOFC system. Data points from Peters et al. [16].

4.2.8.1 LS system

Figure 4.12a shows this balance indeed to be the case for the LS system. For low values of U_f, there exists a maxima in efficiency with varying RR:

- For a U_f of 0.60, a maximum efficiency of 0.60 was achieved with an RR of 0.68, and
- For a U_f of 0.70, a maximum efficiency of 0.60 was achieved with an RR of 0.48.

As RR decreases from the maximum, the increase in fuel consumption causes the efficiency to decrease. For higher values of U_f, the net power decreases faster with increasing RR than the fuel consumption decreases. Therefore, for an U_f of 0.8 and 0.9, the efficiency decreases with increasing RR.

Approaching the other way round, at low RR, increasing U_f increases the efficiency due to the reduced fuel consumption, while at high RR, increasing U_f decreases the efficiency due to the reduced power.

4.2.8.2 SS system

Figure 4.12b shows the variation in efficiency with RR and U_f for the SS system. For an RR less than 0.6, the efficiency increases with U_f because of the reduced fuel consumption. The reduced power begins to have a significant effect once RR increases to 0.7 and once it reaches 0.8 the efficiency has started to decrease with increasing U_f.

From the other perspective, the efficiency tends to increase with increasing RR due to reducing fuel consumption, except at high U_f or RR where the power reduces faster, and hence the efficiency reduces.

4.2.8.3 Comparing the SS and LS systems

In summary, Figure 4.12 shows a complicated interplay between RR and U_f, and their effect on efficiency via the fuel consumption and power. In particular, the variation in

power with RR and U_f is dependent not only on the SOFC stack performance but also on the air blower performance.

The SS results in Figure 4.12b show a different trend to the LS system results in Figure 4.12a. Under most conditions, the SS system results appear to be shifted to the right compared to the LS results, such that the maximum efficiency at each value of U_f is achieved at higher RR. The efficiency is also higher for the SS system than the LS system. This is due to a lower current density, meaning lower fuel consumption, and also lower pressure drop in the SS system, meaning lower parasitic losses relative to the stack power.

It is the high parasitic losses at high RR in the LS system that produce the maximum in system efficiency at fixed U_f, where the effects of power and fuel consumption on efficiency balance out.

4.2.8.4 Comparing to Peters et al.

The model outlined in this chapter shows excellent agreement with the modelling results from Peters et al. [16] for the SS and LS systems in Figure 4.12. This was achieved by adjusting the Nernst composition weighting factor w_x. Its value is listed in Table 4.2. That there is a good fit for data points with a fixed value of the weighting factor indicates that the underlying modelling methodology is consistent with the literature. However, the different values of the Nernst composition weighting factor for the SS system (0.25) and the LS system (0.17) can't be explained through the 0D modelling approach used within this thesis. One possible improvement would be to use a 1D modelling approach for the SOFC stack, as outlined in Section 2.1.1.2. For the dynamic modelling work presented in the following chapters, an average value of the Nernst composition weighting factor of $w_x = 0.21$ is taken with the 0D modelling approach presented in Chapter 3.

4.3 Conclusions

This chapter presented the steady-state validation of the SOFC stack in Section 4.1, and the SOFC system model in Section 4.2. Section 4.1 showed good agreement of the SOFC stack model with iV characteristics produced experimentally in the literature, with an estimated uncertainty of 0.02 V. Section 4.2 showed very good agreement of the SOFC system model with another model presented in the literature [16].

Figures 4.10e and 4.10f showed that the power density of the SOFC stack is increased by operating at low RR and U_f. However, Figures 4.7 and 4.8 showed that an RR above 0.6 and an U_f above 0.6 are required to prevent carbon deposition on the SOFC anode and oxygen starvation on the cathode of the SOFC stack. Figure 4.12 showed that the electrical efficiency of the SOFC system depends greatly on the assumptions of the component models, with the LS and SS systems showing considerably different variation in the efficiency with RR and U_f. The operating constraints for the HEXs, reformer and burner presented by Peters et al. [16] and reviewed in Section 2.2.3, were not included within this chapter. These additional constraints are included in the dynamic modelling results presented in the next Chapter 5. The main purpose of this chapter was to validate the SOFC system model in steady state operation.

Whilst the steady-state analysis in Chapter 4 used similar modelling assumptions and approach as the modelling work of Peters et al. [16], there remain some important differences. Their model was stationary, meaning it was only suitable for simulating stationary operating conditions at a fixed operating point, whereas the model presented in Chapter 3 is dynamic. Peters et al.'s model did not account for the variation in ASR with temperature, and did not include a HEX model. The inclusion of these aspects in the model presented in Chapter 3 means that the performance of the SOFC system can be investigated both in part load operation, and with varying operating conditions, both of which were validated in the Section 4.1 for this model. The dynamic model will be be used within this thesis for investigating the transient response of an SOFC system. In Chapter 6, the dynamic model is applied to an heavy goods vehicle powertrain, and

includes heat losses, especially important for simulating thermal cycling in Chapter 7.

Chapter 5

Transient response

This chapter investigates the transient response of the solid oxide fuel cell (SOFC) system model. The behaviour of the SOFC system under dynamic load is an important aspect of this thesis, because vehicle power requirements can be highly dynamic. This chapter builds upon the steady-state validation presented in Chapter 4, and is the basis for applying dynamic load profiles to the SOFC system model in Chapters 6 and 7.

Since all of the SOFC system components are modelled in 0D, the behaviour of the SOFC system model is independent of size. This is a reasonable assumption for an initial investigation, since the model can be more generalised, and detailed knowledge of the system is not required. The values used for the nominal operating conditions and relevant design parameters are taken from Tables 3.1 to 3.3. These values define the initial conditions of the dynamic modelling.

The dynamic model of the SOFC system consists of four inputs or manipulated variables: the stack current, and the fuel, air, and anode off-gas recirculation (AOGR) flow rates. The desired operating conditions can be achieved by the manipulation of the values of these four inputs. Firstly, this chapter investigates the open loop response of the SOFC system. The open loop response is the system response to an increase in a single input, with the other three inputs held constant. The open loop response of the SOFC system is investigated under four different scenarios:

1. A 10 % increase in current from 100 A to 110 A in Section 5.2,
2. A 10 % increase in fuel flow rate from 15.1 g s^{-1} to 16.6 g s^{-1} in Section 5.3,
3. A 10 % increase in air flow rate from 738 g s^{-1} to 812 g s^{-1} in Section 5.4,
4. A 10 % increase in AOGR flow rate from 1.7 g s^{-1} to 1.78 g s^{-1} in Section 5.5.

An instantaneous 10 % increase in each parameter is considered sufficiently large to show the dynamic response of the system, without pushing the operating conditions far outside the operating constraints. The initial conditions of the open loop response represent 50 % part load, so the SOFC system remains well within its operating range during the open loop response. It also represents a realistic step change in conditions during dynamic operation of a vehicle, and will be investigated further in Chapter 6.

An open loop response to 50 % changes in inputs would lead to unrealistically large changes in operating conditions, that would push the operating conditions far outside the safe operating window without process control. A 10 % decrease in each input is not investigated to avoid repetition, but the likely effects are discussed in the results, where relevant. Section 2.3 showed that the existing literature investigating the dynamic response of SOFC systems is very sparse, and therefore it was not possible to easily verify the dynamic performance of the SOFC system model. Therefore, the open loop response is discussed in a detailed manner in the following, as a method of validating the dynamic model.

After the open loop response, the closed loop or controlled response is presented. The controlled response is the system response to an increase in load with control of the other inputs to ensure the operating conditions of the SOFC system remain within their desired window. The controlled response of the SOFC system model to a 10 % increase in current is investigated in Section 5.7. The controllers defined in Section 3.14 are used to maintain the fuel utilisation (U_f), the steam-to-carbon ratio (S/C ratio), and the SOFC stack temperature. This same approach will be used to maintain the operating parameters when subjected to different load profiles in Chapters 6 and 7.

5.1 Investigating the open loop response

The same workflow is used to investigate the open loop response for each scenario in Sections 5.2 to 5.4, and is as follows:

1. The performance of the SOFC under nominal conditions at the nominal current is defined based on the specification in Tables 3.1 to 3.3,

2. Steady-state simulation of the SOFC system under nominal conditions and nominal current is conducted in Engineering Equation Solver (EES) to calculate the effectiveness of the two heat exchangers,

3. The initial current is defined to be 50 % of the nominal current. The steady-state system model is run again in EES at the initial current and the calculated effectiveness of the heat exchangers. The temperature and composition within each gas compartment are calculated, and these form the initial conditions of the dynamic model. The required flow rates of fuel, AOGR and air as inputs to the dynamic model are also calculated,

4. The dynamic simulation is conducted in Simscape with the initial conditions and inputs gathered from the second EES model. For the open loop response, a 10 % step increase in either the current or one of the flow rates is defined. The variation in composition in each of the gas compartments, the temperature in each of the components, and the electrical performance of the SOFC stack are logged. The resultant data sets are plotted against time, to form the figures displayed in this chapter, and

5. Based on the results, the dynamic performance of the SOFC system is investigated through the electrical, chemical reaction, and thermal responses to the increase in current, or flow rate:

    - The electrical response is the dynamic variation in voltage associated with a change in current, as per the current density-voltage characteristics,

- The chemical reaction response is dynamic variation in reaction rates associated with a change of operating conditions, and
- The thermal response is the dynamic variation in heat production or consumption.

The electrical response is assumed instantaneous. The chemical reaction response initiates changes in gas composition, the rate of which depends upon the volume of the gases participating. The thermal responses initiate changes in component temperatures, the rate of which depends upon the thermal masses of the components. The various transients occur over different timescales, but their behaviours are, however, highly interdependent, so each parameter is considered over the full dynamic response. Section 2.2 of the literature review showed that the voltage and power determine the electrical performance of the SOFC system, whilst the chemical reaction and thermal parameters have windows for safe operation.

The change in each output was calculated in absolute and percentage terms, as well as determining the relaxation time. The relaxation time τ was introduced by Achenbach [92] and is defined based on the variation in the cell voltage V, such that:

$$V\left(t=\tau\right)=V_{\text{initial}}+0.9\left(V_{\text{final}}-V_{\text{initial}}\right) \tag{5.1}$$

5.2 Open loop response to current increase

This section investigates the open loop response to a 10 % step increase in current from 100 A to 110 A. The flow rates of fuel, air and AOGR are held constant at $15.1\,\mathrm{g\,s^{-1}}$, $738\,\mathrm{g\,s^{-1}}$, and $1.7\,\mathrm{g\,s^{-1}}$, respectively..

Figure 5.1 shows the transient response during the first 25 seconds. Figure 5.2 shows the transient response over the first 250 minutes. The step increase in current is shown in Figure 5.1a.

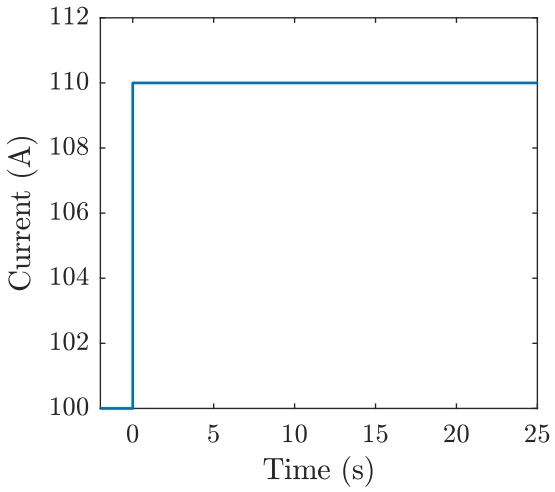

(a) Current.

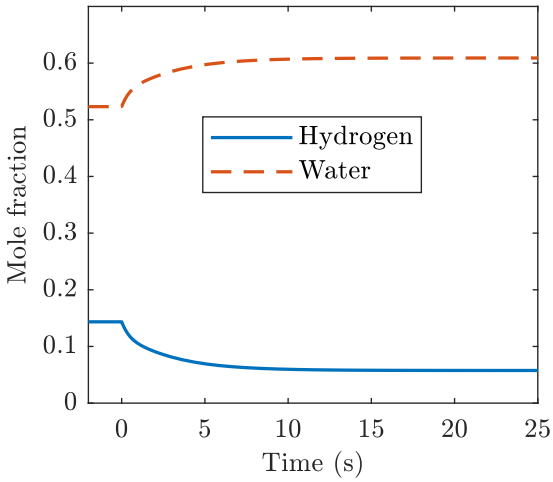

(b) Mole fraction, anode.

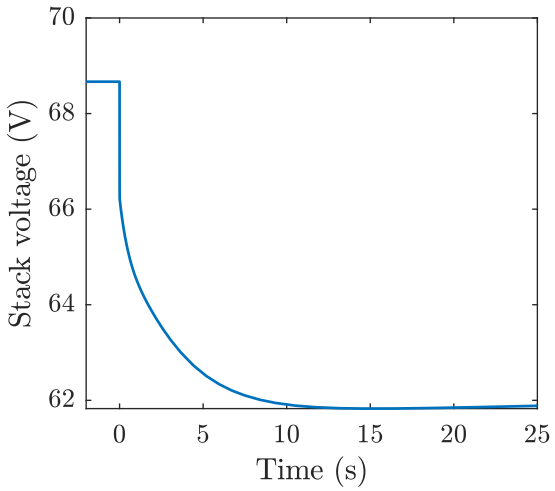

(c) Stack voltage.

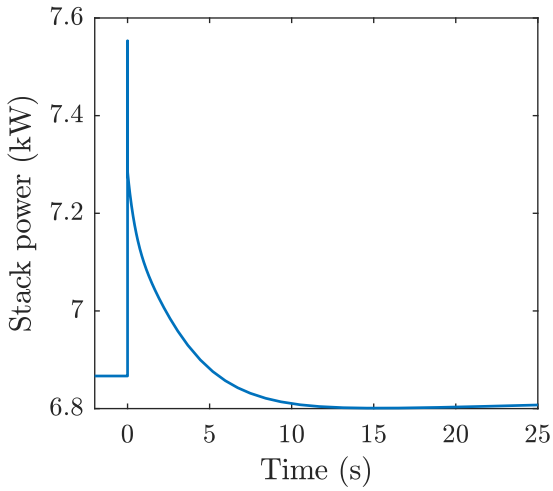

(d) Stack power.

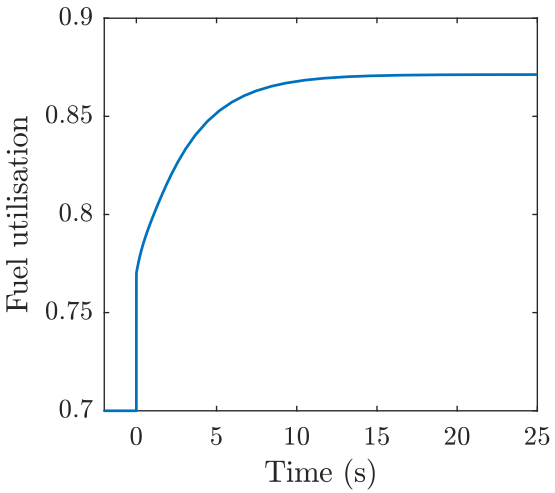

(e) Fuel utilisation, stack.

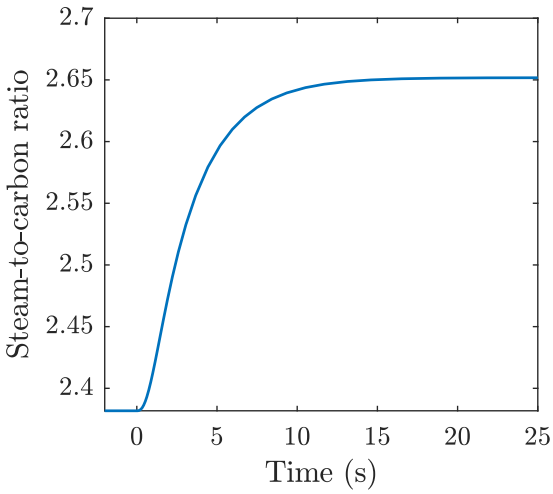

(f) S/C ratio, anode inlet.

Figure 5.1: Open loop response to a 10 % step increase in current over the first 25 seconds.

5.2.1 Instantaneous response

The approach used to model the reaction site of the SOFC stack is defined in Section 3.6.1, in which the electrical and chemical reaction dynamics are assumed to be instantaneous. Therefore, an instantaneous response is observed in stack voltage, power, and U_f in Figures 5.1c to 5.1e, respectively.

The increase in current caused an instantaneous increase in the voltage losses, as per Equation (3.27). Therefore, the stack voltage in Figure 5.1c decreased instantaneously from 68.7 V—by 2.4 V or 3.5 %—to 66.2 V. The power in Figure 5.1d spiked immediately from 6.87 kW to 7.55 kW. Since the decrease in voltage occurred one time step after the increase in current, this spike is neglected as an artefact of the Simscape solving method. In the subsequent time step, the voltage reduced and power reached 7.28 kW, representing a more realistic power spike of 0.41 kW or 6.0 %. The power spike is a balance between the instantaneous increase in current and instantaneous decrease in voltage (3.30).

According to Faraday's law in Equation (3.22) the increase in current causes an instantaneous increase in the rate of the electrochemical oxidation of hydrogen (H2X) reaction in the SOFC stack. Therefore, U_f increased instantaneously from 0.70—by 0.07 or 10 %—to 0.77 in Figure 5.1e. This follows from the definition of U_f in Equation (3.41).

The increase in the rate of the H2X reaction caused an instantaneous decrease in air stoichiometry (λ) from 5.98—by 0.54 or 9.1 %—to 5.44. This follows from the definition of λ in Equation (3.44). Nevertheless, λ remains well above its minimum allowable value of 2 specified in Table 3.1.

No instantaneous changes in composition or temperature were observed, due to the inertia of the chemical reaction and thermal transients.

5.2.2 Response during the first 25 seconds

The chemical reaction transients of all gases participating in each reaction depend on the residence time of the gases within each component. Their residence time is determined by their flow rate through and the gas volume inside each component, as per the dynamic

mass balance in Equation (3.10). The plots in Figure 5.1 show that the relaxation time of the material dynamics was around six seconds. This value took into account the time for gas flows between the stack and anode heat exchanger (AHEX) to equilibriate via the AOGR. The relaxation time is of a similar order of magnitude as that presented by Mueller et al. [47], and reviewed in Section 2.3.

The chemical reaction transients are best illustrated by observing the dynamic response at the anode during the first 25 seconds in Figure 5.1b. The increase in the H2X reaction rate (1.3) led to an instantaneous increase in the rate of consumption of hydrogen and production of water at the anode. Therefore, the mole fraction of hydrogen at the anode decreased from 0.17—by 0.10 or 60 %—to 0.07, and the mole fraction of water at the anode increased from 0.50—by 0.10 or 20 %—to 0.60.

5.2.2.1 Electrical transients

The change in composition in the stack caused the open circuit voltage (OCV) to decrease according to the Nernst equation (3.24), and hence the stack voltage in Figure 5.1c decreased further from 66.2 V—by 4.4 V or 6.6 %—to a minimum of 61.8 V. As a result, the stack power in Figure 5.1d decreased from its peak of 7.28 kW—by 0.48 kW or 6.6 %—to 6.80 kW.

The time taken for gas composition to change due to the volume of gases participating in the reaction relative to the instantaneous increase in voltage losses resulted in a 6.0 % power spike. However, the volume of the gases and their transport behaviour is an uncertainty in this model, and the same behaviour may not be observed in a real system.

5.2.2.2 Chemical reaction transients

AOGR means the change in anode composition affected the stack U_f. The decrease in hydrogen mole fraction at the anode reduced the hydrogen flow rate at the anode outlet, and hence also in the AOGR and at the anode inlet. Therefore, less fuel was available and the initial increase in U_f in Figure 5.1e was followed by a further increase from 0.77—by

0.10 or 13 %—to a new-steady state value of 0.87. This shows that AOGR contributed significantly to the change in U_f, and could lead to the stack moving outside its safe operating window in Table 3.1. This may lead to fuel starvation and cause damage to the stack. Therefore, control of U_f is likely required during an increase in load, such as during start-up. Methods to control U_f will be investigated in Section 5.7.

By the same argument, the increase in water mole fraction at the anode increased the water flow rate and hence the S/C ratio at the anode inlet. No methane was recirculated since the methane steam reforming (MSR) reaction (1.4) in the stack was assumed to go to completion, as per Section 3.6.1.1. Therefore, the S/C ratio at the anode inlet in Figure 5.1f increased from 2.38—by 0.27 or 11 %—to a new steady-state value of 2.65 during the first 25 seconds. An increase in the S/C ratio is of no concern but a step down in load could lead to a decrease in the S/C ratio below its minimum allowable value in Table 3.1 and potentially cause carbon deposition. Therefore, control of the S/C ratio during decreases in load, such as shut-down, is required. Methods to control the S/C ratio will be discussed in Section 5.7 too.

5.2.3 Response during the first 6 minutes

Figure 5.2 shows the open loop response to the step increase in current over the first 250 minutes. Over this time scale the slow thermal transients of the SOFC system dominate, which depend on thermal mass of each component in the SOFC system.

As discussed in Section 5.2.1, the increase in current increases the H2X reaction rate. The reaction is exothermic and leads to an increase in stack temperature, according to the component energy balance (3.17). Figure 5.2a shows the stack temperature increased from 957 K—by 11 K or 1.2 %—to 968 K during the first six minutes.

Figure 5.2b shows the time derivative of the stack temperature ($\mathrm{d}T_S/\mathrm{d}t$) from Figure 5.2a. The $\mathrm{d}T_S/\mathrm{d}t$ increased quickly over 12 seconds from zero to a maximum of $2.9\,\mathrm{K\,min^{-1}}$, and subsequently decreased slowly back to zero over the remainder of the thermal response. The $\mathrm{d}T_S/\mathrm{d}t$ was larger than the maximum allowable $\mathrm{d}T_S/\mathrm{d}t$ in Ta-

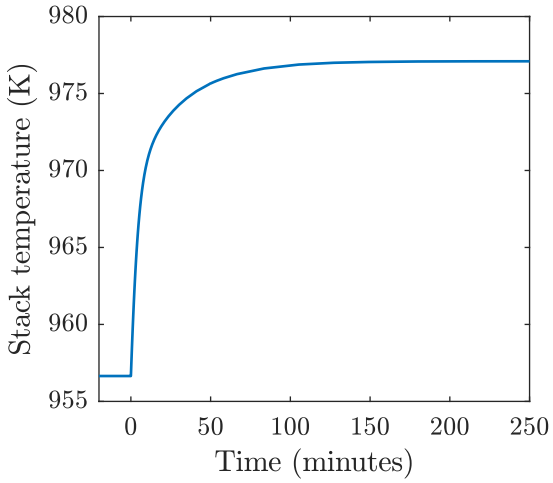

(a) Stack temperature.

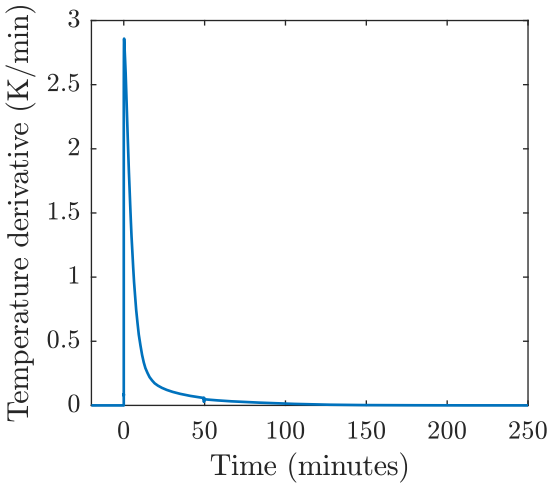

(b) $\mathrm{d}T_S/\mathrm{d}t$.

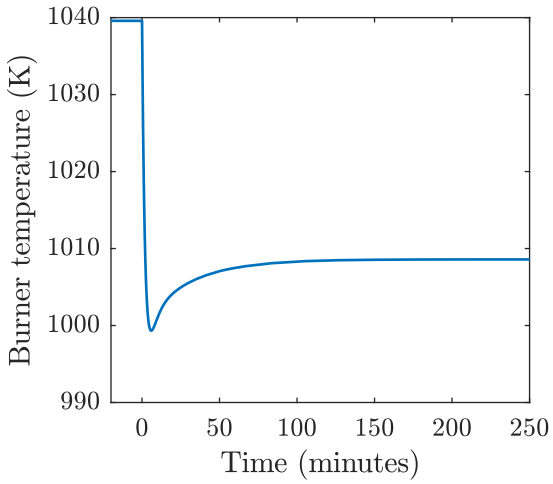

(c) Burner temperature.

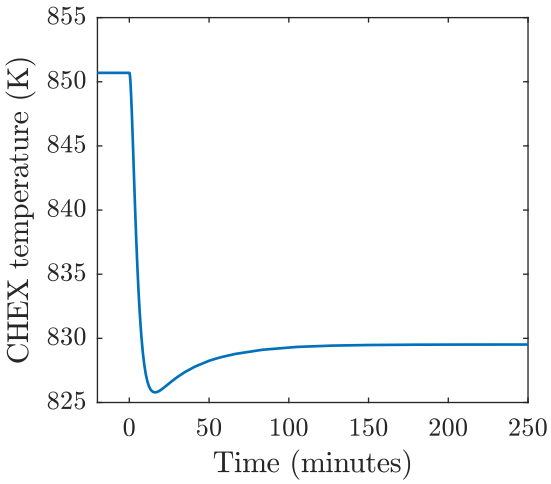

(d) CHEX temperature.

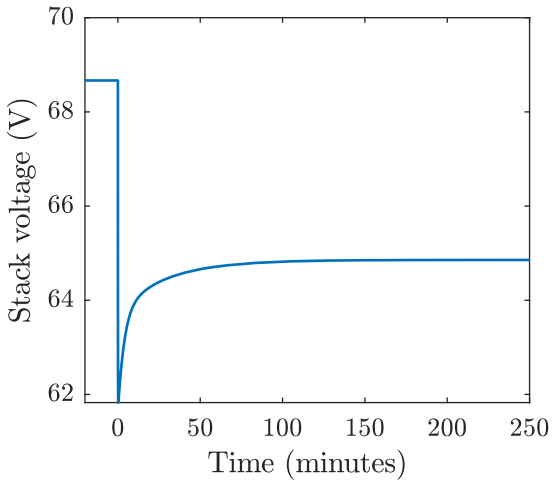

(e) Stack voltage.

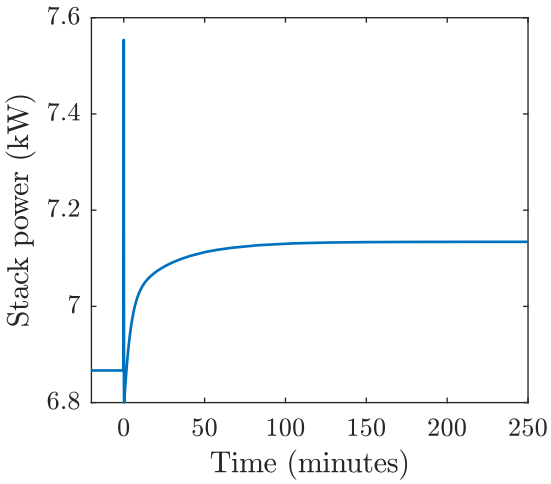

(f) Stack power.

Figure 5.2: Open loop response to a 10 % step increase in current over the first 250 minutes.

ble 3.1, suggesting that control is required to limit those changes.

The increase in U_f in Figure 5.1e caused the hydrogen flow rate entering the burner to decrease, and hence the hydrogen combustion reaction (2.3) rate to decrease. The combustion reaction is exothermic and therefore the burner temperature decreased initially. Figure 5.2c shows that the burner temperature decreased from 1040 K—by 40 K or 4 %—to a minimum of 999 K during the first six minutes. Since the mass of the burner is approximately 10 % of the mass of the stack, the burner's thermal dynamics are approximately ten times faster than the stack. The decrease in the burner temperature reduced the heat flow rate to the cathode heat exchanger (CHEX), and therefore the CHEX temperature in Figure 5.2d decreased during the first six minutes from 851 K—by 17 K or 2 %—to 834 K. The increasing stack temperature caused the burner inlet gases to increase in temperature, and therefore after six minutes the burner temperature in Figure 5.2c reached a minimum. The thermal transients of the SOFC system components following this minimum will be discussed in the following.

5.2.4 Response during the first 250 minutes

After the first six minutes, the stack temperature in Figure 5.2a continued to increase to a new steady-state value of 977 K. There was an overall 20 K or 2 % increase in stack temperature. The relaxation time of the stack temperature in Figure 5.2a was 35 min, showing that the thermal dynamics are indeed orders of magnitude slower than the chemical reaction dynamics.

The slow increase in stack temperature increased the heat flow rate from the stack to the burner, so after six minutes the burner temperature began to increase. The burner thermal dynamics followed the slower stack thermal dynamics, with the burner temperature in Figure 5.2c increasing from the minimum of 999 K—by 9 K or 1 %—to 1009 K. Therefore, the burner temperature remained well below its maximum allowable temperature of 1273 K in Table 3.1. Both high stack U_f and high recirculation ratio (RR) dilute fuel to the burner and therefore favour moderate burner temperatures without the need

for additional air supply to the burner. Moderate burner temperatures reduce thermal degradation of high temperature balance of plant (BoP) components such as the CHEX.

The CHEX temperature in Figure 5.2d lagged the burner temperature, and decreased in the first sixteen minutes from 851 K—by 25 K or 3 %—to a minimum of 826 K. The CHEX temperature increased from the minimum—by 4 K or 0.5 %—to a new steady-state value of 830 K, where it followed the thermal response of the stack, since the stack thermal response was slowest. The thermal response of the AHEX was similar to the CHEX but not plotted here, since the fuel flow rate was much smaller than the air flow rate, and therefore had limited impact on the thermal dynamics of the overall system.

During the 250 minutes, the CHEX temperature in Figure 5.2d decreased by 21 K or 2 %. This decreased the heat flow rate to the stack, and partially offset the increased heat generation in the stack. Therefore, the drop in burner temperature in Figure 5.2c caused by the high U_f, limited the increase in stack temperature in Figure 5.2a. This suggests that operating at constant mass flow rate of fuel is likely to cause less extreme thermal gradients in the stack, and cause less demand on the air blower.

During the first fourteen minutes, the temperature difference between the hot cathode air and the stack increased from 106 K—by 42 K or 39 %—to 148 K. This is well above the maximum allowable temperature difference from Table 3.1, and could lead to large thermal gradients in the stack, which reduce its lifetime. Therefore, while high stack U_f and high RR reduce the burner temperature and improve lifetime in the BoP components, they are also likely to reduce the lifetime of the stack. One way to reduce the stack temperature difference is to use a larger heat exchanger for the CHEX, however this would reduce the compactness of the system and increase the pressure drop that the cathode air blower must overcome. It would also reduce the heat available for the AHEX.

5.2.4.1 Electrical transients

The stack temperature response in Figure 5.2a leads to an electrical response, shown by the stack voltage response in Figure 5.2e and stack power response in Figure 5.2f. An

Table 5.1: Summary of results for 10 % step increase in current from 100 A to 110 A, split between the instantaneous response, the response over 25 seconds, the response over 250 minutes, and the response over 250 minutes.

Parameter	Initial	Instantaneous	Over 25 s	Over 250 min	Final
I	100 A				110 A
$y_{H_2,\text{anode}}$	0.167	± 0	-0.101	≈ 0	0.066
V_{stack}	68.7 V	-2.4 V	-4.4 V	$+3.0$ V	64.9 V
P_{stack}	6.87 kW	$+0.41$ kW	-0.48 kW	$+0.33$ kW	7.13 kW
U_f	0.70	$+0.07$	$+0.10$	≈ 0	0.87
S/C ratio	2.38	± 0	$+0.27$	≈ 0	2.65
λ	5.98	-0.54	± 0	± 0	5.44
T_{stack}	957 K	± 0 K	± 0 K	$+20$ K	977 K
T_{burner}	1040 K	± 0 K	± 0 K	-31 K	1009 K
T_{chex}	851 K	± 0 K	± 0 K	-21 K	830 K
$T_{\text{stack}} - T_{\text{chex}}$	106 K	± 0 K	± 0 K	$+42$ K	148 K

initial drop in stack voltage to 61.8 V was observed in Figure 5.1c due to the increase in voltage losses and the decrease in OCV. This is shown by the undershoot of the voltage in Figure 5.2e, and the minimum of 6.80 kW in the stack power in Figure 5.2f. The subsequent increase in stack temperature reduced the area specific resistance (ASR) of the stack (3.26), and hence the voltage losses decreased.

Therefore, the stack voltage in Figure 5.2e recovered partially from a minimum of 61.8 V to a final new steady-state value of 64.9 V, an increase of 3.0 V or 5 %. As the stack voltage increased, the stack power in Figure 5.2f increased likewise, from a minimum of 6.80 kW—by 0.33 kW or 5 %—to 7.13 kW.

5.2.5 Summarising the results

Table 5.1 summarises the results for a 10 % step increase in current, in terms of the initial value, the dynamic response and the final value, as well as the relaxation time, τ. The

dynamic response is split into the three main response times: the instantaneous response, the response during the first 25 seconds, and the response during the first 250 minutes. Note that the minima for T_{burner} and T_{chex} are not captured in Table 5.1, only the net changes.

Table 5.1 shows that the electrical, chemical reaction and thermal responses all affect the electrical performance of the stack. While the final value for the stack voltage was within the operating window of Table 3.1, the minimum value after the first 25 seconds, fell below the minimum allowable value, and may reduce the lifetime of the stack. The thermal dynamics affected the water gas shift (WGS) reaction rate, and hence the composition, however those changes were so small they were negligible. The U_f increased above its maximum allowable value in response to the step increase in current, while the S/C ratio increased away from its minimum allowable value. The stack temperature increased but remained below its maximum allowable temperature, and the burner temperature reduced away from its maximum allowable temperature. However the temperature difference between the stack and the cathode air increased above its maximum allowable value, thereby leading to large thermal temperature gradients in the stack, potentially reducing stack lifetime.

5.3 Open loop response to fuel flow rate increase

The open loop response to a 10 % step increase in the fuel flow rate from $15.1\,\mathrm{g\,s^{-1}}$ to $16.6\,\mathrm{g\,s^{-1}}$ at the system inlet shown in Figure 5.3a is investigated in the following. The current and flow rates of air and AOGR are held constant at 100 A, $738\,\mathrm{g\,s^{-1}}$, and $1.7\,\mathrm{g\,s^{-1}}$, respectively.

5.3.1 Response during the first 25 seconds

The chemical reaction transients shown in Figure 5.3 have a relaxation time of six seconds, which reflects the residence time of the fuel in the fuel supply, AHEX and stack, including

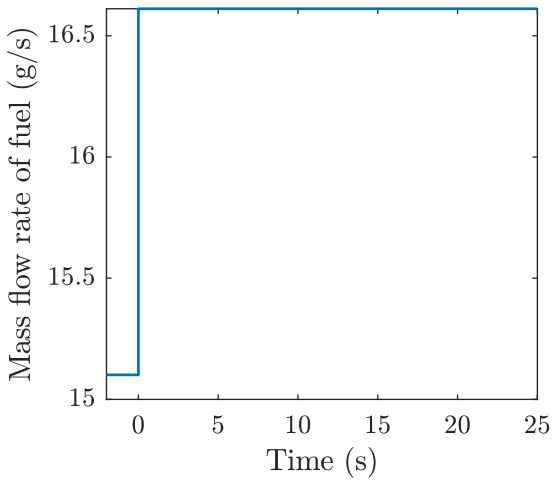

(a) Fuel flow rate.

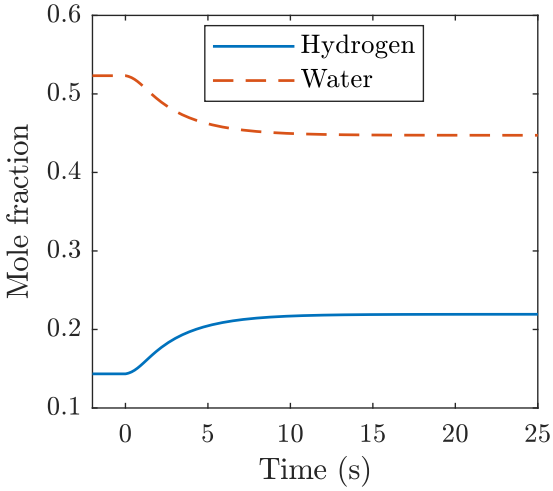

(b) Mole fraction, anode.

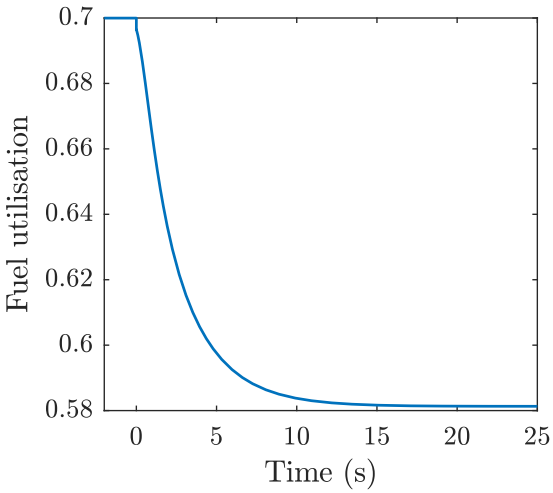

(c) Fuel utilisation, stack.

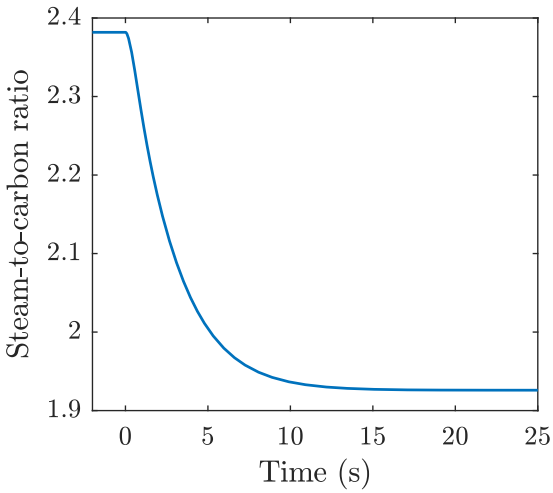

(d) S/C ratio, anode inlet.

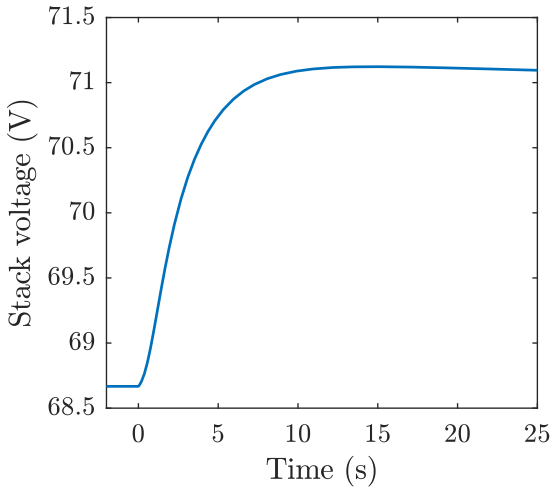

(e) Stack voltage.

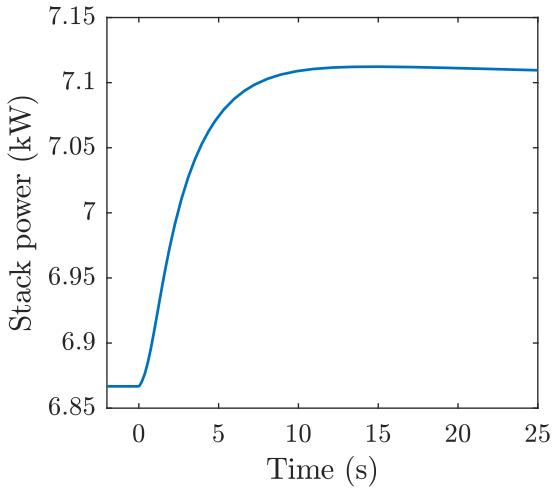

(f) Stack power.

Figure 5.3: Open loop response to a 10 % step increase in fuel flow rate over the first 25 seconds.

the AOGR. The relaxation time was the same as for the increase in current in Section 5.2.

The chemical reaction transients are best illustrated through the change in composition at the anode in Figure 5.3b. The increase in the fuel flow rate increased the MSR reaction (1.4) rate since it went to completion. Therefore, the hydrogen mole fraction at the anode increased from 0.17—by 0.08 or 51 %—to 0.25, and the water mole fraction at the anode decreased from 0.50—by 0.08 or 17 %—to 0.42, as shown in Figure 5.3b.

The increase in the fuel flow rate decreased the stack U_f (3.41) in Figure 5.3c from 0.70—by 0.12 or 17 %—to 0.58, and the S/C ratio at the anode inlet (3.43) in Figure 5.3d from 2.38—by 0.45 or 19 %—to 1.94. The U_f decreased further from its maximum allowable value in Table 3.1. However, the S/C ratio decreased below its minimum allowable value which increased the risk of carbon deposition in the stack.

AOGR increased the magnitude of the changes in anode composition in response to the increase in fuel flow rate. AOGR fed back the increase in hydrogen flow rate and decrease in water flow rate to the anode inlet via the AHEX. Therefore, changes in composition, U_f, S/C ratio, stack voltage and stack power were all accentuated by the presence of AOGR.

5.3.1.1 Electrical transients

The increase in hydrogen mole fraction and decrease in water mole fraction at the anode in Figure 5.3b led to an increase in the OCV according to the Nernst equation (3.24). Therefore, the stack voltage (3.27) increased in Figure 5.3e from 68.7 V—by 2.34 V or 3.4 %—to 71.0 V, and the stack power (3.30) in Figure 5.3f increased from 6.87 kW—by 0.23 kW or 3.4 %—to 7.10 kW. The power response matched the voltage response exactly due to the fixed current value.

During the first 25 seconds, the stack voltage decreased by 10 % in response to a 10 % increase in current, and increased by 3.4 % in response to a 10 % increase in fuel flow rate. This indicates that increasing the fuel flow rate can reduce the temporary drop in stack voltage during increases in current, and help to maintain the stack voltage within the

operating window in Table 3.1. Increasing the current and fuel flow rate both increased the stack power, thereby increasing the power density of the SOFC stack.

5.3.2 Response during the first 5 minutes

The dynamic response during the first 250 minutes in response to a step change in fuel flow rate is shown in Figure 5.4. The stack temperature in Figure 5.4a decreases to a minimum after five minutes and subsequently increases, therefore the thermal response for the first five minutes is discussed first. As outlined in Section 5.3.1, the increase in fuel flow rate increased the rate of the MSR reaction at the anode. The MSR reaction is endothermic, and as a result, the stack temperature in Figure 5.4a decreased from 957 K—by 3 K or 0.3 %—to a minimum of 953 K over the first five minutes.

Figure 5.4d shows the $\mathrm{d}T_S/\mathrm{d}t$ decreased quickly over 9 seconds from zero to a minimum of $1.3\,\mathrm{K\,min^{-1}}$, and subsequently increased to a smaller maximum of $0.51\,\mathrm{K\,min^{-1}}$ after 14 minutes, before returning to zero over the remainder of the thermal response. The $\mathrm{d}T_S/\mathrm{d}t$ was below the maximum allowable value of $2\,\mathrm{K\,min^{-1}}$ in Table 3.1.

The increase in hydrogen mole fraction at the anode in Figure 5.3b led to an increase in the hydrogen flow rate to the burner. This increased the exothermic hydrogen combustion reaction (2.3) rate and hence the the burner temperature in Figure 5.4b increased from 1040 K—by 52 K or 5.0 %—to 1091 K during the first five minutes.

The 52 K increase in burner temperature was much larger in magnitude than the 3 K decrease in stack temperature over the first five minutes because the heat capacity of the burner is around ten times smaller than the stack in Table 3.3. Additionally, the 10 % increase in methane flow rate to the stack resulted in a 64 % increase in the hydrogen flow rate to the burner, so there was a lot more hydrogen to be combusted, and therefore a far greater heat accumulation.

The CHEX temperature lagged the burner temperature, and therefore increased in Figure 5.4c from 851 K—by 19 K or 2.3 %–to 870 K over the first five minutes. As per Section 5.2.3 the thermal dynamics of the AHEX have little impact on the overall system.

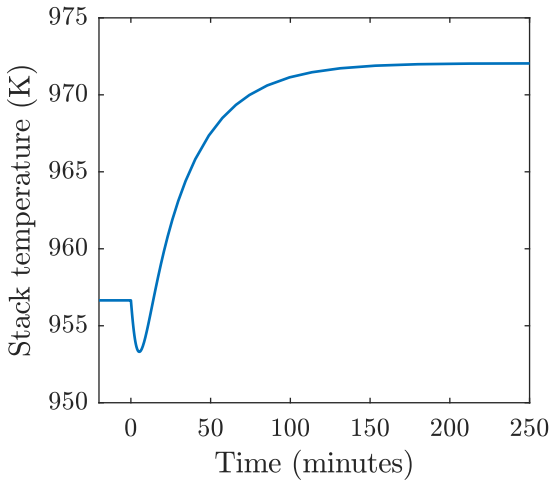

(a) Stack temperature.

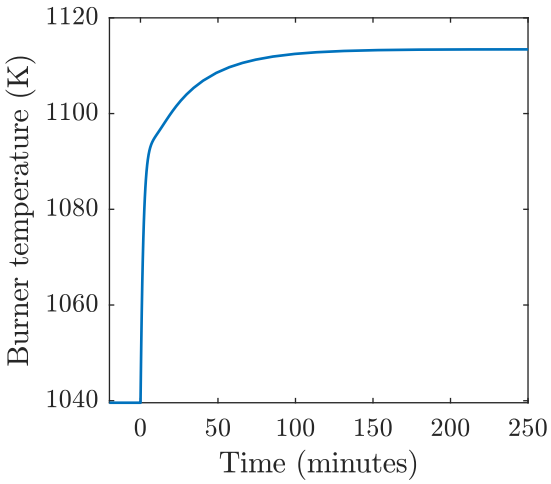

(b) Burner temperature.

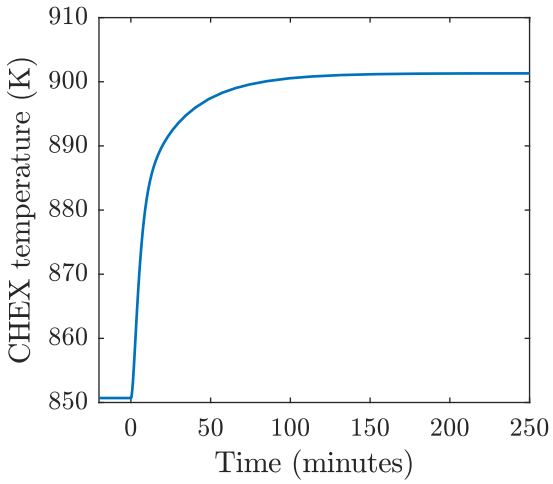

(c) CHEX temperature.

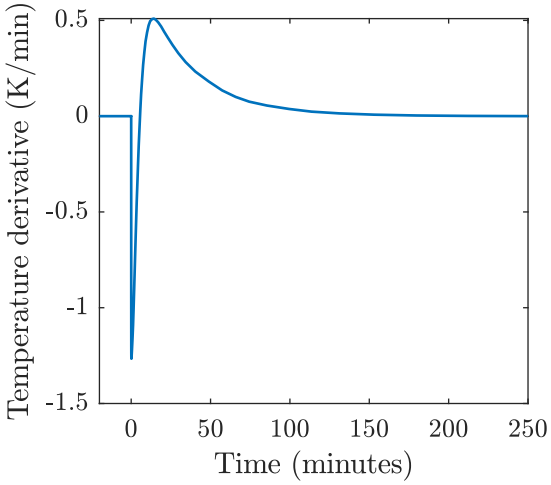

(d) $\mathrm{d}T_S/\mathrm{d}t$.

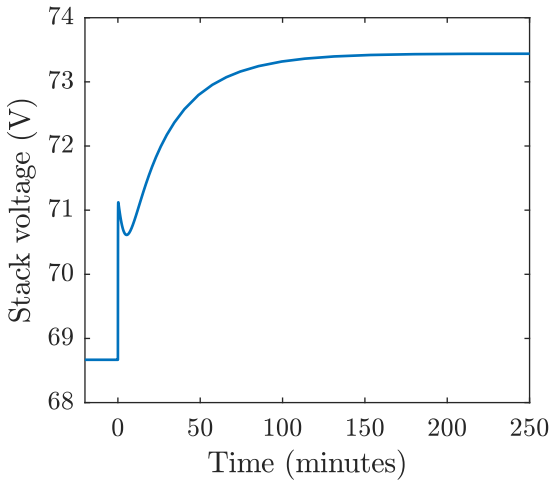

(e) Stack voltage.

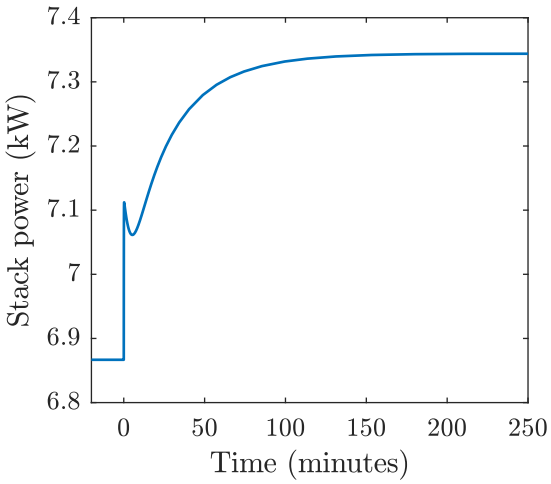

(f) Stack power.

Figure 5.4: Open loop response to a 10 % step increase in fuel flow rate over the first 250 minutes.

The increase in CHEX temperature caused an increase in the heat flow to the stack, and therefore after fives minutes, a minimum stack temperature of 953 K was reached.

5.3.3 Response during the first 250 minutes

After the first five minutes, the increasing temperature of the cathode air flow into the stack meant that, despite the increased rate of heat consumption by the MSR reaction, there was an accumulation of heat in the stack. Therefore, the stack temperature in Figure 5.4a increased from the minimum of 953 K—by 19 K or 2.0 % to a new steady-state value of 972 K.

After the first five minutes, the burner temperature increase in Figure 5.4b was limited by the slower stack thermal transient. Over the full 250 minutes the burner temperature increased from 1040 K—by 74 K or 7.1 %—to 1113 K Figure 5.4b. Therefore, the burner temperature remained well below its maximum of 1273 K. The CHEX temperature followed the thermal transient of the stack in Figure 5.4c after the first five minutes. Over the 250 minutes the CHEX temperature increased from 851 K—by 51 K or 5.9 %—to a new steady-state value of 901 K. As a result, the temperature difference between the stack and the air from the CHEX decreased from 106 K—by 35 K or 33 %—to a new steady-state value of 71 K. This shows that increasing the fuel flow rate helps to reduce the stack temperature difference below the maximum stack temperature difference of 100 K in Table 3.1, and hence the temperature gradients in the stack, primarily due to the significant increase in burner temperature.

5.3.3.1 Electrical transients

The stack voltage and stack power transients during the first 250 minutes to the step change in fuel flow rate are shown in Figure 5.4e and Figure 5.4f. They are governed by the variation in stack temperature in Figure 5.4a. As the stack temperature increased, the ASR of the stack decreased and the reversible voltage decreased. The electrical transients were primarily governed by the sensitivity of the ASR to temperature. The

Table 5.2: Summary of results for 10 % step increase in fuel flow rate.

Parameter	Initial value	Change over 25 s	Change over 250 min	Final value
$\dot{n}_{\text{fuel}}$	$15.1\,\text{g}\,\text{s}^{-1}$			$16.6\,\text{g}\,\text{s}^{-1}$
$y_{\text{H}_2,\text{anode}}$	0.17	+0.08	≈ 0	0.25
V_{stack}	68.7 V	+2.5 V	+2.3 V	73.4 V
P_{stack}	6.87 kW	+0.25 kW	+0.23 kW	7.34 kW
U_f	0.70	−0.12	≈ 0	0.58
S/C ratio	2.38	−0.45	≈ 0	1.94
λ	5.98	?	0	?
T_{stack}	957 K	0	+15 K	972 K
T_{burner}	1040 K	0	+74 K	1113 K
T_{chex}	851 K	0	+51 K	901 K
$T_{\text{stack}} - T_{\text{chex}}$	106 K	0	−35 K	71 K

stack voltage initially decreased with stack temperature from 71.1 V to a minimum of 70.6 V over 5 min, then increased from 70.6 V to a new steady-state of 73.4 V, with a relaxation time of 70 min. The stack power followed the same response. Over the 250 minutes, there was a 4.8 V increase in stack voltage and a 0.48 kW increase in stack power, a 7 % increase. This improvement in electrical performance was caused by the increase in stack temperature, but higher operating temperatures may also reduce the stack lifetime.

5.3.4 Summarising the results

Table 5.2 summarises the results for a 10 % step increase in fuel flow rate from $15.1\,\text{g}\,\text{s}^{-1}$ to $16.6\,\text{g}\,\text{s}^{-1}$, including stack temperature, voltage, and power. The table splits the dynamic response between the changes over the first 25 seconds, and the changes over the following 250 minutes. In contrast to the step in current in Section 5.2, no instantaneous transients are observed because the current remains constant.

A flow chart illustrating how the responses to the step increase in fuel flow rate influ-

enced each other is shown in Figure 5.5:

- The increase in fuel flow rate caused the S/C ratio, U_f and MSR reaction rate to increase in the first 25 seconds. The increase in the MSR reaction rate caused the mole fractions of hydrogen and water at the anode to increase, and decrease, respectively. This caused the cell voltage and stack power to increase.

- During the first 5 minutes, the increase in the MSR reaction rate caused the stack temperature decrease, and therefore, the cell voltage and stack power reduced. However, the increase in the anode hydrogen mole fraction caused the burner temperature to increase, and therefore, the CHEX temperature too.

- The increase in the CHEX temperature increased the stack temperature after 5 minutes, which caused the cell voltage and stack power to further increase.

As discussed in Section 5.3.1, increases in load would likely need to be accompanied by an increase in fuel flow rate to maintain U_f below its maximum allowable value. However, Figure 5.2a and Figure 5.4a show that both increases in current and fuel flow rate increase the stack temperature. Therefore, increased cooling to the stack is likely required to maintain the stack temperature. One way to achieve this would be through increasing the air flow rate, and will be discussed further in Section 5.4.

5.4 Open loop response to air flow rate increase

The open loop response to a 10 % step increase in the air flow rate from $738\,\mathrm{g\,s^{-1}}$ to $812\,\mathrm{g\,s^{-1}}$ shown in in Figure 5.6a is investigated in the following. The current and the flow rates of fuel and AOGR were held constant in the simulations at 100 A, $15.1\,\mathrm{g\,s^{-1}}$, and $1.7\,\mathrm{g\,s^{-1}}$, respectively.

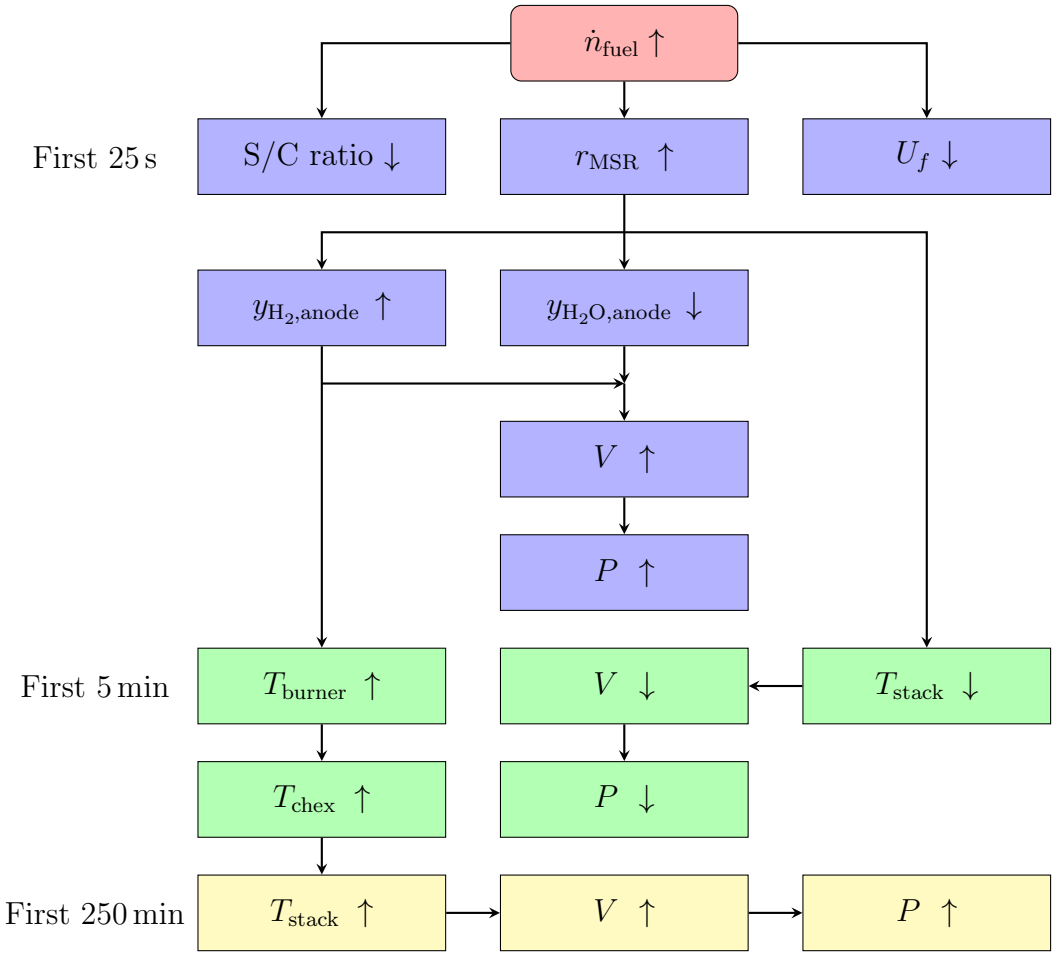

Figure 5.5: Flowchart showing the response to a step increase in fuel flow.

5.4.1 Response during the first second

The 10 % increase in the air flow rate at a fixed current of 100 A in Figure 5.6a increased λ in Figure 5.6b from 5.98—by 0.60 or 10 %—to 6.58. The increase in air flow was instantaneous, so the increase in λ was instantaneous, too. In contrast, the oxygen mole fraction at the cathode in Figure 5.6c remained at 0.18 with only a slight increase of 0.0027 or 1.5 % with a relaxation time of around 0.2 seconds. According to the Nernst equation (3.24), the change in oxygen mole fraction causes only a 0.04 % change in the cell voltage, so the electrical transients are neglected over the first second. The electrical transients in response to the change in stack temperature in Figure 5.7 cancelled out any changes within 20 seconds.

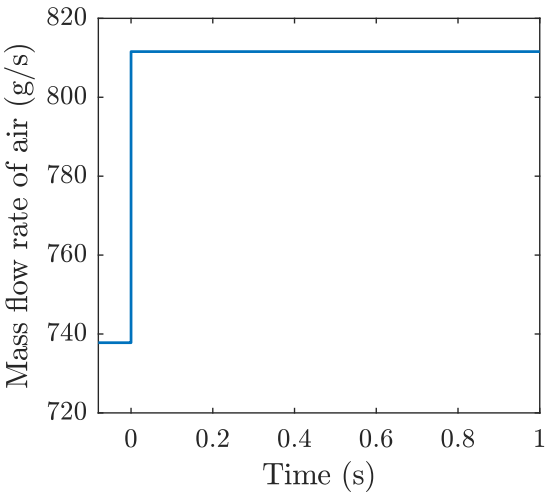

(a) Air flow rate.

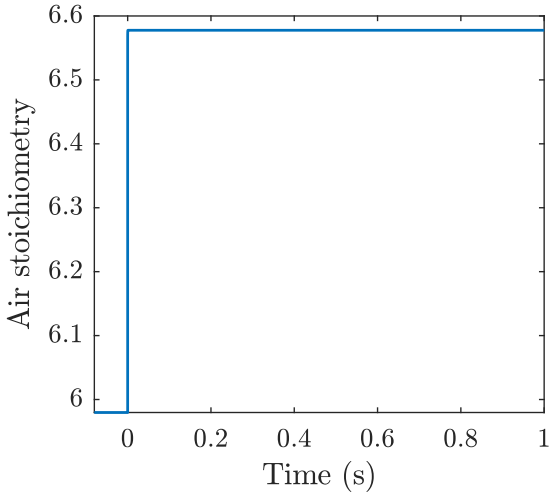

(b) Air stoichiometry.

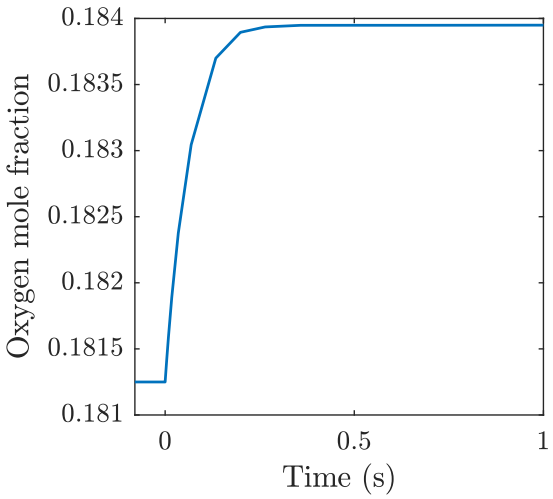

(c) Mole fraction, cathode.

Figure 5.6: Open loop response to step increase in air flow rate over the first 25 seconds.

5.4.2 Response during the first 250 minutes

Figure 5.7a shows the variation in stack temperature over the first 250 minutes. Initially, the air enters the cathode 106 K cooler than the stack temperature, meaning that the air provides cooling to the stack. The increase in air flow rate thereby decreased the stack temperature in Figure 5.7a from 957 K—by 16 K or 1.7 %—to 941 K, with a relaxation time of 50 minutes. The $\mathrm{d}T_S/\mathrm{d}t$ in Figure 5.7b decreased to a minimum of $-0.55\,\mathrm{K\,min^{-1}}$ after 0.4 seconds and then returned slowly back to zero over the remaining 250 minutes. The magnitude of the $\mathrm{d}T_S/\mathrm{d}t$ was smaller than its maximum allowable value of $2\,\mathrm{K\,min^{-1}}$

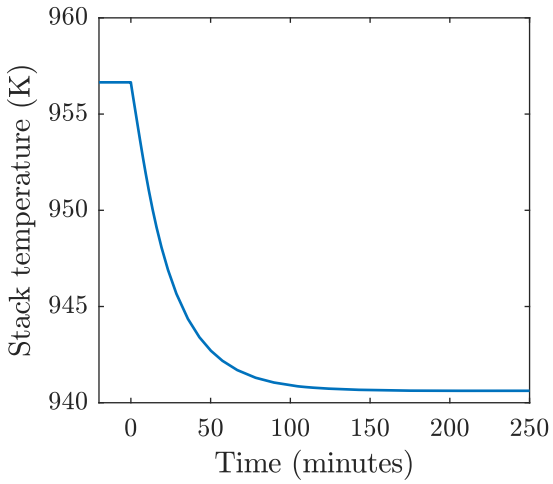

(a) Stack temperature.

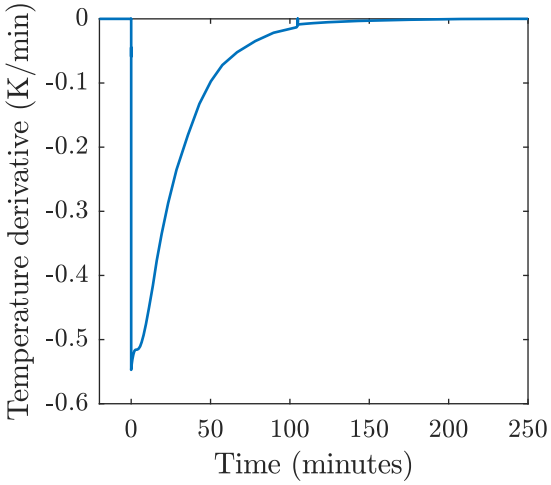

(b) $\mathrm{d}T_S/\mathrm{d}t$.

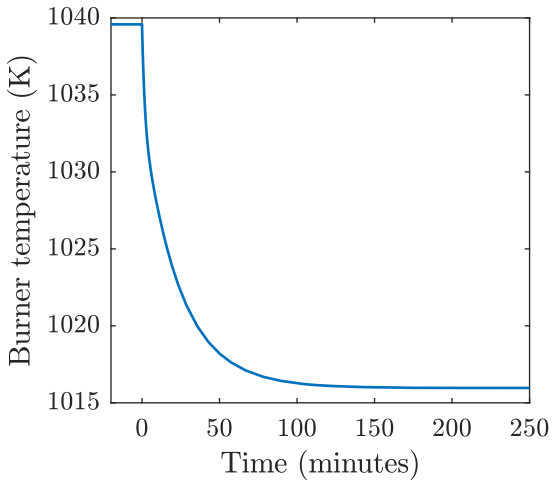

(c) Burner temperature.

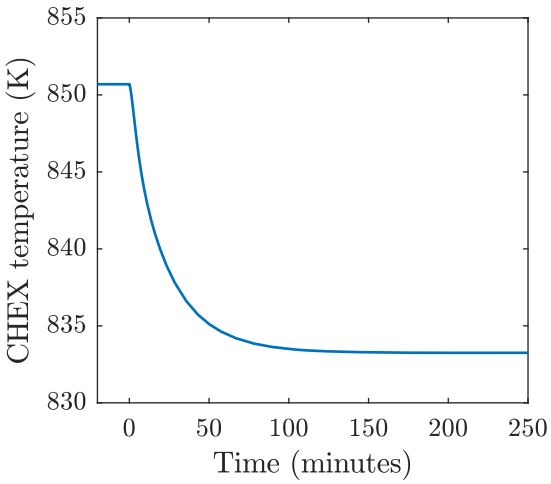

(d) CHEX temperature.

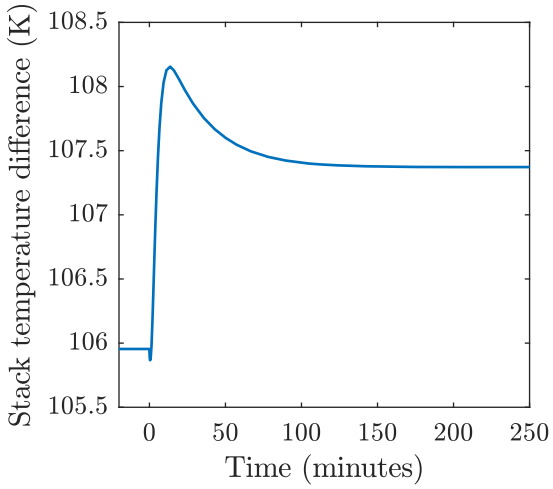

(e) Stack temperature difference.

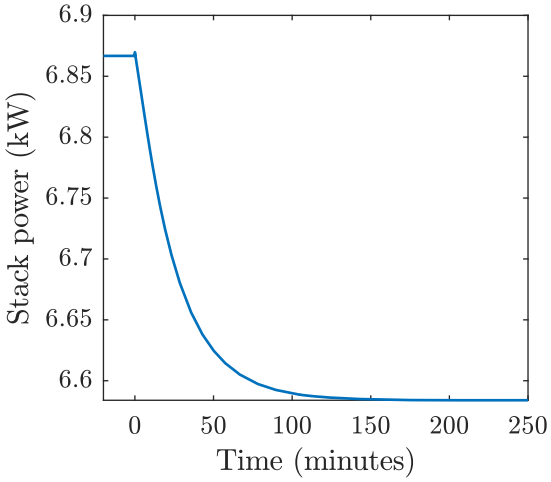

(f) Stack power.

Figure 5.7: Open loop response to 10 % step increase in air flow rate over the first 250 minutes.

in Table 3.1.

The cathode off-gas entered the burner chamber initially 83 K cooler than the burner temperature. The increase in flow rate and cooling of the cathode air caused the burner temperature in Figure 5.7c to decrease from 1040 K—by 24 K or 2.3 %—to a new steady-state value of 1016 K. Like in Sections 5.2 to 5.3, the CHEX thermal transient followed the burner thermal transient. The CHEX temperature in Figure 5.7d decreased from 851 K—by 17 K or 2.1 %—to 833 K.

The temperature response of the burner was initially faster than that of the stack due to its smaller heat capacity. Over time, the burner thermal transient slowed to the same rate as the stack thermal transient, as the burner temperature response was directly tied to the stack temperature response. The magnitude of the thermal responses of the CHEX and the stack were very similar, since the air flow through both was the same, and therefore the change in cooling rate was very similar. Therefore, the stack temperature difference in Figure 5.7e increased from 106 K—by only 1 K or 1.4 %–to 107 K. There was a less than 1 K spike in the stack temperature difference, due to the faster thermal response of the CHEX relative to the stack.

5.4.2.1 Electrical transients

As in Section 5.3, the change in stack temperature induced changes in stack voltage and stack power, due to the higher voltage losses at lower temperature. Therefore, the stack voltage decreased from 68.7 V—by 2.8 V or 4.1 %—to 65.8 V. Likewise, the stack power in Figure 5.7f decreased from 6.87 kW—by 0.28 kW or 4.1 %—to 6.58 kW. Only the stack power is shown, since at constant current, the voltage and power have the same trend.

5.4.3 Summarising the results

Table 5.3 summarises the results for a 10 % increase in air flow rate, with changes split between the instantaneous and the following 250 minutes. Increasing the air flow rate increased λ by 0.6, however this had negligible effect with the oxygen mole fraction at

Table 5.3: Summary of results for a 10 % step increase in the air flow rate.

Parameter	Initial value	Instantaneous	Over 250 min	Final value
$\dot{n}_{\text{air}}$	$738\,\text{g}\,\text{s}^{-1}$			$812\,\text{g}\,\text{s}^{-1}$
$y_{O_2,\text{anode}}$	0.18	+1.5 %	0	0.18
V_{stack}	68.7 V	≈ 0	−2.8 V	65.8 V
P_{stack}	6.87 kW	≈ 0	−0.28 kW	6.58 kW
U_f	0.70	≈ 0	≈ 0	0.70
S/C ratio	2.38	≈ 0	≈ 0	2.38
λ	5.98	+0.60	0	6.58
T_{stack}	957 K	0	−16 K	941 K
T_{burner}	1040 K	0	−24 K	1016 K
T_{chex}	851 K	0	−17 K	833 K
$T_{\text{stack}} - T_{\text{chex}}$	106 K	0	+1 K	107 K

the cathode remaining at 0.18 , and the other parameters being unchanged during the chemical reaction response. The increase in air flow rate, did however cause a decrease in the temperature of all hotbox components. The largest decrease in temperature was in the burner, while the temperature decrease of the CHEX and stack were very similar. The stack temperature difference remained virtually unchanged. This shows that increasing the air flow rate is an effective way to cool the stack and the other hot box components.

5.5 Open loop response to AOGR flow rate increase

The open loop response to a 10 % step increase in the AOGR flow rate from $1.7\,\text{g}\,\text{s}^{-1}$ to $1.87\,\text{g}\,\text{s}^{-1}$ shown in Figure 5.8a was finally investigated. The current and the flow rates of fuel and air were held constant at 100 A, $15.1\,\text{g}\,\text{s}^{-1}$, and $738\,\text{g}\,\text{s}^{-1}$, respectively.

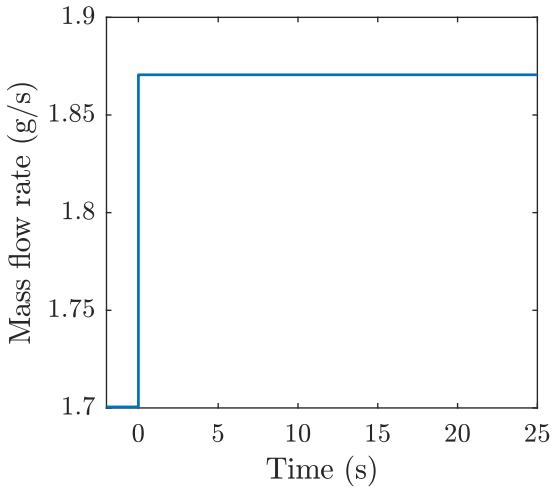

(a) AOGR flow rate.

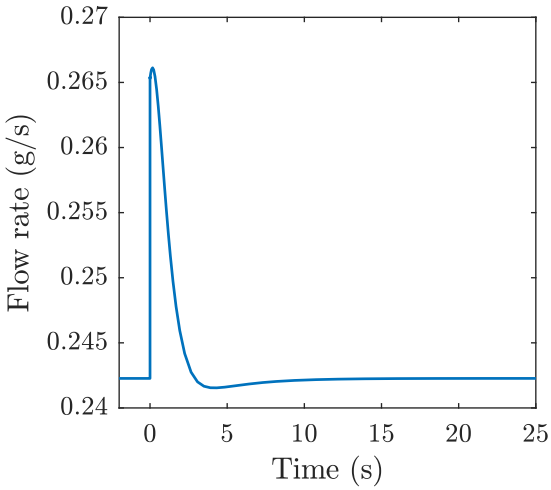

(b) Methane mass flow rate, anode inlet.

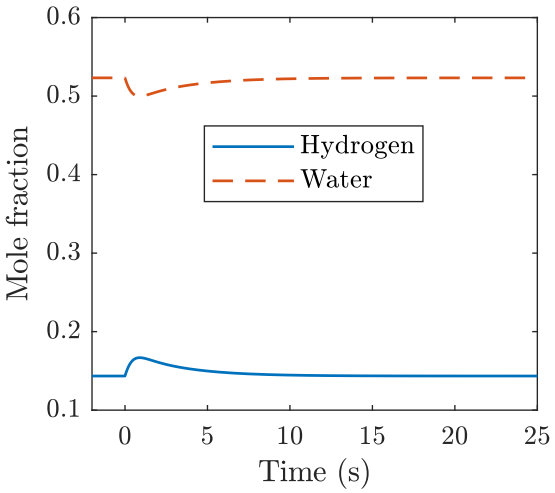

(c) Mole fraction, anode.

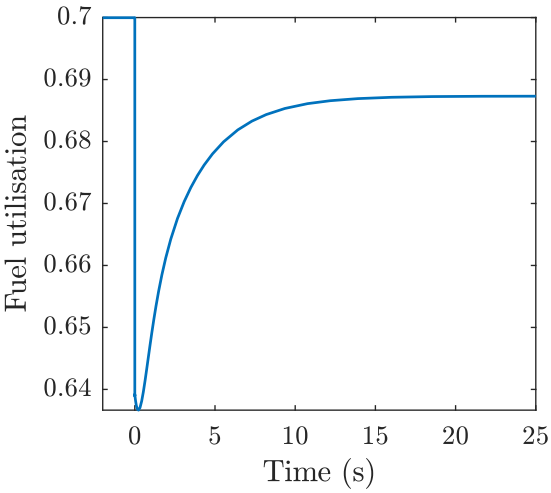

(d) Fuel utilisation, stack.

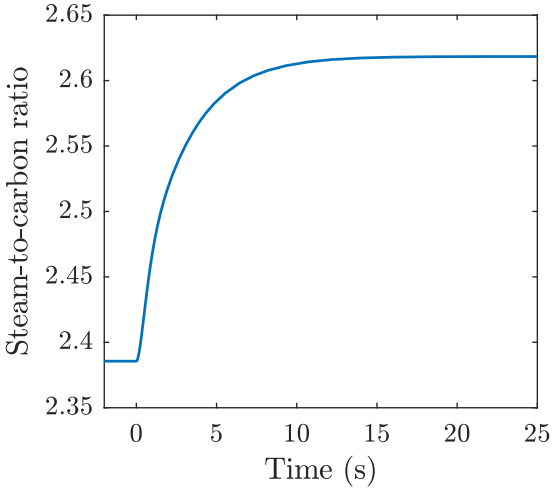

(e) S/C ratio, anode inlet.

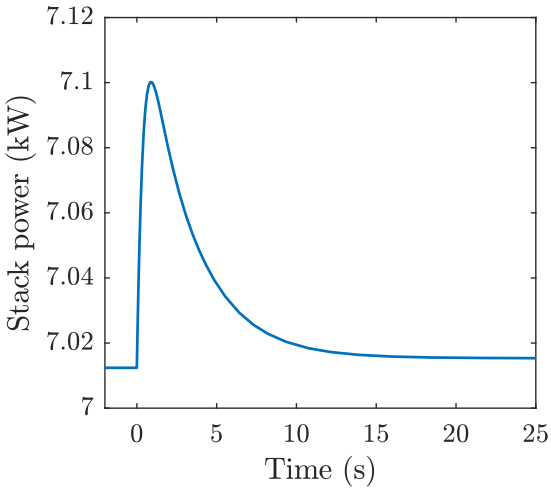

(f) Stack power.

Figure 5.8: Open loop response to a 10 % step increase in AOGR flow rate over the first 25 seconds.

5.5.1 Response during the first 25 seconds

The responses to a step change in AOGR flow rate over the first 25 seconds are shown in Figure 5.8. The primary response is the increase in S/C ratio in Figure 5.8e with a relaxation time of 6 seconds, which reflects the residence time of the AOGR loop including the AHEX and the stack, and is discussed in the following.

The instantaneous increase in the AOGR flow increased the flow rate at the anode by 10 %, including the methane flow rate in Figure 5.8b which increased from 242 mg s^{-1}—by 24 mg s^{-1} or 10 %—to a maximum of 266 mg s^{-1} after 0.2 seconds. As the composition returned back to its steady-state, the methane flow rate returned to its original steady-state value, with a slight overshoot due to the lower mole fraction of methane during the transients in the AHEX.

The spike in the methane flow rate at the anode inlet increased the rate of the MSR reaction (1.4) in the stack since it was assumed to go to completion, and therefore the hydrogen mole fraction increased temporarily in Figure 5.8c from 0.166—by 0.028 or 17 %—to a maximum of 0.193 after 0.8 seconds. The water mole fractions decreased from 0.501—by 0.028 or 6 %—to a minimum of 0.473 also after 0.8 seconds. The response followed the methane mass flow rate in Figure 5.8b, but delayed by the volume inertia of the gases at the anode. The hydrogen and water mole fractions returned back to within 1 % of their original values within 25 seconds, with a slight shift in the WGS reaction equilibrium position.

The increase in methane flow rate at the anode inlet also caused U_f (3.41) in Figure 5.8d to temporarily decrease from 0.700—by 0.063 or 9.0 %—to a minimum of 0.637 after 0.2 seconds. Following this, U_f relaxed to a new steady-state value of 0.687. The net decrease in U_f was caused by the increased flow rates of hydrogen and carbon monoxide at the anode inlet, due to the increased flow rate of the AOGR. The increase in the AOGR flow rate also increased the flow rate of water to the anode inlet, since the composition in Figure 5.8c remained largely unchanged. Therefore, the S/C ratio in Figure 5.8e increases from 2.39—by 0.23 or 10 %—to 2.62.

The temporary increase in hydrogen mole fraction and temporary decrease in water mole fraction in Figure 5.8c caused a temporary increase in the OCV as per the Nernst equation (3.24), and hence in the stack voltage. Therefore, the stack power in Figure 5.8f increased from 7.01 kW—by 0.09 kW or 1 %—to a maximum of 7.10 kW after 0.2 seconds. The power relaxed subsequently back to its original value of 7.01 kW along with the stack voltage, due to the relaxation of the composition in Figure 5.8c.

5.5.2 Response during the first 250 minutes

Figure 5.9 shows the response to the 10 % step increase in AOGR flow rate over the first 250 minutes. The increase in AOGR flow rate provided a slight increase in the amount of cooling to the stack and hot BoP components. However, the air flow rate was much larger than the fuel flow rate, and hence the magnitude of the temperature change was less than 1 K and therefore is negligible when compared to the thermal response of the first three scenarios in Sections 5.2 to 5.4.

5.5.3 Summarising the results

Table 5.4 summarises the results for a 10 % step increase in the AOGR flow rate, with changes split between the first 25 seconds and the following 250 minutes. The responses were limited, with the 0.23 increase in S/C ratio in the first 25 seconds being the notable feature. This shows that increasing the AOGR flow rate is an effective way to manage the S/C ratio and avoid carbon deposition, without having a significant effect on the performance of the system.

5.6 Concluding the open loop response

The four open loop responses presented in this chapter have illustrated the impact of changing the system inputs. Of particular interest is the response of the system to a change in load, as shown in Section 5.2, both in terms of system performance and the

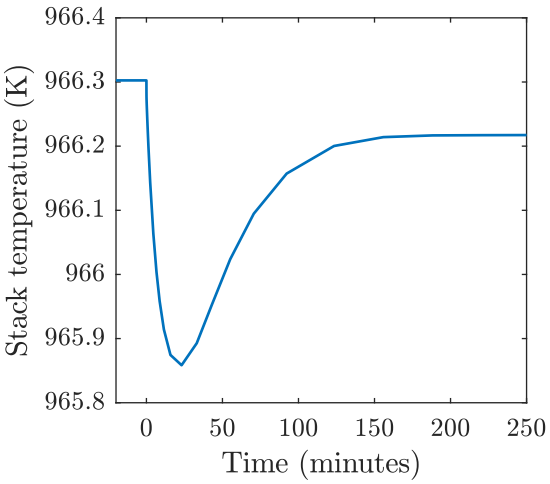

(a) Stack temperature.

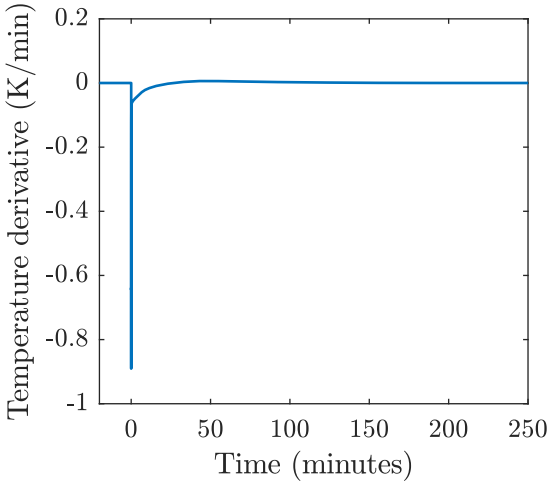

(b) $\mathrm{d}T_S/\mathrm{d}t$.

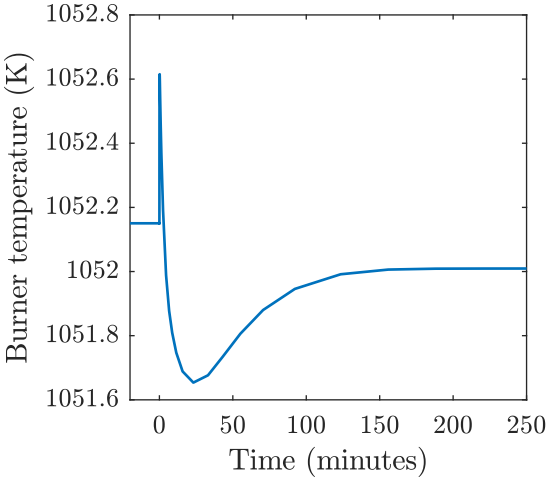

(c) Burner temperature.

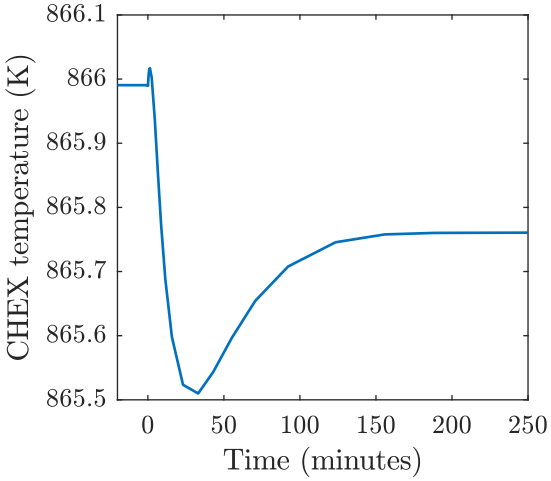

(d) CHEX temperature.

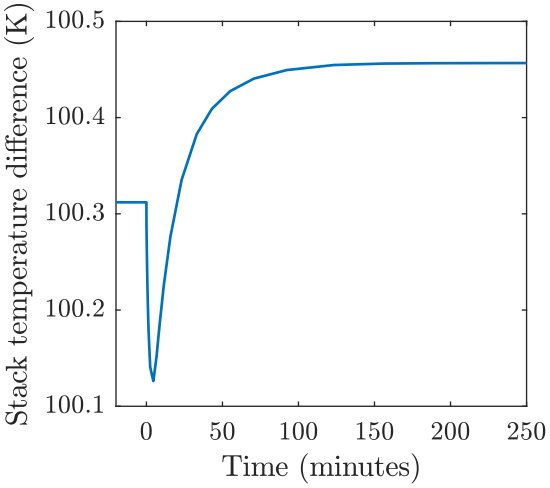

(e) Stack temperature difference.

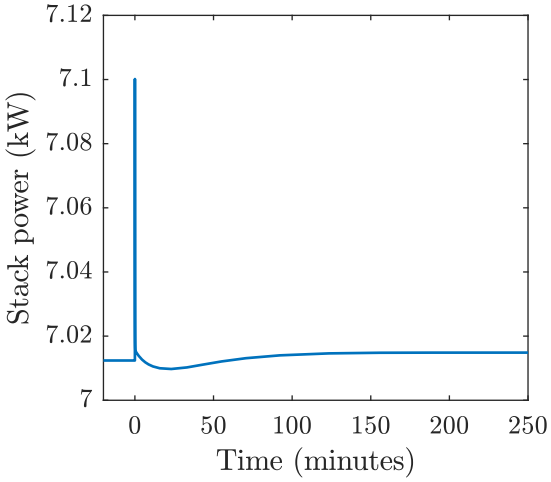

(f) Stack power.

Figure 5.9: Open loop response to a 10 % step increase in AOGR flow rate over the first 250 minutes.

Table 5.4: Summary of results for a 10 % step increase in AOGR flow rate.

Parameter	Initial value	Change over 25 s	Change over 250 min	Final value
$\dot{n}_{\text{aogr}}$	$1.7\,\text{g}\,\text{s}^{-1}$			$1.87\,\text{g}\,\text{s}^{-1}$
$y_{\text{H}_2,\text{anode}}$	0.18	≈ 0	0	0.18
V_{stack}	68.7 V	≈ 0	≈ 0	68.7 V
P_{stack}	6.87 kW	≈ 0	≈ 0	6.87 kW
U_f	0.70	-0.01	≈ 0	0.69
S/C ratio	2.39	$+0.23$	≈ 0	2.62
λ	5.98	0	0	5.98
T_{stack}	957 K	0	≈ 0	957 K
T_{burner}	1040 K	0	≈ 0	1040 K
T_{chex}	851 K	0	≈ 0	851 K
$T_{\text{stack}} - T_{\text{chex}}$	106 K	0	≈ 0	106 K

operational constraints in Table 3.1. Sections 5.3 to 5.5 show how varying the fuel, air and AOGR flow rates could help to keep the system within its safe operational window.

Investigating the open loop responses and the discussion of their results in this chapter has served to validate the dynamic model presented in Chapter 3 in the absence of reproducible results in the literature. The key outcomes of the analysis are outlined in the following.

The 10 % increase in current from 100 A to 110 A in Section 5.2 increased the power output of the stack by 4 %. However, it led to a 24 % increase in U_f, and a 39 % increase in the stack temperature difference, moving both parameters outside their safe operating window from Table 3.1. The stack temperature increased by 2 % and remained below its maximum allowable level, while the burner temperature decreased by 3 %, reducing it further below its maximum allowable temperature. The S/C ratio increased by 11 % further above its maximum allowable value. The λ decreased by 10 %, but was still well above its maximum allowable value. The maximum $\text{d}T_S/\text{d}t$ was well below its maximum

allowable value.

The 10 % increase in fuel flow rate from 15.1 g s^{-1} to 16.6 g s^{-1} in Section 5.3 increased the power output of the stack by 7 %. However, it led to a 19 % decrease in S/C ratio, moving the parameter outside its safe operating window from Table 3.1. The U_f decreased by 17 % away from its maximum allowable value. The stack temperature and burner temperatures increased by 1.6 % and 7.1 %, respectively, but remained below their maximum allowable values. The stack temperature difference decreased by 33 %, so the increase in fuel flow rate helped to reduce the stack temperature gradients.

The 10 % increase in air flow rate from 738 g s^{-1} to 813 g s^{-1} and hence λ in Section 5.4 decreased the stack power by 4.1 %. However, it decreased the stack temperature and burner temperature by 1.7 % and 2.3 %, respectively, moving the parameters further below their maximum allowable values. The stack temperature difference was not affected greatly and increased by only 1.4 %. The U_f and S/C ratio were unaffected.

The 10 % increase in AOGR flow rate from 1.7 g s^{-1} to 1.87 g s^{-1} in Section 5.5 increased the S/C ratio at the stack inlet by 10 %, moving the parameter further above its maximum allowable value. The other system parameters were relatively unaffected.

5.7 Controlled responses to current increase

Following the open loop response, the controlled responses will be presented in this section to investigate keeping the operating constraints within their safe operating window for an SOFC system of 6.9 kW. In the closed loop or controlled response, the cell current was increased by 10 % from 36.0 A to 39.6 A, as shown in Figure 5.10a. The flow rates of fuel, AOGR, and air were manipulated using the approach presented in Section 3.14, in order to maintain U_f, S/C ratio, and the SOFC stack temperature at 0.7, 2.5, and 700°C, respectively. As shown in Table 3.1, the controllers had some additional requirements during transients. The U_f response should remain below 0.8, the S/C ratio response remain above 2, and the $\mathrm{d}T_S/\mathrm{d}t$ should remain below 2 °C min^{-1}.

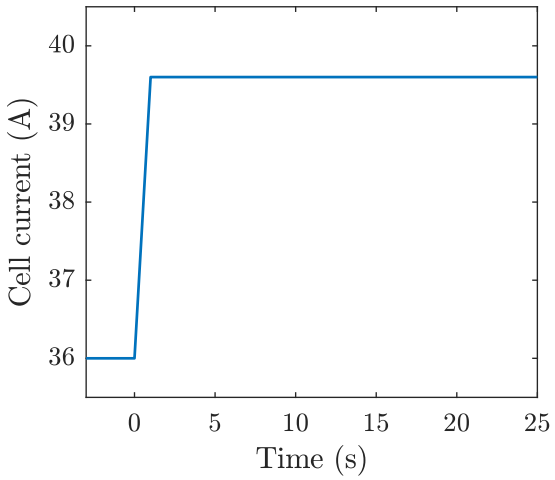

(a) 10 % increase in cell current.

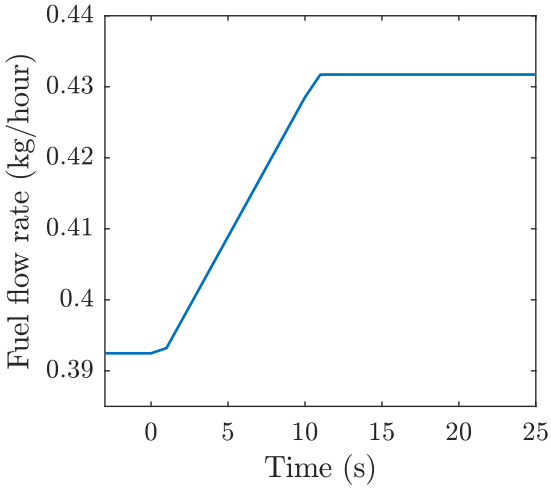

(b) Fuel flow rate response.

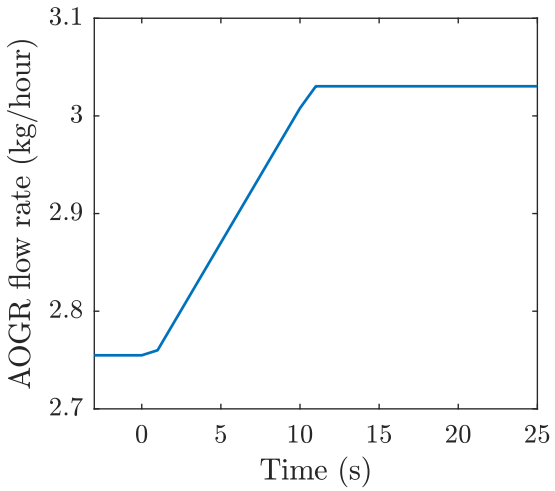

(c) AOGR flow rate response.

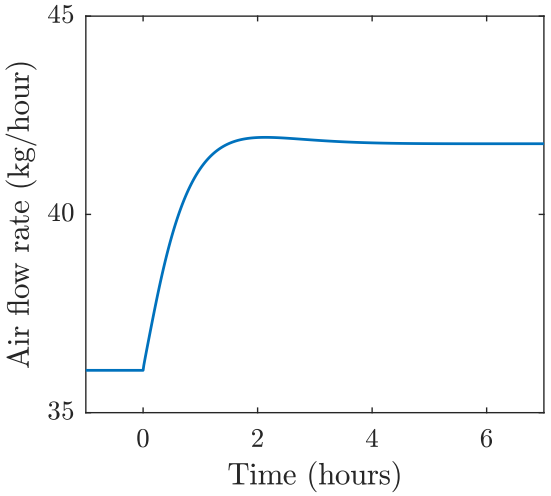

(d) Air flow rate response.

Figure 5.10: Variation in current, and the controlled manipulation of the fuel, AOGR and air flow rates to keep U_f, S/C ratio, and stack temperature constant.

The variations of all manipulated variables are shown in Figure 5.10. The fuel flow rate in Figure 5.10b increased from $0.39\,\mathrm{kg\,h^{-1}}$ to $0.43\,\mathrm{kg\,h^{-1}}$, an increase of 10 %. This is identical to the required percentage increase in current, showing they are close to being directly proportional. The AOGR flow rate in Figure 5.10c increased from $2.75\,\mathrm{kg\,h^{-1}}$ to $3.03\,\mathrm{kg\,h^{-1}}$, an increase of 10 % too. The increases in fuel and AOGR flow rates therefore followed the increase in current, with a response time of 10 seconds. 10 seconds was chosen to meet the 20 second relaxation time of the chemical reaction kinetics observed in the literature [47]. This response time influences the dynamic response of the U_f and

S/C ratio during transients, and in reality would be depend on the positioning times of the mass flow control valves, or the slew rate of the recirculation blower.

The air flow rate in Figure 5.10d was manipulated by the PID controller, as introduced in Section 3.14. The PID Tuner in Matlab/Simulink was used to tune the controller parameters. The following values gave a good response with minimal overshoot: $P = -0.0079$, $I = -3.7 \times 10^{-6}$, and $D = 0.73$. The air flow rate increased initially from $36.0\,\mathrm{kg\,h^{-1}}$ to a maximum of $41.9\,\mathrm{kg\,h^{-1}}$ after 2 hours, before subsequently reducing to a steady-state value of $41.7\,\mathrm{kg\,h^{-1}}$. The slow variation in the air flow rate reflects the slow thermal transients of the SOFC system which will be shown in Section 5.7.2.

5.7.1 Chemical reaction transients

Figure 5.11 shows the chemical reaction transients of the SOFC system in the controlled reponse over the first 60 seconds. The rate limited increase of the fuel flow in Figure 5.10b, led to spikes in U_f in Figure 5.11d, and hydrogen mole fraction on the anode in Figure 5.11a. The U_f increased from 0.70 to a maximum of 0.78 after 1 second, before reducing back to 0.70 over the following 20 seconds. Likewise, the hydrogen mole fraction reduced from 0.14 to 0.10, before increasing back to 0.14 over 20 seconds. The response of the hydrogen mole fraction lagged the U_f slightly, due to the internal gas volume of the anode compartment.

Likewise, the rate limited increase of the AOGR flow rate in Figure 5.10c, caused spikes in the S/C ratio in Figure 5.11e and in the water mole fraction at the anode inlet in Figure 5.11b. The water mole fraction increased briefly from 0.52 to 0.57 before reducing back to 0.52 over a period of 20 seconds. Likewise, the S/C ratio increased from 2.50 to 2.58, and returned to 2.5.

Due to the increased current, the λ and oxygen mole fraction on the cathode initially decreased from 6.2 to 5.7 Figure 5.11f at constant air flow rate, and from 0.182 to 180 in Figure 5.11c, respectively. However, as the air flow rate increased in Figure 5.10d with the PID controller action, the λ and oxygen mole fraction increased to new steady-state

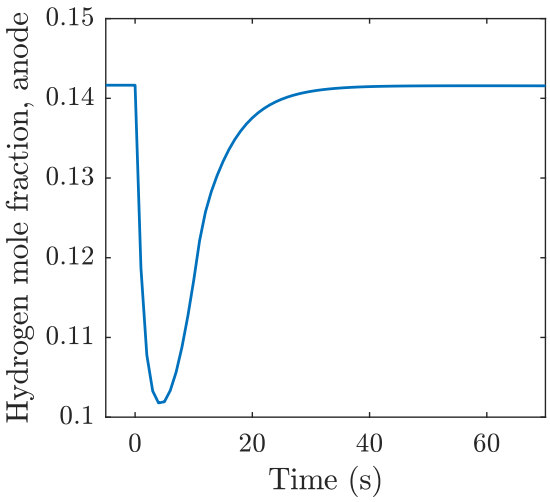

(a) Hydrogen mole fraction, anode.

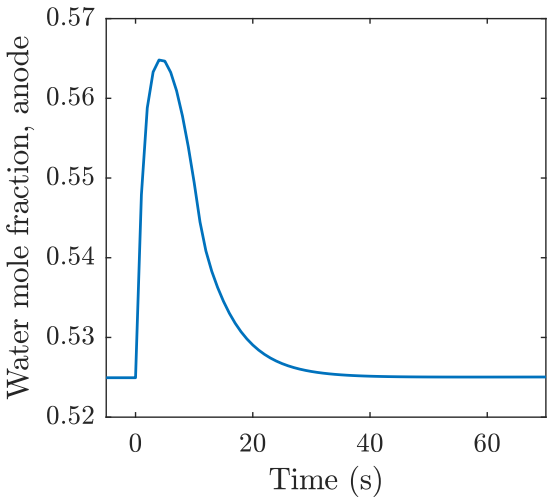

(b) Water mole fraction, anode.

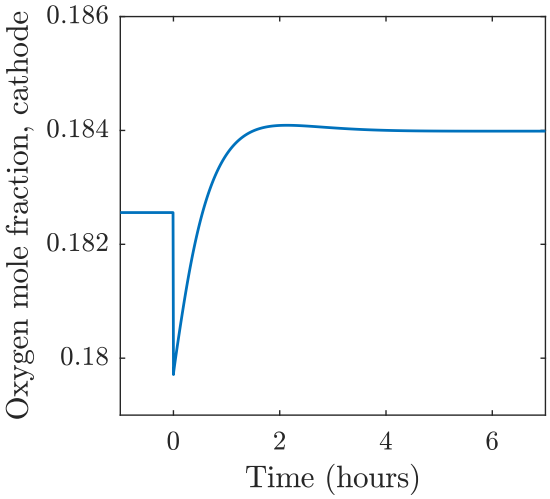

(c) Oxygen mole fraction, cathode.

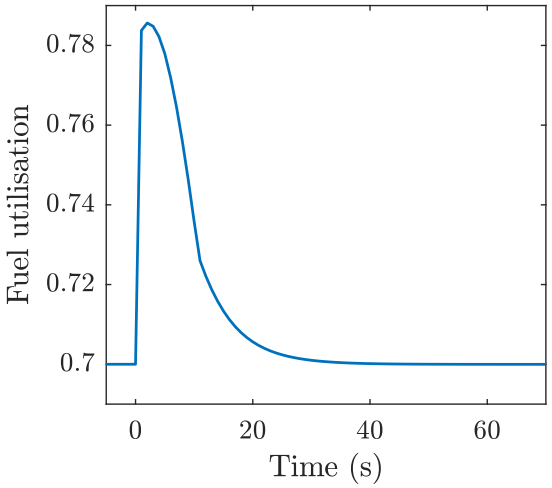

(d) Fuel utilisation.

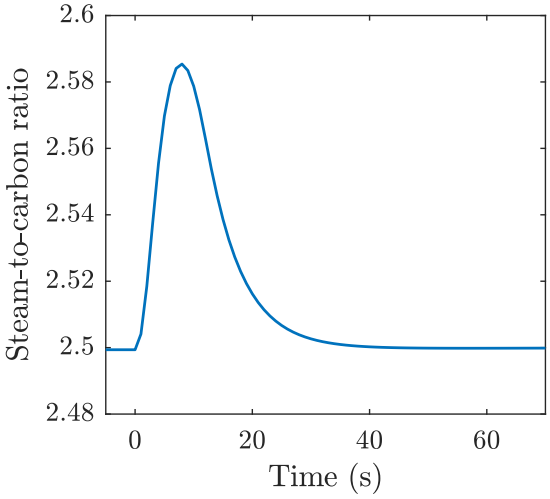

(e) S/C ratio, anode inlet.

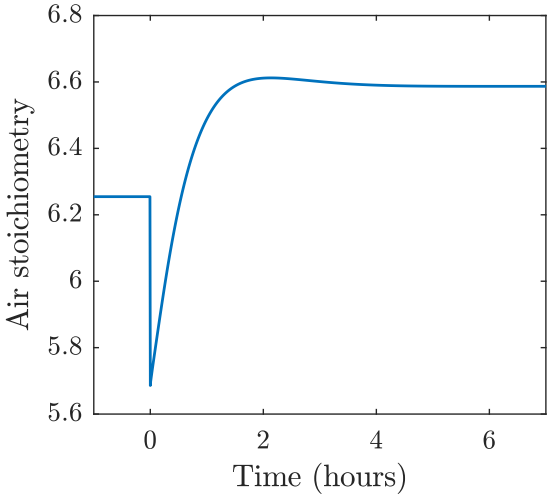

(f) Air stoichiometry.

Figure 5.11: Chemical reaction transients in the controlled response.

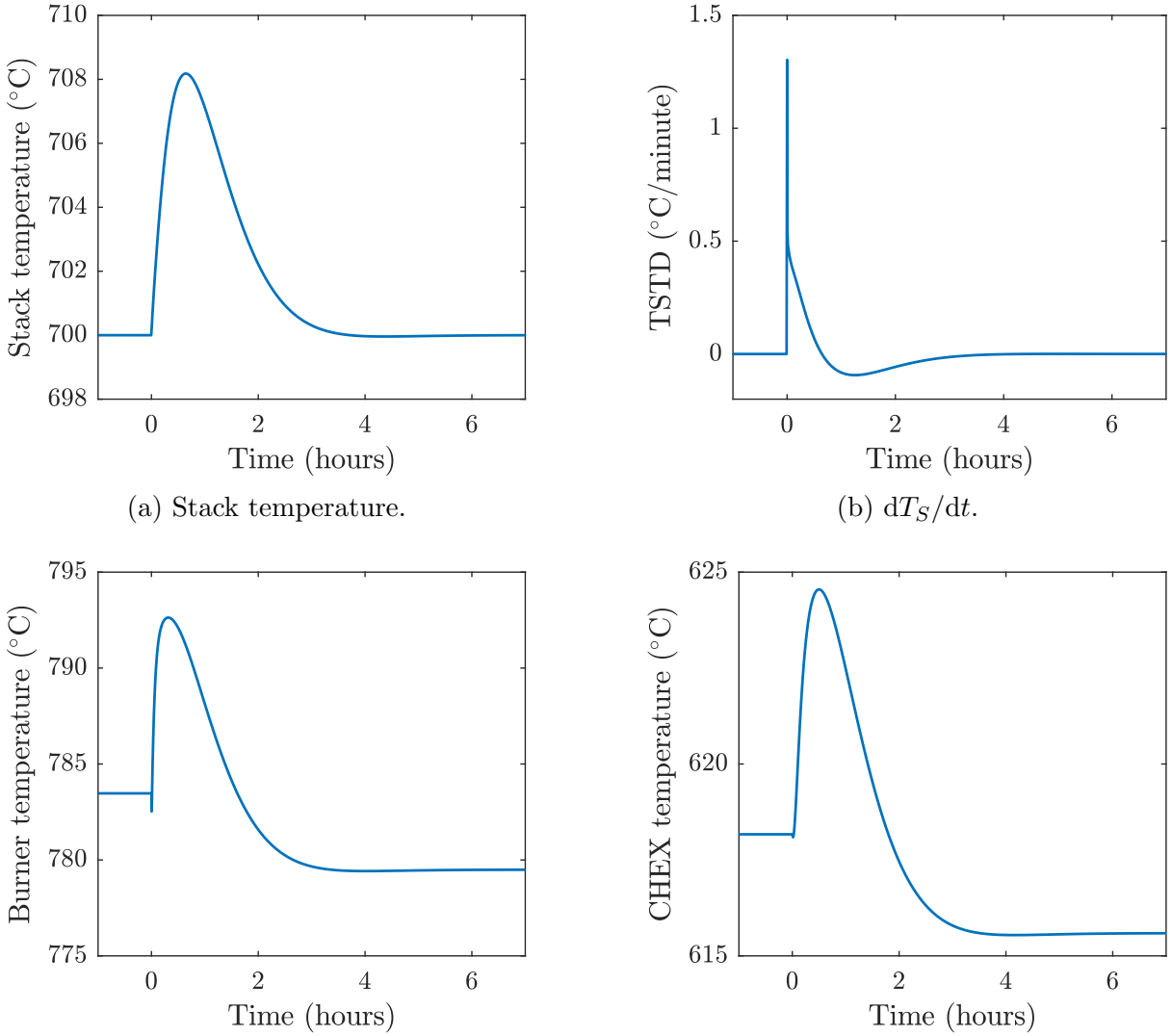

(a) Stack temperature.

(b) dT_S/dt.

(c) Burner temperature.

(d) Cathode inlet temperature.

Figure 5.12: Thermal transients in the controlled response.

values of 6.6 and 2.58 during the 3 hour duration of the thermal response.

5.7.2 Thermal transients

The thermal transients of the SOFC system in the controlled response are shown in Figure 5.12 over the first 6 hours. During the first 20 minutes, the stack temperature increased from 700°C to 708°C in Figure 5.12a, caused by the increased heat production at higher current. However, the PID controller action began to increase the air flow rate, and thereby the stack temperature returned to 700°C in approximately 3 hours. This

highlights the far slower temperature transients of the SOFC system. The initial increase in stack temperature resulted in a maximum $\mathrm{d}T_S/\mathrm{d}t$ of 1.3°C in Figure 5.12b, before the $\mathrm{d}T_S/\mathrm{d}t$ returned to zero at the end of the dynamics. This is within the limits of $2\,^{\circ}\mathrm{C\,min^{-1}}$ defined in Chapter 3.

The burner temperature in Figure 5.12c and the CHEX temperature in Figure 5.12d followed the thermal transients of the SOFC stack. Both increased over the first 30 minutes by around 8°C like the stack. Over the remaining 3 hours, their values decreased to new steady-state value about 4°C lower than their initial values. This decrease in the steady-state burner and CHEX temperatures were caused by the higher λ required to cool the SOFC stack at higher current.

5.7.3 Electrical transients

Figure 5.13 shows the electrical transients during the controlled response, both over the first 60 seconds, and the full response over 6 hours. In the first seconds, the cell voltage in Figure 5.13a decreased rapidly from 0.736 V to a minimum of 0.702 V. This was due to the instantaneous increase in voltage losses with the increased cell current. Despite the drop in cell voltage, the increase in current caused the stack power to increase in Figure 5.13b from 3.32 kW to 3.50 kW over the same period. The variation in hydrogen and water mole fractions during the first 30 seconds in Figure 5.11 caused a decrease and subsequent increase in OCV, and hence both cell voltage and stack power. After 30 seconds a steady-state OCV was achieved, and hence the cell voltage recovered to 0.719 V, and the stack power increased to 3.55 kW.

The slower variations in stack temperature shown in Figure 5.12a over the following 3 hours caused an initial reduction followed by an increase in the ASR of the SOFC stack. This resulted in an increase followed by subsequent decrease in cell voltage and stack power. After around 3 hours, at which the stack temperature had returned to a steady 700°C, the cell voltage was 0.72 V and the stack power was 3.55 kW.

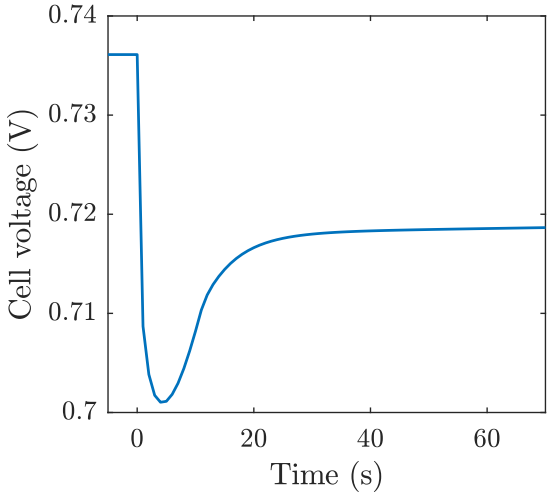

(a) Cell voltage, first minute.

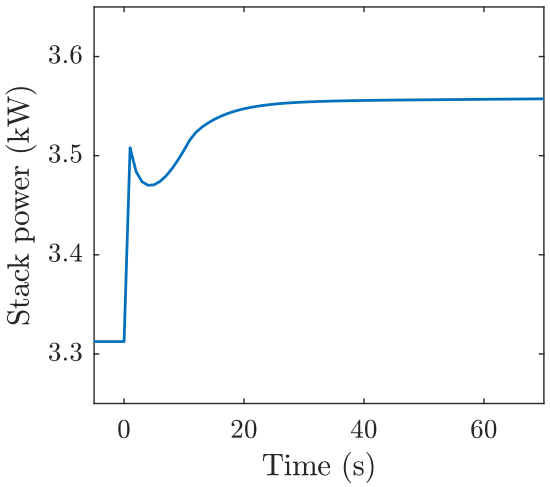

(b) Stack power, first minute.

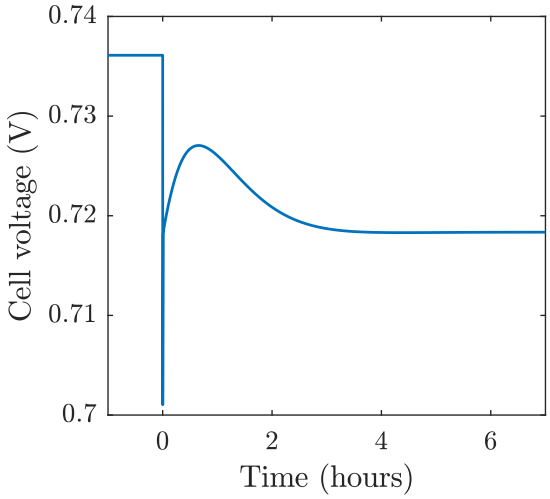

(c) Cell voltage, full response.

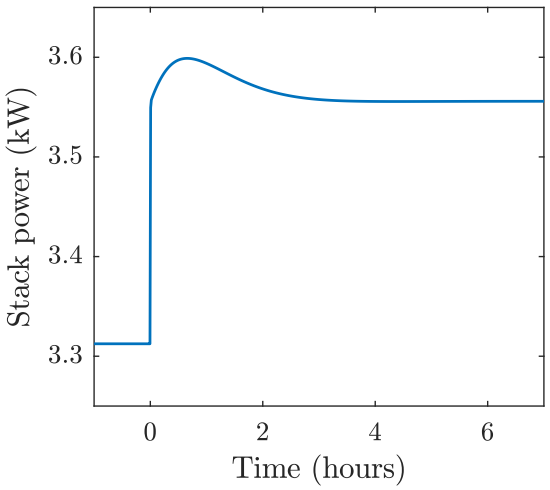

(d) Stack power, full response.

Figure 5.13: Electrical transients in the controlled response.

5.7.4 Conclusions of closed loop response

The closed loop response investigated in this section demonstrated that U_f, S/C ratio and stack temperature can be maintained following a 10 % increase in current. In the first seconds of their responses, the U_f spiked by 0.08, and the hydrogen mole fraction decreased to 0.10, before both returned to their steady-state values over 30 seconds. Similar spikes in water mole fraction and S/C ratio were observed too. The thermal transients were much slower, lasting approximately 3 hours, as a result of the large thermal inertia of the SOFC system. The stack temperature spiked by 8°C, with a $\mathrm{d}T_S/\mathrm{d}t$ of $1.3\,^{\circ}\mathrm{C\,min^{-1}}$ at

maximum.This approach therefore forms the basis used for changes in load required for heavy goods vehicle propulsion in Chapters 6 to 7.

Chapter 6

Fulfilling the power requirements of HGV propulsion

To assess the performance of solid oxide fuel cell (SOFC) systems on heavy goods vehicles (HGVs), this chapter will apply the dynamic model presented in Chapter 5 to a number of standardised drive cycles. This chapter consists of the following sections:

- The standardised drive cycles for HGV propulsion are introduced in Section 6.1,
- The methods used to model the vehicle and calculate the HGV power requirements are outlined in Section 6.2,
- The dynamic performance of the SOFC system when fulfilling the power requirements of the HGV is investigated in Section 6.3, and
- The dynamic performance of a hybrid battery-SOFC system is investigated in Section 6.4.

6.1 Drive cycles for HGV propulsion

A drive cycle describes the required velocity of a vehicle as a function of time. Standardised drive cycles were originally developed to enable reproducible vehicle emissions tests

for legislation such as the European emission standards [194]. Those same drive cycles can equally be used to calculate the power requirements of an engine or powertrain for vehicle propulsion. With the focus of this thesis on utilising SOFC systems for HGV propulsion, four standardised HGV drive cycles were identified in the literature to be considered in this chapter, and are as follows:

- The Composite Urban Emissions Drive Cycle (CUEDC) [195] developed by the National Environment Protection Council in Australia for class NCH vehicles, which are HGVs over 25 t,
- The Heavy Heavy-Duty Diesel Truck (HHDDT) drive cycle [196] developed by the California Air Resources Board and the University of Virginia in the United States with four segments: idle, creep, transient, and high speed (cruise) driving,
- The World Harmonized Vehicle Cycle (WHVC) [197] developed by the United Nations Economic Commission for Europe which consists of three segments: urban, rural, and motorway driving, and
- The Urban Dynamometer Driving Schedule for Heavy-Duty vehicles (UDDS HD) [198] developed by the United States Environmental Protection Agency and focused on urban driving.

The variation of vehicle speed with time for the four drive cycles is shown in Figure 6.1. The drive cycles last between 1000 seconds and 3600 seconds, and each have highly variable vehicle speed requirements between $0\,\mathrm{km\,h^{-1}}$ and $100\,\mathrm{km\,h^{-1}}$. The CUEDC in Figure 6.1a consists predominately of urban and rural driving up to $60\,\mathrm{km\,h^{-1}}$, and concludes with a shorter 200 second section of motorway driving up to $100\,\mathrm{km\,h^{-1}}$. The HHDDT cycle in Figure 6.1b consists of a longer section of high speed driving lasting around 1500 seconds. The shorter creep and transient sections are preceded by an idle section where the vehicle is stationary. The plot of velocity vs time for the WHVC in Figure 6.1c appears very similar to that of the CUEDC. The UDDS HD in Figure 6.1d consists predominately of

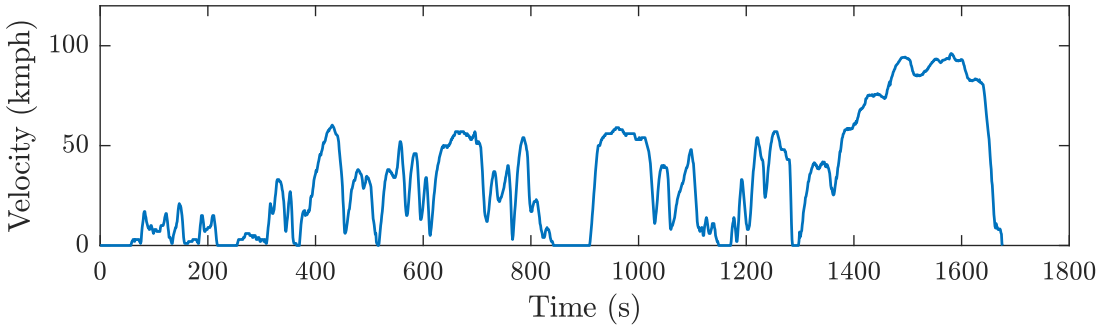

(a) CUEDC NCH (1676 s) [195].

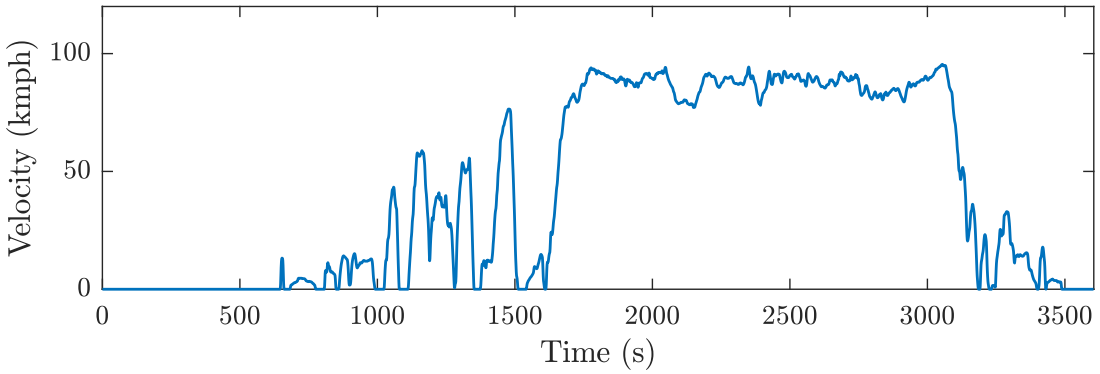

(b) HHDDT (3600 s) [196].

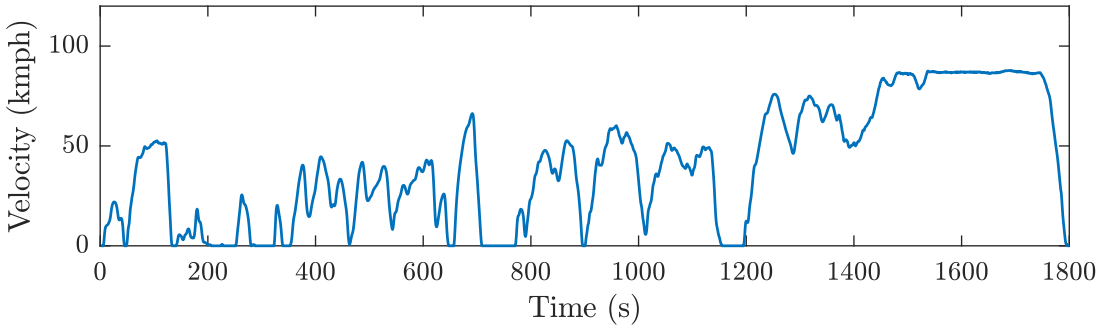

(c) WHVC (1800 s) [197].

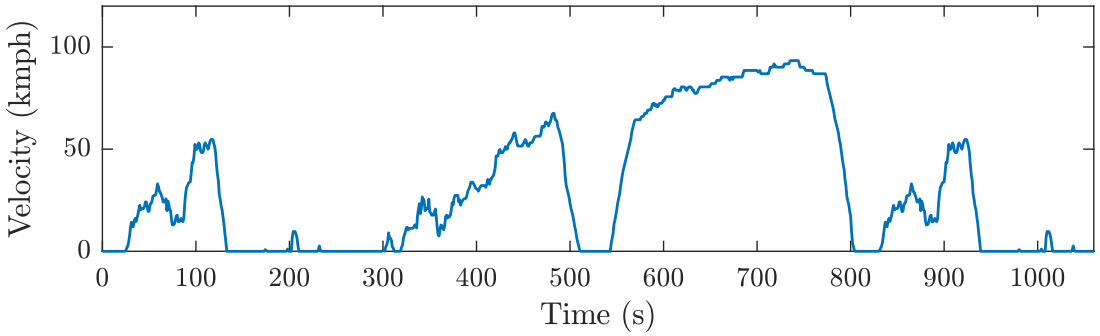

(d) UDDS HD (1060 s) [198].

Figure 6.1: Variation in vehicle velocity with time for different standardised drive cycles.

Table 6.1: Parameters of the HGV model.

Vehicle parameter	Value	
Frontal area, A_v	$10\,\mathrm{m}^2$	[199]
Drag coefficient, C_d	0.5	[199]
Rolling resistance 1, C_{r_1}	0.006	[199]
Rolling resistance 2, C_{r_2}	$2.3 \times 10^{-7}\,\mathrm{s\,m^{-1}}$	[199]
Mass, m_v	40 t	[199]
Acceleration due to gravity, g	$9.81\,\mathrm{m\,s^{-2}}$	[199]
Density of air, ρ_air	$1.292\,\mathrm{kg\,m^{-3}}$	[199]
Electric motor efficiency, η_m	93 %	[200]
Transmission efficiency, η_t	95 %	[200]
Power conditioning efficiency, η_c	98 %	[200]

urban driving, with more rapid acceleration and deceleration than the other three drive cycles.

6.2 Power requirements of an HGV

The vehicle velocity v_v from the standardised drive cycles are applied to an HGV model, to calculate the power requirements of the vehicle as a function of time. In the HGV model, the force F_v required at the wheels is calculated through a force balance as:

$$F_\mathrm{v} = m_\mathrm{v} g(C_{\mathrm{r}_1} + C_{\mathrm{r}_2} v_\mathrm{v}) + \frac{1}{2} C_\mathrm{d} \rho_\mathrm{air} A_\mathrm{v} v_\mathrm{v}^2 + m_\mathrm{v} \frac{\mathrm{d}v_\mathrm{v}}{\mathrm{d}t} \tag{6.1}$$

with each of the variables and their values defined in Table 6.1. The vehicle parameters are primarily adopted from a model of a 40 t HGV [199]. The model was developed in collaboration with Scania CV AB, a Swedish HGV manufacturer, and are reflective of typical HGVs in Europe as of 2018.

Whilst the force balance for the drive cycles are all assumed to take place on a flat road without incline, the drive cycles do all small include fluctuations in speed, which are intended to represent variations in throttle position, changes in incline, and consequences of the movements of other vehicles [194]. On the other hand, the impact of incline or

gradient β could be explicitly added to the force balance in Equation (6.1) by including the weight of the vehicle multiplied by $\sin\beta$. A positive incline would increase the power requirement of the vehicle to maintain the same speed, whilst a negative incline would reduce the power requirement of the vehicle to maintain the same speed.

Following the force balance, the power requirement P_{wheels} at the wheels to meet the demand of the drive cycle is calculated from:

$$P_{\text{wheels}} = F_{\text{v}} v_{\text{v}} \tag{6.2}$$

The power demand of the HGV is therefore sensitive not only to the requested speed, but the vehicle resistances. Vehicle manufacturers are seeking to reduce resistances and increase fuel efficiency, encouraged by EU legislation [201]. An analysis by Delgado et al. showed that both a reduction in rolling resistances by tire improvements, and a reduction in drag coefficients, could reduce HGV power requirements and hence reduce HGV fuel consumption by up to 10 % [202]. Such a reduction can be seen by expression of the vehicle force balance in Equation (6.1).

Losses within the electrical powertrain are assumed to be a fixed percentage of the power demand, based on the approach by Brett et al. [200]. Since the efficiencies are high, the contribution to efficiency losses in the overall powertrain is rather low, when compared to the SOFC system. That said, a more detailed model of their performance could provide more insight into the overall performance of the vehicle. Therefore, the power requirement P_{r} for the propulsion system is calculated from:

$$P_{\text{r}} = \begin{cases} \frac{P_{\text{wheels}}}{\eta_{\text{m}}\eta_{\text{t}}\eta_{\text{c}}} & \text{if } P_{\text{v}} > 0, \\ P_{\text{wheels}}\eta_{\text{m}}\eta_{\text{t}}\eta_{\text{c}} & \text{if } P_{\text{v}} < 0, \end{cases} \tag{6.3}$$

where the values of the electric motor efficiency, η_{m}, the transmission efficiency η_{t}, and the power conversion efficiency η_{c} are listed in Table 6.1. Whilst, an SOFC system is not able to recuperate electrical power on a vehicle, power split with a battery will be

investigated in Section 6.4, which allows the powertrain to recuperate negative power at the wheels, for example during braking.

The power requirements of the propulsion system for the CUEDC, HHDDT and WHVC drive cycles are shown in Figure 6.2. All drive cycles show a highly transient power demand with both negative and positive power requirements, along with with some periods where the vehicle was stationary where the power requirement of the SOFC system was zero. Peak power requirements during acceleration of nearly 1000 kW were observed for the UDDS HD drive cycle in Figure 6.2d and during deceleration of nearly −900 kW for the WHVC drive cycle in Figure 6.2c.

Figure 6.3 shows the probability distributions of the power requirements of the HGV in 40 kW steps for the SOFC system in each of the standardised drive cycles. For both the HHDDT and UDDS HD drive cycles, over 40 % of the time the vehicle power requirement was between 0 kW and 40 kW. The probability distributions of the HHDDT and WHVC in Figures 6.3b to 6.3c both have a relatively flat probability of about 0.1 within each 40 kW steps between 40 kW and 200 kW before decreasing with increasing power demand. Power requirements above 360 kW are rare, with each 40 kW step having less than 0.01 probability. The power requirement of the CUEDC drive cycle in Figure 6.3a is more distributed, with a relatively high probability of 0.1 of a power demand between 40 kW to 80 kW, and a slightly higher probability of power requirements above 400 kW, when compared to the HHDDT and WHVC drive cycles. Negative power requirements reduced in probability with increasing magnitude, in a similar manner to positive power requirements, but were generally less prevalent than positive power requirements.

6.3 Power delivery by the SOFC system

In this section the dynamic performance of the SOFC system is investigated, when only the SOFC system is available to meet the power requirements for HGV propulsion. In such a system, no power can be recuperated when the vehicle power requirement is negative.

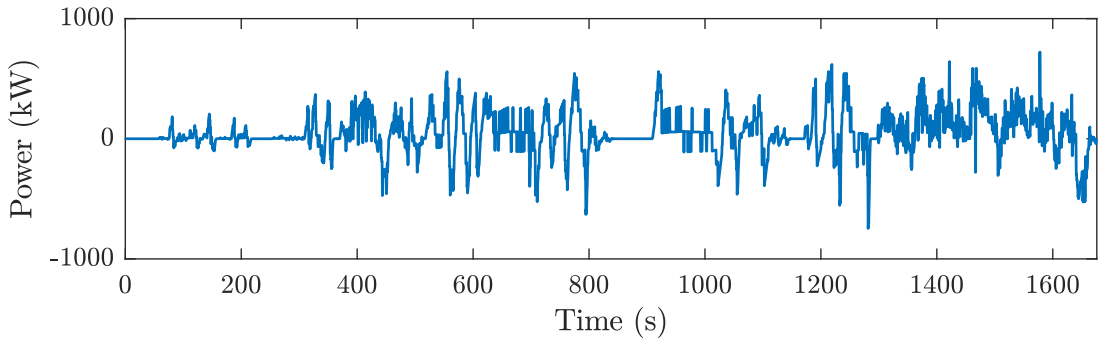

(a) CUEDC NCH (1676 s).

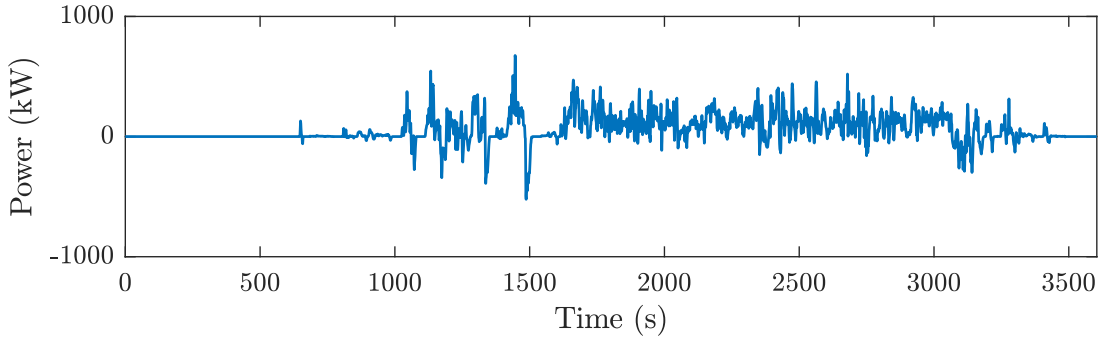

(b) HHDDT (3600 s).

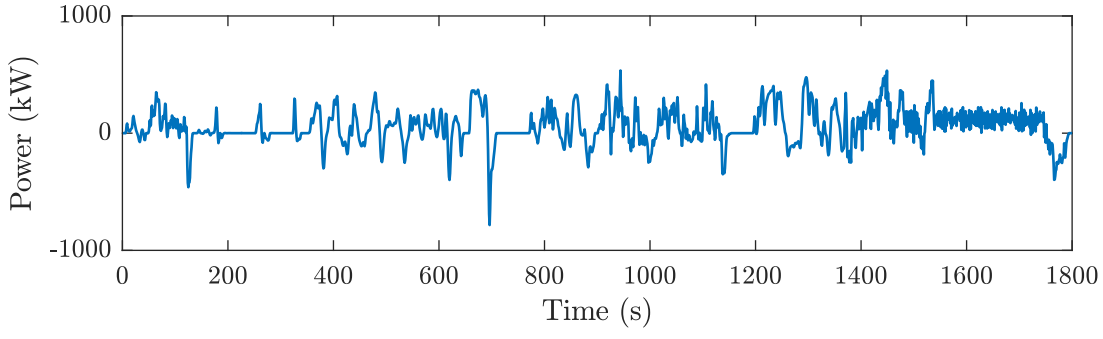

(c) WHVC (1800 s).

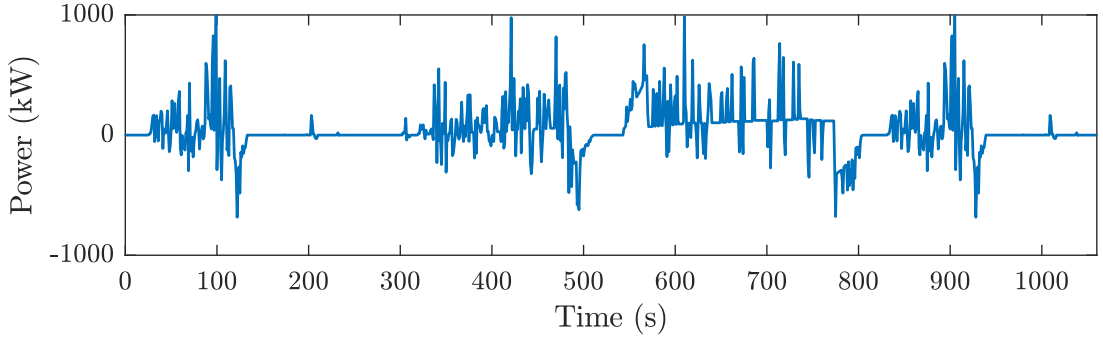

(d) UDDS HD (1060 s).

Figure 6.2: Variation in system power requirement for HGV propulsion with time.

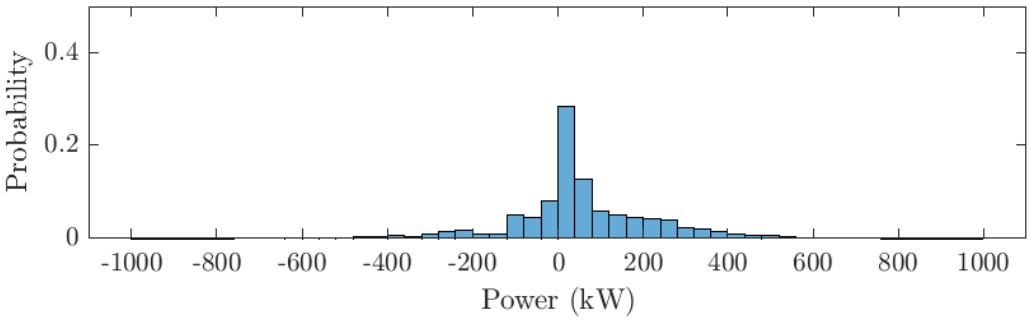

(a) CUEDC NCH (1676 s).

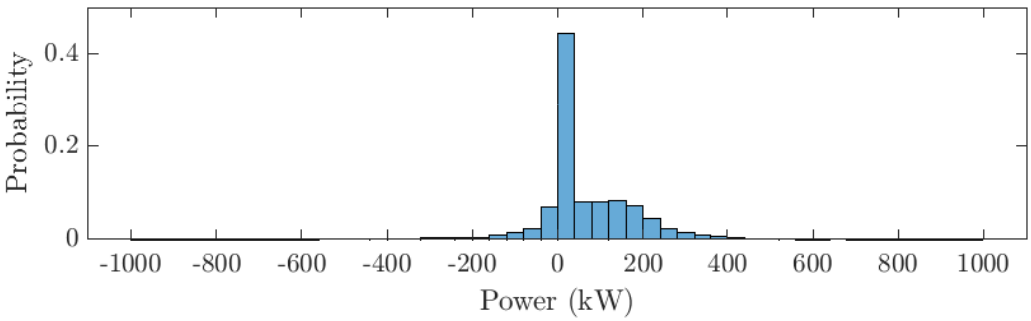

(b) HHDDT (3600 s).

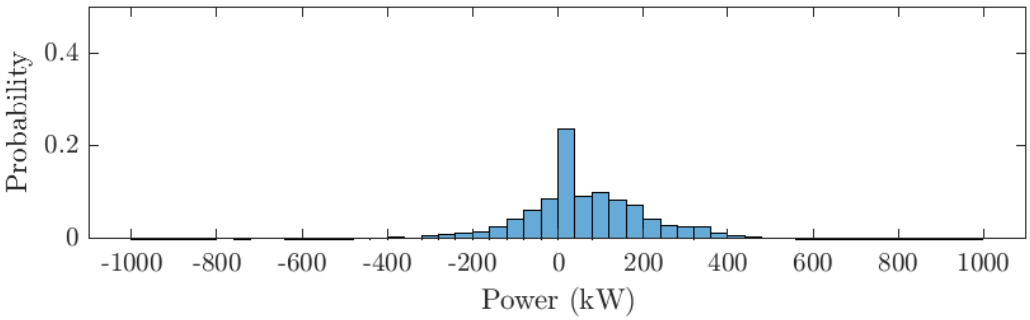

(c) WHVC (1800 s).

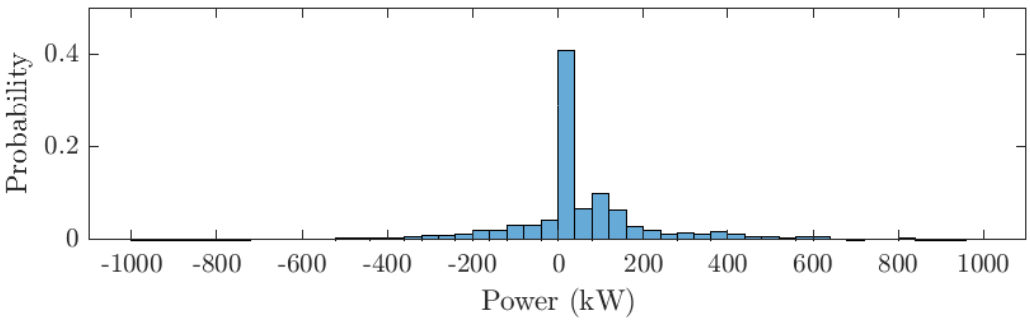

(d) UDDS HD (1060 s).

Figure 6.3: Probability distribution of HGV power requirement.

Due to the highly transient nature of all of the standardised drive cycles, the response of the SOFC system is expected to be relatively similar across each of them. Therefore, the WHVC is taken as reference case for further investigation, with the results and discussion presented in the following assumed to apply to the other drive cycles as well.

The control strategy presented in Section 5.7 is utilised in the following in order for the SOFC system to meet the HGV power requirements, whilst maintaining a single pass fuel utilisation (U_f) of 0.7, a stack temperature of 700°C, and a steam-to-carbon ratio (S/C ratio) of 2.5. The current, fuel, and anode off-gas recirculation (AOGR) flow rates are all manipulated with feed-forward controllers, as presented in Section 3.14. For simplicity, the air flow rate is manipulated with a feed-forward controller also.

The resulting electrical, chemical reaction, and thermal transients are shown in Figure 6.4, and are discussed in the following.

6.3.1 Chemical reaction and electrical transients

Rapid power changes by the SOFC system were required in Figure 6.2c to fulfil the power requirements of HGV following the WHVC. The SOFC current varies with power, and hence the rate of the electrochemical oxidation of hydrogen reaction varies also. The fuel flow rate is manipulated with the load to maintain a constant stack U_f of 0.7. Figure 6.4b shows that whilst U_f is maintained at 0.7 during periods of steady-state operation, there are significant and rapid changes in U_f during transients between 0.27 and 1.64. The volume inertia of the gases in the SOFC systems cause a delay in bringing fresh fuel to the anode, and therefore, during increasing power demand U_f overshoots up to a maximum of 1.64, and during decreasing power demand U_f undershoots down to a minimum of 0.27.

A U_f greater than 1 means that more fuel in the SOFC stack than is supplied to the anode, and therefore that the remaining fuel within the SOFC is consumed. This can occur until the hydrogen mole fraction starts to decrease, and eventually fuel starvation occurs. The U_f varies most rapidly within the motorway section during the final 300 seconds. The changes in U_f and associated increased consumption or depletion of different species at

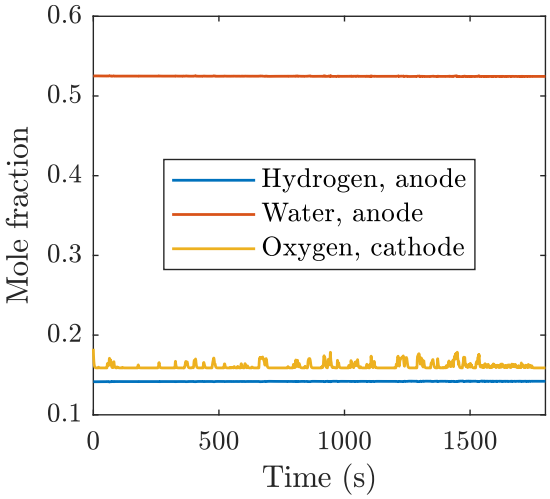

(a) Mole fraction.

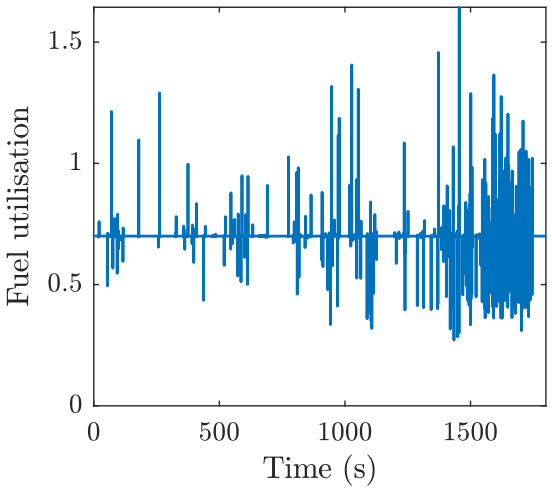

(b) Stack fuel utilisation.

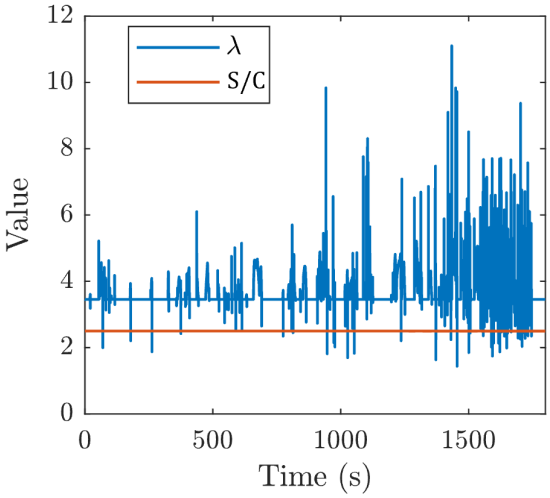

(c) λ and S/C ratio.

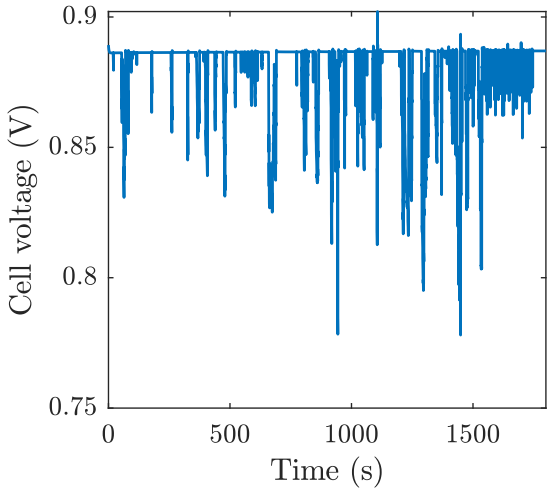

(d) Cell voltage.

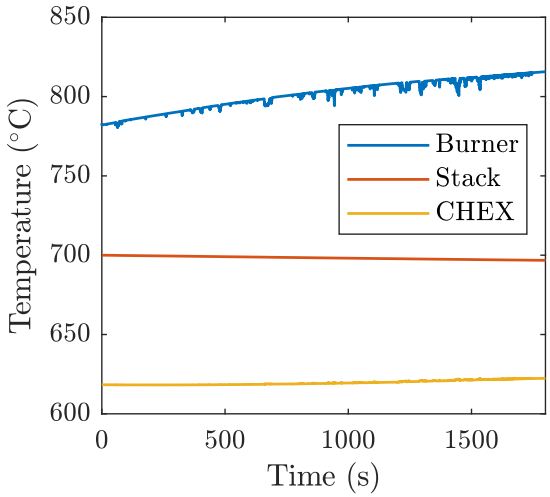

(e) Temperature.

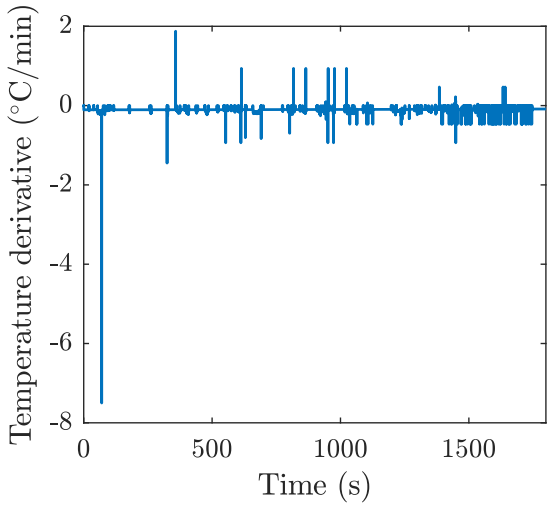

(f) $\mathrm{d}T_S/\mathrm{d}t$.

Figure 6.4: SOFC system performance for HGV propulsion following the WHVC.

the anode approximately 1 second before U_f returns to 0.7. During this short time frame, the volume of hydrogen and water at the anode is sufficient that their compositions do not change, and therefore their mole fractions at the anode shown in Figure 6.4a remains constant. Whilst the Table 3.1 listed a maximum U_f of 0.8, these results show that higher values of U_f may be possible provided the hydrogen mole fraction remains high enough to prevent fuel starvation. These results are in agreement with the controlled response investigated in Section 5.7, where the settling time of the chemical reaction dynamics were about 10 seconds, which is longer than the more rapid changes in U_f. However, in this model the mass transport of gases from the channels to the reaction sites on the electrode is neglected, so fuel starvation may occur more quickly than is suggested by the mole fractions in Figure 6.4a.

In a real SOFC stack there would be mass transport limitations, and the rapid changes in U_f could lead to localised fuel starvation at the anode. In addition, this SOFC system model neglects the lagging caused by the piping connecting each of the components. In a model which better accounts for the internal volume of all components, including the piping, a larger gas volume would likely be found, which would cause more inertia in the system, and which could lead to greater changes in mole fraction of hydrogen and water at the anode of the SOFC stack.

The AOGR flow rate is manipulated to maintain a constant S/C ratio of 2.5 at the anode inlet, as shown in Chapter 5. The volume of the gases at the anode and in the anode pre-heater which feeds it means that the mole fraction of water remains constant even during rapid changes in load, as shown in Figure 6.4a. Since the S/C ratio depends only on the relative mole fractions of water and methane at the anode inlet which remain constant, a constant S/C ratio is maintained in Figure 6.4c, in agreement with the controlled response investigated in Section 5.7.

The air flow rate is manipulated to maintain a constant stack temperature of 700°C. As the load increases, the required air stoichiometry (λ) to keep the stack temperature constant increases also. With the feed-forward controller, the λ varies significantly and

rapidly in direct response to the power requirement between 1.4 and 11 shown in Figure 6.4c. The mole fraction of oxygen at the cathode shown in Figure 6.4a varies more significantly than hydrogen and water at the anode. This is due to the large variation in λ shown in Figure 6.4c, and the cathode flow rate being significantly higher than the anode flow rate. The higher flowrate means residence times of gases at the cathode gas compartment is shorter than at the anode gas compartment. The oxygen mole fraction increases during periods of high λ. A minimum allowable λ of 2 was defined in Section 3.12 to avoid oxygen starvation. The λ drops below 2 only on a few occasions, and for very brief periods, and the oxygen mole fraction is maintained at a value of 0.17, which indicates that oxygen starvation would be avoided. The air blower and recirculation blower have been neglected in the dynamic SOFC system model. They are assumed to be able to switch power and vary the gas flow rate instantaneously. This is likely to be a reasonable assumption for the air blower, since the thermal transients are much slower. The rapid change in λ result from the feed-forward control strategy. Section 5.7 showed that a feedback controller approach would improve stack temperature control.

As the current density increases with power demand, the voltage losses increase with with fixed area specific resistance (ASR), and the voltage decreases, as per the current density-voltage characteristics of the SOFC stack. Therefore, the cell voltage shown in Figure 6.4d responds directly to the drive cycle. As the mole fractions of hydrogen, water, and oxygen all remain approximately constant in SOFC, no variation in the open circuit voltage (OCV) is observed.

In summary, U_f, λ and cell voltage respond instantaneously to the load, whilst the variation in gas composition is dampened by the inertia of the volume of within the compartments of the SOFC system including the stack. This means that fresh fuel, steam and air can be supplied before significant changes in average mole fraction at the anode and cathode are observed. The results show good agreement with the controlled response investigated in Section 5.7.

6.3.2 Thermal transients

The variation in the burner temperature, SOFC stack temperature, and air temperature at the cathode inlet are shown in Figure 6.4e. The air flow rate is manipulated to maintain a constant stack temperature of 700°C, but over the duration of the WHVC, the SOFC stack temperature decreases by 3°C. This is primarily caused by the thermal inertia of the burner. The initial temperature of the burner is found by defining the initial conditions of the SOFC system at steady-state conditions. However, the highly transient drive cycle leads to a gradual increase in burner temperature over the course of 1800 seconds. The cathode air temperature likewise increases by 4°C. Despite the SOFC stack and cathode air temperatures remaining almost constant during the drive cycle, the dynamics do lead to spikes in the time derivative of the stack temperature ($\mathrm{d}T_S/\mathrm{d}t$) shown in Figure 6.4f. All but one of the spikes are smaller in magnitude than the maximum value of $2\,^{\circ}\mathrm{C\,min^{-1}}$ defined in the operating window in Table 3.1. Highly transient operation with sharp temperature gradients would lead to accelerated ageing of the SOFC stack, and the SOFC system should be operated in a manner that reduces its load dynamics, and thus thermal transients. Stack testing under these duty profiles, could ascertain whether such a thermal response is acceptable. The drift in the stack temperature could be avoided with a feedback controller.

6.4 Power split in an SOFC-battery system

Section 6.3 showed that while the SOFC system performs relatively well under a highly dynamic drive cycle, it led to spikes in thermal gradients in the SOFC stack, which are likely to accelerate its ageing and reduce its lifetime. Highly dynamic drive cycles could also lead to fuel or oxygen starvation on the SOFC stack, although the results in Section 6.3 indicate these constraints are less critical, with the notable neglecting of mass transport limitations of at the electrodes.

Section 2.4 of the literature review presented SOFC systems using a battery to help

meet dynamic load requirements. Similarly here, a hybrid SOFC-battery system is used to meet the load requirements of an HGV for propulsion. The battery is modelled with a simple bucket model, which assumes that 70 % of regenerative braking power is captured, and 95 % of energy stored in the battery is delivered to the electric motor of the HGV [203].

Figure 6.5 shows the basic concept of the electrical power-split between the SOFC system and the battery, where:

- The SOFC system delivers electrical power to both the wheels to propel the vehicle and to the battery to charge it,
- When the power requirement of the vehicle is greater than that which can be provided by the SOFC system, the battery also provides electrical power to the wheels and discharges in the process,
- When the power requirement at the wheels is negative, the battery can recuperate some of that energy through regenerative braking, which causes the battery to charge,
- Although reversible solid oxide cells are proven technically, they are not viable for vehicle propulsion, and therefore the SOFC system is only able to deliver power, not receive it.

6.4.1 Sizing the SOFC system and battery

The power requirements for the three drive cycles were shown in Figure 6.2. The inclusion of a battery to meet the dynamic load allows for the SOFC system to be downsized by recuperating energy when the net power requirement is negative. In the extreme case investigated in this section, the SOFC system operates at constant power, and the battery fulfils all of the dynamic load requirements. The hybrid system is designed to operate in a charge sustaining strategy, and thus the SOFC system is sized such that the battery

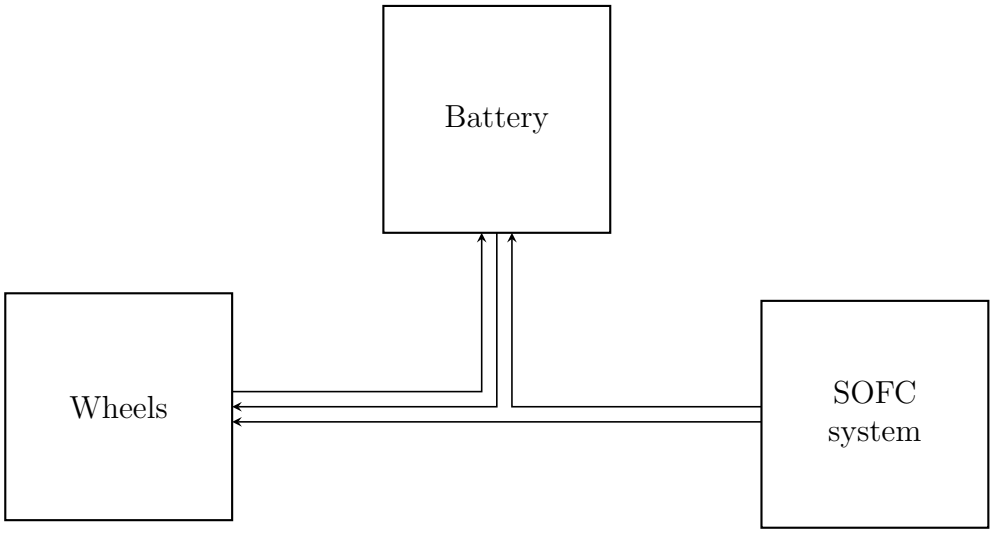

Figure 6.5: Power split schematic of the SOFC-battery hybrid system.

state-of-charge (SoC) at the end of the drive cycle is equal to that at the beginning of the cycle. The SOFC system operates continuously at its design load.

An energy balance calculates the power requirement P_{battery} of the battery from:

$$P_{\text{battery}}(t) = P_{\text{r}}(t) - P_{\text{sofc}} \tag{6.4}$$

The power requirement of the battery $P_{\text{battery}}(t)$ is the difference between the power supplied by the SOFC system, and the overall power requirement of the powertrain, at each point in time t. Power conditioning is modelled assuming a constant efficiency defined in Table 6.1. When $P_{\text{battery}}(t)$ is positive, the battery discharges, and when negative, the battery recharges.

A charge sustaining strategy for the battery is targeted. For each drive cycle, the constant SOFC system power P_{sofc} is found such that the energy stored within the battery at the end of the drive cycle $E_{\text{battery}}(t = t_{\text{end}})$ is equal to the amount of energy stored at the start, as calculated from:

$$E_{\text{battery}}(t = t_{\text{end}}) - E_{\text{battery}}(t = 0) = \int_{t=0}^{t=t_{\text{end}}} P_{\text{r}}(t) - P_{\text{sofc}}\, dt == 0 \tag{6.5}$$

The constant SOFC power P_{sofc} required to meet the equality condition in (6.5) is solved

for each drive cycle. The SOFC power chosen is the maximum from the four drive cycles, and applied to each of the four drive cycles. In this analysis, the maximum SOFC power requirement is calculated to be 54 kW to fulfil the requirements of the HHDDT drive cycle which is the most energy demanding.

This constant SOFC power is applied to all four of the drive cycles and the variation in battery energy is calculated from:

$$E_{\text{battery}}(t) = \int_{t=0}^{t=t} \left(P_{\text{r}}(t) - P_{\text{sofc}}\right)\, dt \tag{6.6}$$

The battery capacity is calculated such that the battery SoC remains between its lower and upper limits during all four drive cycles. Those SoC limits are defined as 10 % and 90 % SoC, respectively.

$$0.1 \leq SoC_{\text{battery}}(t) \leq 0.9 \tag{6.7}$$

A battery capacity of 157 MJ or 46 kW h is found to be required to ensure that the battery SoC remains within those limits for all four drive cycles, assuming the battery starts the cycle at 50 % SoC.

When operating under the HHDDT cycle, which is the most demanding, the SOFC system operates at constant power, and at the end of the duty profile, the battery SoC will have returned to 50 %. Therefore the SOFC system operates under steady-state conditions. The variation in the battery SoC during the HHDDT drive cycle is shown in Figure 6.6. During the first 27 minutes the HGV is either stationary or in urban driving and the power requirements are relatively low.

Therefore, the battery is charged until it reaches 90 % SoC after 27 minutes. After 27 minutes, the HGV switches to motorway driving, and the average power requirements increase significantly. Therefore, the battery is used to provide a significant proportion of the power and it discharges reaching 31 % SoC after 51 minutes. During the final 9 minutes the HGV slows and returns to urban driving, allowing the battery to recharge,

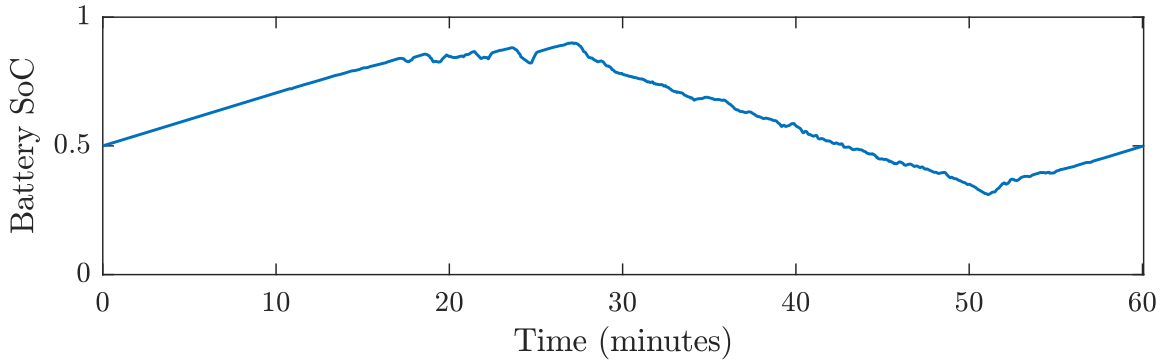

Figure 6.6: Variation in battery SoC for the HHDDT drive cycle.

and returning to 50 % SoC after the full 60 minute drive cycle.

For the three other drive cycles, the SOFC system tends to deliver more power than is required by the vehicle, and the battery charges. Therefore a state machine is implemented, as shown in Figure 6.7. The SOFC system operates initially at its nominal power of 54 kW until the SoC of the battery reaches its maximum allowable value. Then, the power of the SOFC system is ramped down until it reaches its minimum power of 13 kW; defined as the SOFC system power at which an λ of 2 is required to maintain the stack temperature, calculated based upon the lookup table. Under these conditions, the battery discharges until it reaches its minimum SoC, at which point the SOFC system ramps back up to its nominal power. The state machine continues until the drive cycle is complete.

It is worth noting that the energy management strategy includes no predictive control, so the SOFC power is varied between these two powers based only on the battery SoC, even if for a drive cycle a more moderate power would be best suited to maintaining the battery SoC. The introduction of a predictive energy management strategy to limit the SOFC stack power is beyond the scope of this thesis, but could further help to improve the performance of a hybrid SOFC-battery powertrain under a range of drive cycles, such as those that include higher or lower proportions of urban driving.

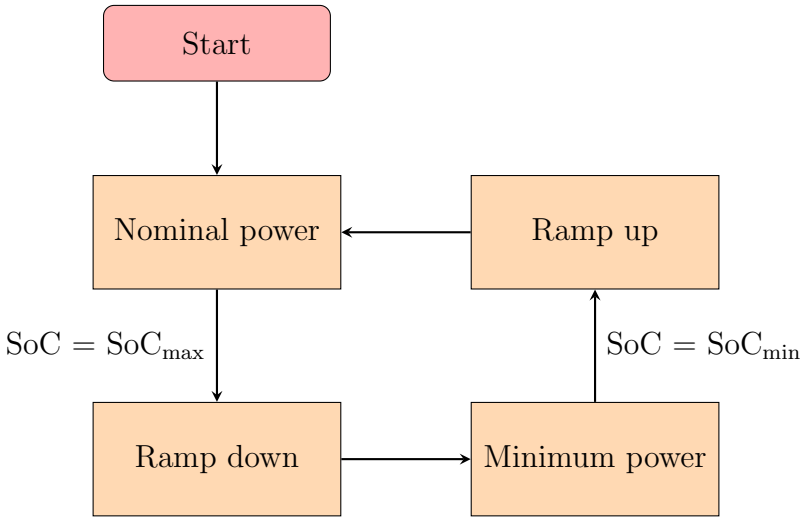

Figure 6.7: State machine of SOFC-battery hybrid system.

6.4.2 Dynamic SOFC performance with a state machine

To investigate the dynamic performance of the SOFC system, a single cycle of the state machine shown in Figure 6.7 is simulated, and the results are presented in Figure 6.8. Figure 6.8a shows that the SOFC stack was operated at its nominal power of 54 kW for the first 20 minutes, before ramping down to the minimum SOFC stack power of 13 kW. The ramp down took 5 minutes, and was followed by operation at the minimum SOFC stack power for the next 25 minutes. Following that, the SOFC stack power ramped back up to its nominal value over 5 minutes. During the remaining 25 minutes, the SOFC remained at its nominal value of 54 kW. The dynamic response of the SOFC system will be investigated in the following.

The current density reduced with the defined stack power. Therefore, the voltage losses decreased, and hence the cell voltage in Figure 6.8b increased from 0.69 V to 0.87 V during ramp-down. During ramp-up, the cell voltage reduced back down to 0.69 V.

The fuel and AOGR flow rates were manipulated with the feed-forward controllers defined in Section 3.14 to keep U_f and S/C ratio constant at 0.7 and 2.5, respectively. Figure 6.8c shows that this was achieved well. As a result, the mole fractions of hydrogen and water at the anode remained constant, as shown in Figure 6.8d.

The air flow rate was manipulated to control the stack temperature with the feedback

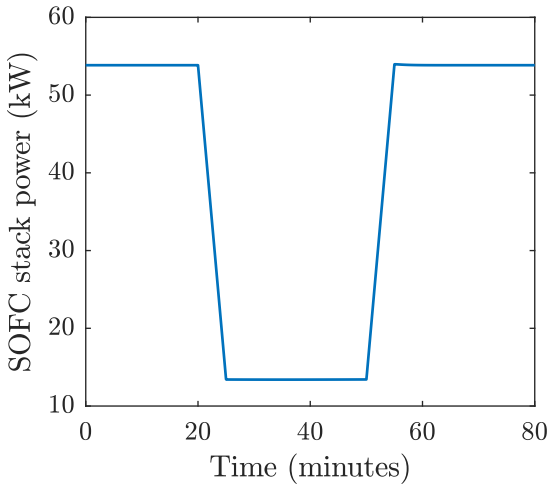

(a) Stack power.

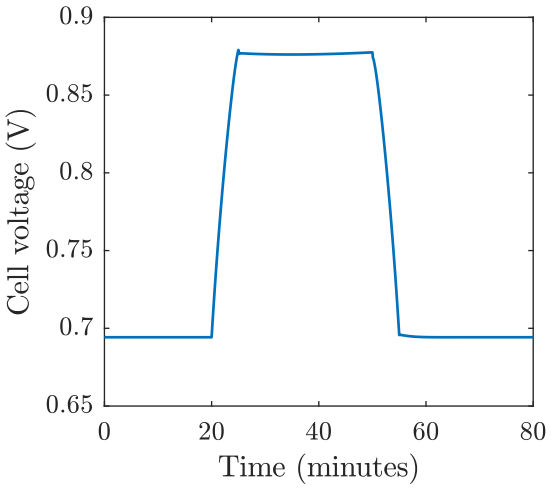

(b) Cell voltage.

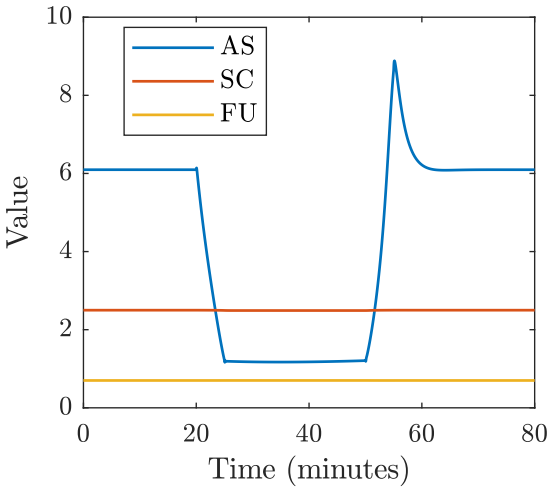

(c) AS, SC and FU.

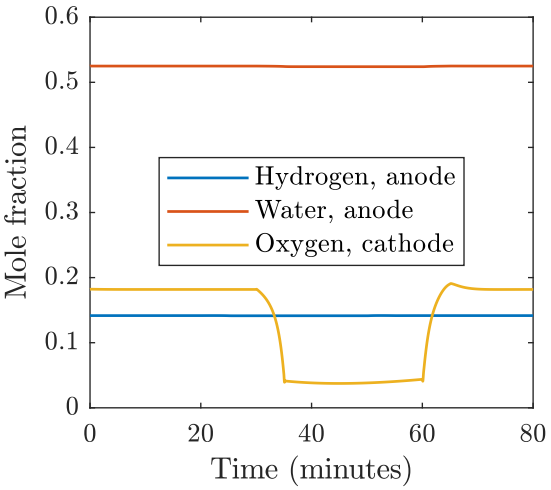

(d) Mole fraction.

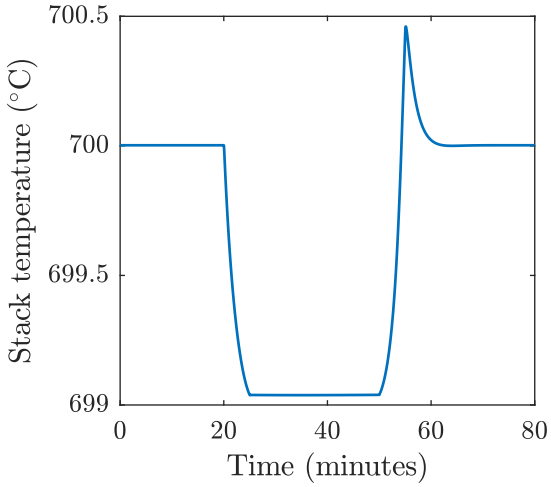

(e) Stack temperature.

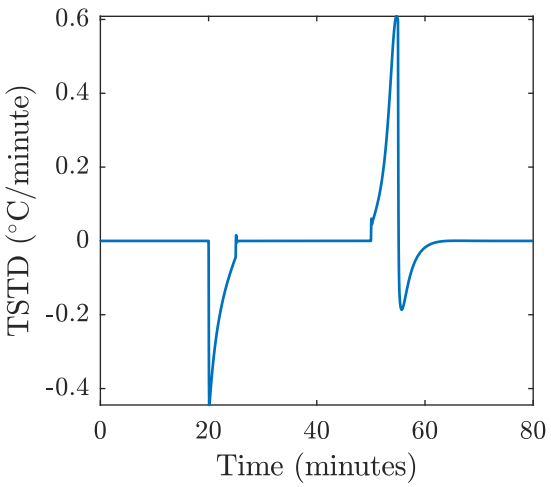

(f) $\mathrm{d}T_S/\mathrm{d}t$.

Figure 6.8: Response of SOFC system to ramp down and ramp up.

controller presented in Section 3.14. This caused the λ to decrease from 6 to 1.2 during ramp-down, as shown in Figure 6.8c. The λ decreased below 2 is despite the minimum stack power of 13 kW being chosen for a specified λ of 2. This is due to the inconsistency of the minimum stack power being calculated based on the lookup table for the feed-forward controller previously, but the air flow rate being controlled with the feedback controller here. Consistent implementation of the air flow rate control would ensure that the λ does not decrease below 2. As a result of the decrease in air flow, the oxygen mole fraction at the cathode in Figure 6.8d decreased from 0.18 to 0.04. Such a low oxygen mole fractions risks localised oxygen starvation at the cathode outlet, and shows the importance of maintaining the λ above 2.

As a result of the manipulation of the air flow rate during ramp-down, the stack temperature decreased from 700°C to 699°C in Figure 6.8e. The offset of 1°C was introduced by the proportional feedback controller. The thermal response during ramp-down was fast, with no overshoot, and a $\mathrm{d}T_S/\mathrm{d}t$ of $0.43\,^{\circ}\mathrm{C\,min^{-1}}$ observed, as shown in Figure 6.8f. This shows that the air flow rate control worked well to minimise thermal transients in the SOFC stack.

During ramp-up, λ overshot from 1.2 up to a maximum of 9 during the 5 minutes, before relaxing to its nominal value of 6, as shown in Figure 6.8c. This was due to the inertia of fuel supply to the SOFC stack when increased dynamically with stack current, and was also observed in Chapter 5. This overshoot could be reduced with a more sophisticated feedback controller, but equally shows that balance of plant components such as the air blower may need to be oversized to adequately manage highly dynamic operation of the SOFC stack.

As a result, the stack temperature in Figure 6.8e increased from 699°C initially up to a maximum of 700.5°C during the 5 minutes of ramp-up, before returning to 700°C over the following 10 minutes. The overshoot of nearly 0.5°C, resulted in a larger magnitude of $\mathrm{d}T_S/\mathrm{d}t$ of $0.61\,^{\circ}\mathrm{C\,min^{-1}}$ during ramp-up than during ramp-down. However, the $\mathrm{d}T_S/\mathrm{d}t$ remained well below its maximum value of $2\,^{\circ}\mathrm{C\,min^{-1}}$. This shows that the feedback

controller was effective at reducing thermal gradients in the SOFC stack.

During ramp-down and ramp-up, U_f, S/C ratio and SOFC stack temperature were all maintained, and the $\mathrm{d}T_S/\mathrm{d}t$ was kept within an acceptable range. The λ dropped below 2 to 1.2, but with consistent implementation of the controller design, this could be avoided. Potential improvements to the feedback controller, such as implementing integral and derivative control to remove the offset and reduce the overshoot, are beyond the scope of this thesis. Nevertheless, the results here confirm the application of the feedback controller presented in Section 3.14 for HGV propulsion with an SOFC-battery hybrid system.

6.4.3 Performance for the standardised drive cycles

This section applies the state machine to the three other standardised drive cycles, which have lower average power requirements than the HHDDT drive cycle. Figure 6.9 shows the variation in the battery SoC and the SOFC stack power for the CUEDC NCH, UDDS HD and WHVC standardised drive cycles repeated over a four hour period. A four hour period was chosen to represent half a day of operation of an HGV. The SOFC stack produced 54 kW nominal power, and the battery had a capacity of 45 kW h, as calculated for the power requirements of the HHDDT drive cycle in Section 6.4.1.

Figure 6.9 shows that in each of the three drive cycles, the SOFC stack initially provided a nominal power of 54 kW. The battery was charged until its SoC reaches 80 %. The SOFC stack power then ramped down to its minimum power of 14 kW over 5 minutes. The battery was subsequently discharged until its SoC reached 30 %, and the SOFC stack power ramped back up to its nominal power over 5 minutes. This process repeated itself, as per the state machine defined in Figure 6.7.

The maximum and minimum battery SoC for each of the three drive cycles in Figure 6.9 varied. This was because of differing vehicle power requirements over the time periods for which the ramp downs and ramp ups of the SOFC stack power occurred. For example, during ramp-ups in SOFC stack power in the CUEDC NCH drive cycle in

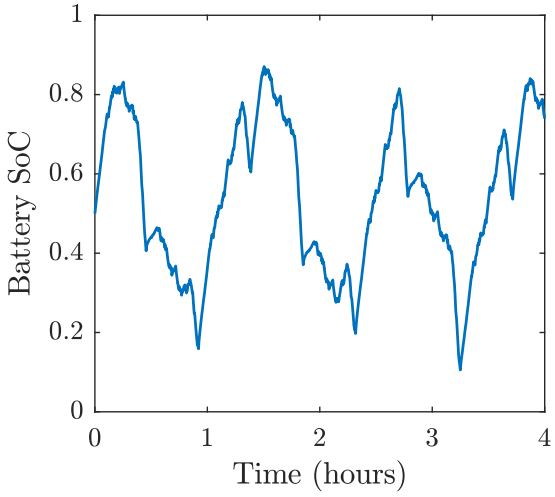

(a) CUEDC NCH.

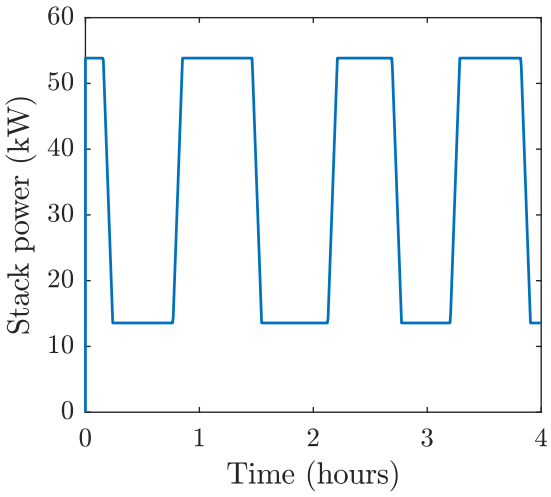

(b) CUEDC NCH.

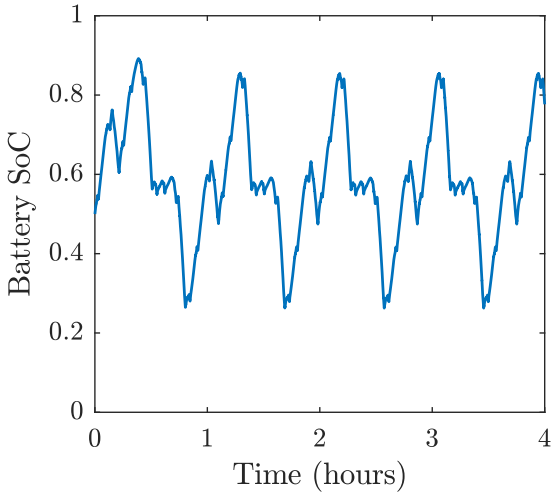

(c) UDDS HD.

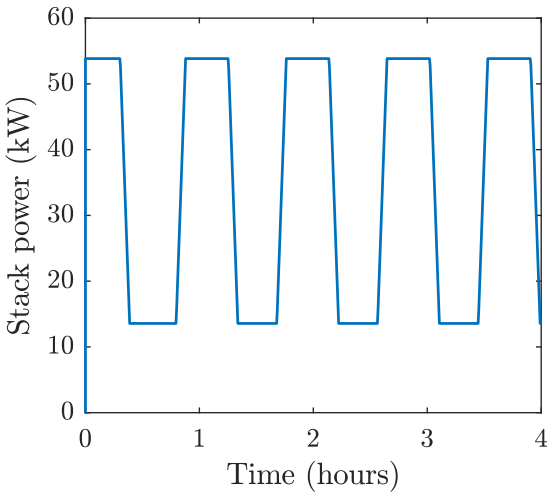

(d) UDDS HD.

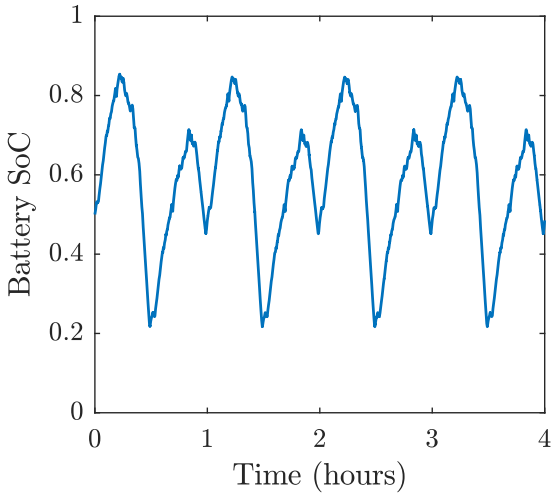

(e) WHVC.

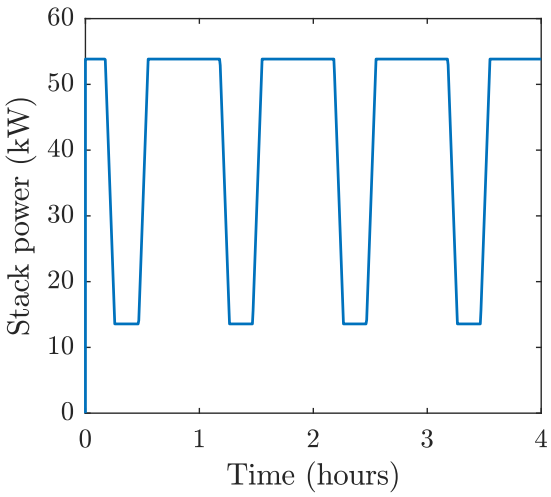

(f) WHVC.

Figure 6.9: Variation in battery SoC and SOFC stack power.

Table 6.2: Time spent by the SOFC stack in each operating state.

Drive cycle	Time spent in hours at the		Number of	
	Nominal power	Minimum power	Ramp downs	Ramp ups
HHDDT	4	0	0	0
CUEDC NCH	1.79	1.63	4	3
UDDS HD	1.81	1.44	5	4
WHVC	2.52	0.82	4	4

Figure 6.9a, the vehicle accelerated and depleted the battery SoC down to a minimum of 0.1. After 5 minutes, the SOFC stack reached nominal module power, the vehicle stopped accelerating, and the battery recharged. In all three cases, the battery SoC limits of 0.9 and 0.1 were not exceeded.

Table 6.2 shows the time spent by the SOFC stack in each operating state over the four-hour period, and the number of ramp ups and ramp downs, as illustrated in Figure 6.9. The SOFC stack power was calculated for a charge sustaining strategy for the HHDDT drive cycle, and therefore for that cycle the SOFC stack operated constantly at the nominal power over the four-hour period.

The other three drive cycles had lower power requirements, and therefore spent periods operating at minimum SOFC stack power, as shown in Figure 6.9. Of the three other drive cycles, WHVC had the highest average power requirements, and therefore the SOFC system spent 2.52 hours at the nominal module power. Four periods of operation at the minimum SOFC stack power were required to ensure that the battery SoC did not exceed 0.9, with a cumulative duration of 0.82 hours.

Both the CUEDC NCH and UDDS HD drive cycles had lower average power requirements, and therefore both spend less than 50 % of their duration at the nominal module power, cumulatively about 1.8 hours. Since the power requirements of the UDDS HD drive cycle were more dynamic than that of the CUEDC NCH, an additional ramp down and ramp up of the SOFC stack power were required for the UDDS HD drive cycle.

This analysis shows that the battery SoC can be maintained within its limits with a state machine that alternates the SOFC stack power between its nominal and minimum

values. The average power requirements of each drive cycle can be observed based on the proportion of time that the SOFC system operates at its nominal power. Drive cycles such as the UDDS HD with more extreme dynamics, required more frequent ramp ups and ramp downs. The three drive cycles with lower average power requirements required approximately one ramp up and one ramp down per hour of vehicle operation.

The liquefied natural gas (LNG) consumption for the four drive cycles was on average 29 litre per 100 km, where LNG was assumed to be 100 % methane. The average fuel consumption of new diesel HGVs in 2015 in the European Union and the United States in 2015 was about 38 litre per 100 km [204]. Therefore, switching from diesel to SOFC-battery hybrid powertrains with LNG fuel offer potential fuel savings of 25 %.

One potential application for SOFC systems is refrigerated transport on HGVs. An analysis by Venkataraman et al. [25] showed that a thermal power of approximately 10 kW would be required for a refrigerated HGV. This suggests that the 50 kW SOFC system used for vehicle propulsion would be of an appropriate capacity to comfortably provide the thermal power for a vapour absorption refrigeration system.

6.4.4 Comparing to power delivery by the SOFC system

Hybridising the SOFC system with a battery, as presented in this section, has a number of significant advantages over the strategy presented in Section 6.3, where 100 % of the power demand was delivered by the SOFC system:

- The SOFC system components including the SOFC can be downsized significantly. This reduces the weight and volume footprint of the SOFC system, and saves on the capital cost of the SOFC system components themselves.

- When operating under the HHDDT drive cycle, which includes significant motorway driving, the SOFC system operates constantly at its nominal load, which minimises degradation and maximises lifetime of the SOFC system.

- Under the other drive cycles, such as the CUEDC NCH drive cycle, a state machine,

rotates the SOFC stack power between its nominal and minimum values which maintains the battery within its SoC limits. The dynamic response of the SOFC system is defined by the ramp-rate during ramp-down and ramp-up. The dynamic response can be well predicted. Slowing down the ramp-rate increases the required battery capacity required to stop the SoC limits being crossed (especially the minimum SoC), but reduces the thermal gradients in the SOFC stack. Therefore, the smaller the allowable thermal gradients in the SOFC stack, the larger the battery must be.

One potential improvement to the state machine would be to vary the SOFC system power based upon the SoC of the battery. This would increase the dynamic operation of the SOFC system but allow for the battery to be downsized. This will be discussed as potential future work in Chapter 8.

6.5 Long term performance

In this section, the long term performance of the 54 kW SOFC system is considered. The degradation model outlined in Section 3.6.2 is implemented, with an ASR degradation rate of $10\,\mathrm{m\Omega\,cm^2\,kh^{-1}}$.

Figure 6.10 shows the variation in ASR over the lifetime of the the SOFC system. With a constant operating temperature of 700°C in Figure 6.10b, the ASR in Figure 6.10a increased from $0.42\,\Omega\,\mathrm{cm^2}$ to $0.77\,\Omega\,\mathrm{cm^2}$ over more than 5 years or around 50,000 hours of operation. Figure 6.10a also shows that to maintain the ASR constant at $0.42\,\Omega\,\mathrm{cm^2}$, the SOFC stack temperature would have to increase by 80°C to 780°C during the 5 years of operation.

Figure 6.11 shows two potential operating strategies for long term SOFC system operation to account for degradation. In the first operating strategy, the SOFC stack temperature and current density are held constant. The increase in ASR with time at constant temperature shown in Figure 6.10a, led to declining cell voltage, as shown in Figure 6.11b. Over 50,000 hours of operation, the cell voltage decreased from 0.7 V to 0.5 V. Therefore,

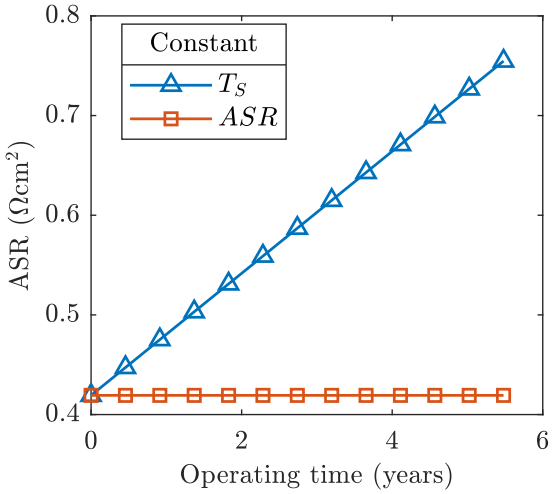

(a) Variation in ASR with time at fixed T_S.

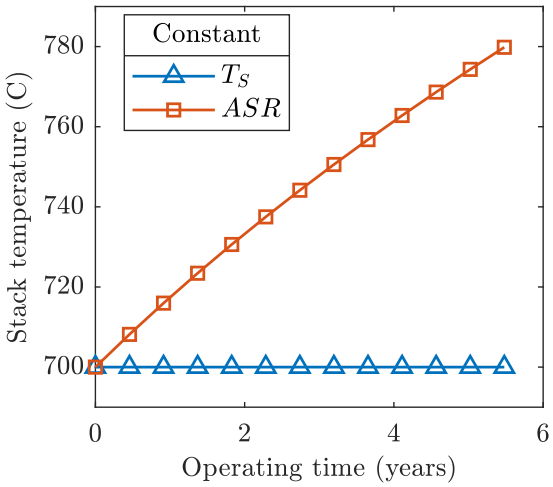

(b) Variation in T with time at fixed ASR.

Figure 6.10: Variation in ASR and SOFC stack temperature during long-term operation.

the SOFC stack power was no longer able to achieve 54 kW, and as shown in Figure 6.11c, its power reduced to 38 kW after 50,000 hours of operation. Likewise, the SOFC stack electrical efficiency in Figure 6.11d decreased from 57 % to 41 % over the operating period.

In the second operating strategy, it was attempted to maintain a constant SOFC stack power of 54 kW throughout the SOFC lifetime. This was achieved through an increase in the SOFC stack operating temperature in Figure 6.10b to maintain the ASR in Figure 6.10a. The increased SOFC stack operating temperature reduced the OCV, as per Equation (3.24), and therefore, the current density in Figure 6.11a increased from 0.60 A cm^{-2} to 0.65 A cm^{-2} over the course of the stack lifetime to compensate. Figure 6.11c shows that the stack power could be maintained at 54 kW, with a slight reduction in efficiency due to the increased fuel consumption with current density to maintain a U_f of 0.70.

6.5.1 Implications for vehicle operation

The two operating strategies present some challenges for SOFC operation on a vehicle. The declining SOFC power output with the first operating strategy meant that the SOFC would no longer be able to maintain a charge sustaining energy management strategy when conducting the HHDDT drive cycle. One possible workaround is to oversize the SOFC

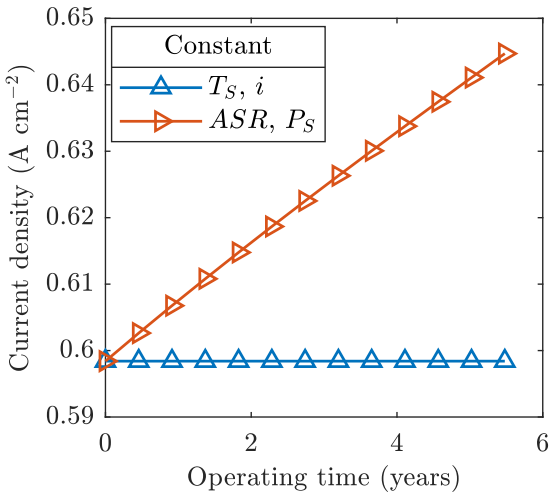

(a) SOFC current density.

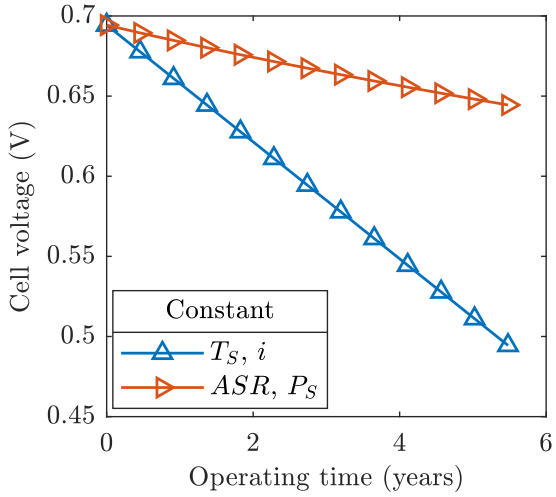

(b) SOFC cell voltage.

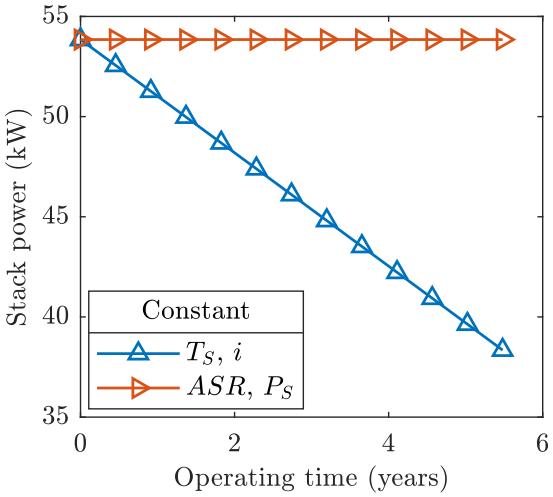

(c) SOFC stack power.

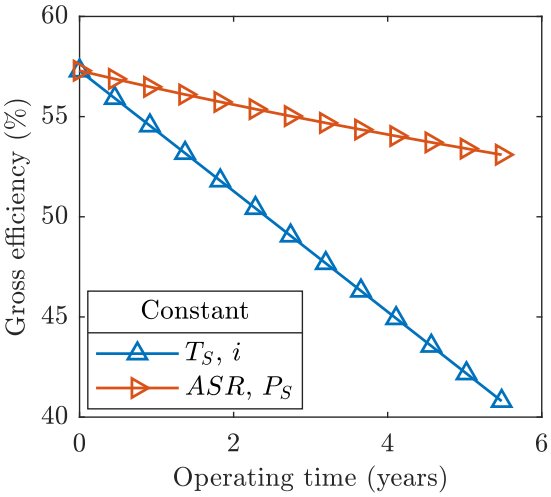

(d) SOFC gross efficiency.

Figure 6.11: Degradation performance.

stack at beginning of its life, to ensure that it still able to achieve 54 kW power output at the end of its operating life.

Whilst the second operating strategy is able to maintain the SOFC stack power this is associated with an 80°C increase in the stack operating temperature. Such an increase in stack operating temperature may lead to higher degradation rates, and other performance issues. In practice, a combined approach could be used, where the SOFC stack temperature is increased as far as allowable during the stacks operating lifetime. At the point in which the SOFC stack can no longer be operated hotter, it should switch to constant temperature mode. The subsequent reduction in SOFC power output can be factored

into the sizing of the SOFC system before installation in the vehicle.

Chapter 7

HGV operation over one week

Chapter 6 presented the performance of the SOFC system in response to the power requirements of a heavy goods vehicle (HGV) following a number of standardised drive cycles, each about one hour in duration. This chapter investigates the performance of the SOFC system for propulsion of an HGV over a one-week period, in which the HGV is assumed to be:

- Operational from 08:00 hours to 16:00 hours on weekdays, and
- Stationary with no power requirement overnight and over the weekend.

These operating hours over a one week period are a conservative interpretation of the Regulation 561/2006 of the European Union, which permits up to nine hours driving time per day, and an average of 45 hours driving time per week [205]. A conservative schedule is chosen because longer periods where the vehicle is stationary are expected to result in larger thermal cycling.

The hybrid SOFC-battery powertrain, as presented in Section 6.4, is considered. During HGV operation, the SOFC system provides a constant output of 54 kW, and the battery meets the dynamic load requirements. The resulting SOFC system power demand is shown in Figure 7.1.

As discussed in Section 2.6 of the literature review, when power is not required, the SOFC system can either be shut down or enter hot standby mode. In vehicle applica-

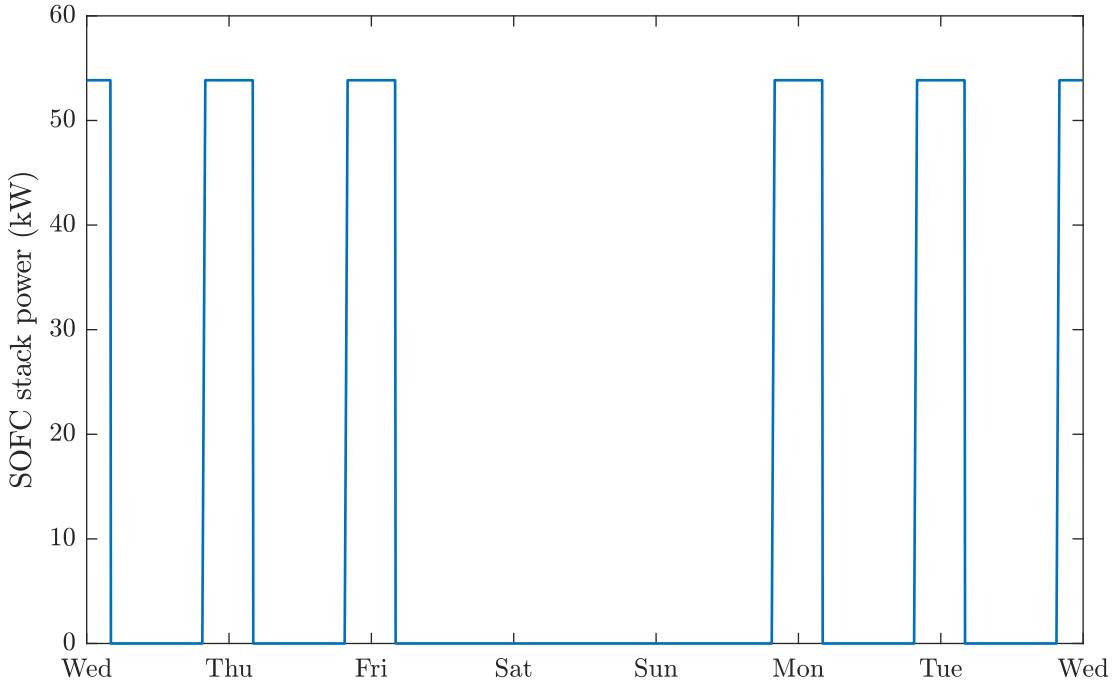

Figure 7.1: Power requirements of the solid oxide fuel cell (SOFC) system over a one-week period.

tions, hot standby is considered to be undesirable due to the additional fuel consumption required. In the following, therefore, shut-down of the SOFC system is investigated when there is no power demand overnight and over the weekend. Following shut-down, the SOFC system cools down naturally. When power is next required, the SOFC system starts back up. Based on the findings of the literature review in Section 2.6, it is assumed that start-up can commence immediately provided the stack temperature is above 600°C. At low stack temperatures, the area specific resistance (ASR) is raised, and SOFC load operation more effective at heating the stack than external heating [115]. This has the benefit that with sufficient insulation, the stack proceed straight to start-up after cool-down. If not, the SOFC system components must heat up sufficiently beforehand.

To investigate shut-down, cool-down, and start-up, some changes to the methodology are made in this chapter. They are outlined in Section 7.1. Sections 7.2 and 7.3 investigate the system response during shut-down and cool-down, respectively. Start-up following both overnight and weekend cool-down is investigated in Section 7.4.

7.1 Changes to the methodology

The SOFC system model introduced in Chapter 3, and presented in Chapters 4 to 6 is utilised in the following, albeit with three differences:

- The Nernst weighting factor in Equation (3.25) is set to zero to avoid instability in the dynamic model when simulating shut-down and start-up. This means the average composition at the anode and cathode are equal to that at their respective outlets. Therefore, the composition at the anode and cathode inlets are not accounted for in the Nernst equation, and the open circuit voltage (OCV) is calculated to be lower than in Chapters 4 to 6. This assumption is unlikely to impact the results presented in this chapter, since the focus is not on load operation, and instead the dynamic response during cool-down and start-up. Accurate estimation of the OCV has limited impact on the cases studied within this chapter.

- The lookup tables introduced in Section 3.14 for feed-forward control defined the variation in current, fuel flow, and anode off-gas recirculation (AOGR) flow between the minimum stack power and the nominal stack power during load operation. In this chapter, the lookup tables are extrapolated from the minimum stack power to zero. For simplicity, over this lower region of the lookup table, the current, fuel flow rate, and AOGR flow rate are defined to be directly proportional to the power requirement of the SOFC system. The aim of the controller is to move the SOFC system to an operating region where the process parameters can be maintained as fast as possible, since longer operation at such low current densities not possible without additional heating.

- Due to the significant variation in stack temperature during start-up and shut-down, the air flow rate is varied using the feed-forward control approach, which is a lookup table based upon the stack power demand. The feedback control presented in Section 3.14 does not work for start-up and shut-down, because it requires the stack temperature to be close to its design temperature. The drawback of the feed-

forward approach is that it results in larger stack temperature gradients during start-up and shut-down.

With these assumptions, the modelling results for shut-down, cool-down, and start-up are presented in the following.

7.2 Shut-down

In this chapter, the SOFC system is assumed to operate at constant power of 54 kW whilst the vehicle is operational, since this was the required power of the SOFC system in Chapter 6. At 16:00 hours each weekday, power is no longer required by the vehicle. To shut down the SOFC system, the current, fuel flow rate, air flow rate, and AOGR flow rate are switched off over a duration of one second. Because the shut-down is near instantaneous, the thermal transients of the SOFC system are negligible. There are, however, chemical reaction and and electrical transients observed in the SOFC stack, both of which are shown in Figure 7.2, and will be discussed in the following.

7.2.1 Instantaneous response

When the SOFC system is switched off at 16:00 hours, the cell voltage in Figure 7.2a increases instantaneously from the operating voltage of 0.67 V to an OCV of 0.91 V, an increase of 0.25 V. This follows the current density-voltage characteristics of the SOFC stack defined in Section 3.6.

7.2.2 Response over the following 20 minutes

Over the subsequent minutes, chemical reaction transients are observed. With no fuel flow after shut-down, the anode compartment contains a static volume of gas, and hence transients in composition shown in Figure 7.2b are much slower than shown in Chapter 5 with a relaxation time of about 4 minutes.

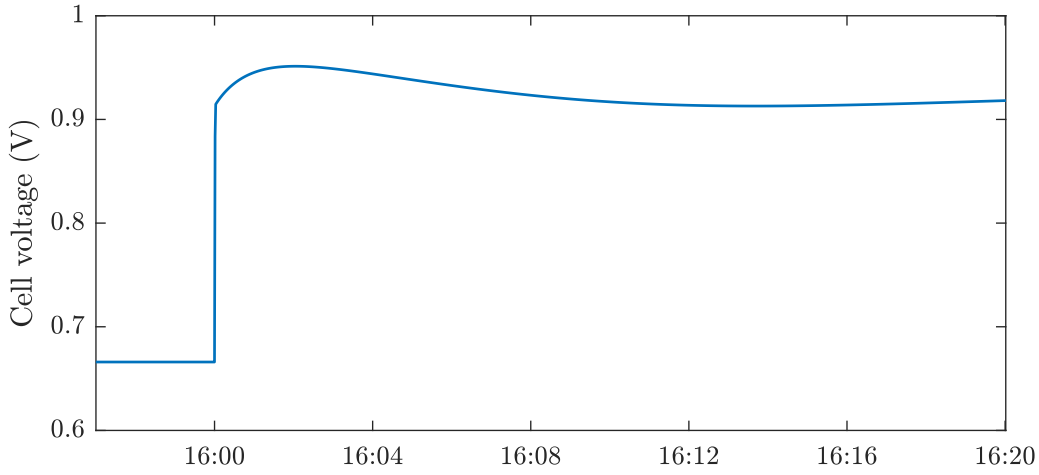

(a) Cell voltage.

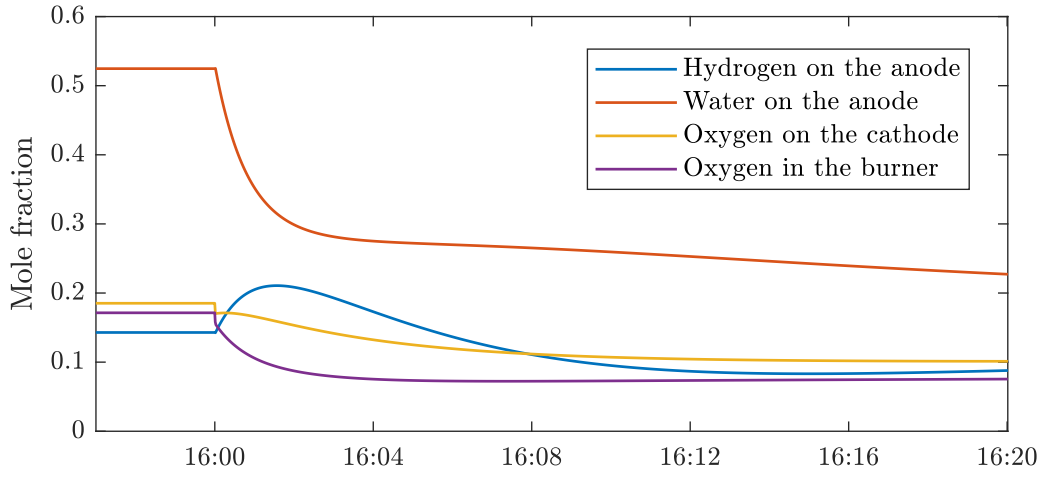

(b) Stack and burner composition.

Figure 7.2: The electrical and material response during shut-down.

With no current being drawn from the SOFC, the consumption of hydrogen through the electrochemical oxidation of hydrogen (H2X) reaction stops at 16:00 hours. However, any leftover methane at the anode is still consumed through the methane steam reforming (MSR) reaction. The MSR reaction consumes water and produces hydrogen, and hence the water and hydrogen mole fractions, in Figure 7.2b, decrease from 0.52 to 0.30, and increase from 0.14 to 0.21, respectively, over the first two minutes until 16:02 hours. This change is influenced also by the equilibrium position of the water gas shift (WGS) reaction. The decrease in the water mole fraction, and increase in the hydrogen mole fraction both decrease the equilibrium constant of the WGS reaction from Equation (3.7). This favours the reverse WGS reaction, and the conversion of hydrogen back to water.

Even after 16:04 hours, a slow variation in the gas composition is observed in Figure 7.2b. The cause of this behaviour is natural convection accounted for in the gas compartment model in Simscape presented in Section 3.3. This phenomenon exists for the case of no flow between components of the SOFC system; in particular, between the burner, the SOFC stack, and the heat exchangers. The transients here are suspected of being exaggerated due to the relatively small internal gas volume of the overall SOFC system, since no consideration is made to the interconnecting pipes between components.

Any remaining hydrogen or carbon monoxide at the burner is combusted, and hence the oxygen mole fraction at the burner slowly decreases from 0.18 to 0.08 at 16:04 hours, at which point the combustion reactions are complete. Over the subsequent 20 minutes, natural convection between the cathode and the burner causes the oxygen mole fractions at the cathode and in the burner to tend towards each other or equilibriate out to about 0.10 if return flow through the exhaust pipe is neglected.

The initial sharp decrease in water mole fraction from 0.52 to 0.30 over the first two minutes after shut-down in Figure 7.2b causes the OCV, and hence cell voltage in Figure 7.2a, to increase from 0.91 V to 0.95 V. As the hydrogen and oxygen mole fractions subsequently decrease through natural convection, on the anode and cathode, respectively, in Figure 7.2b, the cell voltage in Figure 7.2a decreases until a local minimum of 0.91 V is reached at 16:14 hours. After this point, the thermal transients associated with cool-down take over, and the composition in Figure 7.2b stabilises. The thermal transients associated with cool-down will be discussed in Section 7.3.

The trend in gas composition in Figure 7.2b indicates that the system can be safely shut down within 1 second.

7.3 Cool-down

As discussed in Section 2.6.2 of the literature review, the cool-down characteristics of an SOFC system depend upon the insulation and mass of the system components, and

Table 7.1: Temperature and voltage values before and after cool-down.

	Before	Overnight	Weekend
Stack temperature	700°C	654°C (−46°C)	523°C (−178°C)
Burner temperature	778°C	699°C (−79°C)	542°C (−236°C)
AHEX temperature	600°C	504°C (−95°C)	331°C (−269°C)
CHEX temperature	600°C	552°C (−48°C)	430°C (−170°C)
Open cell voltage	0.913 V	0.958 V (+0.045 V)	1.005 V (+0.092 V)

on how long the system is left idle for. For application in an HGV, two scenarios are considered:

1. 16 hours of cool-down between 16:00 hours on a weekday afternoon to 08:00 hours the following morning, and

2. 2 days and 16 hours of cool-down between 16:00 hours on Friday afternoon and 08:00 hours on the following Monday morning.

For the SOFC-battery hybrid system presented in Section 6.4, an SOFC system of 54 kW was required. The solid heat capacity of each component, insulation thickness, and insulation thermal conductivity of the SOFC system were all defined in Table 3.2.

The mass of each component and the outer surface area of the insulation were calculated based upon the scaling factors presented in Table 3.3. For a 54 kW SOFC system, the insulation surface area was calculated to be 1.12 m^2, and the SOFC stack, burner, anode heat exchanger (AHEX), and cathode heat exchanger (CHEX) were estimated to have masses of 154 kg, 43 kg, 28 kg, and 78 kg, respectively. As discussed in Chapter 3, the four hot box components in the SOFC system were assumed to be perfectly insulated from each other, and their heat losses were to the surroundings only. For simplicity, the heat transfer area for the heat losses through the insulation were assumed to be shared equally between the four components. This allowed calculation of the variation of their temperatures during cool-down without definition of the system geometries.

The variation in the temperatures of each component during cool-down is calculated from Equation (3.17). The temperatures of the SOFC system components before and

after cool-down, both overnight and over the weekend, are shown in Table 7.1. Following overnight cool-down, the stack temperature decreased to 652°C, 48°C below its operating temperature, so start-up of the SOFC system could start immediately. Following the weekend cool-down, the stack temperature decreased to 522°C, 178°C below its operating temperature, and therefore heat-up of the SOFC system was required before start-up.

In a real SOFC system, the hot components are typically housed within the same insulation. Therefore thermal coupling between the components means that the components would likely tend towards the same temperature during cool-down. Due to having the highest mass, the variation in the stack temperature is expected to dominate. However, the impact of this is not investigated further in this thesis, as to avoid definition of the hotbox geometries. Accurate estimation of the stack temperature is seen as the most critical to the following analysis.

7.4 Start-up

In this section the performance of the SOFC system during start-up is investigated. Start-up of the SOFC system involves ramp-up of the stack power from zero to its nominal value of 54 kW, and the accompanying flows of fuel, AOGR, and air.

Based on Section 2.6.3 of the literature review, heat-up of the SOFC system is required if the stack temperature falls below 600°C during cool-down, which Section 7.3 showed to be the case during weekend cool-down. As discussed in Section 2.6 of the literature review, heat-up of the SOFC system can be achieved either by burning fuel in a burner, or through electrical heating using heating elements situated within or around components of the SOFC system. In the powertrain simulated in Section 6.4, a battery was included to meet the transient power demands. For this reason the possibility of using chemical energy stored within the battery to heat the SOFC system electrically will be investigated in the following.

Based on the results of the cool-down in Section 7.3, two scenarios for start-up are

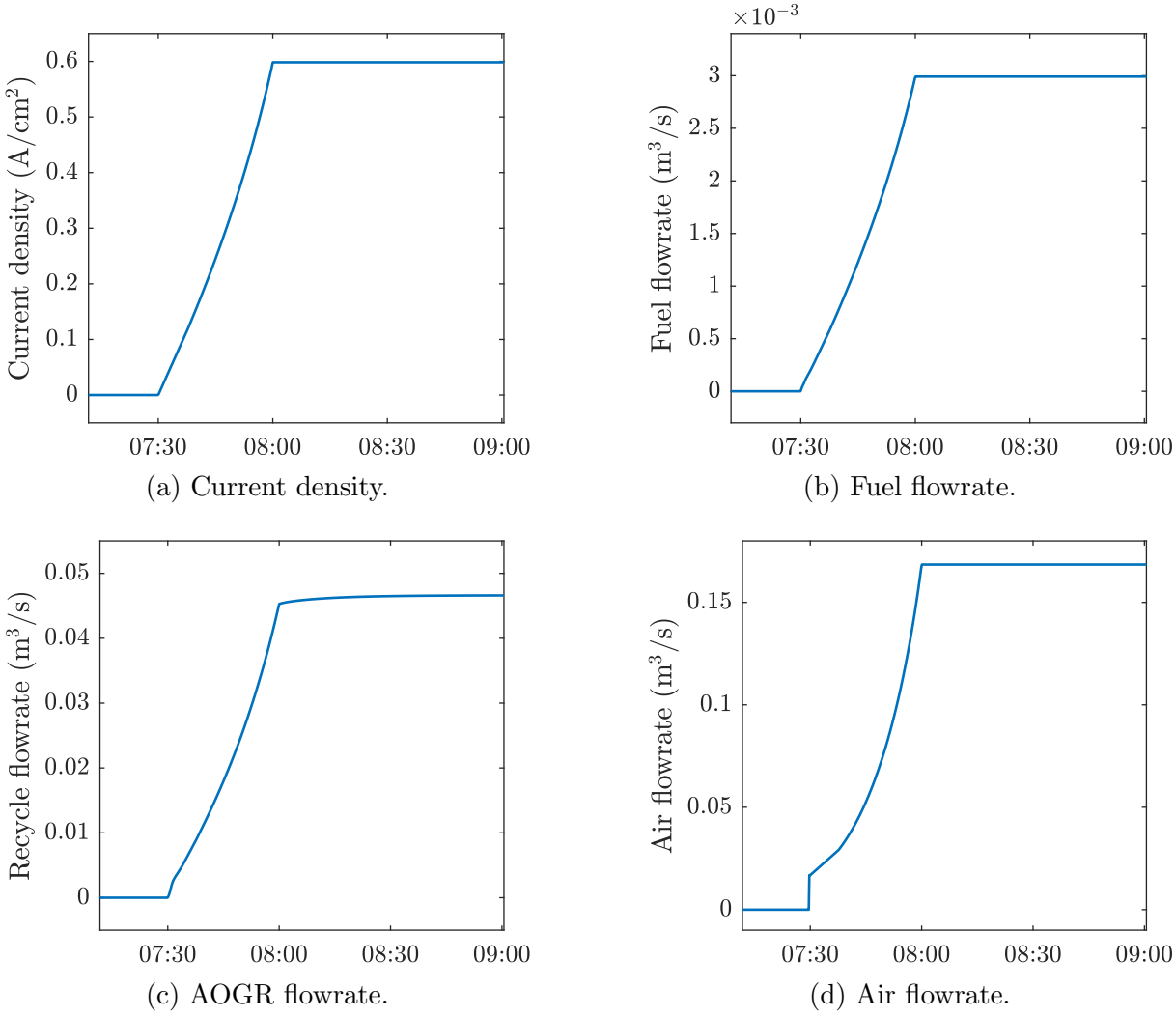

(a) Current density.

(b) Fuel flowrate.

(c) AOGR flowrate.

(d) Air flowrate.

Figure 7.3: Variation in current and gas flow rates during start-up.

investigated:

- Scenario 1: Start-up following overnight cool-down, in which the stack temperature is above 600°C, as shown in Table 7.1, with no electrical heating required, and
- Scenario 2: Start-up following weekend cool-down, with prior electrical heating of the SOFC system, since the stack temperature cooled below 600°C, as shown in Table 7.1.

7.4.1 Start-up procedure

A start-up duration of 30 minutes is specified, defined to be the time taken for the nominal current density to increase from zero to its nominal value of $0.6\,\mathrm{A\,cm^{-2}}$, as shown in Figure 7.3a. A duration of 30 minutes corresponds to start-up times investigated in simulations conducted by M.-H. Chen et al. [119], and the state-of-the-art reported by Schauperl in the COMPASS project [138]. Therefore, for full load operation at 08:00 hours, ramp-up of the current commences at 07:30 hours. The current density is increased using the feed-forward controller lookup table approach, to attempt to achieve a linear ramp-up of stack power.

The fuel, AOGR, and air flow rates are increased with the current, according to the feed-forward control strategy presented in Section 3.14, and are shown in Figures 7.3b to 7.3d. To initiate the reforming reactions before start-up, a small quantity of additional fuel and steam are provided to the anode shortly before 07:30 hours. The steam could be provided either by a water tank and steam generator or using a catalytic partial oxidation reformer, however, neither are modelled in this thesis. The internal reforming reactions generate hydrogen, and since there is no current, no hydrogen is consumed in the stack initially. This hydrogen therefore combusts in the burner, generating a large quantity of heat. To limit the temperature rise of the burner, additional cooling air is provided to the system at the beginning of start-up, as shown in Figure 7.3d.

The thermal, chemical reaction, and electrical transients during start-up will all be presented in the following. Discussion of the thermal transients are split between Scenarios 1 and 2. However, the chemical reaction and electrical transients are largely identical for both scenarios, and hence only the results following overnight cool-down will be presented.

7.4.2 Thermal transients following overnight cool-down

The thermal response of the SOFC system during start-up is shown in Figure 7.4, following both overnight and weekend cool-down. After overnight cool-down, the stack temperature in Figure 7.4a decreased initially from 652°C to a minimum of 628°C at 07:40 hours due

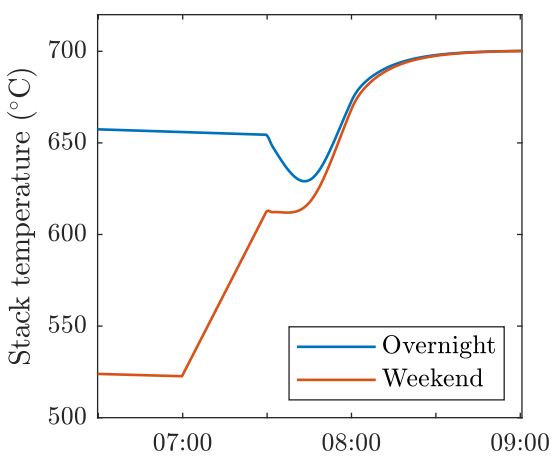

(a) Stack temperature.

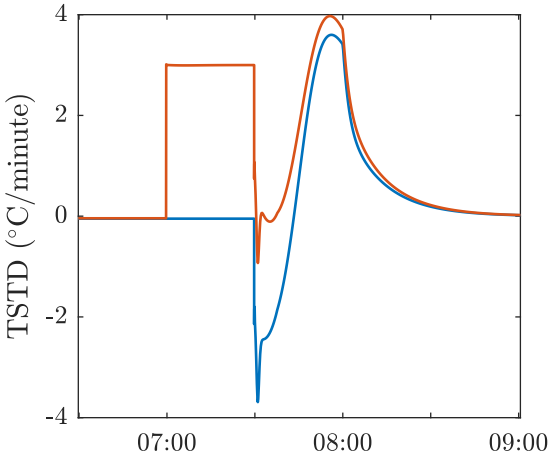

(b) $\mathrm{d}T_S/\mathrm{d}t$.

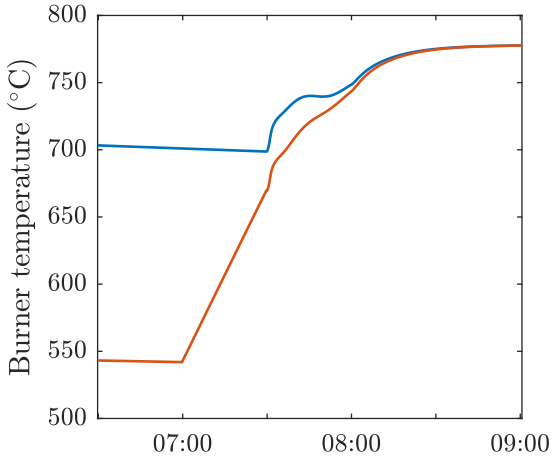

(c) Burner temperature.

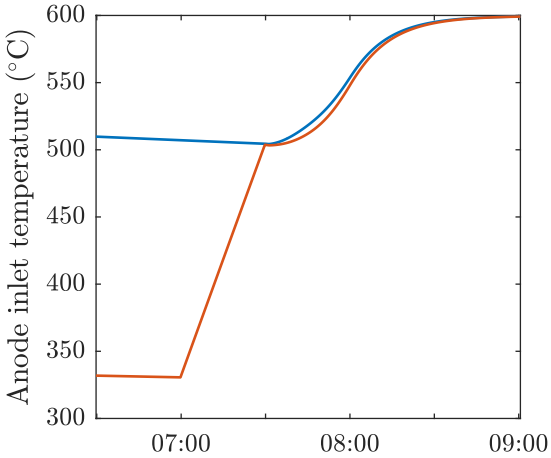

(d) Anode inlet temperature.

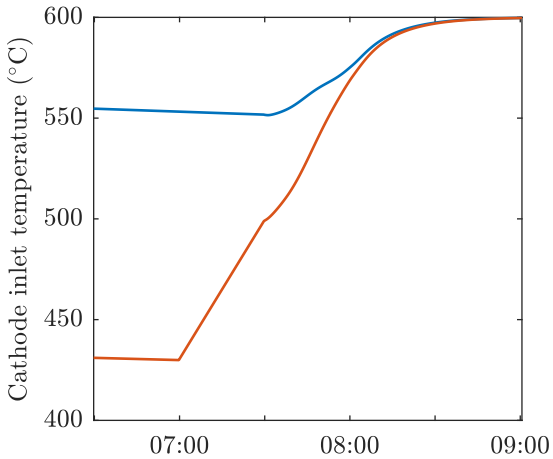

(e) Cathode inlet temperature.

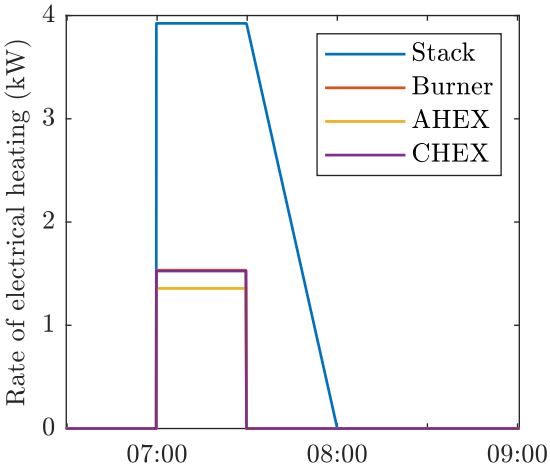

(f) Heat-up power after weekend.

Figure 7.4: Thermal transients during start-up after overnight and weekend cool-downs.

to the initial cooling from the reforming reactions during start-up. As the current density increased, the heat generation from the H2X reaction within the SOFC increased, and subsequently the stack temperature increased. At 08:00, the nominal stack current had been reached, but the thermal inertia of the SOFC system meant that the design stack temperature of 700°C was not reached until 09:00 hours, one hour later.

The initial decrease and subsequent increase in temperature caused two spikes in the time derivative of the stack temperature ($\mathrm{d}T_S/\mathrm{d}t$) shown in Figure 7.4b, each with a magnitude of nearly $4\,^{\circ}\mathrm{C\,min^{-1}}$. The $\mathrm{d}T_S/\mathrm{d}t$ returned to zero once the stack temperature reached its steady-state value of 700°C at 09:00 hours. Despite the relatively slow ramp rate, the magnitude of the $\mathrm{d}T_S/\mathrm{d}t$ was significantly larger than during load changes in Chapter 5, and larger than the maximum $\mathrm{d}T_S/\mathrm{d}t$ of $2\,^{\circ}\mathrm{C\,min^{-1}}$ allowed in the constraints defined in Table 3.1. This was due in part to the reduced performance of the feed-forward controller of the air flow rate uses in this chapter. It would be desirable for a system designer to implement an improved feedback control strategy for the flow rate which can better minimise thermal gradients during start-up, as presented in Chapter 5. Thereby, the temperature gradients could be reduced without having to reduce the current ramp-rate.

The reforming reactions generated hydrogen which when combusted in the burner produced additional heat. Therefore, the burner temperature in Figure 7.4c increased from 699°C at 07:30 hours, initially very steeply and until reaching 740°C at 07:45 hours. The burner temperature then levelled off due to the reduction in the hydrogen mole fraction in the anode off-gas, and the cooler stack off-gas. Following that, the burner temperature trends followed the stack temperature, until the burner temperature reached its design value of 777°C at 09:00 hours. The cathode inlet and anode inlet temperatures in Figures 7.4d to 7.4e followed the trend in burner temperature during start-up, increasing from 504°C and 552°C to their design value of 600°C at 09:00 hours. The thermal inertia of the AHEX and CHEX meant their temperature increases were smoother than the temperature increase of the burner.

7.4.3 Thermal transients following weekend cool-down

Following weekend cool-down, electrical heating of the SOFC components is required. The rate of electrical heating within each of the SOFC system components is shown in Figure 7.4f. The rate of electrical heating was calculated such that the SOFC system components could be heated to within 100°C of their design values after 30 minutes of heating. Because the SOFC stack is the heaviest component, it required nearly 4 kW heating power during the 30 minutes heat-up. The burner, AHEX, and CHEX all required about 1.5 kW heating power during the 30 minutes heat-up.

The electrical heating elements for all four of the hot SOFC system components are switched on at 07:00 hours on Monday morning. At 07:30 hours, start-up commences, and the heating of the AHEX, CHEX, and burner are switched off. The rate of electrical heating in the stack is gradually decreased during the 30 minutes of start-up, to help counter the cooling effect of internal reforming during start-up, seen in Figure 7.4a.

The thermal transients of the SOFC system following weekend cool-down are also shown in Figure 7.4. The electrical heating caused the temperature of the four hot SOFC system components to increase to within 100°C of their operating temperature between 07:00 and 07:30. The stack temperature increased from 520°C to 610°C in Figure 7.4a, the burner temperature increased from 540°C to 670°C in Figure 7.4c, the anode inlet temperature increased from 330°C to 500°C in Figure 7.4d, and the cathode inlet temperature increased from 430°C to 500°C in Figure 7.4e.

From 07:30 hours, start-up of the SOFC system proceeded in the same way as following overnight cool-down. The thermal transients in each of the four components were very similar to those observed following overnight cool-down, shown in the same plots in Figure 7.4. The notable differences between the two responses was the initial more rapid temperature increase after 07:30 hours following weekend cool-down. This was achieved partly by the gradual ramp-down of the electrical heating power in the SOFC stack, as shown in Figure 7.4f. This heating effect counteracted the stack cooling by the endothermic internal reforming reactions in the stack at the beginning of start-up. Therefore, no

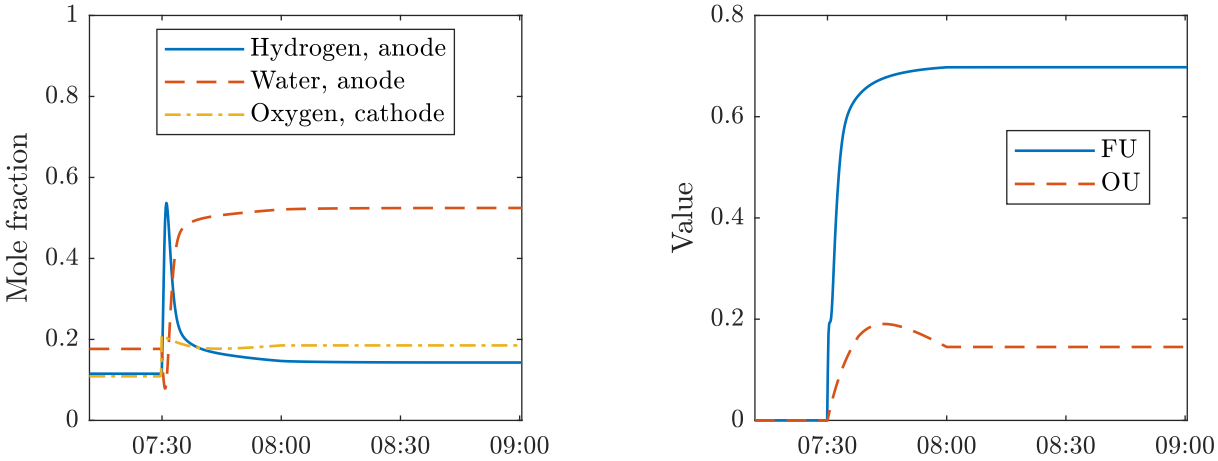

(a) Mole fraction. (b) U_f, U_o.

Figure 7.5: Chemical reaction transients during start-up.

significant decrease in stack temperature was observed at 07:30 in Figure 7.4a, and only a very brief negative $\mathrm{d}T_S/\mathrm{d}t$ of $0.4\,^{\circ}\mathrm{C\,min^{-1}}$ was observed in Figure 7.4b.

7.4.4 Chemical reaction transients

The chemical reaction transients of the SOFC system during start-up are shown in Figure 7.5. Figure 7.5a shows the hydrogen mole fraction at the anode spiked up to 0.55, and the water mole fraction dropped down to 0.1, at the beginning of start-up at 07:30 hours. The production of hydrogen and consumption of water were due to the internal reforming of the methane when fuel methane was first supplied to the SOFC system at 07:30 hours. After 07:30 hours, the current was ramped-up leading to the H2X reaction consuming hydrogen and producing water at the anode. Therefore, between 07:30 hours and 08:00 hours, the mole fraction of hydrogen decreased to a steady state value of 0.18, and the mole fraction of water increased to a steady state value of 0.53.

As the current and flow rates are ramped-up during start-up between 07:30 hours and 08:00 hours, the fuel utilisation (U_f) and oxygen utilisation (U_o) in Figure 7.5b increased. The U_f reached its steady-state design value of 0.7 at 08:00. The U_o overshot, due to the lower air stoichiometry required at low current densities. This can be seen by the more curved ramp-up in the air flow rate according to the lookup table approach presented in

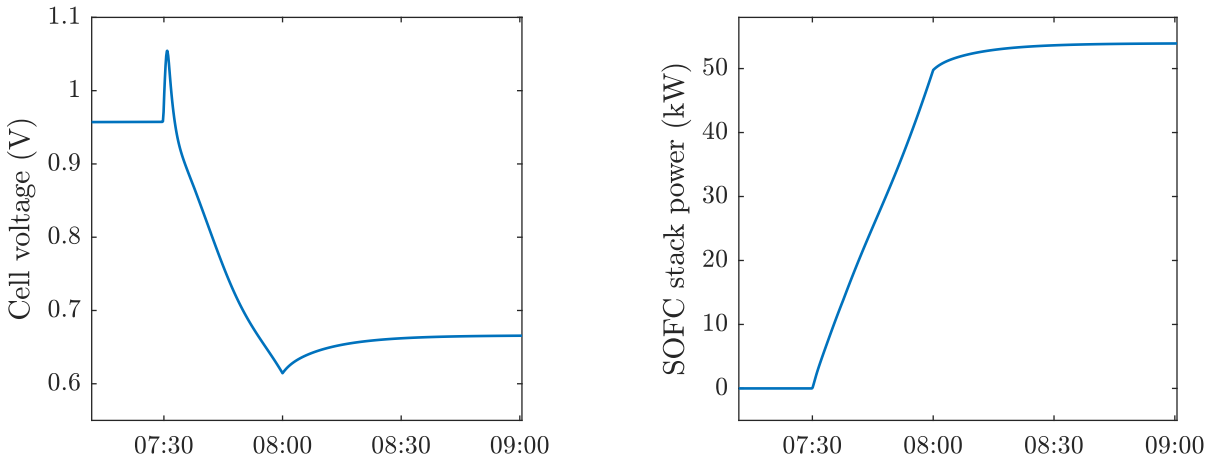

(a) Cell voltage.

(b) Stack power.

Figure 7.6: Electrical transients during start-up.

Figure 7.3d.

7.4.5 Electrical transients

The electrical responses of the SOFC system are discussed in this section. Figure 7.6a shows the variation in cell voltage during start-up. Initially, when no current is drawn, the cell voltage is the OCV. At 07:30 hours, when fuel was supplied to the anode, the cell voltage increased rapidly from its initial value of 0.96 V to a maximum of 1.05 V. This was caused by the increase in the hydrogen mole fraction and decrease in the water mole fraction shown in Figure 7.5a. As the current in Figure 7.3a ramped-up, and the hydrogen mole fraction decreased and the water mole fraction increased at the anode, the OCV returned to its initial value of 0.96 V. The increasing voltage losses associated with the increasing current, meant the cell voltage decreased from 07:30 hours to a minimum of 0.62 V at maximum power at 08:00 hours, at which point the current density had reached its nominal value. As the stack continued to heat-up after 08:00 hours, the ASR decreased, and the cell voltage recovered to 0.67 V.

The variation in the stack power during start-up is shown in Figure 7.6b. The stack power increased with the current relatively linearly up to 50 kW at 08:00. The thermal inertia of the SOFC system caused the undershoot of the cell voltage in Figure 7.6a, and

meant that the nominal stack power of 54 kW was reached only once the stack temperature in Figure 7.4a reached 700°C at 09:00 hours. This could be accounted for by a power-based controller, rather than the current-based controller currently implemented. In such a controller, the current density could be raised to increase the SOFC power despite the reduced temperature. One alternative for the SOFC-battery hybrid system presented in Section 6.4, would be to temporarily increase the output of the battery, which would result in a higher rate of discharge. The SOFC would then be able to recharge the battery once it had reached maximum power.

7.4.6 Limitations of the feed-forward control strategy

In this chapter, the feed-forward controller was used to determine the air flow rate based upon the power demand during start-up. This approach, whilst easy to implement in the simulations, has two disadvantages:

- The maximum $\mathrm{d}T_S/\mathrm{d}t$ of up to $4\,^{\circ}\mathrm{C\,min^{-1}}$ observed during start-up was about 10 times larger in magnitude than the $\mathrm{d}T_S/\mathrm{d}t$ observed for load changes in Section 6.4 with the feedback controller. These temperature gradients are outside the safe operating window presented in Section 3.12, and are likely to lead to accelerated degradation of the SOFC stack.

- The lookup tables are tabulated for a stack temperature of 700°C, however at 08:00 hours the stack temperature was about 650°C, which meant that the cooling flow rate was too high, and the full 54 kW was not attained until the stack temperature reached 700°C. The lookup tables for the fuel and AOGR flow rates are also only calculated for 700°C, however, this is acceptable, since U_f and steam-to-carbon ratio are much less sensitive to temperature.

It is expected that with an improved control strategy for the air flow rate, the thermal transients of the SOFC system could be reduced, but such work is considered to be beyond the scope of this thesis.

7.5 Discussion and conclusions

This chapter presented the cool-down, shut-down and start-up of an SOFC system on an HGV vehicle over a one-week period with 8 hours of operation each weekday. It was shown in Section 7.2 that the SOFC system could be shut-down safely within a few seconds when the vehicle systems are switched off. The SOFC system was insulated with 15 cm of micro-porous insulation, and after overnight cool-down, the stack had cooled down by less than 100°C, so no heat-up was required the next day prior to start-up.

Start-up was identified as the most challenging aspect of the operation. A small quantity of steam was required to initiate the internal reforming reactions before current was drawn. The feed-forward control strategy for the air flow rate resulted in a maximum $\mathrm{d}T_S/\mathrm{d}t$ of $4\,^{\circ}\mathrm{C\,min^{-1}}$, double the value of $2\,^{\circ}\mathrm{C\,min^{-1}}$ permitted by the safe operating window in Table 3.1, despite a start-up time of 30 minutes. Therefore, the requirements to protect stack lifetime were not met, and unless an improved control strategy could reduce the maximum $\mathrm{d}T_S/\mathrm{d}t$, a slower start-up would be required. This risks accelerated degradation, and reduced SOFC performance in comparison to the lifetime analysis presented in Section 6.5. Additionally, the specification of the lookup table for the air flow rate at 700°C meant that the nominal stack power was not reached until the stack temperature reached 700°C almost an hour after start-up had completed.

The start-up time of 30 minutes for the SOFC system is a disadvantage for vehicle applications, although HGVs do benefit from having a predictable weekly schedule [205]. The SOFC system would need to be started prematurely each day before driving, up to a maximum of 30 minutes before. How quickly the vehicle could start moving would depend on the state-of-charge of the battery onboard. Provided the battery had sufficient capacity, driving could commence before the SOFC system has reached its nominal power. The optimum time to start the SOFC system could be further investigated in future work. If necessary the capacity of the battery could also be increased.

One option would that the vehicle could start driving once the SOFC system has reached its minimum part load of 13 kW defined in Section 6.4. Hybridisation with a

battery provides the benefit that the vehicle can already start driving, even if the SOFC has not reached its nominal power.

After weekend cool-down, heat-up of the SOFC system was required before start-up could commence. Heat-up took 30 minutes and required 4 kW h of electrical heating distributed over the four hotbox components. This was less than 10 % of the 46 kW h battery capacity required for a charge-sustaining strategy for an HGV driving the Heavy Heavy-Duty Diesel Truck drive cycle presented in Chapter 6. This shows that the same battery could be used to heat-up the SOFC system, and it would still have enough capacity to complete the required drive cycles during HGV operation.

Chapter 8

Conclusions & Outlook

This final chapter presents the conclusions and identifies future work that could be conducted.

Looking back to Chapter 1, it was illustrated that despite commitments to reduce greenhouse gas (GHG) emissions from transport, the GHG emissions from this sector are rising faster than any other sector globally, and remain the largest contributing sector in Europe. Within the transport sector, heavy goods vehicles (HGVs) were identified as particularly challenging to decarbonise, because zero-emission technologies such as batteries and hydrogen fuel cells may not possess the energy densities required to meet the high power and range requirements.

With that in mind, solid oxide fuel cells (SOFCs) were proposed for HGV propulsion. SOFCs are a high temperature fuel cell that can achieve high system efficiencies of at least 64 %, and internally reform fuels of higher energy density, such as natural gas. This means SOFCs can utilise the existing liquefied natural gas refuelling infrastructure in Europe, whilst synthetic natural gas from renewable sources can be phased in without any changes to refuelling infrastructure or vehicle powertrains, nevertheless offering zero-fossil carbon transport. The production of off-heat for coupled refrigeration or air-conditioning, and the ease in which they can be integrated into a hybrid electric powertrain with a battery, were identified as additional advantages of SOFC systems.

To date there has been no demonstration of SOFC systems for HGV propulsion. Previous experimental studies have focused either on SOFC system as range extenders for passenger vehicles, or as auxiliary power units (APUs) for HGVs. This, therefore, was identified as the main gap in the literature. This thesis set about addressing this gap through dynamic modelling of SOFC systems, as means to investigate the potential of the technology for HGV propulsion. Particular attention was given to the start-up of SOFC systems and thermal gradients, as challenges for their application for HGV propulsion.

8.1 Designing the SOFC system model

Process simulation is a powerful tool to investigate the behaviour of SOFC systems under a variety of operating conditions and scenarios. Chapter 2 reviewed the existing literature, with a particular focus on prior dynamic modelling of SOFC systems, and their application in transport applications. The literature review identified the research gaps to be addressed within this thesis, and, therefore guided the methodology used to model the SOFC system presented in Chapter 3, and the results in the following chapters.

The literature review found that simulations of SOFC systems modelled the components in in either 0D or 1D. Whilst 2D and 3D component models were common too, especially of the SOFC stack, they provide too high a computational burden for control orientated modelling. Of the SOFC system models reviewed, reactions were assumed either at chemical equilibrium or calculated using chemical kinetics. An important distinction of 1D models from their 0D counterparts is their ability to evaluate the spatial variation of the variables within each component. Despite this, the components of the SOFC system were modelled in 0D in this thesis. This was justified on the basis of reduced model complexity allowing different operating scenarios to be more readily investigated, and the ability for all calculated parameters to be measured and validated experimentally. The results presented in Chapter 5 to Chapter 7 focused on the variation of the variables with time, with time derivative of the stack temperature ($\mathrm{d}T_S/\mathrm{d}t$) and fuel util-

isation (U_f) identified as key parameters. Generalised component models were set up to model each of the SOFC system components, including conservation of mass, energy, and species. An electrical model for the SOFC stack calculated the voltage losses using a temperature-dependent area specific resistance (ASR) equation, a simple method suitable for 0D models. The performance of the heat exchangers could be adequately estimated by assuming they maintained constant effectiveness in part load operation. This formed the basis of both the steady-state and dynamic simulations conducted within this thesis.

The electrical efficiency of SOFC systems was identified as a key performance indicator in the literature review, with the steady-state sensitivity to a number of system parameters commonly investigated. In Chapter 3, the U_f was constrained to prevent fuel starvation, and subsequent oxidation of the anode. The steam-to-carbon ratio (S/C ratio) was constrained to prevent carbon deposition at the anode. The stack temperature, stack temperature difference, and burner temperature were shown to be important parameters for design of an SOFC system under steady-state conditions, and required suitable sizing of the blowers and heat exchangers. During dynamic operation, the $\mathrm{d}T_S/\mathrm{d}t$ was an additional parameter selected to maximise the lifetime of the SOFC stack. The $\mathrm{d}T_S/\mathrm{d}t$ was constrained to prevent high thermal stresses within the SOFC stack. These criteria were used to form a process control strategy for the SOFC system. The literature review showed that whilst a number of authors had developed dynamic SOFC system models, very few investigated transient responses, open loop or closed loop, in a systematic way.

A number of authors identified that SOFC systems can be combined with a battery in a hybrid system, and presented energy management strategies for a variety of stationary and mobile applications. In most cases, the SOFC stack was operated under steady-state conditions: only Sorrentino et al. [38] and Kistner et al. [105] presented dynamic control strategies for the SOFC system.

The literature review found that SOFC systems have primarily been deployed in stationary applications, but that a number of projects have demonstrated SOFC systems as APUs, especially for HGVs and in shipping. However, there has been no demonstra-

tion of SOFC systems for HGV propulsion to date, and this therefore helps to form the motivation of this thesis.

The SOFC system model in this thesis was first developed in Engineering Equation Solver (EES) to conduct the steady-state simulations, whilst Simscape in the MATLAB Simulink environment was used to conduct the dynamic simulations. Simulation workflows combining the two were introduced in Chapter 3 and used in the subsequent result chapters of this thesis. The advantages of EES were its in-built thermodynamic properties, and the ease of solving complex systems of algebraic equations. The advanced differential equation solvers, and the ability to effectively dynamically model physical systems of coupled thermal, chemical and electrical transients, were key advantages of Simscape for the dynamic simulations.

A number of important gaps in the literature were identified, and based on this the objectives of the thesis were set. Few dynamic process simulations in the literature modelled heat losses adequately, and investigated different operational modes including start-up, shut-down, and load change necessary for HGV propulsion. No existing literature was identified which conducted dynamic process simulation of SOFC systems when subjected to drive cycles associated with HGV propulsion. Additionally, none of the dynamic simulations reviewed published data on the thermal properties of the components they modelled, making it challenging to compare and validate the work in this thesis with prior dynamic modelling work conducted. This thesis sought to address those gaps.

8.2 Presenting and validating the model

The steady-state characteristics of the SOFC system model were presented in Chapter 4. The current density-voltage (iV) characteristics were validated against results from numerous experimental studies in the literature. They showed that the open circuit voltage (OCV) agreed well with the results found. The assumption that the voltage losses could be calculated with an ASR was shown to be reasonable at least for operation with wet

hydrogen or methane, including the variation in ASR with temperature. The ASR at the reference temperature was extracted from the literature, and its variation with temperature from the Arrhenius parameters from Gubner [73].

No suitable experimental data was identified in the literature to validate the SOFC system model, and therefore, the model was validated against a steady-state model presented by Peters et al. [16] instead. A detailed analysis of the steady-state electrical, chemical reaction, and thermal performance of the SOFC system with varying U_f and recirculation ratio was performed to sense-check the model. The results showed excellent agreement with those presented by Peters et al. [16], and included a weighting factor to account for the effect of the reforming reactions on gas composition at the anode, when calculating the OCV in the electrical model of the SOFC stack. The model presented here expanded upon theirs by including an heat exchanger model, heat losses, and accumulation terms to conduct a transient analysis in the following chapters.

To meet the first objective of Section 2.8.4, Chapter 5 presented the dynamic response of the SOFC system modelled using Simscape. A detailed analysis of the open loop responses to steps in current, and fuel, air, and anode off-gas recirculation (AOGR) flow rates was used as a basis to validate the dynamic model. The controlled response presented in Chapter 5 showed that U_f and S/C ratio could be maintained with feed-forward controllers for the fuel and AOGR flow rates, respectively. It also showed that the SOFC stack temperature can be well maintained during dynamic operation with a feedback controller for the air flow rate. During the controlled transients, the air stoichiometry, burner temperature, stack temperature difference, and $\mathrm{d}T_S/\mathrm{d}t$ all remained within their allowable operating constraints, and thus fulfilled the second objective identified in Section 2.8.4.

8.3 Simulating the SOFC system on an HGV

Chapter 6 and Chapter 7 applied the dynamic SOFC system model presented in Chapter 5 to investigate its performance for HGV propulsion.

Chapter 6 calculated the power requirements for propulsion of a 40 tonne HGV for a number of standardised duty cycles, and found peak power requirements as high as 700 kW, but with significant periods of less than 60 kW power demand. Even with effective control of the fuel, AOGR, and air flows, a 700 kW SOFC system in Section 6.3 was exposed to rapid and large variations in U_f, cell voltage, and temperature gradient during the large transients, due to the rapid variation in power or current demand. Even if maintained within its operating window, significant periods where the SOFC system would need to operate below 10 % part load would pose challenges to maintaining the SOFC stack temperature, as shown in the literature review. There were also concerns about the footprint of a 700 kW SOFC system, or any fuel cell system of this power rating, and whether it would be suitable for an HGV. This analysis met the third objective defined in Section 2.8.4.

Therefore, an SOFC-battery hybrid system was investigated in Section 6.4, to fulfil the fourth objective from Section 2.8.4. The battery was introduced as an energy buffer, with a state machine introduced to vary the SOFC stack power based upon the battery state-of-charge (SoC). Combined with the air flow rate control introduced in Chapter 5, spikes in the SOFC stack $\mathrm{d}T_S/\mathrm{d}t$ could be kept to a minimum, and the other relevant system parameters were likewise maintained. In contrast to Section 6.3, the current or power ramp rate of the SOFC system was determined as an optimization variable to limit the spikes in $\mathrm{d}T_S/\mathrm{d}t$. Despite the relatively large battery, the ten-fold downsizing of the SOFC system is expected to reduce capital costs for the powertrain, and illustrates the advantages of a hybrid powertrain. Section 6.5 showed that the decline in SOFC performance caused by degradation caused issues for long term operation on an HGV. Compensation strategies from a system perspective were proposed, towards meeting the fifth objective in Section 2.8.4.

Chapter 7 extended the drive cycles to cover a one-week period including overnight and weekend cool-down. As per the sixth objective, a heat network was developed to model heat losses from the SOFC system components. The results showed that following

overnight cool-down, the SOFC system components were still hot enough to proceed directly to start-up. However, start-up was relatively challenging: It could be achieved in 30 minutes with a maximum $\mathrm{d}T_S/\mathrm{d}t$ of nearly $4\,^{\circ}\mathrm{C\,min^{-1}}$, which was significantly larger than for the load changes presented in Chapter 6. Following weekend cool-down, a heat-up procedure for the SOFC system was required, with the heat provided by electrical heating elements within each of the hot box components. Heat-up of the SOFC system could be achieved within 30 minutes, with start-up taking a further 30 minutes. This investigation took place in light of the seventh and final objective. The electrical energy requirement for heat-up was less than 10 % of required battery capacity for propulsion, and could therefore be comfortably achieved without increasing the battery capacity on the vehicle.

8.4 Summary and future work

This thesis has presented and validated a flexible SOFC system model which investigated the potential of SOFC systems for HGV propulsion. It has shown that with adequate control, and with hybridisation with a battery, SOFC systems can meet the propulsion requirements of an HGV. Achieving rapid start-up of the SOFC system was identified as the most challenging aspect of SOFC system operation, because of the difficulties in limiting temperature gradients, as well as the reduced performance of the SOFC system.

In terms of the modelling, a key uncertainty was the lack of suitable experimental data to validate the model, but through detailed analysis of the steady-state and dynamic results, the model behaviour could be sense-checked. The model developed in this thesis was generalised, and can therefore be easily applied to a great number of different applications and drive cycles. The model was developed from scratch, and can help form the basis of future work on the subject. Firstly, possible improvements to the model are suggested, followed by additional results that could be collected.

8.4.1 Improving the SOFC stack model

The system model has some limitations, and can be improved in a number of ways. A main limiting factor are the thermal gradients within the SOFC stack during dynamic operation. This could be investigated in more detail by constructing a 1D model of the SOFC stack. A 1D model offers two main advantages over a 0D model:

- Spatial thermal gradients are resolved in the direction of gas flow. This is useful when investigating the impact of transient conditions on system operation, and provides additional insight when compared to the $\mathrm{d}T_S/\mathrm{d}t$ and stack temperature difference, which are the parameters used in the 0D model of the SOFC stack. In particular, cold-spots due to the cooling effect of the endothermic methane steam reforming reaction could be identified.

- The variation in composition in the anode and cathode channels is resolved in the direction of gas flow. The OCV can be calculated more accurately based upon the average local composition. This avoids the issue in the 0D stack model, where a composition weighting factor was used to estimate the OCV. The variation in current density in the direction of gas flow can likewise be calculated.

Switching from 0D to a 1D SOFC stack model would require calculating the rate of the internal reforming reactions using chemical kinetics, as shown in Section 2.1.4 of the literature review. This has the disadvantage that a more detailed knowledge of the stack geometries is required, and thus the model becomes less generalised.

Further refinements of the SOFC stack model could be the relaxation of some of the model assumptions. In the model presented in this thesis, it was assumed that carbon deposition could be avoided by maintaining the S/C ratio at 2.5. Peters et al. [16] calculated the rate of the carbon deposition reactions based upon the equilibrium assumption. The advantage of this approach is that it takes into account the effect of both temperature and composition of the anode channel. This is potentially important during start-up following cool-down, where the stack temperature is lower initially.

8.4.2 Improving the BoP component models

There is also room for improvement of the balance of plant (BoP) models. A number of the model assumptions applied not only to the SOFC stack but also to the BoP components. One notable assumption of this model was the fixed heat capacity of the solid system components. Inclusion of the variation of their heat capacity with temperature may have an impact on the heat losses during overnight pauses and longer shutdowns. Of the BoP component models, the cathode heat exchanger could be improved by taking into account the variation in effectiveness at part load. There was also a lack of data in the literature about the mass of the components. If reliable data could be provided, this would increase confidence in the thermal transients results presented in this thesis.

The blower model was assumed to operate at fixed efficiency. A constant pressure drop on both the air side and fuel side of the SOFC system was assumed. The steady-state results validated against those of Peters et al. [16] in Chapter 4, showed that the efficiency of the system was sensitive to the blower model assumptions. The blower models could be improved by taking into account the variation in their efficiency, and the pressure drop across the system components under part load operation.

8.4.3 Improving the stack temperature control

The proportional feedback controller presented in this thesis enabled tight control of the SOFC stack temperature following changes in load by manipulating the air flow. Consideration of the feasibility of the controller on a real SOFC system was not covered within this thesis. One likely issue on a real system is the precision of the thermocouples. Additionally, the proportional controller only worked when the stack temperature was close to its design temperature. During start-up a lookup table approach had to be used, which resulted in a much larger $\mathrm{d}T_S/\mathrm{d}t$. Future work could investigate a method to control the stack temperature during start-up, which improves upon the lookup table approach.

The state machine presented in Chapter 6 could also be improved by including additional states. This would result in a more granular control of the power demand from

the SOFC system based on the battery SoC, and could potentially allow for downsizing of the battery.

8.4.4 Improving the validation work

Within this thesis, only the iV characteristics were validated against experimental data, whilst the SOFC system results were validated only against other modelling results. A full validation of the dynamic modelling results was not conducted, only a comparison with the settling times. Therefore, the validation work could be significantly expanded and improved, particularly for the dynamic response presented in Chapter 5. One challenge has been the lack of experimental work in the literature with sufficient data such as the thermal mass of the system components published accompanying their results.

Therefore, the validation could ideally be performed with experimental work in the laboratory at the Centre for Fuel Cell and Hydrogen Research in the University of Birmingham. Of particular interest in the dynamic validation would be the measured $\mathrm{d}T_S/\mathrm{d}t$ during load changes and start-up, as well as the U_f during load changes to avoid fuel starvation, since this was identified as the most critical for operation of the SOFC system on an HGV.

8.4.5 Presentation of further results

With the model presented in this thesis, further results could be presented. A few of the possibilities are proposed in the following.

- Based upon the sizing of the SOFC-battery hybrid system for HGV propulsion, an estimation of the footprint of the powertrain could be made. As a result, the feasibility of an SOFC powertrain being installed on a vehicle could be assessed in more detail.

- An additional sensitivity analysis to a number of parameters could be performed. The dynamic performance of the SOFC system with varying mass of the system

components could be of particular interest. If future improvements in stack and BoP components can reduce their size and volume footprint, SOFC technology could become more attractive for vehicle propulsion.

- Integrating the ageing model introduced for the SOFC stack into the dynamic SOFC system model and including the operating strategies presented in Section 6.5. This would allow for more accurate sizing of the SOFC system and battery in Chapter 6 to meet the power requirements of the various drive cycles for HGV propulsion. The ageing model could be expanded to include the effect of thermal cycling and temperature gradients in the degradation rate, to investigate the role that repeated cool-down and start-up of the SOFC stack plays in its lifetime performance.

- Consideration of the thermal power requirements, in addition to the electrical power requirements, for applications where the heat of the SOFC system can be used. For example, for refrigeration onboard an HGV [25], or for air conditioning onboard a construction vehicle.

References

[1] IPCC. *Climate Change 2022: Mitigation of Climate Change. Contribution of Working Group III to the Sixth Assessment Report of the Intergovernmental Panel on Climate Change*. Cambridge University Press: Cambridge, UK, 2022. DOI: 10.1017/9781009157926.

[2] European Environment Agency. *Approximated estimates for greenhouse gas emissions, 2022*. EEA: Brussels, Belgium, 2023.

[3] Department for Transport. *Greenhouse gas emissions by transport mode: United Kingdom, 1990-2021*. ENV0201. HM Government: London, UK, 2023.

[4] European Environment Agency. *Reducing greenhouse gas emissions from heavy-duty vehicles in Europe*. EEA: Brussels, Belgium, 2022. DOI: 10.2800/066953.

[5] European Automobile Manufacturers' Association. *Vehicles on European Roads, February 2024*. ACEA: Brussels, Belgium, 2024.

[6] European Commission. *Impact Assessment, Accompanying the document: Proposal for a Regulation of the European Parliament and of the Council setting CO2 emission performance standards for new heavy duty vehicles*. European Commission: Brussels, Belgium, 2018.

[7] Department for Transport. *Average heavy goods vehicle fuel consumption, Great Britain: 2003 to 2016*. Table TSGB0304 (ENV0104). HM Government: London, UK, 2017.

[8] Department for Transport. *Average new car and light goods vehicle (LGV) fuel consumption: Great Britain, 1997-2020*. Table ENV0103 (TSGB0303). HM Government: London, UK, 2021.

[9] C. Cunanan, M.-K. Tran, Y. Lee, S. Kwok, V. Leung, & M. Fowler. "A Review of Heavy-Duty Vehicle Powertrain Technologies: Diesel Engine Vehicles, Battery Electric Vehicles, and Hydrogen Fuel Cell Electric Vehicles". *Clean Technologies* **3** (2021), 474–489. DOI: 10.3390/cleantechnol3020028.

[10] Natural Gas Vehicle Association Europe. *Natural Gas Vehicle Catalogue 2019*. NGVA Europe: Brussels, Belgium, 2019.

[11] Forschungzentrum Jülich. *brennstoffzelle-aufbau.poster.jpeg*. 2022. URL: https://www.fz-juelich.de/en/images/energyenvironment/brennstoffzelle-aufbau (visited on 02/02/2023).

[12] A. J. Jacobson. "Materials for Solid Oxide Fuel Cells". *Chemistry of Materials* **22** (2010), 660–674. DOI: 10.1021/cm902640j.

[13] L. Blum, H.-P. Buchkremer, S. Gross, A. Gubner, L. G. J. de Haart, H. Nabielek, W. J. Quadakkers, U. Reisgen, M. J. Smith, R. Steinberger-Wilckens, R. W. Steinbrech, F. Tietz, & I. C. Vinke. "Solid Oxide Fuel Cell Development at Forschungszentrum Juelich". *Fuel Cells* **7** (2007), 204–210. DOI: 10.1002/fuce.200600039.

[14] R. Peters, L. Blum, R. Deja, I. Hoven, W. Tiedemann, S. Küpper, & D. Stolten. "Operation Experience with a 20 kW SOFC System". *Fuel Cells* **14** (2014), 489–499. DOI: 10.1002/fuce.201300184.

[15] R. T. Leah, A. Bone, E. Hammer, A. Selcuk, M. Rahman, A. Clare, L. Rees, N. Lawrence, A. Ballard, T. Domanski, S. Mukerjee, & M. Selby. "Development of High Efficiency Steel Cell Technology for Multiple Applications". *ECS Transactions* **78** (2017), 2005. DOI: 10.1149/07801.2005ecst.

[16] R. Peters, R. Deja, L. Blum, J. Pennanen, J. Kiviaho, & T. Hakala. "Analysis of solid oxide fuel cell system concepts with anode recycling". *International Journal of Hydrogen Energy* **38** (2013), 6809–6820. DOI: 10.1016/j.ijhydene.2013.03.110.

[17] H. Apfel, M. Rzepka, H. Tu, & U. Stimming. "Thermal start-up behaviour and thermal management of SOFC's". *Journal of Power Sources* **154** (2006), 370–378. DOI: 10.1016/j.jpowsour.2005.10.052.

[18] M. Halinen, O. Thomann, & J. Kiviaho. "Experimental study of SOFC system heat-up without safety gases". *International Journal of Hydrogen Energy* **39** (2014), 552–561. DOI: 10.1016/j.ijhydene.2013.10.043.

[19] N. P. Brandon, P. Aguiar, D. Brett, R. N. Bull, I. Coop, R. Galloway, G. Hayes, K. Lillie, C. Mellors, M. Millward, & A. Tilley. "Design and Characterisation of a Fuel Cell-Battery Powered Hybrid System for Vehicle Applications". Vehicle Power and Propulsion Conference. IEEE: Windsor, UK, 2006, pp. 1–6. DOI: 10.1109/VPPC.2006.364381.

[20] Y. Bessekon, P. Zielke, A. C. Wulff, & A. Hagen. "Simulation of a SOFC/Battery powered vehicle". *International Journal of Hydrogen Energy* **44** (2019), 1905–1918. DOI: 10.1016/j.ijhydene.2018.11.126.

[21] Elcogen. *Solid Oxide cell stack*. URL: https://elcogen.com/products/solid-oxide-cell-stacks/ (visited on 10/04/2022).

[22] B. P. Borglum & H. Ghezel-Ayagh. "Development of Solid Oxide Fuel Cells at Versa Power Systems and Fuel Cell Energy". *ECS Transactions* **57** (2013), 61–66. DOI: 10.1149/05701.0061ecst.

[23] J. A. Sanguesa, V. Torres-Sanz, P. Garrido, F. J. Martinez, & J. M. Marquez-Barja. "A Review on Electric Vehicles: Technologies and Challenges". *Smart Cities* **4** (2021), 372–404. DOI: 10.3390/smartcities4010022.

[24] K. Poornesh, K. P. Nivya, & K. Sireesha. “A Comparative study on Electric Vehicle and Internal Combustion Engine Vehicles”. 2020 International Conference on Smart Electronics and Communication (ICOSEC). IEEE: Trichy, India, 2020, pp. 1179–1183. DOI: 10.1109/ICOSEC49089.2020.9215386.

[25] V. Venkataraman, A. W. Pacek, & R. Steinberger-Wilckens. “Coupling of a Solid Oxide Fuel Cell Auxiliary Power Unit with a Vapour Absorption Refrigeration System for Refrigerated Truck Application”. *Fuel Cells* **16** (2016), 273–293. DOI: 10.1002/fuce.201500124.

[26] M. A. Khaleel & J. R. Selman. “Chapter 11 - Cell, Stack and System Modelling”. *High Temperature and Solid Oxide Fuel Cells*. Ed. by S. C. Singhal & K. Kendall. Elsevier Science: Amsterdam, 2003, pp. 291–331. DOI: 10.1016/B978-185617387-2/50028-3.

[27] EG&G Technical Services, Inc. *Seventh Edition Fuel Cell Handbook*. Technical Report. National Energy Technology Laboratory: Pittsburgh, US and Morgantown, US, 2004. DOI: 10.2172/834188.

[28] M. Bavarian, M. Soroush, I. G. Kevrekidis, & J. B. Benziger. “Mathematical Modeling, Steady-State and Dynamic Behavior, and Control of Fuel Cells: A Review”. *Industrial & Engineering Chemistry Research* **49** (2010), 7922–7950. DOI: 10.1021/ie100032c.

[29] F. Mueller, F. Jabbari, R. Gaynor, & J. Brouwer. “Novel solid oxide fuel cell system controller for rapid load following”. *Journal of Power Sources* **172** (2007), 308–323. DOI: 10.1016/j.jpowsour.2007.05.092.

[30] S. M. C. Ang, E. S. Fraga, N. P. Brandon, N. J. Samsatli, & D. J. L. Brett. “Fuel cell systems optimisation – Methods and strategies”. *International Journal of Hydrogen Energy* **36** (2011), 14678–14703. DOI: 10.1016/j.ijhydene.2011.08.053.

[31] C. Bao, Y. Wang, D. Feng, Z. Jiang, & X. Zhang. “Macroscopic modeling of solid oxide fuel cell (SOFC) and model-based control of SOFC and gas turbine hybrid

system". *Progress in Energy and Combustion Science* **66** (2018), 83–140. DOI: 10.1016/j.pecs.2017.12.002.

[32] J. Meusinger, E. Riensche, & U. Stimming. "Reforming of natural gas in solid oxide fuel cell systems". *Journal of Power Sources* **71** (1998), 315–320. DOI: 10.1016/S0378-7753(97)02763-8.

[33] A. Chitsaz, J. Hosseinpour, & M. Assadi. "Effect of recycling on the thermodynamic and thermoeconomic performances of SOFC based on trigeneration systems; A comparative study". *Energy* **124** (2017), 613–624. DOI: 10.1016/j.energy.2017.02.019.

[34] F. Yilmaz & M. Ozturk. "Design and modeling of an integrated combined plant with SOFC for hydrogen and ammonia generation". *International Journal of Hydrogen Energy* **47** (2022), 31911–31926. DOI: 10.1016/j.ijhydene.2022.01.249.

[35] A. Akroot, L. Namli, & H. Ozcan. "Compared Thermal Modeling of Anode- and Electrolyte-Supported SOFC-Gas Turbine Hybrid Systems". *Journal of Electrochemical Energy Conversion and Storage* **18** (2021), 011001. DOI: 10.1115/1.4046185.

[36] P. Lisbona, A. Corradetti, R. Bove, & P. Lunghi. "Analysis of a solid oxide fuel cell system for combined heat and power applications under non-nominal conditions". *Electrochimica Acta* **53** (2007), 1920–1930. DOI: 10.1016/j.electacta.2007.08.046.

[37] J. Kupecki. "Off-design analysis of a micro-CHP unit with solid oxide fuel cells fed by DME". *International Journal of Hydrogen Energy* **40** (2015), 12009–12022. DOI: 10.1016/j.ijhydene.2015.06.031.

[38] M. Sorrentino & C. Pianese. "Control Oriented Modeling of Solid Oxide Fuel Cell Auxiliary Power Unit for Transportation Applications". *Journal of Fuel Cell Science and Technology* **6** (2009), 041011. DOI: 10.1115/1.3081475.

[39] M. Gallo, D. Marra, M. Sorrentino, C. Pianese, & S. F. Au. "A versatile computational tool for model-based design, control and diagnosis of a generic Solid Oxide Fuel Cell Integrated Stack Module". *Energy Conversion and Management* **171** (2018), 1514–1528. DOI: 10.1016/j.enconman.2018.06.062.

[40] J. Saarinen, M. Halinen, J. Ylijoki, M. Noponen, P. Simell, & J. Kiviaho. "Dynamic Model of 5kW SOFC CHP Test Station". *Journal of Fuel Cell Science and Technology* **4** (2007), 397–405. DOI: 10.1115/1.2759502.

[41] D. Saebea, S. Authayanun, Y. Patcharavorachot, & A. Arpornwichanop. "Effect of anode-cathode exhaust gas recirculation on energy recuperation in a solid oxide fuel cell-gas turbine hybrid power system". *Energy* **94** (2016), 218–232. DOI: 10.1016/j.energy.2015.10.138.

[42] S. Huang, C. Yang, H. Chen, N. Zhou, & D. Tucker. "Coupling impacts of SOFC operating temperature and fuel utilization on system net efficiency in natural gas hybrid SOFC/GT system". *Case Studies in Thermal Engineering* **31** (2022), 101868. DOI: 10.1016/j.csite.2022.101868.

[43] R. J. Braun, S. A. Klein, & D. T. Reindl. "Evaluation of system configurations for solid oxide fuel cell-based micro-combined heat and power generators in residential applications". *Journal of Power Sources* **158** (2006), 1290–1305. DOI: 10.1016/j.jpowsour.2005.10.064.

[44] L. Mantelli, M. De Campo, M. Ferrari, & L. Magistri. "Fuel flexibility for a turbocharged SOFC system". *Energy Procedia* **158** (2019), 1974–1979. DOI: 10.1016/j.egypro.2019.01.454.

[45] L. Nousch, M. Hartmann, & A. Michaelis. "Improvements of Micro-CHP SOFC System Operation by Efficient Dynamic Simulation Methods". *Processes* **9** (2021), 1113. DOI: 10.3390/pr9071113.

[46] K. J. Albrecht & R. J. Braun. "Dynamic Modeling of SOFC Cogeneration Systems for Light Commercial Applications". ASME 2014 12th International Conference on

Fuel Cell Science, Engineering and Technology. Boston, Massachusetts, USA, 2014, pp. 1–10. DOI: 10.1115/FuelCell2014-6403.

[47] F. Mueller, J. Brouwer, F. Jabbari, & S. Samuelsen. "Dynamic Simulation of an Integrated Solid Oxide Fuel Cell System Including Current-Based Fuel Flow Control". *Journal of Fuel Cell Science and Technology* **3** (2005), 144–154. DOI: 10.1115/1.2174063.

[48] Lin Zhang, Xi Li, Jianhua Jiang, Shuanghong Li, Jie Yang, & Jian Li. "Dynamic modeling and analysis of a 5-kW solid oxide fuel cell system from the perspectives of cooperative control of thermal safety and high efficiency". *International Journal of Hydrogen Energy* **40** (2015), 456–476. DOI: 10.1016/j.ijhydene.2014.10.149.

[49] R. Roberts & J. Brouwer. "Dynamic simulation of a pressurized 220 kW solid oxide fuel-cell-gas-turbine hybrid system: Modeled performance compared to measured results". *Journal of Fuel Cell Science and Technology* **3** (2006), 18–25. DOI: 10.1115/1.2133802.

[50] M. Engelbracht, R. Peters, L. Blum, & D. Stolten. "Analysis of a Solid Oxide Fuel Cell System with Low Temperature Anode Off-Gas Recirculation". *Journal of The Electrochemical Society* **162** (2015), F982–F987. DOI: 10.1149/2.0371509jes.

[51] D. Andersson, E. Åberg, J. Eborn, J. Yuan, & B. Sundén. "Dynamic modeling of a solid oxide fuel cell system in Modelica". *Proceedings 8th International Modelica Conference*. Linköping University Electronic Press, Linköpings universitet: Dresden, Germany, 2011, pp. 593–602. DOI: 10.3384/ecp11063593.

[52] S. K. Mazumder, S. K. Pradhan, J. Hartvigsen, D. Rancruel, M. R. von Spakovsky, & M. Khaleel. "A multidiscipline and multi-rate modeling framework for planar solid-oxide-fuel-cell based power-conditioning system for vehicular APU". *SIMULATION* **84** (2008), 413–426. DOI: 10.1177/0037549708097713.

[53] M. Peksen, A. Al-Masri, L. Blum, & D. Stolten. "3D transient thermomechanical behaviour of a full scale SOFC short stack". *International Journal of Hydrogen Energy* **38** (2013), 4099–4107. DOI: 10.1016/j.ijhydene.2013.01.072.

[54] R. J. Braun. "Optimal Design and Operation of Solid Oxide Fuel Cell Systems for Small-scale Stationary Applications". PhD thesis. University of Wisconsin-Madison: Madison, US, 2002.

[55] G. A. Whyatt & L. A. Chick. *Electrical Generation for More-Electric Aircraft Using Solid Oxide Fuel Cells*. U.S. Department of Energy Report. Pacific Northwest National Laboratory: Richland, US, 2012, p. 9.2.

[56] I. Rossi, A. Traverso, & D. Tucker. "SOFC/Gas Turbine Hybrid System: A simplified framework for dynamic simulation". *Applied Energy* **238** (2019), 1543–1550. DOI: 10.1016/j.apenergy.2019.01.092.

[57] D. Lee, T.-Q. Quach, T. P. Israel, K. Y. Ahn, Y. Bae, & Y. S. Kim. "Analysis of start-up behavior based on the dynamic simulation of an SOFC–engine hybrid system". *Energy Conversion and Management* **272** (2022), 116384. DOI: 10.1016/j.enconman.2022.116384.

[58] M. Engelbracht, R. Peters, L. Blum, & D. Stolten. "Comparison of a fuel-driven and steam-driven ejector in solid oxide fuel cell systems with anode off-gas recirculation: Part-load behavior". *Journal of Power Sources* **277** (2015), 251–260. DOI: 10.1016/j.jpowsour.2014.12.009.

[59] P. Aguiar. "Modelling studies of solid oxide fuel cells with internal methane steam reforming". PhD thesis. Imperial College London: London, UK, 2003.

[60] E. Achenbach. "Three-dimensional and time-dependent simulation of a planar solid oxide fuel cell stack". *Journal of Power Sources* **49** (1994), 333–348. DOI: 10.1016/0378-7753(93)01833-4.

[61] R. T. Leah, A. Bone, E. Hammer, A. Selcuk, M. Rahman, A. Clare, S. Mukerjee, & M. Selby. "Development Progress on the Ceres Power Steel Cell Technology Platform: Further Progress Towards Commercialization". *ECS Transactions* **78** (2017), 87. DOI: 10.1149/07801.0087ecst.

[62] P. Aguiar, C. S. Adjiman, & N. P. Brandon. "Anode-supported intermediate temperature direct internal reforming solid oxide fuel cell. I: model-based steady-state performance". *Journal of Power Sources* **138** (2004), 120–136. DOI: 10.1016/j.jpowsour.2004.06.040.

[63] P. Aguiar, D. J. L. Brett, & N. P. Brandon. "Feasibility study and techno-economic analysis of an SOFC/battery hybrid system for vehicle applications". *Journal of Power Sources* **171** (2007), 186–197. DOI: 10.1016/j.jpowsour.2006.12.049.

[64] J. Xu & G. F. Froment. "Methane steam reforming, methanation and water-gas shift: I. Intrinsic kinetics". *AIChE Journal* **35** (1989), 88–96. DOI: 10.1002/aic.690350109.

[65] M. Andersson, J. Yuan, & B. Sundén. "Review on modeling development for multiscale chemical reactions coupled transport phenomena in solid oxide fuel cells". *Applied Energy* **87** (2010), 1461–1476. DOI: 10.1016/j.apenergy.2009.11.013.

[66] J. Milewski. "A Mathematical Model of SOFC: A Proposal". *Fuel Cells* **12** (2012), 709–721. DOI: 10.1002/fuce.201100150.

[67] M. Sorrentino, C. Pianese, & Y. G. Guezennec. "A hierarchical modeling approach to the simulation and control of planar solid oxide fuel cells". *Journal of Power Sources* **180** (2008), 380–392. DOI: 10.1016/j.jpowsour.2008.02.021.

[68] X. Zhang, J. Li, G. Li, & Z. Feng. "Development of a control-oriented model for the solid oxide fuel cell". *Journal of Power Sources* **160** (2006), 258–267. DOI: 10.1016/j.jpowsour.2006.01.024.

[69] E. Ivers-Tiffée & A. V. Virkar. "Electrode Polarisations". *High Temperature and Solid Oxide Fuel Cells*. Elsevier, 2003, pp. 229–260. DOI: 10.1016/B978-185617387-2/50026-X.

[70] R. P. O'Hayre, S.-W. Cha, W. G. Colella, & F. B. Prinz. *Fuel Cell Fundamentals*. Third edition. Citation Key Alias: OHayre2016a. John Wiley & Sons Inc: Hoboken, New Jersey, 2016. 1 p.

[71] U. G. Bossel. *Final report on SOFC Data: Facts and Figures*. International Energy Agency: Berne, Switzerland, 1992.

[72] N. F. Bessette, W. J. Wepfer, & J. Winnick. "A Mathematical Model of a Solid Oxide Fuel Cell". *Journal of The Electrochemical Society* **142** (1995), 3792. DOI: 10.1149/1.2048415.

[73] A. Gubner. "Non-Isothermal and Dynamic SOFC Voltage-Current Behavior". *ECS Proceedings Volumes* **2005-07** (2005), 814–826. DOI: 10.1149/200507.0814PV.

[74] Q. Fang, L. Blum, R. Peters, M. Peksen, P. Batfalsky, & D. Stolten. "SOFC stack performance under high fuel utilization". *International Journal of Hydrogen Energy* **40** (2015), 1128–1136. DOI: 10.1016/j.ijhydene.2014.11.094.

[75] A. T. Schmidt. "Dynamic Modeling Of Solid Oxide Fuel Cell Systems For Commercial Building Applications". Master of Science (Engineering). Colorado School of Mines: Golden, Colorado, 2011.

[76] W. M. Kays & A. L. London. *Compact heat exchangers*. 2nd ed. Mechanical Engineering. McGraw-Hill: New York; London, 1964. 272 pp.

[77] E. Riensche, U. Stimming, & G. Unverzagt. "Optimization of a 200 kW SOFC cogeneration power plant: Part I: Variation of process parameters". *Journal of Power Sources* **73** (1998), 251–256. DOI: 10.1016/S0378-7753(98)00002-0.

[78] Bosal. *Sizing Calculator*. 2019. URL: https://calculator.eci.bosal.com/request/input (visited on 12/22/2022).

[79] S. K. Hong, S. K. Dong, & J. B. Yang. "Experimental and simulated investigation of 1 kW solid oxide fuel cell balance of power system". *Journal of Power Sources* **214** (2012), 28–32. DOI: 10.1016/j.jpowsour.2012.04.044.

[80] J. Kupecki, K. Motylinski, & J. Milewski. "Dynamic Modelling of the Direct Internal Reforming (DIR) of Methane in 60-cell Stack with Electrolyte Supported Cells". *Energy Procedia* **105** (2017), 1700–1705. DOI: 10.1016/j.egypro.2017.03.553.

[81] S. Yu, D. Hong, Y. Lee, S. Lee, & K. Ahn. "Development of a catalytic combustor for a stationary fuel cell power generation system". *Renewable Energy* **35** (2010), 1083–1090. DOI: 10.1016/j.renene.2009.10.015.

[82] K. Zhang, A. El-Kharouf, J.-E. Hong, & R. Steinberger-Wilckens. "The effect of aluminium addition on the high-temperature oxidation behaviour and Cr evaporation of aluminised and alumina-forming alloys for SOFC cathode air pre-heaters". *Corrosion Science* **169** (2020), 108612. DOI: 10.1016/j.corsci.2020.108612.

[83] Bosal ECI. *Bosal P5 thin walled exchangers for 400 – 1100°C / 750 – 2000°F*. Datasheet. Bosal Energy Conversion Industry: Vianen, Netherlands, 2018, p. 2.

[84] Y. Wang, L. Wehrle, A. Banerjee, Y. Shi, & O. Deutschmann. "Analysis of a biogas-fed SOFC CHP system based on multi-scale hierarchical modeling". *Renewable Energy* **163** (2021), 78–87. DOI: 10.1016/j.renene.2020.08.091.

[85] M. Gallo, D. Marraa, M. Sorrentino, C. Pianese, & S. F. Aub. "Development of a Dynamic Model for Diagnosis and Control of an Integrated Stack Module Based on Solid Oxide Fuel Cells". *Energy Procedia* **105** (2017), 1936–1941. DOI: 10.1016/j.egypro.2017.03.563.

[86] R. Peters, M. Engelbracht, W. Tiedemann, I. Hoven, R. Deja, V. N. Nguyen, L. Blum, & D. Stolten. "Development and Test of a Solid Oxide Fuel Cell Subsystem with a Low Temperature Anode Off-Gas Recirculation". *ECS Transactions* **78** (2017), 2489. DOI: 10.1149/07801.2489ecst.

[87] M. Powell, K. Meinhardt, V. Sprenkle, L. Chick, & G. McVay. "Demonstration of a highly efficient solid oxide fuel cell power system using adiabatic steam reforming and anode gas recirculation". *Journal of Power Sources* **205** (2012), 377–384. DOI: 10.1016/j.jpowsour.2012.01.098.

[88] S. Inac, S. O. Unverdi, & A. Midilli. "A parametric study on thermodynamic performance of a SOFC oriented hybrid energy system". *International Journal of Hydrogen Energy* **44** (2019), 10043–10058. DOI: 10.1016/j.ijhydene.2019.01.247.

[89] P. H. Wagner, Z. Wuillemin, D. Constantin, S. Diethelm, J. Van herle, & J. Schiffmann. "Experimental characterization of a solid oxide fuel cell coupled to a steam-driven micro anode off-gas recirculation fan". *Applied Energy* **262** (2020), 114219. DOI: 10.1016/j.apenergy.2019.114219.

[90] Z. Zeng, Y. Qian, Y. Zhang, C. Hao, D. Dan, & W. Zhuge. "A review of heat transfer and thermal management methods for temperature gradient reduction in solid oxide fuel cell (SOFC) stacks". *Applied Energy* **280** (2020), 115899. DOI: 10.1016/j.apenergy.2020.115899.

[91] P. Aguiar, C. S. Adjiman, & N. P. Brandon. "Anode-supported intermediate-temperature direct internal reforming solid oxide fuel cell: II. Model-based dynamic performance and control". *Journal of Power Sources* **147** (2005), 136–147. DOI: 10.1016/j.jpowsour.2005.01.017.

[92] E. Achenbach. "Response of a solid oxide fuel cell to load change". *Journal of Power Sources* **57** (1995), 105–109. DOI: 10.1016/0378-7753(95)02263-5.

[93] H. Cao & X. Li. "Thermal Management-Oriented Multivariable Robust Control of a kW-Scale Solid Oxide Fuel Cell Stand-Alone System". *IEEE Transactions on Energy Conversion* **31** (2016), 596–605. DOI: 10.1109/TEC.2015.2510030.

[94] Y. Xing, R. Costa-Castelló, J. Na, & H. Renaudineau. "Control-oriented modelling and analysis of a solid oxide fuel cell system". *International Journal of Hydrogen Energy* **45** (2020), 20659–20672. DOI: 10.1016/j.ijhydene.2020.02.061.

[95] T. Xue, X. Wu, D. Zhao, Y. Xu, J. Jiang, Z. Deng, X. Fu, & X. Li. "Fault-tolerant control for steam fluctuation in SOFC system with reforming units". *International Journal of Hydrogen Energy* **44** (2019), 23360–23376. DOI: 10.1016/j.ijhydene.2019.07.007.

[96] S. Rafikiran, C. H. Basha, M. Murali, & F. Fathima. "Design and performance evaluation of solid oxide-based fuel cell stack for electric vehicle system with modified marine predator optimized fuzzy controller". *Materials Today: Proceedings* **60** (2022), 1898–1904. DOI: 10.1016/j.matpr.2022.01.002.

[97] X.-l. Wu, Y.-w. Xu, D.-q. Zhao, X.-b. Zhong, D. Li, J. Jiang, Z. Deng, X. Fu, & X. Li. "Extended-range electric vehicle-oriented thermoelectric surge control of a solid oxide fuel cell system". *Applied Energy* **263** (2020), 114628. DOI: 10.1016/j.apenergy.2020.114628.

[98] G. Sandrini, M. Gadola, D. Chindamo, & L. Zecchi. "Model of a Hybrid Electric Vehicle Equipped with Solid Oxide Fuel Cells Powered by Biomethane". *Energies* **16** (2023), 4918. DOI: 10.3390/en16134918.

[99] C.-H. Yang, S.-C. Chang, Y.-H. Chan, & W.-S. Chang. "A Dynamic Analysis of the Multi-Stack SOFC-CHP System for Power Modulation". *Energies* **12** (2019), 3686. DOI: 10.3390/en12193686.

[100] Z. Wu, P. Zhu, J. Yao, P. Tan, H. Xu, B. Chen, F. Yang, Z. Zhang, E. Porpatham, & M. Ni. "Dynamic modeling and operation strategy of natural gas fueled SOFC-Engine hybrid power system with hydrogen addition by metal hydride for vehicle applications". *eTransportation* **5** (2020), 100074. DOI: 10.1016/j.etran.2020.100074.

[101] I. Ismael, A. A. El-Fergany, E. A. Gouda, & M. F. Kotb. "Cooperation search algorithm for optimal parameters identification of SOFCs feeding electric vehicle at steady and dynamic modes". *International Journal of Hydrogen Energy* **50** (2024), 1395–1407. DOI: 10.1016/j.ijhydene.2023.07.027.

[102] A. Elakya, J. S. Geetha, M. S. Moorthy, & S. Surya. "Revolutionizing EV Charging: Mobile Power Solutions with SOFC Technology". 2024 International Conference on Inventive Computation Technologies (ICICT). IEEE: Lalitpur, Nepal, 2024, pp. 1–7. DOI: 10.1109/ICICT60155.2024.10544751.

[103] Z. Dimitrova & F. Maréchal. "Environomic design for electric vehicles with an integrated solid oxide fuel cell (SOFC) unit as a range extender". *Renewable Energy* **112** (2017), 124–142. DOI: 10.1016/j.renene.2017.05.031.

[104] L. Nousch & M. Hartmann. "Hot Stand-by Operation Effect of a SOFC Hybrid System for Decentralized Power Generation in Single-Family Homes". *Proceedings of the 15th European SOFC and SOE Forum*. EFCF 2022. Lucerne, Switzerland, 2022, pp. 359–368.

[105] L. Kistner, A. Bensmann, & R. Hanke-Rauschenbach. "Optimal Design of a Distributed Ship Power System with Solid Oxide Fuel Cells under the Consideration of Component Malfunctions". *Applied Energy* **316** (2022), 119052. DOI: 10.1016/j.apenergy.2022.119052.

[106] S. J. McPhail, S. Frangini, J. Laurencin, E. Effori, A. Abaza, A. K. Padinjarethil, A. Hagen, A. Léon, A. Brisse, D. Vladikova, B. Burdin, F. R. Bianchi, B. Bosio, P. Piccardo, R. Spotorno, H. Uchida, P. Polverino, E. A. Adinolfi, F. Postiglione, J.-H. Lee, H. Moussaoui, & J. Van Herle. "Addressing planar solid oxide cell degradation mechanisms: A critical review of selected components". *Electrochemical Science Advances* **2** (2022), e2100024. DOI: 10.1002/elsa.202100024.

[107] T. Skafte, J. Hjelm, P. Blennow, & C. Graves. “Quantitative review of degradation and lifetime of solid oxide cells and stacks”. *Proceedings of the 12th European SOFC and SOE Forum*. EFCF 2016. 2016.

[108] R. Leah, A. Bone, P. Hjalmarsson, A. Selcuk, M. Lankin, M. Rahman, A. Clare, G. Reade, F. Felix, J. De Vero, X. Wang, S. Mukerjee, & M. Selby. “Commercialization of the Steel Cell® technology: Latest Update”. 14th European SOFC & SOE Forum 2020. Zenodo: Lucerne, 2021. DOI: 10.5281/zenodo.4518770.

[109] Q. Fang, U. De Haart, D. Schäfer, F. Thaler, V. Rangel-Hernandez, R. Peters, & L. Blum. “Degradation Analysis of an SOFC Short Stack Subject to 10,000 h of Operation”. *Journal of The Electrochemical Society* **167** (2020), 144508. DOI: 10.1149/1945-7111/abc843.

[110] T. Horita. “Recent achievements of advanced evaluation and analysis technologies for the durability of Solid Oxide Fuel Cells stacks in Japan”. *Proceedings of the 15th European SOFC and SOE Forum*. EFCF 2022. **A**. Lucerne, Switzerland, 2022, pp. 20–28.

[111] M. Noponen, H. Granö-Fabritius, S. Pylypko, & E. Õunpuu. “SOC development at Elcogen”. *Proceedings of the 15th European SOFC and SOE Forum*. EFCF 2022. **A**. Lucerne, Switzerland, 2022, pp. 68–73.

[112] A. Mai, J. G. Grolig, V. Sarda, H. Bausinger, A. Schuler, A. Chakradeo, & S. R. Mayur. “Status of Hexis and mPower’ SOFC and SOEC Activities”. *Proceedings of the 15th European SOFC and SOE Forum*. EFCF 2022. **A**. Lucerne, Switzerland, 2022, p. 57.

[113] C. Walter, K. Schwarze, M. Boltze, K. Herbrig, & A. Surrey. “Status of Stack & System Development at Sunfire”. 14th European SOFC & SOE Forum 2020. Zenodo: Lucerne, 2021. DOI: 10.5281/zenodo.4518729.

[114] P. Holtappels, H. Mehling, S. Roehlich, S. S. Liebermann, & U. Stimming. "SOFC System Operating Strategies for Mobile Applications". *Fuel Cells* **5** (2005), 499–508. DOI: 10.1002/fuce.200400088.

[115] L. Petruzzi, S. Cocchi, & F. Fineschi. "A global thermo-electrochemical model for SOFC systems design and engineering". *Journal of Power Sources* **118** (2003), 96–107. DOI: 10.1016/S0378-7753(03)00067-3.

[116] A. Selimovic, M. Kemm, T. Torisson, & M. Assadi. "Steady state and transient thermal stress analysis in planar solid oxide fuel cells". *Journal of Power Sources* **145** (2005), 463–469. DOI: 10.1016/j.jpowsour.2004.11.073.

[117] M. Hanasaki, C. Uryu, T. Daio, T. Kawabata, Y. Tachikawa, S. M. Lyth, Y. Shiratori, S. Taniguchi, & K. Sasaki. "SOFC Durability against Standby and Shutdown Cycling". *Journal of The Electrochemical Society* **161** (2014), F850–F860. DOI: 10.1149/2.0421409jes.

[118] Y. Kim, M. Son, & I.-B. Lee. "Numerical Study of a Planar Solid Oxide Fuel Cell during Heat-up and Start-up Operation". *Industrial & Engineering Chemistry Research* **50** (2011), 1360–1368. DOI: 10.1021/ie100783g.

[119] M.-H. Chen & T. L. Jiang. "The analyses of the start-up process of a planar, anode-supported solid oxide fuel cell using three different start-up procedures". *Journal of Power Sources* **220** (2012), 331–341. DOI: 10.1016/j.jpowsour.2012.08.018.

[120] V. Lawlor. *Method for quickly heating a fuel cell system.* Patent WO2019068123A1. AVL List GmbH: Graz, Austria, 2019.

[121] M. Carré, R. Brandenburger, W. Friede, F. Lapicque, U. Limbeck, & P. da Silva. "Feed-forward control of a solid oxide fuel cell system with anode offgas recycle". *Journal of Power Sources* **282** (2015), 498–510. DOI: 10.1016/j.jpowsour.2015.02.053.

[122] M.-H. Chen & T. L. Jiang. "The analyses of the heat-up process of a planar, anode-supported solid oxide fuel cell using the dual-channel heating strategy". *International Journal of Hydrogen Energy* **36** (2011), 6882–6893. DOI: 10.1016/j.ijhydene.2011.02.129.

[123] A. Hagen, A. Wulff, P. Zielke, X. Sun, B. Talic, I. Ritucci, H. Frandsen, S. Jensen, W. Kiebach, & P. Hendriksen. "SOFC stacks for mobile applications with excellent robustness towards thermal stresses". *International Journal of Hydrogen Energy* **45** (2020), 29201–29211. DOI: 10.1016/j.ijhydene.2020.07.159.

[124] U. Bossel. "Rapid Startup SOFC Modules". *Energy Procedia* **28** (2012), 48–56. DOI: 10.1016/j.egypro.2012.08.039.

[125] M. Peksen. "3D transient multiphysics modelling of a complete high temperature fuel cell system using coupled CFD and FEM". *International Journal of Hydrogen Energy* **39** (2014), 5137–5147. DOI: 10.1016/j.ijhydene.2014.01.063.

[126] D. Hart, S. Jones, X. Cordobes, G. Bates, & J. Lewis. *The Fuel Cell Industry Review 2022*. ERM: London, UK, 2023, p. 84.

[127] J. Zizelman, S. Shaffer, & S. Mukerjee. "Solid Oxide Fuel Cell Auxiliary Power Unit - A Development Update". SAE 2002 World Congress & Exhibition. Society of Automotive Engineers, Inc.: Detroit, Michigan, USA, 2002, pp. 2002–01–0411. DOI: 10.4271/2002-01-0411.

[128] D. T. Hennessy. *Solid Oxide Fuel Cell Development for Auxiliary Power in Heavy Duty Vehicle Applications*. U.S. Department of Energy Report. Delphi Automotive Systems, LLC.: Washington, DC, United States, 2010. DOI: 10.2172/1055694.

[129] G. E. Geiger. *Recovery Act: Solid Oxide Fuel Cell Diesel Auxiliary Power Unit Demonstration*. U.S. Department of Energy Report. Delphi Automotive Systems, LLC.: Washington, DC, United States, 2013. DOI: 10.2172/1196763.

[130] C. J.-P. Vesely, B. S. Fuchs, & C. W. Booten. *Diesel Fueled SOFC for Class 7/Class 8 On-Highway Truck Auxiliary Power*. U.S. Department of Energy Report. Cummins Power Generation: Minneapolis, Minnesota, United States, 2010. DOI: https://doi.org/10.2172/1083010.

[131] J. Rechberger, A. Kaupert, J. Hagerskans, & L. Blum. "Demonstration of the First European SOFC APU on a Heavy Duty Truck". *Transportation Research Procedia* **14** (2016), 3676–3685. DOI: 10.1016/j.trpro.2016.05.442.

[132] K. Kendall, J. Newton, & M. Kendall. "Microtubular SOFC (mSOFC) System in Truck APU Application". *ECS Transactions* **68** (2015), 187–192. DOI: 10.1149/06801.0187ecst.

[133] V. Venkataraman. "Coupling of a solid oxide fuel cell with a vapour absorption refrigeration system for refrigerated truck application". PhD thesis. University of Birmingham: Birmingham, UK, 2017.

[134] B. Pandya. "Integration of a Solid Oxide Fuel Cell system with a heat driven refrigeration system for refrigerated transportation application". PhD thesis. University of Birmingham: Birmingham, UK, 2023.

[135] J. J. Botti, M. J. Grieve, & J. A. Macbain. "Electric Vehicle Range Extension Using an SOFC APU". SAE 2005 World Congress & Exhibition. Society of Automotive Engineers, Inc.: Detroit, Michigan, USA, 2005, pp. 2005–01–1172. DOI: 10.4271/2005-01-1172.

[136] "Nissan SOFC powered vehicle system runs on bioethanol". *Fuel Cells Bulletin* **2016** (2016). Ed. by S. Barrett, 2–3. DOI: 10.1016/S1464-2859(16)30165-1.

[137] V. Lawlor, M. Reissig, J. Makinson, & J. Rechberger. "SOFC System for Battery Electric Vehicle Range Extension: Results of the First Half of the Mestrex Project". *ECS Transactions* **78** (2017), 191. DOI: 10.1149/07801.0191ecst.

[138] R. Schauperl. *Competitive Auxiliary Power Units for vehicles based on metal supported stack technology*. Presentation slides. FCH JU: Brussels, Belgium, 2017.

[139] A. Ballard, T. Domanski, L. Rees, C. Nobbs, N. Lawrence, K. Heffer, J. Harman, C. Evans, P. Barnard, S. Mukerjee, & M. Selby. "Development of the 5kWe SteelCell® Technology Platform for Stationary Power and Transport Applications". *ECS Transactions* **91** (2019), 117. DOI: 10.1149/09101.0117ecst.

[140] E. Skerritt. *Ceres Power Holdings plc Trading update*. Regulatory News Service: London, UK, 2024, p. 2.

[141] "Atrex, Ascend Energy demonstrate ATV with SOFC range-extender". *Fuel Cells Bulletin* **2017** (2017). Ed. by S. Barrett, 3–4. DOI: 10.1016/S1464-2859(17)30139-6.

[142] X. Qin, J. Cao, G. Geng, Y. Li, Y. Zheng, W. Zhang, & B. Yu. "Solid oxide fuel cell system for automobiles". *International Journal of Green Energy* (2022), 1–10. DOI: 10.1080/15435075.2022.2065454.

[143] Y. Miura, S. Takemiya, Y. Fukuyama, T. Kato, S. Taniguchi, & K. Sasaki. "Improvement of the internal reforming of metal-supported SOFC at low temperatures". *International Journal of Hydrogen Energy* **48** (2023), 25487–25498. DOI: 10.1016/j.ijhydene.2023.03.195.

[144] T.-I. Tsai, S. Du, A. Dhir, A. A. Williams, & R. Steinberger-Wilckens. "Modelling a Methane Fed Solid Oxide Fuel Cell With Anode Recirculation System". *ECS Transactions* **57** (2013), 2831–2839. DOI: 10.1149/05701.2831ecst.

[145] A. J. Majewski, U. Bossel, & R. Steinberger-Wilckens. "Catalytic Reforming System Suitable for Transportation Applications". *Fuel Cells* **18** (2018), 535–542. DOI: 10.1002/fuce.201700135.

[146] O. Hodjati-Pugh. "Simulation and Fabrication of a Microtubular Solid Oxide Fuel Cell Stack with Novel Anode Current Collection and Enhanced Thermofluidynamics". PhD thesis. University of Birmingham: Birmingham, UK, 2021.

[147] Y. Al-Sagheer & R. Steinberger-Wilckens. “Energy Management Controller for Fuel Cell Hybrid Electric Vehicle Based on Sat-Nav Data”. *Fuel Cells* **20** (2020), 420–430. DOI: 10.1002/fuce.201900196.

[148] N. Khan, Y. Al-Sagheer, & R. Steinberger-Wilckens. “PEFC System Reactant Gas Supply Management and Anode Purging Strategy: An Experimental Approach”. *Energies* **15** (2022), 288. DOI: 10.3390/en15010288.

[149] F. De Oliveira Gonçalves, E. Savioli Lopes, M. Savioli Lopes, & R. Maciel Filho. “Evaluation of the feasibility of ethanol and gasoline in solid oxide fuel cell vehicles in Brazil”. *International Journal of Hydrogen Energy* **46** (2021), 36381–36397. DOI: 10.1016/j.ijhydene.2021.08.165.

[150] S. Ma, X. Hu, Y. Zhao, X. Wang, & C. Dong. “Design and Evaluation of a Metal-Supported Solid Oxide Fuel Cell Vehicle Power System with Bioethanol Onboard Reforming”. *ACS Omega* **6** (2021), 29201–29214. DOI: 10.1021/acsomega.1c04698.

[151] J. E. Velandia Vargas & J. E. A. Seabra. “Fuel-cell technologies for private vehicles in Brazil: Environmental mirage or prospective romance? A comparative life cycle assessment of PEMFC and SOFC light-duty vehicles”. *Science of The Total Environment* **798** (2021), 149265. DOI: 10.1016/j.scitotenv.2021.149265.

[152] H. Heidary, A. El-Kharouf, R. Steinberger-Wilckens, S. Bozorgmehri, M. Salimi, & M. Golmohammad. “Life cycle assessment of solid oxide fuel cell vehicles in a natural gas producing country; comparison with proton electrolyte fuel cell, battery and gasoline vehicles”. *Sustainable Energy Technologies and Assessments* **59** (2023), 103396. DOI: 10.1016/j.seta.2023.103396.

[153] C. Liao, Y. Tang, Y. Liu, Z. Sun, W. Li, & X. Ma. “Life cycle assessment of the solid oxide fuel cell vehicles using ammonia fuel”. *Journal of Environmental Chemical Engineering* **11** (2023), 110872. DOI: 10.1016/j.jece.2023.110872.

[154] "Wärtsilä marine SOFC for Wallenius car-carrier". *Fuel Cells Bulletin* **2010** (2010). Ed. by S. Barrett, 1. DOI: 10.1016/S1464-2859(10)70169-3.

[155] P. Nehter, B. Wildrath, A. Bauschulte, & K. Leites. "Diesel Based SOFC Demonstrator for Maritime Applications". *ECS Transactions* **78** (2017), 171–180. DOI: 10.1149/07801.0171ecst.

[156] K. Leites. "SchIBZ ® - experiences with liquid fuelled SOFC for ship applications". 14th European SOFC & SOE Forum. European Fuel Cell Forum AG: Lucerne, Switzerland, 2020.

[157] "ShipFC project on first maritime fuel cell to run on green ammonia". *Fuel Cells Bulletin* **2020** (2020). Ed. by S. Barrett, 5–6. DOI: 10.1016/S1464-2859(20)30054-7.

[158] "Norwegian project for ships, offshore power". *Fuel Cells Bulletin* **2020** (2020). Ed. by S. Barrett, 7. DOI: 10.1016/S1464-2859(20)30511-3.

[159] B. McKenna. *Solid Oxide Fuel Cell (SOFC) 4 Maritime*. Mærsk Mc-Kinney Møller Center for Zero Carbon Shipping. 2022. URL: https://www.zerocarbonshipping.com/projects/solid-oxide-fuel-cell-sofc-4-maritime/ (visited on 02/03/2023).

[160] Nautilus. *Newsletter Issue 1*. FCH JU Project. Deutsches Zentrum für Luft- und Raumfahrt: Stuttgart, Germany, 2021.

[161] CEA Tech. *Fuel cell demonstrator to be used on board cruise ship*. CEA. 2020. URL: https://www.cea.fr/cea-tech/english/Pages/2020/fuel-cell-demonstrator-to-be-used-on-board-cruise-ship-fuel-cells-aspx.aspx (visited on 02/22/2022).

[162] "Bloom Energy joins with Samsung Heavy for clean ship power". *Fuel Cells Bulletin* **2020** (2020). Ed. by S. Barrett, 6. DOI: 10.1016/S1464-2859(20)30284-4.

[163] "Doosan and Navig8 to develop marine system with Ceres SOFC unit". *Fuel Cells Bulletin* **2020** (2020). Ed. by S. Barrett, 8. DOI: 10.1016/S1464-2859(20)30575-7.

[164] H. Sumi, S. Nakabayashi, T. Kawada, Y. Uchiyama, N. Uchiyama, & K. Ichihara. "Demonstration of SOFC Power Sources for Drones (UAVs; Unmanned Aerial Vehicles)". *ECS Transactions* **91** (2019), 149. DOI: 10.1149/09101.0149ecst.

[165] "World's first SOFC powered drone uses Elcogen technology". *Fuel Cells Bulletin* **2020** (2020). Ed. by S. Barrett, 6. DOI: 10.1016/S1464-2859(20)30390-4.

[166] HyGear Fuel Cell Systems. *SUAV Main S&T results and foregrounds*. FCH JU: Brussels, Belgium, 2016.

[167] C. Li, K. Cheng, C. Li, X. Xiu, H. Liu, F. Guo, & J. Qin. "Performance analysis of multi turbines and SOFC combined power generation system for hypersonic vehicles". *Applied Thermal Engineering* **257** (2024), 124461. DOI: 10.1016/j.applthermaleng.2024.124461.

[168] D. Tew. *Range Extenders for Electric Aviation with Low Carbon and High Efficiency*. Advanced Research Projects Agency - Energy, U.S. Department of Energy. 2019. URL: https://arpa-e.energy.gov/technologies/programs/reeach (visited on 02/22/2022).

[169] A. Yasin, A. R. Yasin, M. B. Saqib, S. Zia, M. Riaz, R. Nazir, R. A. E. Abdalla, & S. Bajwa. "Fuel Cell Voltage Regulation Using Dynamic Integral Sliding Mode Control". *Electronics* **11** (2022), 2922. DOI: 10.3390/electronics11182922.

[170] R. H. Perry, D. W. Green, & J. O. Maloney, eds. *Perry's chemical engineers' handbook*. 7th ed. McGraw-Hill: New York, 1997. 1 p.

[171] M. Chase Jr., C. Davies, J. Downey Jr., D. Frurip, R.A. McDonald, & A. Syverud. *NIST-JANAF Thermochemical Tables - SRD 13*. National Institute of Standards and Technology: Gaithersburg, MD, United States, 1998. DOI: 10.18434/T42S31.

[172] Mathworks. *Chamber with fixed volume of gas mixture and variable number of ports*. The MathWorks, Inc.: Natick, MA, United States, 2020.

[173] L. van Biert, M. Godjevac, K. Visser, & P. V. Aravind. "Dynamic modelling of a direct internal reforming solid oxide fuel cell stack based on single cell experiments". *Applied Energy* **250** (2019), 976–990. DOI: 10.1016/j.apenergy.2019.05.053.

[174] *Ergonomics of the thermal environment — Methods for the assessment of human responses to contact with surfaces*. Version Edition 1. Geneva, Switzerland, 2006.

[175] Y. Tanaka, K. Sato, A. Yamamoto, & T. Kato. "Development of Anode Off-Gas Recycle Blowers for High Efficiency SOFC Systems". *ECS Transactions* **57** (2013), 443. DOI: 10.1149/05701.0443ecst.

[176] P. Boldrin & N. P. Brandon. "Progress and outlook for solid oxide fuel cells for transportation applications". *Nature Catalysis* **2** (2019), 571–577. DOI: 10.1038/s41929-019-0310-y.

[177] B. Dolenc, P. Boškoski, A. Pohjoranta, M. Noponen, & Đ. Juričić. "Hybrid Approach to Remaining Useful Life Prediction of Solid Oxide Fuel Cell Stack". *ECS Transactions* **78** (2017), 2251–2264. DOI: 10.1149/07801.2251ecst.

[178] Etex Industry. *Promat Technical Data Sheet: PROMALIGHT*. Etex Industry: Sint-Niklaas, Belgium, 2018.

[179] Mathworks. *Simscape Getting Started Guide R2021b*. The MathWorks, Inc.: Natick, MA, United States, 2021.

[180] Mathworks. *Fluid System Modeling - MATLAB & Simulink*. 2022. URL: https://www.mathworks.com/help/simscape/ug/fluid-system-modeling.html (visited on 11/28/2022).

[181] Mathworks. *Gas Models - MATLAB & Simulink*. 2022. URL: https://www.mathworks.com/help/simscape/gas-models.html (visited on 11/25/2022).

[182] M. Riegraf, N. Sata, & R. Costa. "Sulfur-Activated SFM-Based Fully Ceramic Fuel Electrodes for Solid Oxide Cells". *Proceedings of the 15th European SOFC and SOE Forum*. EFCF 2022. **B**. Lucerne, Switzerland, 2022, pp. 28–33.

[183] C. Ferchaud, F. v. Berkel, L. Berkeveld, M. Heijink-Smith, J. Veldhuis, & H. v. Wees. "Cobalt-free air electrode for the next generation of Solid Oxide Cells based on (La,Sr)FeO3 materials". *Proceedings of the 15th European SOFC and SOE Forum*. EFCF 2022. **B**. Lucerne, Switzerland, 2022, pp. 169–178.

[184] S. Golani, A. Weber, F. Wankmüller, W. Herzhof, C. Dellen, & N. H. Menzler. "Impact of GDC interlayer microstructure on strontium zirconate interphase formation and cell performance". *Proceedings of the 15th European SOFC and SOE Forum*. EFCF 2022. **A**. Lucerne, Switzerland, 2022, pp. 173–180.

[185] L. Blum, P. Batfalsky, Q. Fang, L. G. J. d. Haart, J. Malzbender, N. Margaritis, N. H. Menzler, & R. Peters. "SOFC Stack and System Development at Forschungszentrum Jülich". *Journal of The Electrochemical Society* **162** (2015), F1199. DOI: 10.1149/2.0491510jes.

[186] X. Sun, A. K. Clausen, P. V. Hendriksen, A. Hauch, T. Lehtinen, & M. Noponen. "Effect of inlet gas composition on the durability of solid oxide electrolysis cells". *Proceedings of the 15th European SOFC and SOE Forum*. EFCF 2022. **B**. Lucerne, Switzerland, 2022, pp. 489–495.

[187] M. Hauck, M. Schmid, S. Herrmann, B. Polat, B. Steinrücken, L. Poblotzki, J. Weinrich, M. Gaderer, & H. Spliethoff. "Modelling of an RSOC with Open Source Tools". *Proceedings of the 15th European SOFC and SOE Forum*. EFCF 2022. **B**. Lucerne, Switzerland, 2022, pp. 792–801.

[188] M. Yu, X. Sun, Y. Liu, Y. Shang, & M. Chen. "Electrochemical performance of solid oxide cells operated in CO2 electrolysis". *Proceedings of the 15th European SOFC and SOE Forum*. EFCF 2022. **B**. Lucerne, Switzerland, 2022, pp. 893–904.

[189] U. de Haart, Q. Fang, N. H. Menzler, & R. Peters. "Performance enhancement in SOFC stacks with LSC cathodes and LSC cathode contact layers". *Proceedings of the 15th European SOFC and SOE Forum*. EFCF 2022. **A**. Lucerne, Switzerland, 2022, pp. 221–230.

[190] P. Pretschuh, E. Bucher, A. Egger, F. F. Chamasemani, R. Brunner, & W. Sitte. "Electrochemical characterization of the high entropy perovskite La0.2Pr0.2... for solid oxide cell air electrodes". *Proceedings of the 15th European SOFC and SOE Forum*. EFCF 2022. **B**. Lucerne, Switzerland, 2022, pp. 224–235.

[191] S. Chen, Y. Xiao, & Z. Jiao. "Status of SOC Development at Chaozhou Three-Circle". *ECS Transactions* **111** (2023), 565–570. DOI: 10.1149/11106.0565ecst.

[192] A. Mai, J. G. Grolig, V. Sarda, M. Dold, & A. Schuler. "Status of HEXIS' SOFC Module Development". 14th European SOFC & SOE Forum 2020. Zenodo: Lucerne, 2021. DOI: 10.5281/zenodo.4518797.

[193] H. Ghezel-Ayagh & B. P. Borglum. "Review of Progress in Solid Oxide Fuel Cells at FuelCell Energy". *ECS Transactions* **78** (2017), 77. DOI: 10.1149/07801.0077ecst.

[194] T. J. Barlow, S. Latham, I. S. McCrae, & P. G. Boulter. *A reference book of driving cycles for use in the measurement of road vehicle emissions*. ISBN: 978-1-84608-924-4. Transport Research Laboratory: Wokingham, UK, 2009, p. 280.

[195] S. Brown, C. Bryett, & M. Mowle. *In-Service Emissions Performance - Drive Cycles*. National Environment Protection Council: Adelaide, Australia, 1999, p. 43.

[196] F. Zhen, N. N. Clark, C. R. Bedick, M. Gautam, W. S. Wayne, G. J. Thompson, & D. W. Lyons. "Development of a Heavy Heavy-Duty Diesel Engine Schedule for Representative Measurement of Emissions". *Journal of the Air & Waste Management Association* **59** (2009), 950–959. DOI: 10.3155/1047-3289.59.8.950.

[197] United Nations Economic Commission for Europe. *UN GTR No. 4 - Test procedure for compression-ignition (C.I.) engines and positive-ignition (P.I.) engines fuelled with natural gas (NG) or liquefied petroleum gas (LPG) with regard to the emission of pollutants*. Addendum. United Nations: Geneva, Switzerland, 2007, p. 126.

[198] National Renewable Energy Laboratory. *NREL DriveCAT - Chassis Dynamometer Drive Cycles*. URL: https://www.nrel.gov/transportation/drive-cycle-tool (visited on 02/10/2024).

[199] L. Eriksson. *Truck Benchmark model - An open Matlab/Simulink model of a Heavy Duty Truck*. Linköpings universitet. 2018. URL: https://www.vehicular.isy.liu.se/Software/TruckBenchmark_AAC2016/ (visited on 01/02/2020).

[200] D. J. L. Brett, P. Aguiar, N. P. Brandon, R. N. Bull, R. C. Galloway, G. W. Hayes, K. Lillie, C. Mellors, C. Smith, & A. R. Tilley. "Concept and system design for a ZEBRA battery–intermediate temperature solid oxide fuel cell hybrid vehicle". *Journal of Power Sources* **157** (2006), 782–798. DOI: 10.1016/j.jpowsour.2005.12.054.

[201] E. Mulholland. *The revised CO2 standards for heavy-duty vehicles in the European Union*. Policy update. International Council on Clean Transportation: Washington DC, USA, 2024, p. 22.

[202] O. Delgado, F. Rodríguez, & R. Muncrief. *Fuel efficiency technology in European heavy-duty vehicles: Baseline and potential for the 2020–2030 timeframe*. White Paper. International Council on Clean Transportation: Washington, DC, United States, 2017.

[203] A. H. Salari, H. Mirzaeinejad, & M. Fooladi Mahani. "A new control algorithm of regenerative braking management for energy efficiency and safety enhancement of electric vehicles". *Energy Conversion and Management* **276** (2023), 116564. DOI: 10.1016/j.enconman.2022.116564.

[204] B. Sharpe & R. Muncrief. *Literature Review: Real-World Fuel Consumption of Heavy-Duty Vehicles in the United States, China, and the European Union*. International Council on Clean Transportation: Washington, DC, United States, 2015.

[205] European Parliament & Council of the European Union. *Regulation (EC) No 561/2006 of the European Parliament and of the Council of 15 March 2006 on the harmonisation of certain social legislation relating to road transport and amending Council Regulations (EEC) No 3821/85 and (EC) No 2135/98 and repealing Council Regulation (EEC) No 3820/85*. Regulation (EC). European Union: Brussels, Belgium, 2006, pp. L102/1–13.